ON THE MELT RATE OF SUBMERGED SEDIMENT-LADEN ICE

by

Gregory C. Trowse

Submitted in partial fulfillment of the requirements
for the degree of Master of Science

at

Dalhousie University
Halifax, Nova Scotia
April 2013

DALHOUSIE UNIVERSITY

DEPARTMENT OF OCEANOGRAPHY

The undersigned hereby certify that they have read and recommend to the Faculty of Graduate Studies for acceptance a thesis entitled “ON THE MELT RATE OF SUBMERGED SEDIMENT-LADEN ICE” by Gregory C. Trowse in partial fulfillment of the requirements for the degree of Master of Science.

Dated: April 16, 2013

External Examiner: Dominic Groulx, Ph.D., P.Eng.

Supervisor: Alex Hay, Ph.D.

Readers: Paul Hill, Ph.D.

Tetjana Ross, Ph.D.

Barry Ruddick, Ph.D.

DALHOUSIE UNIVERSITY

DATE: April 16, 2013

AUTHOR: Gregory C. Trowse

TITLE: ON THE MELT RATE OF SUBMERGED SEDIMENT-LADEN ICE

DEPARTMENT OR SCHOOL: Department of Oceanography

DEGREE: M.Sc. CONVOCATION: October YEAR: 2013

Signature of Author

This work is dedicated to my beautiful, magnificent, and wondiferous wife Courtney and Rowan Marie Trowse … our greatest gift.

TABLE OF CONTENTS

List of Tables . . . . **viii**

List of Figures . . . . **ix**

Abstract . . . . **xiv**

List of Symbols Used . . . . **xv**

Acknowledgements . . . . **xix**

Chapter 1 Introduction **1**

- 1.1 Outline 1
- 1.2 The Problem 2
  - 1.2.1 Similarities with other off-shore industries 5
- 1.3 Objective 5
- 1.4 Organization 7

Chapter 2 On Ice and Sea Ice **8**

- 2.1 Physical properties of ice and sea ice 8
  - 2.1.1 Density of ice 9
  - 2.1.2 Sea ice salinity 10
  - 2.1.3 Sediment content 13
- 2.2 Thermal properties of ice and sea ice 17
  - 2.2.1 Thermal properties of fresh water ice 17
  - 2.2.2 Thermal properties of sea ice 19
  - 2.2.3 Thermal properties of sediment-laden ice 22
  - 2.2.4 Thermal properties of sediment-laden bubbly sea ice 25
- 2.3 Iceberg deterioration 26
- 2.4 Ice melting due to buoyant vertical convection 29
  - 2.4.1 On gravitational free convection 29
  - 2.4.2 On free convective melting of freshwater ice in freshwater 33

2.4.3 On free convective melting of freshwater ice in saltwater 34

Chapter 3 Ice Melt Rate Theory 46
3.1 General Theory 46
3.1.1 Laminar Case 49
3.1.2 Turbulent Case 50
3.1.3 General Case 50
3.2 Simplified Spherical Theory 51

Chapter 4 Methods 52
4.1 Ice Formation 52
4.1.1 Sediment Addition 53
4.1.2 Ice Density 54
4.1.3 Ice Salinity 55
4.2 Setup 56
4.3 Conditions (S,T,P) 57
4.4 Measuring the Rate of Change 59
4.4.1 Directly Measured Mass 59
4.4.2 Optical Measurement of Volume 61
4.4.3 Line tension 71

Chapter 5 Results 73
5.1 Observations 73
5.2 Interpretation 76
5.2.1 Statistics 76
5.2.2 Nusselt number (Nu) from ice melt data 83

Chapter 6 Discussion 89
6.1 Prandtl Number (Pr) 90
6.2 Grashof Number (Gr) 92
6.2.1 Buoyancy 92
6.2.2 Viscosity 95
6.2.3 Cohesion 96
6.2.4 Transition to turbulence 101

6.3 Rayleigh Number (Ra) 103
6.4 Nusselt Number (Nu) 103
6.5 Melt rate predictions 108

Chapter 7 Conclusions 119
7.1 Heat Requirement (F) 119
7.2 Heat Supply (Q) 120
7.3 Melt Rate (dm/dt) 121
7.4 Future Work 122

Bibliography 125

Appendix A Photographs 129

Appendix B PT and CTD Sensor Data 138

LIST OF TABLES

Table 2.1 Approximate thermal values for ice, sediment, water, and mixtures of, near 0 °C, without consideration of saline effects 25

Table 2.2 Josberger ice melt conditions 43

Table 4.1 Small block ice density 55

Table 4.2 Large block ice density 56

Table 4.3 Summary of averaged far-field conditions 58

Table 4.4 Tower tank gravitational stability 59

Table 4.5 Camera calibration parameters 62

Table 4.6 Small ice block camera test 63

Table 4.7 Dot board camera test 67

Table 4.8 Glass sphere camera test 69

Table 5.1 Small ice block melt statistics 79

Table 5.2 Large ice block melt statistics 80

Table 5.3 Nusselt number statistics 85

Table 6.1 Summary of Prandtl numbers by ice type 92

Table 6.2 Average wall and far field density 94

Table 6.3 Critical length scales for transition to turbulent flow over the region $10^8 \leq \mathrm{Gr_c} \leq 10^9$ 102

Table 6.4 Summary of B, from $\overline{\mathrm{Nu}} = B(\overline{\mathrm{Ra}})^n$ 105

Table 6.5 Predicted lifetimes for ice blocks with initial mass (m_0) of 5000 kg and final mass of 1 kg 113

Table B.1 PT and CTD sampling period and depth 139

Table B.2 Far-field temperature measurements 140

Table B.3 Far-field salinity measurements 141

LIST OF FIGURES

Figure 1.1 Extracted power and reduction in Minas Basin tidal range (*Karsten et al.*, 2008) 3

Figure 2.1 Density of fluid fresh water and sea water as a function of temperature ($T < 10$ °C) 9

Figure 2.2 Density of solid and fluid fresh water ($-6 < T < 6$ °C) 10

Figure 2.3 Sea ice salinity (S_i) as a function of ice growth rate (v_g) for $S_{cw} =$ 30 ppt 13

Figure 2.4 Sediment-laden ice on the banks of the Shubenacadie river 15

Figure 2.5 Ice density and water density as functions of sediment concentration 16

Figure 2.6 Fresh water ice heat capacity and thermal conductivity as functions of temperature 20

Figure 2.7 Sea ice heat capacity and latent heat of fusion as functions of ice temperature (T_i) and ice salinity (S_i) 21

Figure 2.8 Sea ice and bubbly sea ice thermal conductivity as functions of temperature and salinity 23

Figure 2.9 Latent heat of fusion and theoretical melt rate of sediment-laden ice as functions of ice salinity and sediment concentration. 26

Figure 2.10 Average Nusselt number for free-convection flows on a vertical plate (*Eckert and Jackson*, 1951) 32

Figure 2.11 T-S diagram for salt-water solutions showing the location of the freezing point depression line T_{fp}, and maximum density line $T_{\rho max}$ (*Josberger and Martin*, 1981) 36

Figure 2.12 A sketch of the observed flow next to the ice for $T_d < 20$ °C and $30 \leq S_\infty \leq 35$ psu (region II) (*Josberger and Martin*, 1981) 38

Figure 2.13 A sketch of the observed flow next to the ice for $T_d > 25$ °C (region III) (*Josberger and Martin*, 1981) 39

Figure 2.14 Effect of far-field temperature (T_∞) on ice wall temperature (T_w) for sea water salinity (S_∞) of 31 psu 44

Figure 2.15 Effect of far-field temperature (T_∞) on $T_d = T_\infty - T_{fp}$ and $\Delta T = T_\infty - T_w$ for sea water salinity (S_∞) of 31 psu 45

Figure 3.1 Stefan number for freshwater ice and saltwater ice 48

Figure 4.1 Complete distortion model. Contours and arrows representative of spatial correction in pixels due to fisheye lens. 63

Figure 4.2 Barrel camera test photograph - end view 64

Figure 4.3 Barrel camera test photograph - side view 65

Figure 4.4 Sample dot board camera test photograph 66

Figure 4.5 Sample glass sphere image 69

Figure 5.1 Small block sediment-free freshwater (FW) ice, showing melt rate dependence on thermal driving (T_d) for length scales up to 0.3 m ($L \leq 0.3$ m) 74

Figure 5.2 Small block sediment-free freshwater (FW) and sediment-laden freshwater ($\mathrm{FW_{sed}}$) ice, showing melt rate dependence on sediment content for length scales up to 0.3 m ($L \leq 0.3$ m), ($T_d = 15.02$ °C) 74

Figure 5.3 Small block sediment-free saltwater (SW) and sediment-laden saltwater ($\mathrm{SW_{sed}}$) ice, showing melt rate dependence on sediment content for length scales up to 0.3 m ($L \leq 0.3$ m), ($T_d = 15.02$ °C) 75

Figure 5.4 Small block sediment-free freshwater (FW) and sediment-fee saltwater (SW) ice, showing melt rate dependence on salinity for length scales up to 0.3 m ($L \leq 0.3$ m), ($T_d = 15.02$ °C) 75

Figure 5.5 Small block sediment-laden freshwater ($\mathrm{FW_{sed}}$) and sediment-laden saltwater ($\mathrm{SW_{sed}}$) ice, showing melt rate dependence on salinity for length scales up to 0.3 m ($L \leq 0.3$ m), ($T_d = 15.02$ °C) 76

Figure 5.6 Large block sediment-free freshwater (FW) and sediment-laden freshwater ($\mathrm{FW_{sed}}$) ice, showing melt rate dependence on thermal driving (T_d [°C]) and sediment content for length scales greater than 0.3 m ($L > 0.3$ m) 77

Figure 5.7 Small block sediment-free freshwater (FW) ice, showing melt rate dependence on thermal driving (T_d) for length scales up to 0.3 m ($L \leq 0.3$ m), $\zeta = 5/12$ 78

Figure 5.8 Small block sediment-free freshwater (FW) and sediment-laden freshwater ($\mathrm{FW_{sed}}$) ice, showing melt rate dependence on sediment content for length scales up to 0.3 m ($L \leq 0.3$ m), ($T_d = 15.02$ °C), $\zeta = 5/12$ 80

Figure 5.9 Small block sediment-free saltwater (SW) and sediment-laden saltwater ($\mathrm{SW_{sed}}$) ice, showing melt rate dependence on sediment content for length scales up to 0.3 m ($L \leq 0.3$ m), ($T_d = 15.02$ °C), $\zeta = 5/12$ 81

Figure 5.10 Small block sediment-free freshwater (FW) and sediment-fee saltwater (SW) ice, showing melt rate dependence on salinity for length scales up to 0.3 m ($L \leq 0.3$ m), ($T_d = 15.02$ °C), $\zeta = 5/12$ 81

Figure 5.11 Small block sediment-laden freshwater ($\mathrm{FW_{sed}}$) and sediment-laden saltwater ($\mathrm{SW_{sed}}$) ice, showing melt rate dependence on salinity for length scales up to 0.3 m ($L \leq 0.3$ m), ($T_d = 15.02$ °C), $\zeta = 5/12$ 82

Figure 5.12 Large block sediment-free freshwater (FW) and sediment-laden freshwater ($\mathrm{FW_{sed}}$) ice, showing melt rate dependence on thermal driving (T_d [°C]) and sediment content for length scales greater than 0.3 m ($L > 0.3$ m), $\zeta = 4/15$ 82

Figure 5.13 Nusselt number vs length scale ($0 < L < 0.3$) 86

Figure 5.14 Nusselt number vs length scale ($0.2 < L < 0.6$) 87

Figure 5.15 Nusselt number vs length scale ($0 < L < 0.6$) 88

Figure 6.1 Prandtl number as a function of temperature and salinity 90

Figure 6.2 Prandtl number parameters as functions of temperature and salinity 91

Figure 6.3 Grashof number vs length scale 93

Figure 6.4 Grashof number vs length scale, showing the effect of increasing viscosity due to sediment 97

Figure 6.5 Evidence of Shubenacadie River sediment cohesion. Showing sediment transport to Shad Bay, NS. 98

Figure 6.6 Large block sediment-laden ice photo, showing presence of a turbidity current. 98

Figure 6.7 Sandy sediment-laden ice melt photos 99

Figure 6.8 Fine grained sediment-laden ice melt photos 100

Figure 6.9 Rayleigh number vs length scale 104

Figure 6.10 Rayleigh number vs length scale - with adjustments for cohesion, and viscosity of sediment-laden fluid ($\lambda = 0.5$ and $\Gamma = 1.2$) 104

Figure 6.11 Nusselt number vs Rayleigh number 106

Figure 6.12 Data and theory comparison for Nu as a function of Ra 107

Figure 6.13 Melt rate (dm/dt) for $T_\infty = 5$ °C and $S_\infty = 31$ psu 110

Figure 6.14 Melt rate model and data comparison for sediment-laden and sediment-free freshwater ice 111

Figure 6.15 Melt prediction for an ice block with an initial mass (m_0) of 50 kg, showing the effect of sediment inclusion at small length scales . . 112

Figure 6.16 Melt predictions for ice blocks with initial mass (m_0) of 5000 kg for $T_\infty = -1$°C 114

Figure 6.17 Melt predictions for ice blocks with initial mass (m_0) of 5000 kg for $T_\infty = 0$°C 114

Figure 6.18 Melt predictions for ice blocks with initial mass (m_0) of 5000 kg for $T_\infty = 1$°C 115

Figure 6.19 Melt predictions for ice blocks with initial mass (m_0) of 5000 kg for $T_\infty = 2$°C 115

Figure 6.20 Melt predictions for ice blocks with initial mass (m_0) of 5000 kg for $T_\infty = 4$°C 116

Figure 6.21 Half-life melt predictions for ice blocks with initial mass (m_0) of $500 \leq m_0 \leq 10000$ kg for $T_\infty = 1$°C 117

Figure 6.22 Melt predictions for ice blocks with initial mass (m_0) of $500 \leq m_0 \leq 10000$ kg to be reduced to 1 kg for $T_\infty = 1$°C 118

Figure A.1 April 14, 2009 - Aquatron Pool Tank 1 129

Figure A.2 April 14, 2009 - Aquatron Pool Tank 2 130

Figure A.3 January 28, 2011 - Aquatron Tower Tank 1 130

Figure A.4 January 28, 2011 - Aquatron Tower Tank 2 131

Figure A.5 April 14, 2009 - freshwater ice - initial condition, fractured block . 131

Figure A.6 April 14, 2009 - freshwater ice - melt photo, complex geometry . . 132

Figure A.7 July 28, 2009 - freshwater ice - initial conditions 132

Figure A.8 July 28, 2009 - saltwater ice - initial conditions 133

Figure A.9 July 28, 2009 - sediment laden freshwater ice - initial conditions . 133

Figure A.10 July 28, 2009 - sediment laden saltwater ice - initial conditions . . 134

Figure A.11 July 28, 2009 - sediment laden freshwater ice - melt photo (12:11) 134

Figure A.12 January 28, 2011 - freshwater ice - top fracturing 135

Figure A.13 January 28, 2011 - freshwater ice - initial conditions 135

Figure A.14 January 28, 2011 - freshwater ice - melt photo 1, bottom end view(16:20) 136
Figure A.15 January 28, 2011 - freshwater ice - melt photo 2, side view (16:20) 136
Figure A.16 January 28, 2011 - freshwater ice - melt photo 3, top end view (16:20)137

Figure B.1 Far-field PT sensor data - April 14, 2009 142
Figure B.2 Far-field PT sensor data - April 22, 2009 143
Figure B.3 Far-field PT and CTD sensor data - July 28, 2009 144
Figure B.4 Far-field PT sensor data - Feb 2, 2010 145
Figure B.5 Far-field PT and CTD sensor data 1 - March 3 and 4, 2010 146
Figure B.6 Far-field PT and CTD sensor data 2 - March 3 and 4, 2010 147
Figure B.7 Far-field CTD sensor data - April 15, 2010 148
Figure B.8 Far-field PT and CTD sensor data - Jan 25, 2011 149
Figure B.9 Far-field PT and CTD sensor data 1 - Jan 26 and 27, 2011 150
Figure B.10 Far-field PT and CTD sensor data 2 - Jan 26 and 27, 2011 151
Figure B.11 Far-field PT and CTD sensor data 1 - Feb 21 and 22, 2011 152
Figure B.12 Far-field PT and CTD sensor data 2 - Feb 21 and 22, 2011 153
Figure B.13 PT and CTD sensor data - Mar 30, 2011 154
Figure B.14 Far-field PT and CTD sensor data - Mar 30, 2011 155
Figure B.15 Tower tank depth profile - July 28, 2009 157
Figure B.16 Tower tank depth profile - April 15, 2010 158
Figure B.17 Tower tank depth profile - Jan 25, 2011 159
Figure B.18 Tower tank depth profile - Feb 21, 2011 160
Figure B.19 Tower tank depth profile - Mar 30, 2011 161

ABSTRACT

Submerged sediment-laden ice blocks that form on the intertidal mud flats of the Minas Basin pose a potential threat to tidal turbines planned for deployment in the Minas Passage.

Laboratory prepared ice blocks of varying sediment content, salinity, and length scale were melted in seawater of different temperatures. The effect of sediment inclusions on melt rate is related to changes in heat supply and the heat required to melt a unit mass of ice, where the former is affected by the strength of the convective current and the latter by the ice block properties.

A melt rate model for submerged sediment-laden ice is developed, with free convection the dominant deterioration mechanism. The model provides probable upper limits to the lifetimes of submerged ice blocks in the field, and has been used to predict lifetimes of large submerged ice blocks using temperatures representative of seawater in the Minas Basin.

LIST OF SYMBOLS USED

Roman symbol	Description	Units
A	area	m^2
B	constant ($\overline{Nu} = B(\overline{Ra})^n$)	none
b_1	constant	none
b_2	constant	none
C	sediment concentration	mg/L or ppt or g/g
c	specific heat capacity	J kg^{-1} °C^{-1} or J g^{-1} °C^{-1}
D_f	diffusion coefficient	m^2/s
D	diameter	m
D_{sl}	saline diffusivity	m^2/s
d	depth	m
d_x	aspect ratio correction factor	none
F	latent heat of fusion	J kg^{-1} or J g^{-1}
F_T	tension force	N
fc	focal length	pixels
g	gravitational acceleration	m s^{-2}
g'	buoyancy-reduced gravitational acceleration	m s^{-2}
H	enthalpy per unit mass	J g^{-1}
h	convective heat transfer coefficient	W m^{-2} °C^{-1}
k	thermal conductivity	W m^{-1} °C^{-1}
L	length	m
MSE	mean squared error	(as variable)^2
m	mass	g or kg
N	Brunt-Vaisala frequency	Hz (s^{-1})
n	constant ($n_l = 1/4$,$n_t = 2/5$)	none
P	pressure	MPa or dbar
Q_1	heat	J
Q	heat transfer or heating rate	W (J/s)
q	heat flux	W m^{-2}

Roman symbol	Description	Units
r	radius	m
r_1	thermal parameter	none
r_2	thermal parameter	none
S	salinity	psu or ppt
s	solute distribution coefficient	none
T	temperature	°C or K
T_d	thermal driving temperature	°C or K
t	time	s or min or hr
u	x direction velocity	m/s
V	volume	l or m^3
v	y direction velocity	m/s
W	gravitational force (weight)	N
w	z direction velocity	m/s
v_g	ice growth rate	cm/s or cm/day
v_f	volume fraction	none
Gr	Grashof number	none
Pr	Prandtl number	none
Ra	Rayleigh number	none
Nu	Nusselt number	none
Sc	Schmidt number	none
St	Stefan number	none
Le	Lewis number	none
FW	sediment-free freshwater ice	n/a
FW_{sed}	sediment-laden freshwater ice	n/a
SW	sediment-free saltwater ice	n/a
SW_{sed}	sediment-laden saltwater ice	n/a
X	used to define the following subscripts	
X_i	pure ice	as variable
X_{bi}	bubbly ice	as variable
X_{ci}	sea ice	as variable
X_{bci}	bubbly sea ice	as variable

Roman symbol	Description	Units
X_{si}	sediment-laden ice	as variable
X_{sci}	sediment-laden sea ice	as variable
X_s	sediment	as variable
X_f	fluid	as variable
X_{mw}	melt water	as variable
X_{cw}	sea water	as variable
X_{fw}	fresh water	as variable
X_{sf}	sediment-laden fluid	as variable
X_a	air	as variable
X_T	total	as variable
X_c	critical value	as variable
X_l	laminar flow	as variable
X_t	turbulent flow	as variable
X_{inv}	inversion value	as variable
$X_{\rho max}$	value at maximum density	as variable
X_{fp}	freezing point value	as variable
X_w	wall value	as variable
X_∞	far-field value	as variable
X_0	initial value (at t=0)	as variable
X_r	relative value	as variable

Greek symbol	Description	Units
α_v	volumetric thermal expansion coefficient	°C^{-1}
α	melt rate constant	kg$^{\zeta}$/min
β_v	volumetric saline expansion coefficient	psu^{-1} or ppt^{-1}
Γ	constant	none
γ^2	statistical measure	none
ζ	melt rate constant ($\zeta_l = 5/12$,$\zeta_t = 4/15$)	none
θ	angle from vertical	degrees
κ	thermal diffusivity	m^2 s^{-1}
λ	constant	none
μ	absolute (or molecular shear, or dynamic) viscosity	kg m^{-1} s^{-1}

Greek symbol	Description	Units
ν	kinematic viscosity	m^2 s^{-1}
ρ	density	kg m^{-3} or g cm^{-3} or kg/L
σ^2	variance	(as variable)^2
τ	shear force	N
ϕ	particle concentration by volume	m^3_s / m^3_f
φ	constant	as in context
ω	Nusselt number constant	Nu/m

ACKNOWLEDGEMENTS

- Dalhousie Oceanography Acoustics Group
- Aquatron Laboratory Staff
- NSERC, Industrial Postgraduate Scholarships Program
- Nova Scotia Power Inc.

CHAPTER 1

INTRODUCTION

1.1 Outline

The *overall objective* of this thesis is to develop a first-order accurate melt rate model for sediment-laden ice in seawater. Submerged sediment-laden ice is not subjected to wind forcing or wave erosion. Ice blocks of approximate neutral buoyancy are assumed to travel with the mean fluid flow and buoyancy induced free convection shall be the dominant deterioration mechanism.

The *approach* involves melting laboratory prepared ice blocks in seawater at the Aquatron Laboratory to form the basis for the model. Melts are conducted with freshwater, sediment-laden freshwater, saltwater, and sediment-laden saltwater ice blocks over different length scales and far-field temperatures to determine a melt rate as a function of ice block sediment concentration, ice block salinity, length scale and far-field temperature and salinity.

The *significance* of this research is that submerged sediment-laden ice blocks pose a potential threat to tidal turbines planned for deployment in the Minas Passage. The melt rate model provides probable upper limits to actual lifetimes of sediment-laden ice blocks under field conditions. These lifetimes, when incorporated into existing numerical models of the tidal flow, will yield a probable range of trajectories. Combined with initial conditions and ice strength characteristics this would form the basis for assessing the risk of damage to tidal turbines deployed near regions where sediment-laden ice forms.

1.2 The Problem

The Minas Passage in the Bay of Fundy is being actively investigated as a potential site for large scale production of in-stream tidal power. The Bay of Fundy has a resonant period of about 13 hours, which is close to the 12 hour and 25 minute dominant lunar tide of the Atlantic Ocean (*Garrett*, 1972) (*Garrett and Greenberg*, 1977). This near resonance results in one of the largest tidal ranges in the world. The Bay of Fundy tidal range increases from about 4 m at the mouth of the bay to a maximum of 17 m at the head (*OReilly et al.*, 2005). The extremely large tidal range results in large volumes of water passing through flow restrictions such as the Minas Passage, where flow velocities have been measured in excess of 5 m/s, and estimates of the maximum extractable power by in-stream tidal turbines range from 7 to 8.5 GW (*Karsten et al.*, 2008)[1]. However, numerical simulations predict that extracting as much as 7 GW of energy from the flow would result in a significantly reduced tidal range within the Minas Basin (*Karsten et al.*, 2008), while increasing the tidal amplitude in Bay of Fundy / Gulf of Maine region (*Garrett and Greenberg*, 1977). As shown in Figure 1.1, predictions from the Finite Volume Community Ocean Model (FVCOM) numerical model suggest 2.5 GW may be extracted with a minimal change in the natural tidal range, and for low levels of power extraction, the model predicts that 0.77 GW can be extracted for each percentage reduction in the Minas Basin tides.

What do these levels of power extraction mean for Nova Scotia? Two useful benchmarks are: 1) the province of Nova Scotia requires an estimated 2.3 GW of power at peak load; and 2) an installation of 415 turbines, each producing 1 MW would provide instantaneous power equal to the maximum capacity of the Tufts Cove Generating Station (*Trowse and Karsten*, 2010).

Tidal energy appears to be an abundant resource in Atlantic Canada. However, an assessment of available energy must not be based on flow disturbance alone. Tidal power projects are currently in the R&D phase. Questions with respect to environmental effects must be answered, project costs are high, and significant challenges exist which must be overcome prior to installing devices with a production capacity equal to a small fraction of the above estimates. Focusing on environmental challenges, in high energy tidal environments not only the effect of turbines on the environment must be considered, but

---

[1] based on results from a two-dimensional, finite-volume model (FVCOM) (*Karsten et al.*, 2008) and an analytical model derived from the Navier-Stokes equations (*Blanchfield et al.*, 2008)

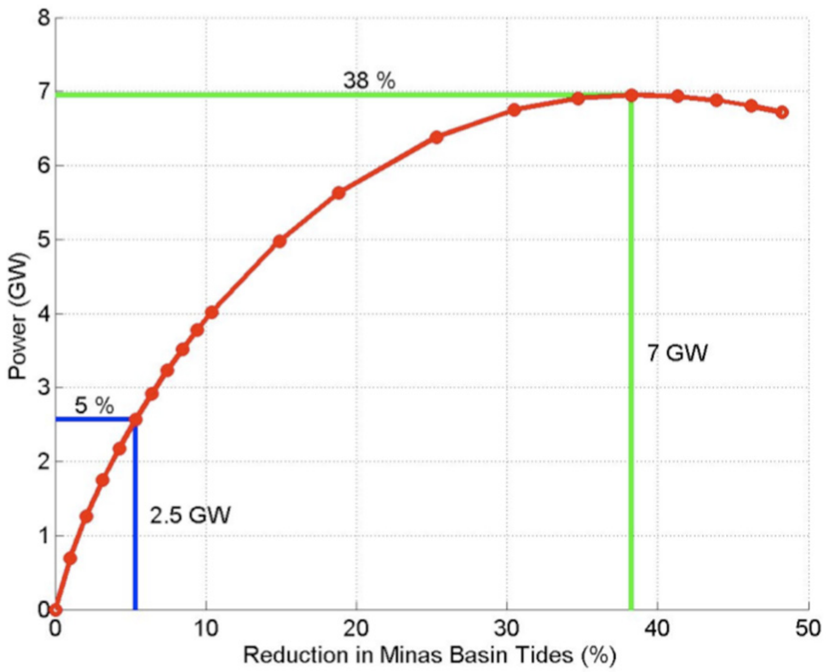

Figure 1.1: Extracted power and reduction in Minas Basin tidal range (*Karsten et al.*, 2008)

also the effects of the environment on the turbines. This thesis explores aspects of one such effect, the potential impact of submerged sediment-laden ice.

The water bodies with the four largest recorded tidal ranges in the world are, in descending order, the Bay of Fundy, Ungava Bay in northern Quebec, the Severn Estuary in Great Britain, and Turnagain Arm of the Cook Inlet in Alaska (*NOAA*, 2011). Three of the four are located in climates where ice forms in the winter, with the Severn being the exception. The Bay of Fundy and Cook Inlet both have extensive mud flats located in their upper estuaries where shore-fast ice forms with high concentrations of sediment, which can make the ice neutrally or negatively buoyant. Under certain meteorological and tidal conditions that are not well defined, this sediment-laden ice is released, and according to fishermen who work in the Bay of Fundy, can travel through the Minas Passage. Such blocks, moving with tidal currents that range from approximately 2 to 10 knots, pose a threat to planned in-stream tidal turbine developments in the Minas Passage and between East and West Foreland in Cook Inlet.

The Nova Scotia Department of Energy commissioned the Offshore Environmental Energy Research Association (OEER) to conduct a Strategic Environmental Assessment

(SEA) (*OEER*, 2008) focusing on tidal energy development in the Bay of Fundy. The SEA was conducted to provide advice on whether, when and under what conditions tidal energy demonstration and commercial projects should be allowed in the Bay of Fundy. Sanders Resource Management Inc. received funding through the SEA Participation Support program to investigate the issue of submerged ice in the Bay of Fundy. The work conducted by Sanders is documented in *Sanders and Baddour* (2006), *Sanders and Baddour* (2007), and *Sanders et al.* (2008) and concludes,

> "We find sufficient circumstantial evidence for migratory submerged ice to warrant direct investigations, designed to quantify the risk of collisions between neutrally and negatively buoyant sub-surface ice and the tidal current harvesting devices planned for Nova Scotia's energy rich tidal currents" (*Sanders et al.*, 2008).

Based on the findings of Sanders, the SEA states,

> "Tidal currents could potentially carry large blocks of sediment-laden ice below the surface of the water where they might come into contact with tidal in-stream turbines." (*OEER*, 2008).

Personal correspondence with former and existing Fundy Ocean Research Centre for Energy (FORCE) berth holders has confirmed that potential interactions between submerged ice and in-stream tidal energy conversion (TEC) devices is a significant issue of concern for deployments in the Minas Passage. Three critical and inter-related questions must be addressed regarding the potential impact of sediment-laden ice on in-stream tidal power generation in the upper Bay of Fundy:

1. What is the range of time scales, from seasonal to tidal, at which sediment-laden ice occurs?
2. What is the range of lifetimes of fully immersed sediment-laden ice blocks?
3. What are possible observational tools for warning the industry of the presence of fully immersed ice?

The first question relates to the timing of the threat; the second to duration and the maximum areal extent of the threat; the third to the potential for mitigative measures to reduce the threat. The focus of this thesis is the development of a melt rate model in order to predict the lifetimes and thereby the probable range of trajectories of sediment-laden ice blocks, thus addressing the second question.

1.2.1 Similarities with other off-shore industries

The probability of encountering icebergs and calved glacier ice is of significant interest to marine transportation and offshore resource development.

> “The accuracy of predicting the numbers and positions of Arctic icebergs that may pose a threat to offshore activities on the Canadian east coast depends not only on reliable iceberg drift data but also on dependable estimates of their life expectancy. Thus iceberg deterioration is an integral part of iceberg forecasting” (*El-Tahan et al.*, 1987).

Ice pieces of similar size to the sediment-laden ice present the Bay of Fundy (bergy bits[2] and growlers[3]) can cause large forces upon impact with offshore structures or vessels. Bergy bits and growlers were incorporated into an operational iceberg drift and deterioration model developed for the Canadian Ice Service (CIS) (*Kubat et al.*, 2007). Initial conditions are represented by a size-frequency distribution function for the ice pieces that are generated by calving of large parent bergs (*Savage et al.*, 2000). Due to the small above water volume, bergy bits are particularly difficult to study. Populations were estimated through use of a ratio of bergy bits to ’parent’ icebergs (*Crocker et al.*, 2004). Bergy bits and growlers then disperse from the parent iceberg and melt as individual entities. Depending on the relative velocities of the ice pieces and parent iceberg there will be a maximum distance that the bergy bits and growlers travel before melting to a size of negligible significance (*Savage et al.*, 2001).

1.3 Objective

The overall objective of this thesis is to develop a first-order accurate melt rate model for sediment-laden ice in seawater. Submerged sediment-laden ice is not subjected to

---

[2] Bergy Bits - Generally showing 1 to less than 5 m above sea level, with a length of 5 to less than 15 m. They normally have an area of 100-300 m^2 (*CIS*, 2005)

[3] Growler - Extending less than 1 m above the sea surface and normally occupying an area of about 20 m^2. (*CIS*, 2005)

wind forcing or wave erosion. Ice blocks of approximate neutral buoyancy are assumed to travel with the mean fluid flow and buoyancy induced free convection is assumed to be the dominant deterioration mechanism.

The melt rate (dm/dt) relationship is

$$\frac{dm}{dt} = \frac{Q}{F} \tag{1.1}$$

where positive dm/dt [kg s^{-1}] represents the rate of mass lost from ice and gained by fluid, Q [W] is the rate of heat transfer to the ice surface, and F is the latent heat of fusion [J kg^{-1}].

Equation (1.1) assumes the heat requirement for phase transition from solid to liquid (F) is much greater than the additional heat required to raise the ice temperature to its melting point ($c_i \Delta T$). Algebraically, $F >> c_i \Delta T$ where c_i is the heat capacity of ice [J kg^{-1} °C^{-1}], $\Delta T = T_\infty - T_i$, T_∞ is the far-field water temperature, and T_i is the ice block temperature. The ratio of these two values is the Stefan number $\mathrm{St} = (c_i \Delta T)/F$. With this assumption F becomes the total heat requirement to melt a unit mass of ice. The thermal properties of ice are discussed in further detail in Section 2.2 and this assumption in Section 3.1.

From Equation (1.1), any effect of sediment inclusions on melt rate must be related to a change in heat supply (Q) or heat requirement (F) to melt a unit mass of sediment-laden ice, where Q is affected by the strength of the convective current and F by the ice block sediment content, salinity, and temperature. The effects of sediment inclusions on Q and F are the primary focus of this thesis.

The model will be tested with measurements of melt rate in the laboratory, and will predict the lifetimes of sediment-laden ice blocks. These lifetimes, when incorporated into existing numerical models of the tidal flow, will yield a probable range of trajectories. This initial model neglects wallowing and overturning which will likely occur under natural conditions as a result of shear forces generated from small scale eddies and ambient turbulence in the tidal flow. Consequently, the predicted lifetimes will represent probable upper limits to actual lifetimes under field conditions.

1.4 Organization

Information on ice and sea ice is presented in Chapter 2, including physical and thermodynamic properties, iceberg deterioration mechanisms, and a summary of work conducted on ice melting due to buoyant vertical convection.

The information presented in Chapter 2 was used to develop melt rate theory for submerged sediment laden ice as presented in Chapter 3, including comparison to a simple model for melting of a submerged ice sphere.

Chapter 4 describes experiment methodology, including the ice formation method, melt experiment setup, experiment conditions (far-field seawater salinity, far-field seawater temperature, and ice depth), three methods used for measuring the rate of change for ice mass, and data analysis tools.

Results of the ice melt experiments are presented in Chapter 5.

Results are discussed in Chapter 6, including use of the Prandtl, Grashof, Rayleigh, and Nusselt numbers and presentation of a model for predicting the melt rate for submerged sediment laden ice.

Conclusions are provided in Chapter 7.

Recommendations for future work are provided in Chapter 8.

CHAPTER 2

ON ICE AND SEA ICE

The focus of this work is the melt rate of ice. The following discussion focuses on the basic structure, thermodynamic properties, ablation (or deterioration) mechanisms of sea ice, and gravitational free convection with focus on prior experiments where buoyancy induced flow originates from submerged ice. A comprehensive discussion of fresh and sea water ice is provided in the following works which are referenced for this work: *Weeks* (2010), *Thomas and Dieckmann* (2003), *Lock* (1990), and *Pounder* (1965).

2.1 Physical properties of ice and sea ice

There is a sharp contrast between ice that forms from a freshwater source and that which forms from sea water. This contrast is governed during ice formation by differences in the lattice structure of the ice crystal. With respect to lattice structure, there are a wide variety of forms of solid H_2O (*Pounder*, 1965). However, ice crystals are known to be organized with symmetry in a hexagonal system, as can be seen on the macroscopic scale in most snow crystals (*Pounder*, 1965).

The most important aspect of the ice crystal lattice is highly selective bonds that accept no substitutions for hydrogen and oxygen atoms, with a relatively unimportant exception of the fluorine ion (*Pounder*, 1965). Upon freezing, the major ions in sea water (Na^+, K^+, Ca^{2+}, Mg^{2+}, Cl^-, SO_4^{2-}) then cannot be incorporated into the ice crystal lattice and are rejected by the advancing ice-water interface during crystal growth (*Thomas and Dieckmann*, 2003). The formation of an ice cover on sea water is then a refining process, by which most of the salt is rejected; however, the growth rate is usually too rapid for complete rejection (*Pounder*, 1965). Part of the salt is retained as brine liquid inclusions within the solid ice, while a larger fraction is rejected into the underlying water (*Thomas and Dieckmann*, 2003).

2.1.1 Density of ice

The anomalous liquid density and expansion of H_2O upon freezing are well known. The density maximum of freshwater at 4 ° C, and the effect of increased salinity, increasing density and pushing the maximum towards the freezing point are shown in Figure 2.1. Density was calculated for one atmosphere of pressure, using Unesco 1983 polynomials (*Fofonoff and Millard*, 1983).

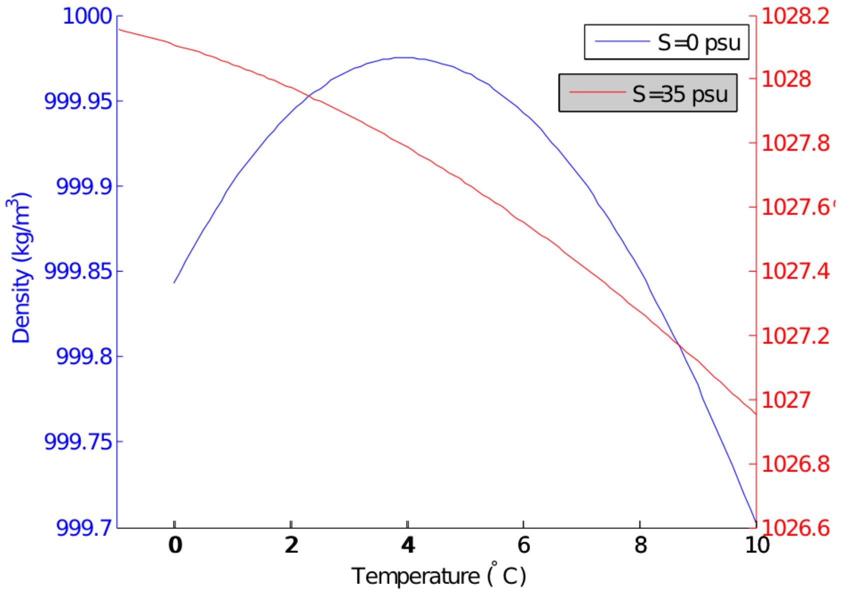

Figure 2.1: Density of fluid fresh water ($S = 0$ psu) and sea water ($S = 35$ psu) as a function of temperature ($T < 10$ °C)

The packing density of frozen water molecules in ice is less than that in fluid water (*Thomas and Dieckmann*, 2003). The freezing of H_2O results in a sharp density decrease. Using the mass of the water molecule as 2.992×10^{-26} kg, and tetrahedral geometry with oxygen atoms spaced 2.76 Å apart, the density of ice is calculated to be 0.9167 g/cm^3, which is in agreement with measurements at the datum freezing temperature (*Lock*, 1990). The temperature dependence of the density of pure ice is given as

$$\rho_i = 0.917 - 1.403 \times 10^{-4} T \tag{2.1}$$

where ρ_i is in g/cm^3 and T is temperature in °C (*Thomas and Dieckmann*, 2003). Equation (2.1) was used to produce Figure 2.2, which is consistent with the observations of *Pounder* (1965) and others, and shows an expansion of about 9% for fresh water upon freezing. The presence of brine or sediment inclusions would of course increase the density of ice, while the presence of air bubbles decreases density.

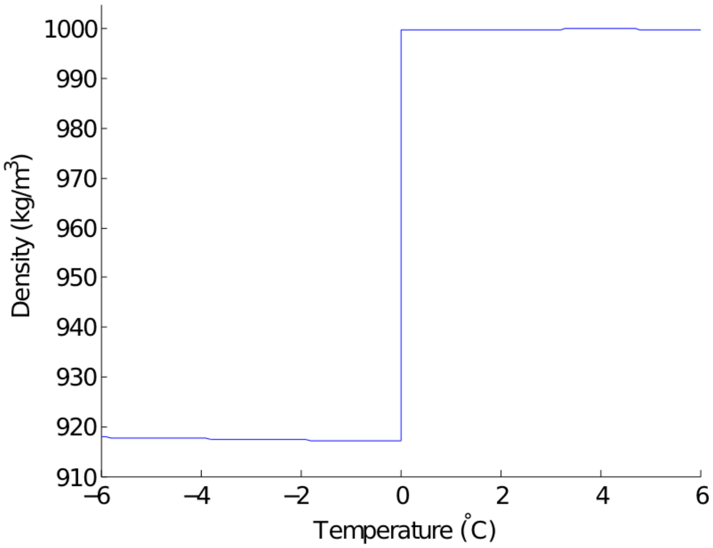

Figure 2.2: Density of solid and fluid fresh water ($-6 < T < 6$ °C)

2.1.2 *Sea ice salinity*

Sea ice salinity is governed by a number of processes, and as such, a sea water line was not included in Figure 2.2. The salinity of ice (S_i) is a function of sea water salinity (S_{cw}), ice growth rate (v_g), and ice age. As *Weeks* (2010) states,

> “The fact that bulk sea ice contains sea salts and that the amounts of these salts vary with the age of the ice has been known for a very long time by the native peoples living in the far north. The reason that this is important is that the water produced by melting the upper portions of hummocks and ridges in old ice types is quite potable, whereas the water produced by melting most FY (first year) sea ice is usually not suitable for drinking. In fact, the earliest study of a possible mechanism for the natural desalination of sea ice was undertaken as the result of a suggestion by the explorer Stefansson that this

> was a scientific problem worthy of investigation. He had undoubtedly used the above knowledge to obtain drinking water in his travels over sea ice. The resulting paper (*Whitman*, 1926) is excellent for it's time, and although the mechanism suggested therein does occur in sea ice, it is currently not believed to be a major contributor to natural desalination. As will be seen[1], the factors controlling the salinity of sea ice are surprisingly varied, complex, and still not understood."

The mechanism suggested by *Whitman* (1926) was downward brine pocket migration, which would occur due to vertical temperature and salinity gradients in sea ice. Whitman realized that an Arctic ice temperature gradient increasing with depth and salinity gradient decreasing with depth would cause diffusion of salt from the top of a brine pocket to the bottom, resulting in ice formation at the top and melting at the bottom. Other mechanisms outlined by Weeks include; brine expulsion, gravity drainage, stalactites, and flooding and flushing caused by heavy snowfall. For our work it will suffice to say that sea ice salinity decreases with increasing age due to a number of mechanisms. Fortunately, we may set aside the effect of age on sea ice salinity as all sediment-laden ice which forms in the inner Bay of Fundy has a life time of less than one year.

Focusing on the salinity of first year (FY) ice, large variability is observed which is dependent on the air temperature to which the sea surface is exposed, and hence the ice growth rate. When an ice cover is broken in the Arctic, sea water is exposed to air temperatures in the range of -30 to -40 °C resulting in ice formation with salinity as high as 20 ppt, but for a cover of annual ice a typical average is 4 ppt (*Pounder*, 1965).

Following *Weeks* (2010), to quantify the effect of ice growth rate on salinity it is useful to define the effective solute distribution coefficient (s) as

$$s \equiv \frac{S_i}{S_{cw}} \tag{2.2}$$

where S_i is the salinity of ice and S_{cw} is the salinity of sea water, which is also consistent with *Thomas and Dieckmann* (2003). To estimate initial entrapment of salt, Weeks then assumes that due to mixing, the salinity concentration S approaches a constant value of S_l at some distance δ ahead of the advancing solid-liquid interface, and for distances less than

---

[1] if you read Weeks' book

δ the velocity component normal to the interface approaches that due to crystal growth (v_g). The steady state continuity equation for $x < \delta$ is then

$$D_f \frac{d^2S}{dx^2} + v_g \frac{dS}{dx} = 0 \tag{2.3}$$

where D_f is a diffusion coefficient with units of length^2/time. Weeks then applies boundary conditions

$$(S_1 - S_2)v_g + D_f \frac{dS}{dx} = 0 \; at \; x = 0 \tag{2.4}$$

where S_1 and S_2 are the salt concentrations in the liquid and solid at the interface, respectively; and

$$S = S_l \; at \; x \geq \delta \tag{2.5}$$

Weeks then solves Equation (2.3) to obtain,

$$s = \frac{s_0}{s_0 + (1 - s_0)\exp[-\frac{\delta v_g}{D_f}]} \tag{2.6}$$

where $s_0 = S_2/S_1$, which may be considered the value of s at $v_g = 0$ (*Weeks*, 2010). Equation (2.6) is then fit to a salinity vs. growth rate data set for FY sea ice in the high Arctic (*Nakawo and Sinha*, 1981) to obtain values of $s_0 = 0.12$ and $\delta/D_f = 4.2 \times 10^4$ s/cm. For initial salinity of sea ice we may then use

$$S_i = S_{cw}[\frac{0.12}{0.12 + 0.88\exp(-4.2 \times 10^4 v_g)}] \tag{2.7}$$

where S_i and S_{cw} have units of ppt and v_g has units of cm/s, valid over the range of $0 < v_g < 2.5 \times 10^{-5}$ cm/s ($0 < v_g < 2$ cm/day) (*Weeks*, 2010).

Similarly, as outlined in *Thomas and Dieckmann* (2003), Cox & Weeks derived the following dependence of s on growth rate based on laboratory experiments (*Cox and Weeks*, 1981) and field data (*Nakawo and Sinha*, 1981)

$$s = \frac{0.26}{0.26 + 0.74\exp(-7243 v_g)} \quad , \quad v_g > 3.6 \times 10^{-5} \text{ cm/s} \tag{2.8}$$

$$s = 0.8925 + 0.0568\ln(v_g) \quad , \quad 2.0 \times 10^{-6} \leq v_g \leq 3.6 \times 10^{-5} \text{ cm/s} \tag{2.9}$$

$$s = 0.12 \quad , \quad v_g < 2.0 \times 10^{-6} \text{ cm/s} \tag{2.10}$$

where v_g has units of cm/s. Equations (2.7) and (2.8) through (2.10) are plotted in Figure 2.3 for $S_{cw} = 30$ ppt.

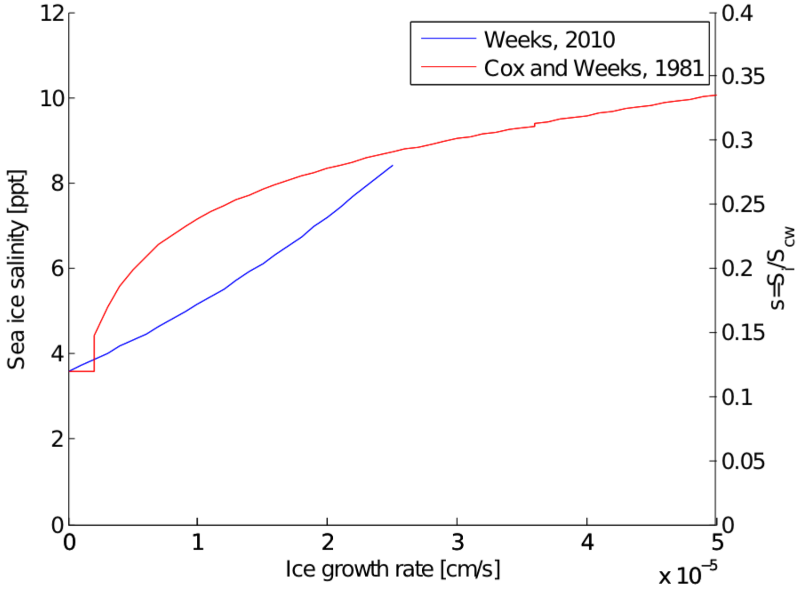

Figure 2.3: Sea ice salinity (S_i) as a function of ice growth rate (v_g) for $S_{cw} = 30$ ppt

2.1.3 *Sediment content*

Sediment can be found within or on the surface of sea ice throughout the ice-covered Arctic Ocean, where sediment concentrations range from 5-500 mg/L, and vary both horizontally and vertically down to the centimeter scale (*Smedsrud*, 2001). Although these concentrations are far from sufficient to produce neutrally or negatively buoyant ice, works such as those by *Smedsrud* (2001) are useful in evaluating the processes by which sediment becomes incorporated in sea ice. Smedsrud conducted laboratory experiments with the objective of evaluating the efficiency by which frazil[2] ice crystals can entrain sediment into the surface ice layer. Smedsrud observed the effects of waves, currents, air-temperature (or heat flux from water to air, or ice growth rate), sediment concentration in sea water, and to some extent sediment type on the resulting sediment concentration in the ice. Useful observations from Smedsrud's work include:

- The mass of sediment incorporated into the sea ice cover increased with time when formed under a constant level of turbulence.

---

[2] Frazil ice is one of the first stages in ice formation. Frazil ice consists of small (maximum dimension $\approx$ 2.5 cm) spicules or discs that typically form in the top few centimetres of water (*Pounder*, 1965).

- The ice formed during his experiments had ratios of sediment concentration in ice (C_i) to sediment concentration in sea water (C_{cw}) as high as $C_i/C_{cw} \approx 11$ after 24 hours, with average values between 2 and 10. The maximum value of C_i/C_{cw} being from $C_{cw} = 18.1$ mg/L and the resultant $C_i = 198.5$ mg/L, formed with silt and sand, air temperature $T = -17.17$ °C, and current speed $u = 25.05$ cm/s.
- Levels of sediment incorporation (C_i) were affected by three variables: sediment concentration in the water, turbulence, and heat flux (or frazil ice growth rate)[3].

The values of C_i/C_{cw} greater than unity are an interesting result, which is supported by other research cited by *Smedsrud* (2001). Although the experiments conducted by Smedsrud were not conducted within a range of C_{cw} sufficient to produce neutrally buoyant sea ice, his results highlight the ability of suspended frazil ice crystals to scavenge sediment, resulting in surface slush containing sediment.

Concentrations of sediment in heavily sediment-laden ice that forms on inter-tidal mud flats of sediment rich rivers flowing into the inner Bay of Fundy are not well studied. Work is currently underway at Dalhousie University under the supervision of Dr. Paul Hill, an objective of which is to produce a density distribution for sediment-laden ice samples collected from the banks of the Avon River, Shubenacadie River, and tributaries thereof. Sediment-laden ice blocks formed on the banks of the Shubenacadie River are shown in Figure 2.4.

An environment similar to the inner Bay of Fundy exists within Cook Inlet, Alaska, where the Matanuska, Knik, and Susitna Rivers, contribute approximately 70 percent of the freshwater discharged annually into Cook Inlet and about 20 million tons of sediment (*Smith et al.*, 2003). The maximum recorded mean tidal range in the Bay of Fundy is 11.7 m at the Burntcoat Head tidal station in the Minas Basin. For comparison, the Sunrise tidal station in Turnagain Arm of Cook Inlet has recorded a mean tidal range of 9.2 m (*NOAA*, 2011). The large tidal range and sediment supply create extensive mud flats in the Knik Arm and Turnagain Arm of Cook Inlet, similar to those in the inner Bay of Fundy. From studies conducted in Cook Inlet by Orson Smith the NOAA *Observers Guide to Sea Ice* has given the name **beach ice**[4] to,

---

[3] i.e. inversely proportional to air temperature

[4] Smith first gave the more interesting name **stamukha** to this ice. He later learned in Gdansk that the Russian word “stamukha” is not appropriate as it had already been assigned more generally to an individual piece of stranded ice, regardless of it’s sediment content (*Smith*, 2009).

Figure 2.4: Sediment-laden ice on the banks of the Shubenacadie river

> irregular, sediment-laden blocks that are grounded on tidelands, repeatedly submerged, and floated free, generally, by spring tides (*Smith*, 2007).

Although the definition of **beach ice** suggests a process involving positive buoyancy, Smith states that, "on melting, it's conceivable they could become neutrally buoyant" (*Smith*, 2009). Smith collected sea-ice cores offshore in the Forelands region of Cook Inlet, and from beach ice located in the Turnagain Arm during February and March of 1999, respectively. Sediment concentrations were measured by sieving and filtering melted samples, and salinity was also measured.

Supporting the laboratory findings of Smedsrud discussed above, Smith cites field studies that show high concentrations of incorporated sediments associated with dynamically grown ice, especially in frazil ice grown in highly turbulent water (*Eicken et al.*, 1997), and suspension freezing to be the principal mechanism for incorporating sediment in Arctic sea ice (*Reimnitz et al.*, 1993).

From the Cook Inlet Forelands, 83 ice samples were collected with a mean sediment concentration of 433 ± 185 mg/L, and mean salinity of 6.41 ± 1.97 ppt. From six surface water samples taken in the vicinity of the ice cores, the mean suspended particle matter (SPM) concentration was 164 mg/L and the mean salinity was 27.4 ppt (*Smith et al.*, 1999).

Consistent with Smedsrud, the results indicate that sea ice can become enriched with sediment, in this case with $C_i/C_{cw} \approx 3$. One core was collected from beach ice from the Turnagain Arm . The mean sediment concentration in the beach ice core was 24,938 mg/L and the mean salinity was 1.07 ppt.

To illustrate the effect of sediment incorporation on ice density, using an approximate sediment density $\rho_s = 2.6$ kg/L and pure ice density of $\rho_i = 0.9$ kg/L, freshwater ice density as a function of sediment concentration is plotted in Figure 2.5. The density of non-saline water of temperature $T = 0°$C (or just above freezing) has also been included as a function of sediment concentration, which is of interest later with respect to melt plumes. To facilitate direct comparison of fluid and solid H_2O sediment concentrations, the ratio of sediment mass to total mass has been used. A dashed green horizontal line has been plotted across Figure 2.5 at the density of sea water with $T = 4$ °C, $S = 31$ psu, and $C = 0$. The intersection points at $C_i = 186$ ppt and $C_{mw} = 39$ ppt are the approximate sediment concentrations at which the ice and melt water are neutrally buoyant with respect to seawater of low sediment concentration. Allowing for direct comparison to the concentration values presented by Smedsrud and Smith, $C_i = 186$ ppt is equivalent to 190,600 mg of sediment per L of ice, or 210,000 mg of sediment per L of fluid.

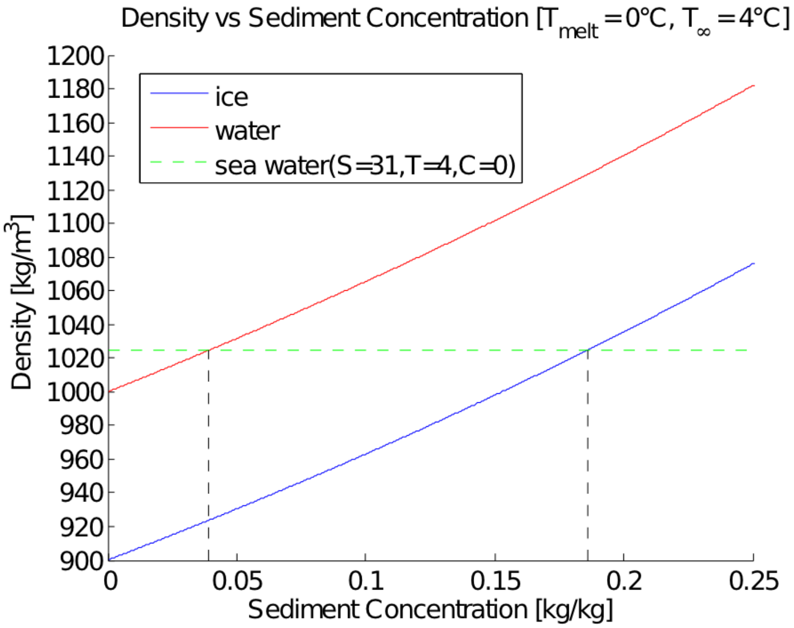

Figure 2.5: Ice density and water density as functions of sediment concentration. Referenced to sea water $T = 4$ °C, $S = 31$ psu plotted as dashed green line.

2.2 Thermal properties of ice and sea ice

Investigating the melt rate of sediment-laden ice, interest lies in,

1. The energy required to raise a unit mass of ice by a unit of temperature at constant pressure (or the ability of the ice crystal lattice to store thermal energy, essentially in the form of vibrations (*Lock*, 1990)), which defines the heat capacity of ice $c = (\partial H/\partial T)_p$ at constant pressure, where H is the enthalpy per unit mass. Heat capacity (c) has units of energy per unit mass and temperature [J kg^{-1} °C^{-1}] or [J g^{-1} °C^{-1}][5].

2. The change in enthalpy when a unit mass of ice is converted isothermally and reversibly into liquid water, which defines the latent heat of fusion for ice F (*Weeks*, 2010), which has units of energy per unit mass [J kg^{-1}] or [J g^{-1}].

3. The rate of conductive heat flux (energy per time and area, J s^{-1} m^{-2} or W m^{-2}) through ice, which by Fourier's Law is $q = -kdT/dx$ where k is the thermal conductivity of ice [W m^{-1} °C^{-1}] and dT/dx is the temperature gradient measured parallel to heat flow.

The heat capacity c, latent heat of fusion F, and thermal conductivity k of ice and sea ice are discussed in the following subsections with consideration given to the effects of included salt and sediment.

2.2.1 *Thermal properties of fresh water ice*

The thermal properties of fresh water ice are well understood, with much experimentation done prior to 1938. The heat capacity of ice is influenced by impurities, the effect of which is significant for the case of sea ice, but can not be neglected even for ice frozen from carefully distilled water (*Pounder*, 1965). Pounder presents the relation,

$$c_{obs} = a + bT - d/T^2 \tag{2.11}$$

where c_{obs} is the measured heat capacity [J g^{-1} °C^{-1}] (at constant pressure) for four ice samples created with high (but different) impurities, T is ice temperature [°C], and a, b,

---

[5] Note that mixed units of J g^{-1} [kg m^2 s^{-2} g^{-1}] have been used in some equations rather than J kg^{-1} [m^2 s^{-2}] for consistency with previous works

and d are empirical coefficients. The values of a and b were constant for all four samples, and d was found to decrease with increasing sample purity. From dimensional analysis of Equation (2.11), we see that d has units of energy temperature per mass (or J °C g^{-1}). d/F is then °C, which was interpreted as the freezing point of the solution, with values in the range $-0.5 \times 10^{-4} < d/F < -0.1 \times 10^{-2}$ °C. The first two terms in Equation (2.11) were then taken to represent the true heat capacity of pure ice at constant pressure, with the numerical values,

$$c_i = 2.1153 + 0.0078T \tag{2.12}$$

and units of T in °C and c_i in J g^{-1} °C^{-1}, at atmospheric pressure but with small change in c_i over the natural pressure range (*Pounder*, 1965). Equation (2.12) is then applicable to fresh water ice in all but the most extreme pressure conditions, such as the bottom of the Greenland ice sheet. Similarly, *Weeks* (2010) gives,

$$c_i = 2.7442 + 0.1282T \tag{2.13}$$

with units of T in K and c_i in J mol^{-1} K^{-1}, which as shown in Figure 2.6 is nearly equivalent to Equation (2.12) after accounting for differences in units. *Pounder* (1965) gives the latent heat of fusion of pure ice at 0 °C as $F_i = 333.678$ J/g with slight influence by trace impurities, which may be neglected in fresh water ice. *Weeks* (2010) gives, $F_i = 335$ J/g at 0 °C, with a linear decrease to 274 J/g at $T = -10$ °C, beyond which the decrease is somewhat less.

The thermal conductivity of pure ice is

$$k_i = 2.24 - 0.01T_i \tag{2.14}$$

from *Pounder* (1965), or

$$k_i = 2.14 - 0.011T_i \tag{2.15}$$

from *Weeks* (2010), or

$$k_i = 2.22 - 0.01T_i + 3.45 \times 10^{-05}T^2 \tag{2.16}$$

from *Thomas and Dieckmann* (2003), with units of T in °C and k in W m^{-1} °C^{-1}. However, fresh water ice often contains air bubbles which act as nearly perfect insulators as the thermal conductivity of air is less than 1% that of pure ice (*Weeks*, 2010), decreasing k. Assuming a uniform distribution of air bubbles throughout the ice, the effect of bubbles on thermal conductivity can be calculated using the volume fraction $v_f = V_a/V_T$, where V_a is the air volume, V_T is the volume of pure ice of mass m (*Pounder*, 1965). With no other impurities $V_T = V_a + V_i$. *Pounder* (1965) presents

$$k_{bi} \approx 2k_i(\frac{1 - v_f}{2 + v_f}) \tag{2.17}$$

With no other impurities present ice density is a unique function of air content, and Equation (2.17) may be algebraically rearranged to obtain,

$$k_{bi} = \frac{2k_i\rho_{bi}}{3\rho_i - \rho_{bi}} \tag{2.18}$$

where subscript bi denotes bubbly ice, subscript i pure ice, and k_i is obtained from Equation (2.14) (*Pounder*, 1965).

Plots of c_i using Equation (2.12), k_i using Equation (2.14), and k_{bi} vs temperature, where the density of pure ice (ρ_i) was calculated using Equation (2.1) and $\rho_{bi} = 0.85\rho_i$ are presented in Figure 2.6.

2.2.2 Thermal properties of sea ice

The thermodynamic properties of sea ice are considerably more complex than that of fresh water ice. As previously discussed, in its natural state sea ice contains cells or pockets of liquid brine. Any change in temperature must then involve a phase change for some of the water substance. The heat capacity and latent heat of fusion are then strongly interrelated. *Pounder* (1965) suggests that,"in fact a definite latent heat of fusion for sea ice must be abandoned since the phase change from solid to liquid is a continuous process."

The salinity of the brine contained in sea ice is in equilibrium at a given temperature. As sea ice temperature rises from T to T', the brine is diluted to an equilibrium concentration corresponding to T' by melting of pure ice at the ice-brine interface (*Ono*, 1967). The heat capacity becomes the total amount of heat required to raise the temperature of sea ice constituents (ice and brine) by one unit of temperature, plus the heat associated with the phase change associated with by melting pure ice at the brine-ice interfaces (*Weeks*, 2010).

Based on parameterizations from experimental data primarily conducted by *Ono* (1967),

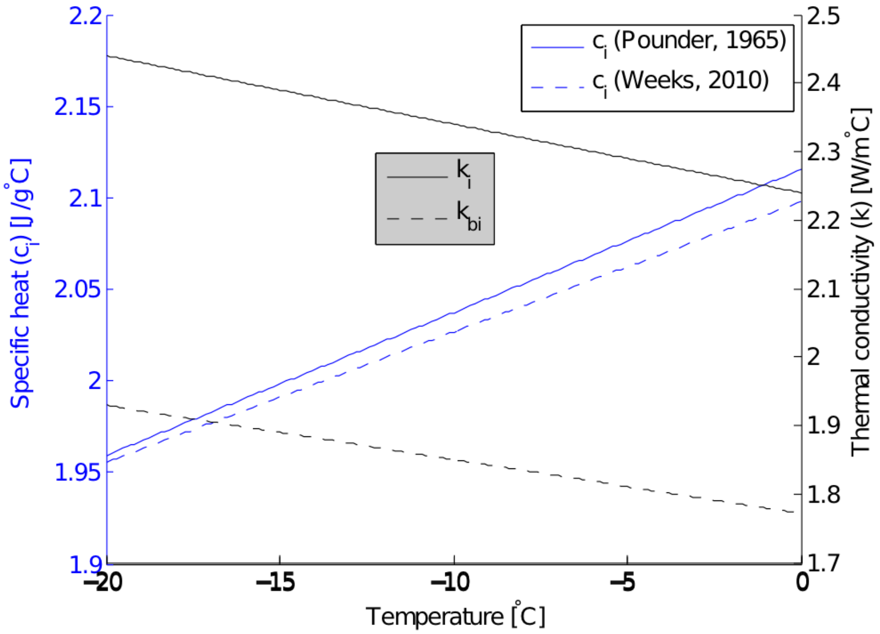

Figure 2.6: Fresh water ice heat capacity and thermal conductivity as functions of temperature

Weeks (2010) gives the heat capacity of sea ice as,

$$c_{ci} = 2.113 + 0.0075T_i + 18.04(\frac{S_i}{T_i^2}) - 0.0034S_i + 8.4 \times 10^{-5}(S_iT_i) \tag{2.19}$$

with units of c_{ci} in J g^{-1} °C^{-1}, S_i in ppt, and T_i in °C, the subscript c indicates sea, and $c_i = 2.113 + 0.0075T_i$ is used as the heat capacity of pure ice. *Ono* (1967) points out that the fourth and the fifth terms on the right side are negligibly small in comparison to the third term, and

$$c_{ci} = 2.113 + 0.0075T_i + 18.04(\frac{S_i}{T_i^2}) \tag{2.20}$$

Integrating Equation (2.19) or (2.20) from T to T' gives the amount of heat required to raise the temperature of one gram of sea ice from T to T'. To obtain the latent heat of fusion, *Ono* (1967) integrated Equation (2.19) to the melting temperature T_m to obtain,

$$F_{ci} = 333.40 - 2.113T_i - 0.114S_i + 18.04(\frac{S_i}{T_i}) + 0.0033S_iT_i - 0.038T_i^2 \tag{2.21}$$

with units of F_{ci} in J g^{-1}, S_i in ppt, and T_i in °C, as presented by *Thomas and Dieckmann* (2003). *Ono* (1967) suggests the fourth and fifth terms can be neglected with sufficient accuracy for practical purposes, and

$$F_{ci} = 333.40 - 2.113T_i - 0.114S_i + 18.04(\frac{S_i}{T_i}) \tag{2.22}$$

which is consistent with *Weeks* (2010). Interestingly, the model indicates $F_i = 333.40 - 2.113T_i$ for pure ice, showing the latent heat to increase with decreasing temperature. This does not fit Weeks' earlier observation of a linear decrease to 274 J/g at $T = -10$ °C.

Plots of c_{ci} and F_{ci} as functions of temperature and salinity based on Equations (2.19) through (2.22) are presented in Figure 2.7. Equations (2.19) and (2.21) are plotted with a solid lines. The dashed lines of the slightly less accurate Equations (2.20) and (2.22) are not discernible, except for a slight increase in the latent heat of fusion. Consequently, Equations (2.20) and (2.22) will be used in this work for calculation of the heat capacity and latent latent of fusion of sea ice, respectively.

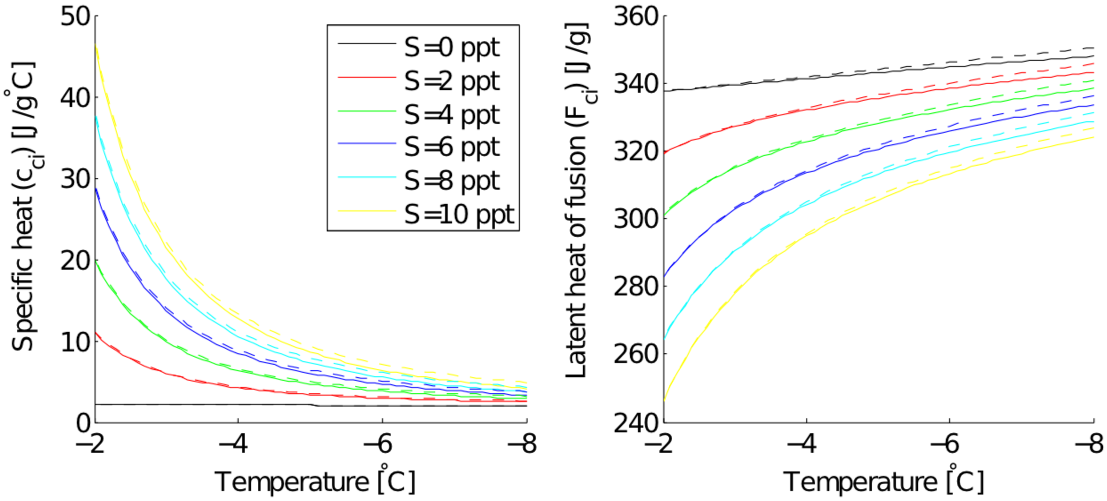

Figure 2.7: Sea ice heat capacity and latent heat of fusion as functions of ice temperature (T_i) and ice salinity (S_i). The maximum ice temperature plotted is $T_{ci} = -2$ °C due to the asymptotic nature of the parameterizations for c_{ci} and F_{ci} to approach $+\infty$ and $-\infty$ as T_{ci} approaches 0 °C.

With respect to the thermal conductivity of sea ice (k_{ci}), brine has a thermal conductivity of approximately 25% that of pure ice (*Weeks*, 2010). Near melting temperatures where the brine volume is high the thermal conductivity of sea ice should be reduced. Conversely, at low temperatures where the brine volume is reduced k_{ci} should increase to approach k_i (*Weeks*, 2010). *Weeks* (2010) presents, $k_{ci} = 2.03 - 0.117(S_i/T_i)$, which does not fit the expectation of $k_{ci} \propto 1/T_i$. Assuming the negative sign to be incorrect we have,

$$k_{ci} = 2.03 + 0.117(\frac{S_i}{T_i}) \tag{2.23}$$

with units of k_{ci} in W m^{-1} °C^{-1}, T_i in °C, and S_i in ppt, which closely matches the equation given by *Thomas and Dieckmann* (2003),

$$k_{ci} = k_i + 0.13(\frac{S_i}{T_i}) \tag{2.24}$$

and plots included by *Weeks* (2010) from a study published by Ono in 1968.

As with fresh water ice, the effect of bubble inclusions must also be accounted for. To model the thermal conductivity for bubbly sea ice (k_{bci}), as we would expect to find with most FY ice, *Weeks* (2010) suggests,

$$k_{bci} = \frac{\rho_{bci}}{\rho_i}(2.11 - 0.011T_i + 0.09\frac{S_i}{T_i}) \tag{2.25}$$

where $\rho_i = 0.917$ g/cm^3 is used as the density of pure ice, ρ_{bci} requires units consistent with ρ_i, and the model applies over the density, salinity, and temperature ranges $0.840 < \rho_{bsi} < 0.940$ g/cm^3, $0 < S_i < 10$ ppt, and $-30 < T_i < -1.8$ °C. Plots of k_{ci} (Equation (2.23)) and k_{bci} (Equation (2.25)) versus temperature are presented in Figure 2.8, where the density of pure ice (ρ_i) was calculated using Equation (2.1) and $\rho_{bci} = 0.90\rho_i$.

2.2.3 Thermal properties of sediment-laden ice

Combined with the effects of salinity, the heat capacity of sediment-laden sea ice becomes the total amount of heat required to raise the temperature of ice, brine, and sediment by one unit of temperature, plus the heat associated with the phase change as the brine becomes less saline by melting pure ice at the brine-ice interfaces. The heat capacity of sediment-laden freshwater ice may be evaluated using a volumetric ratio if the heat capacity of dry sediment is known. Oceanographic measurements of sediment heat capacity are typically collected from sediment on the sea floor. These measurements are influenced by water contained in the sediment pore space, with pore space decreasing with increasing depth (or pressure). Similarly, bulk heat capacity measurements of fresh water ice blocks of varying sediment concentration could be measured where pore space is occupied by ice. Equation (2.12) then becomes a function of temperature and sediment concentration. For a

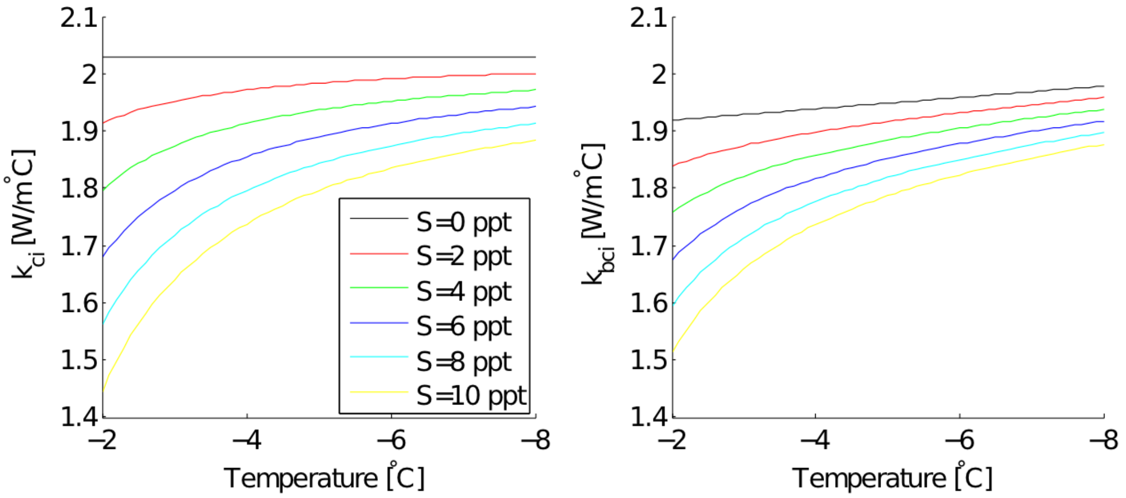

Figure 2.8: Sea ice and bubbly sea ice thermal conductivity as functions of temperature and salinity. The maximum ice temperature plotted is $T_{ci} = -2$ °C due to the asymptotic nature of the parameterization for k_{ci} to approach $-\infty$ as T_{ci} approaches 0 °C.

general assessment under the assumption that the sediment is primarily terrestrial in nature, a representative heat capacity is that of quartz, which at 0 °C is equal to 0.71 J g^{-1} °C^{-1}. The heat capacity of sediment is then approximately $1/3$ that of pure ice, which suggests c_i is inversely related to C_i.

With respect to thermal conductivity, similar to earlier discussions regarding the insulating effects of air bubbles and brine, the inclusion of sediment must be considered in the overall thermal conductivity of the ice block. However, in this case the thermal conductivity of quartz (3 W m^{-1} °C^{-1}) is approximately $1/3$ greater than that of pure ice, which suggests k_i is directly related to C_i.

With respect to the latent heat of fusion, no phase change occurs for sediment over the range of temperatures where ice melts in natural conditions. Solid sediment is incorporated in the ice crystal lattice during formation, then released from the ice block upon melting provided gravitational and frictional forces exceed sediment cohesion. There is then no change in enthalpy related to the presence of sediment upon ice melting, and latent heat of fusion is considered as the energy required to reduce sediment-laden ice by one unit mass.

Considering that latent heat is required to produce a phase change only for the H_2O portion of the ice, due to a fraction of ice block mass being comprised of sediment, the latent heat required to melt a unit mass of sediment-laden ice block must be reduced in comparison to a unit mass of pure ice. To quantify this relationship, a unit of heat (Q_1) supplied to an ice block will melt mass m_i of pure ice, or m_{si} of sediment-laden ice following,

$$Q_1 = m_i F_i = m_{si} F_{si} \tag{2.26}$$

Now rearranging and substituting in $m_{si} = m_i + m_s$ we have,

$$F_{si} = \frac{m_i}{m_i + m_s} F_i \tag{2.27}$$

or,

$$F_{si} = (1 - \frac{m_s}{m_i + m_s}) F_i \tag{2.28}$$

Ice block sediment concentration in units of sediment mass per total mass is $C_i = m_s/(m_i + m_s)$, thus

$$F_{si} = (1 - C_i) F_i \tag{2.29}$$

Now following similar logic to that used for Equation (2.29), but considering the rate at which heat is supplied to the ice block Q $[W]$ we have,

$$Q \Delta t = \Delta m_{si} F_{si} \tag{2.30}$$

where Δt is the time period over which the heat is supplied and Δm is the corresponding mass melted from the ice block. Rearranging Equation (2.30), letting $\Delta t \to 0$, and substituting in Equation (2.29) for F in the general case,

$$\frac{dm}{dt} = \frac{Q}{(1 - C_i) F_i} \tag{2.31}$$

where for dm/dt in kg s^{-1}, Q is in W and F_i is in J kg^{-1}. Equation (2.31) shows that under constant rate of heating and $C_i << 1$ we expect the relationship $dm/dt \propto C_i$ due to a decreased heat requirement to melt a unit mass of sediment-laden ice. The experiments discussed in the following sections evaluate the effect of sediment inclusion on the rate of heat transfer to the ice surface.

Provided that sediment is released from the ice block into the surrounding fluid, the overall effect of sediment inclusions on the thermal behaviour of ice is increased thermal conductivity, reduced heat capacity, and lower heat of fusion. However, potential effects

Substance	c (J/g °C)	k (W/m °C)	F (J/g)
ice	2.1	2.2	334
sediment	0.7	3.0	N/A
water	4.2	0.6	N/A
25%sed 75%ice	1.7	2.4	<334
25%sed 75%water	3.3	1.2	N/A

Table 2.1: Some approximate thermal values near 0 °C, without consideration of saline effects. Including approximate values for sediment mixtures with ice and water by mass.

of sediment cohesion represent an interesting complication, with the mixture now having blended c and k representative of sediment and water, rather than sediment and ice. Approximate values of c and k are presented in Table 2.1 for ice, sediment, and water near 0 °C. The ratios of heat capacity $c_i/c_s = 3.0$ and $c_{fw}/c_s = 6.0$ indicate that a mixture of sediment and water will require more energy to raise one unit mass by one unit temperature than sediment-laden ice of approximately equal sediment concentration. Similarly, $k_i/k_s = 0.7$ and $k_{fw}/k_s = 0.2$ indicate that a sediment water mixture will be less conductive than sediment-laden ice of approximately equal sediment concentration. Values representative of 1 part sediment and 3 parts water and ice mixtures by mass are included in Table 2.1. A sediment water mixture would then have insulating properties in comparison to the sediment-laden ice block.

2.2.4 Thermal properties of sediment-laden bubbly sea ice

The thermal properties of sediment-laden ice formed on the mud banks of the inner Bay of Fundy will be subject to the combined effects of sediment, salinity, and air bubbles. The thermal conductivity (k) may be determined from the volume ratios taking into account the individual thermal conductivities of ice, brine, sediment and air. As discussed by *Ono* (1967) the heat capacity (c) and latent heat of fusion (F) become intertwined due to brine inclusions in sea ice. With respect to melt rate, the latent heat of fusion becomes our primary focus, and shall be considered as the energy required to reduce sediment-laden ice (with brine, sediment, and air inclusions) by one unit mass. The general logic used to produce Equation (2.29) may be expanded to include the effects of salinity, giving the following system of equations,

$$F_{ci} = 333.40 - 2.113T_i - 0.114S_i + 18.04(\frac{S_i}{T_i}) \tag{2.32}$$

$$F_{sci} = (1 - C_i)F_{ci} \tag{2.33}$$

$$\frac{dm}{dt} = \frac{Q}{F_{sci}} \tag{2.34}$$

where to calculate dm/dt in kg s^{-1}, F_{ci} from Equation 2.32 in J g^{-1} must be converted to J kg^{-1}.

Plots of F_{sci} [J g^{-1}] and dm/dt [g s^{-1}] as functions of sediment concentration for ice salinity values over the range $0 \leq S_i \leq 10$ ppt with $\Delta S = 2$ ppt for $Q = 1$ W assuming $T_i = -1$ °C are presented in Figure 2.9.

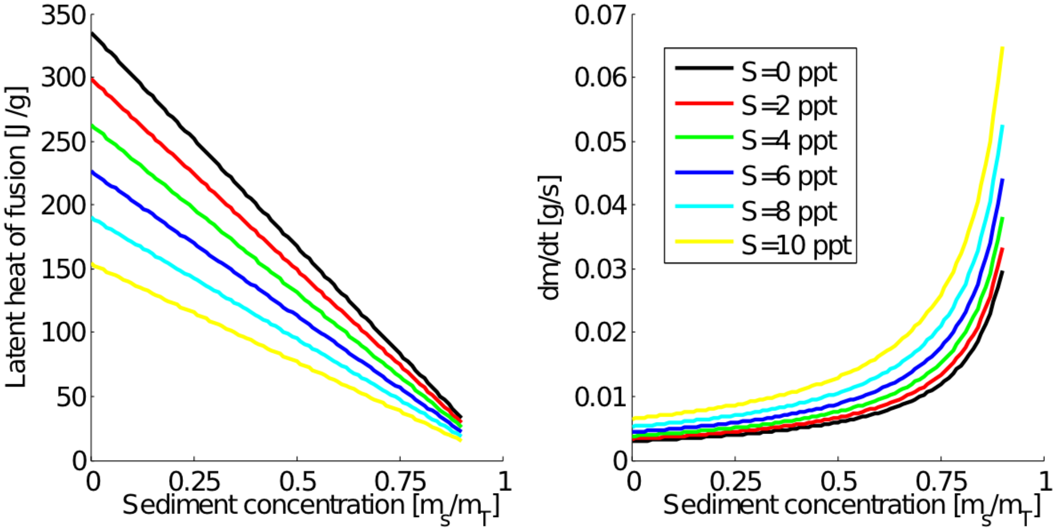

Figure 2.9: Latent heat of fusion and theoretical melt rate of sediment-laden ice as functions of ice salinity and sediment concentration.

2.3 Iceberg deterioration

In glaciology, ablation refers to all processes that remove snow, ice, or water from a glacier. In the context of the present study the word ablation may be used interchangeably with deterioration. The following deterioration mechanisms for Arctic ice were originally presented in a feasibility assessment for towing icebergs to southern waters for freshwater supply (*Job*, 1978). For this assessment it was necessary to determine the rate of deterioration to assess water loss in transport of unprotected (non-insulated) icebergs. The major mechanisms of deterioration presented by Job include:

1. Melting of the top surface by solar radiation and atmospheric convection.
2. Forced-convection melting of the submerged sides and bottom due to the differential velocity between the wind driven iceberg and the seawater current. Potentially enhanced by surface waviness, roughness, and turbulence.
3. Buoyancy-induced free convection along the submerged sides, and to a lesser extent the bottom. Potentially enhanced by the buoyancy of air bubbles released along with the melting ice.
4. Convection induced by wallowing or overturning due to a calving event or after melting to an unstable shape.
5. Waterline wave erosion and undercutting, followed by calving of the undercut ice slabs.
6. Differential melting along cracks, faults, or inhomogeneous inclusions, leading to further calving.
7. Subsurface calving due to the upthrust on underwater shelves formed by other melting mechanisms.
8. Possible break-up of the iceberg due to thermal stresses induced in warm waters.

Theoretical estimates of the above mechanisms were produced with emphasis on moderate sized irregular icebergs typical of the Labrador Sea and Newfoundland Bank (*White et al.*, 1980). The goal of the study was to produce engineering predictions sufficiently quantitative such that they could be used in the field to predict the estimated loss of mass of an iceberg based on exposed iceberg size, sea state, water temperature, and wind velocity. Mechanisms 6, 7, and 8 were considered practically impossible to quantify due to lack of available theory or shape effects. Mechanism 4 was considered insignificant due to the short time spent in the wallowing or overturning states. Melting due to solar radiation and atmospheric convection were shown to be of minor importance, with estimates of approximately 7 cm day^{-1} on a clear day in June in the Labrador Sea, and 8 mm day^{-1} °C^{-1} of atmospheric to ice temperature difference under a 20 knot sustained wind, respectively. Buoyant vertical convection was of moderate importance, with melt rates of approximately 2 cm day^{-1} °C^{-1} of water to ice temperature difference. Forced convection was shown to contribute substantially to iceberg deterioration with rates of 5 to 20 cm day^{-1} °C^{-1} where local winds drive icebergs at velocities of 10 to 20 cm s^{-1} compared to the reference seawater current. Wave erosion was the primary cause of iceberg deterioration due to high melting rates and subsequent calving. Waterline melt rates due to wave erosion were shown to be as high as 105 cm day^{-1} °C^{-1}. (*White et al.*, 1980)

El-Tahan et al. (1987) conducted a validation and quantitative assessment of the deterioration mechanisms considered significant by White, where estimates were produced for daily melt rates and life expectancy of typical icebergs in the Labrador Sea and Grand Banks during different months of the year. The model was validated using field data from Grand Banks and Labrador. The model predicts that for strong wind-driven relative velocities (with respect to local current) melting rates of icebergs from forced convection are significantly larger (about 6 times) than those from buoyant (free) convection. When wind speeds are very small or negligible, icebergs drift with the water current and no melting occurs due to forced convection. Consistent with White, wave erosion was most important deterioration mechanism. Wave erosion accounts for more than 80 percent of total mass loss, forced convection accounts for 16 percent, free convection 2 percent, and wind convection and solar radiation less than 0.5 percent each (*El-Tahan et al.*, 1987).

For the case of bergy bits and growlers, small ice pieces are expected to be carried along with wave motion to a larger degree than the case of icebergs, lessening the effect of waterline erosion (*Savage et al.*, 2001). Savage used dimensional analysis to obtain a heat flux / melt rate equation, in which the dominant deterioration mechanisms for the small ice pieces were assumed to be wave erosion and forced convection. The melt rate equation took the form:

$$\frac{Q}{k\Delta T W_h} = \varphi \left[\frac{W_h^2}{\tau\nu}\right]^{a_1} \left[\frac{W_h}{g\tau^2}\right]^{a_2} \left[\frac{L}{W_h}\right]^{a_3} \tag{2.35}$$

where Q is heat flux [W], k is thermal conductivity [W m^{-1} °C^{-1}], T is temperature [°C], W_h is wave height [m], τ is the wave period [s], ν is kinematic viscosity [m^2 s^{-1}], g is gravitational acceleration [m s^{-2}], L is the representative ice waterline length [m], the parameter $Q/k\Delta TW_h$ is the dimensionless heat flux, $W_h^2/\tau\nu$ is a wave Reynolds number, $W_h/g\tau^2$ is proportional to wave steepness, L/W_h is an ice piece length to wave height ratio, and φ, a_1, a_2, and a_3 are constants to be determined by fitting to laboratory and/or field data. The constants were determined by least squares fits to lab tests of floating ice pieces subjected to wave action, tank tests of submerged blocks forced harmonically under water, and field tests involving bergy bits. A range of values for the constants was obtained. The final equation for small ice piece melt rate used in the Canadian Ice Service (CIS) Iceberg Drift and Deterioration model was based on field data alone.

The equation for rate of mass loss for small ice pieces was used to account for deterioration in the size distribution function (*Savage et al.*, 2000). Size distribution is then a function of time, which may be integrated over ice piece lengths to obtain probable numbers of ice pieces greater than a specified size as a function of time. Combined with the drift model, it is then possible to determine total numbers of small ice pieces of significant size and their dispersion from the parent iceberg (*Savage et al.*, 2001).

The influence of melting icebergs in oceanographic conditions has been considered, where a case is made that free convective upwelling may leave a trail of nutrient enhanced surface fluid behind slowly moving icebergs (*Neshyba*, 1977). Supporting this hypothesis, Conductivity Temperature Depth (CTD) sections taken in the vicinity of a melting iceberg in the Labrador Sea indicate that upwelling occurs as a result of the natural turbulent convection in the iceberg meltwater plume (*Josberger*, 1977).

2.4 Ice melting due to buoyant vertical convection

2.4.1 On gravitational free convection

Free (or natural) convection arises in various ways. *Eckert and Jackson* (1951) present the classic example of a heated object placed in a fluid, otherwise at rest, the density of which varies with temperature. Heat is then transferred from the surface of the object to the surrounding fluid. Heat transfer produces a temperature gradient in the fluid, with temperature decreasing with distance from the heated object. The fluid density is a function of temperature, creating differences in relative buoyancy through the thermal boundary layer. The warmer, lower density fluid adjacent to the boundary then rises and creates free convective flow which transports heat away from the object. The inverse holds for a cold object. Heat then flows from the relatively warmer fluid to the colder object creating a gradient of increasing temperature away from the object. Colder and denser fluid adjacent to the object then sinks, resulting in convective heat transport toward the object.

The onset and magnitude of natural convection is related to the Rayleigh number (*Turner*, 1973). For free convection the Rayleigh number is the product of the Grashof number and the Prandtl number (*Turner*, 1973). The Grashof number is the ratio of buoyancy to viscous forces. For buoyancy differences arising from a temperature gradient the Grashof number is,

$$\mathrm{Gr} = \frac{g\alpha_v \Delta T L^3}{\nu^2} \tag{2.36}$$

where g is gravitational acceleration [m s^{-2}], $\alpha_v = -1/V(\partial V/\partial T)_p = -1/\rho(\partial \rho/\partial T)_p$ is the volumetric thermal expansion coefficient [°C^{-1}], $\Delta T = T_w - T_\infty$ [°C], T_w is the wall temperature, T_∞ is the far field temperature, L is a vertical length scale [m], and ν is the kinematic viscosity [m^2 s^{-1}] of the fluid. The Prandtl number is the ratio of momentum diffusivity to thermal diffusivity,

$$\mathrm{Pr} = \frac{\nu}{\kappa} = \frac{c\,\mu}{k} \tag{2.37}$$

where κ is thermal diffusivity [m^2 s^{-1}], μ is the molecular shear (dynamic) viscosity ($\mu = \rho\nu$) [kg m^{-1} s^{-1}], and k is thermal conductivity [W m^{-1} °C^{-1}]. The Prandtl number also provides a measure of the ratio of the momentum boundary layer and thermal boundary layer thickness (*Schlichting*, 1960). Combining Gr and Pr the Rayleigh number is,

$$\mathrm{Ra} = \frac{g' L^3}{\nu\kappa} = \frac{g\alpha_v \Delta T L^3}{\nu\kappa} \tag{2.38}$$

where g' is the buoyancy-reduced gravitational acceleration, and Ra expresses the balance between driving buoyancy forces and the two diffusive processes (thermal and momentum) which retard the motion and tend to stabilize it (*Turner*, 1973). For a fluid heated from below, Lord Rayleigh first proposed a critical value of $\mathrm{Ra_c} = \frac{27}{4}\pi^4 = 657.5$ for the onset of free convection, below which the fluid is stable to small disturbances (*Turner*, 1973). Later work corrects this to $\mathrm{Ra_c} = 1708$ for two rigid boundaries, and $\mathrm{Ra_c} = 1108$ for one rigid and one free boundary, where the additional rigid boundary stabilizes flow (*Turner*, 1973).

The Nusselt number (Nu) is defined as the ratio of the actual heat transport to the purely diffusive flux which would occur through a linear temperature gradient between two boundaries (*Turner*, 1973), and is expressed as the ratio of convective to conductive heat transfer across a boundary,

$$\mathrm{Nu} = \frac{hL}{k} \tag{2.39}$$

where L is the characteristic length of the boundary surface (length scale) [m], k is thermal conductivity [W m^{-1} °C^{-1}], $h = q/\Delta T$ is the convective heat transfer coefficient [W m^{-2} °C^{-1}], and q is the heat flux [W/m^2].

Turner (1973) points out that Nu must be a function of Ra and Pr and suggests that $\mathrm{Nu} = B\mathrm{Ra}^{1/3}$ for Ra near the critical value $\mathrm{Ra_c}$. For larger values of Ra where flow approaches or exceeds the transition to turbulence, *Turner* (1973) finds an increasing dependence on Pr, such that steady convection can persist in high viscosity fluids such as silicon oils and liquid metals. The Nusselt number is then related to Ra and Pr as $\mathrm{Nu} = B\mathrm{Ra}^n\mathrm{Pr}^m$.

Bringing our focus to fluids with lower Pr (such as water with $\mathrm{Pr} \approx 7$ at 20 °C), experiments for which natural convection is driven by a heated flat plate, or heat transfer to a melting body, indicate that the average Nusselt number over the surface of the body may be calculated as:

$$\overline{\mathrm{Nu}} = B(\overline{\mathrm{Ra}})^n \tag{2.40}$$

Coefficients for Equation (2.40) were first derived and compared to experimental results for the case of a free convection boundary layer near a vertical heated flat plate (*Eckert and Jackson*, 1951). For this case, thermal free convection was driven by an upward buoyant force due to thermal expansion of fluid in the neighbourhood of a hot solid wall. As shown on Figure 2.10, Eckert found that the data supported Equation (2.40), obtaining $\overline{\mathrm{Nu_l}} = 0.555(\overline{\mathrm{Ra}})^{1/4}$ for laminar flow and $\overline{\mathrm{Nu_t}} = 0.021(\overline{\mathrm{Ra}})^{2/5}$ for turbulent, where the transition takes place between $10^8 < \mathrm{Ra} < 10^{10}$.

For laminar boundary layers, an approximate solution to the Navier-Stokes equations forced by thermal expansion of the fluid, and the Fourier-Poisson equations for heat transfer, has been derived (*Merk and Prins*, 1954a). The study was confined to $\mathrm{Ra} > 10^4$ to restrict all viscous and thermal effects to a thin boundary layer close to the wall, and $\mathrm{Ra} < 10^9$ to avoid turbulence. The Grashof and Prandtl numbers were found to govern the

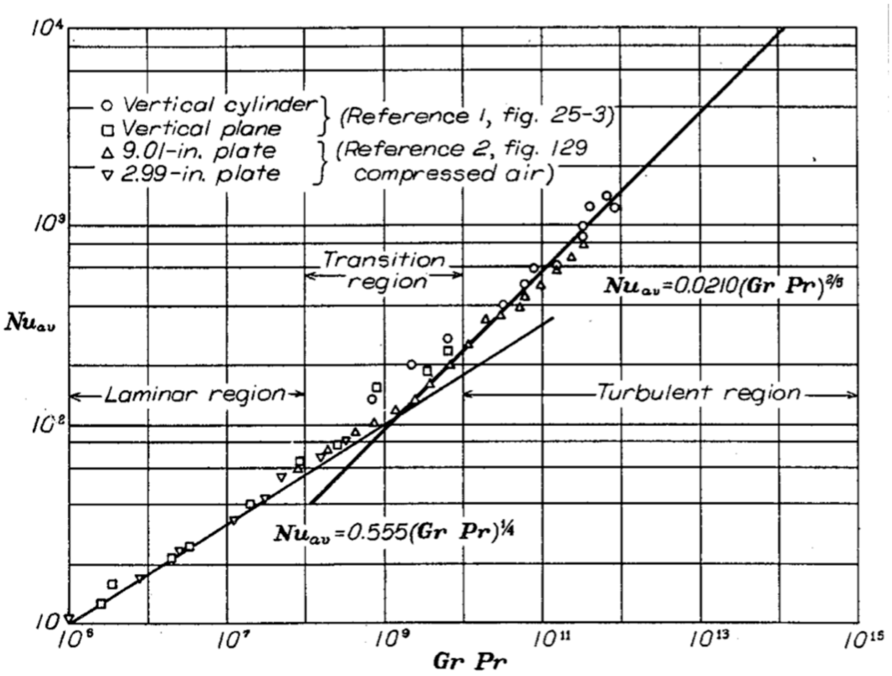

Figure 2.10: Average Nusselt number for free-convection flows on a vertical plate (*Eckert and Jackson*, 1951)

solution and it was shown that, to a first approximation,

$$\overline{\mathrm{Nu}_\mathrm{l}} = B(\overline{\mathrm{Ra}})^{1/4} \tag{2.41}$$

where $0.5 < B < 0.6$ provided $\mathrm{Pr} > 1$. Assuming equal thermal and viscous boundary layer thickness ($\mathrm{Pr} = 1$) values of B were obtained for a vertical flat plate, stagnation point of horizontal cylinder, inclined flat plate, stagnation point of sphere, and vertical cone (*Merk and Prins*, 1954b). Laminar thermal convection for horizontal cylinders and spheres was investigated for $0.7 < Pr < \infty$. For the case of a horizontal cylinder and Pr = 10 , $B = 0.52$ (*Merk and Prins*, 1954c). Additional theoretical values for the simple case of a horizontal heated cylinder submerged in freshwater are presented in *Incropera et al.* (2006), including the general equation

$$\mathrm{Nu} = (0.6 + \frac{0.387\mathrm{Ra}^{1/6}}{[1 + (0.559/\mathrm{Pr})^{9/16}]^{8/27}})^2 \tag{2.42}$$

for $\mathrm{Ra} \leq 10^{12}$, and use of $\mathrm{Nu} = B(\mathrm{Ra})^n$, where $B_l = 0.480$ and $n_l = 1/4$ for laminar and $B_t = 0.125$ and $n_t = 1/3$ for turbulent with $\mathrm{Ra_c} = 10^7$.

2.4.2 On free convective melting of freshwater ice in freshwater

Thermal free convection driven by a melting solid body has been investigated by several authors. The effect of a thin moving boundary layer created by melt liquid has been evaluated and shown to reduce heat transfer compared to estimates of free convection driven by a heated surface by reducing the temperature gradient at the fluid-solid surface (*Merk*, 1954). For the case of ice melting in fresh water, the anomalous thermal expansion of water causes convective inversion (*Merk*, 1954). The direction of motion for water in the boundary layer is opposite at the two sides of the inversion temperature (T_{inv}). Heat transfer (Nu) must then approach a minimum as T_∞ approaches T_{inv}. Merk calculated an inversion temperature of 5.005 °C, which differs from the theoretical value of 4 °C, but points out that his boundary layer approximations are not valid near the inversion point as the boundary layer thickness would be infinite. Merk concluded that heat transfer reaches a minimum in the neighbourhood of $T \approx 5$ °C, and that the flow direction is reversed. This conclusion was confirmed through experiments with melting ice spheres submerged in water (*Dumore et al.*, 1953). Flow field stagnation due to temperature density inversion (natural convection stagnation), was observed near the predicted value, resulting in minimum heat transfer at Nu = 2, the value for pure conduction in a stationary infinite fluid.

To avoid the problem of convective inversion, studies have been performed by melting solid benzene spheres in liquid benzene. The experimental results show average heat transfer to be represented as $\overline{\mathrm{Nu}} = 0.525(\overline{\mathrm{Ra}})^{1/4}$ for $10^4 < \mathrm{Ra} < 10^9$ (*Burgh*, 1960). Local heat transfer as a function of the angular distance from the stagnation point for flow around a sphere has also been evaluated (*Kranse and Schenk*, 1965). A minimum heat transfer of $\mathrm{Nu} = 2$ is shown to occur at the flow stagnation point.

Schenk and Schenkels (1968) conducted a study of melting ice spheres submerged in water of a uniform bulk temperature, which was varied between $0 < T_\infty < 10$ °C. The ice spheres were produced by freezing a 3 mm thick ice layer onto a hollow copper sphere with a diameter of 3.2 cm. For $T_\infty < 4$ °C the melt water is positively buoyant with respect to the surrounding bulk fluid and upward flow was observed. For $4 < T_\infty < 6$ °C dual flow was observed: i.e. flow near the ice surface was upward, with a transition to downward further from the ice surface. At $T_\infty = 5.3$ °C a very thin layer of practically stagnant water was observed along the sphere surface, corresponding to a minimum in convective heat transfer. The thickness of the upward flow decreased with increasing T_∞, with downward flow approaching the ice surface as T_∞ approached 6 °C. For $T_\infty > 6$ °C the entire boundary layer fluid was negatively buoyant and downward flow was observed. For this case, the flow separation point was observed to move downward with increasing T_∞. The continuous production of melt fluid was accounted for by applying Merk's correction to the heat transfer coefficient. The correction was less than 3 percent for $T_\infty < 4$ °C, and about 6 percent at $T_\infty = 10$ °C (*Schenk and Schenkels*, 1968).

Vanier and Tien (1970) carried out similar measurements for small ice spheres (5.08, 7.62, and 10.16 cm) melting in water, over the temperature range of $1 < T_\infty < 22$ °C. The rate of change of apparent weight was measured to calculate $\overline{\mathrm{Nu}}$. The results agreed with the theory for laminar flow convection from a heated flat plate with $B = 0.422$ for $T_\infty > 7$ °C, $B = 0.573$ for $T_\infty < 3.6$ °C, and $B = 0.362$ for $4.8\ °C < T_\infty < 7.1$ °C. The authors note the advantage of measuring weight change to avoid error from trapped air bubbles. However, this method does not allow local heat transfer measurements and is restricted to average Nusselt number ($\overline{\mathrm{Nu}}$) (*Vanier and Tien*, 1969).

2.4.3 On free convective melting of freshwater ice in saltwater

The melting of freshwater ice in sea water produces fluid with a salinity less than the surrounding sea water and a temperature equal to the freezing point at that salinity (*Gade*, 1979). It follows that the freezing point is less than 0°C, and at temperatures less than 0°C melting continues, driven by the difference in salt concentration between the ice and seawater (*Greisman*, 1979). Thermal and saline boundary layers are present, through which temperature and salinity transition from that of the melt water to those of the surrounding sea water. Within these boundary layers free convection is present which is driven not only by thermal, but also by saline effects.

Two important physical phenomena complicate the process: (1) convective inversion resulting from the anomalous thermal expansion of fresh and salt water, and (2) the much lower diffusivity of salt compared to heat (*Josberger and Martin*, 1981). Two regions of the T-S diagram for salt-water solutions are presented in Figure 2.11. The regions are separated by the maximum density line $T_{\rho max}$ and freezing point depression line T_{fp}, plotted at one atmosphere of pressure using Unesco 1983 polynomials (*Fofonoff and Millard*, 1983). The behaviour of convective flows within the regions of the T-S diagram are partially governed by the saline and thermal expansion coefficients. At constant temperature, the dilution of salt water with fresh produces less dense water as the coefficient of saline expansion (β_v) [psu^{-1} or ppt^{-1}]

$$\beta_v = \frac{1}{\rho}\frac{\partial \rho}{\partial S} \tag{2.43}$$

is positive. Cooling may produce either lighter or denser water depending on whether T and S fall in regions I or II, respectively. The coefficient of thermal expansion (α_v) [°C^{-1} or K^{-1}]

$$\alpha_v = \frac{1}{\rho}\frac{\partial \rho}{\partial T} \tag{2.44}$$

changes sign at the maximum density line. For solutions in region I, cooling and dilution cause reinforcing upward buoyancy forces. For solutions in region II, cooling and dilution produce opposing buoyancy forces (*Josberger and Martin*, 1981).

The effects of salt and heat on convection are best discussed through use of dimensionless numbers. For laminar boundary layers adjacent to a flat plate the magnitudes of the Prandtl $\mathrm{Pr} = \nu/\kappa$ and Schmidt $\mathrm{Sc} = \nu/D_{sl}$ (where D_{sl} is the mass diffusivity of salt [m^2 s^{-1}] and other parameters have been defined previously) numbers relate relative thickness of heat and salinity boundary layers to that of velocity, respectively. The Lewis number $\mathrm{Le} = \mathrm{Sc}/\mathrm{Pr}$ relates the relative thickness of the thermal and salinity boundary layers. (*Schlichting*, 1960)

Using values of kinematic viscosity $\nu = 1.8 \times 10^{-6}$ m^2 s^{-1}, thermal diffusivity $\kappa = 1.44 \times 10^{-7}$ m^2 s^{-1} (*Neumann and Pierson*, 1966), and saline diffusivity $D_{sl} = 6.3 \times 10^{-10}$ m^2 s^{-1} (*Caldwell*, 1974) the velocity δ_u, heat δ_Q, and salt δ_S boundary layer thicknesses may be expressed as:

$$\frac{\delta_Q}{\delta_u} \approx \mathrm{Pr}^{-1/2} \approx 0.3 \tag{2.45}$$

$$\frac{\delta_S}{\delta_u} \approx \mathrm{Sc}^{-1/2} \approx 0.02 \tag{2.46}$$

$$\frac{\delta_S}{\delta_Q} \approx \mathrm{Le}^{-1/2} \approx 0.07 \tag{2.47}$$

The larger δ_Q compared to δ_S suggests that the opposing heat and saline buoyancy forces present for fluids in region II of Figure 2.11 will act in different regions of the velocity boundary layer δ_u, which is thicker than either δ_Q or δ_S. (*Josberger and Martin*, 1981)

Josberger (1977) conducted laboratory studies to investigate the processes that govern

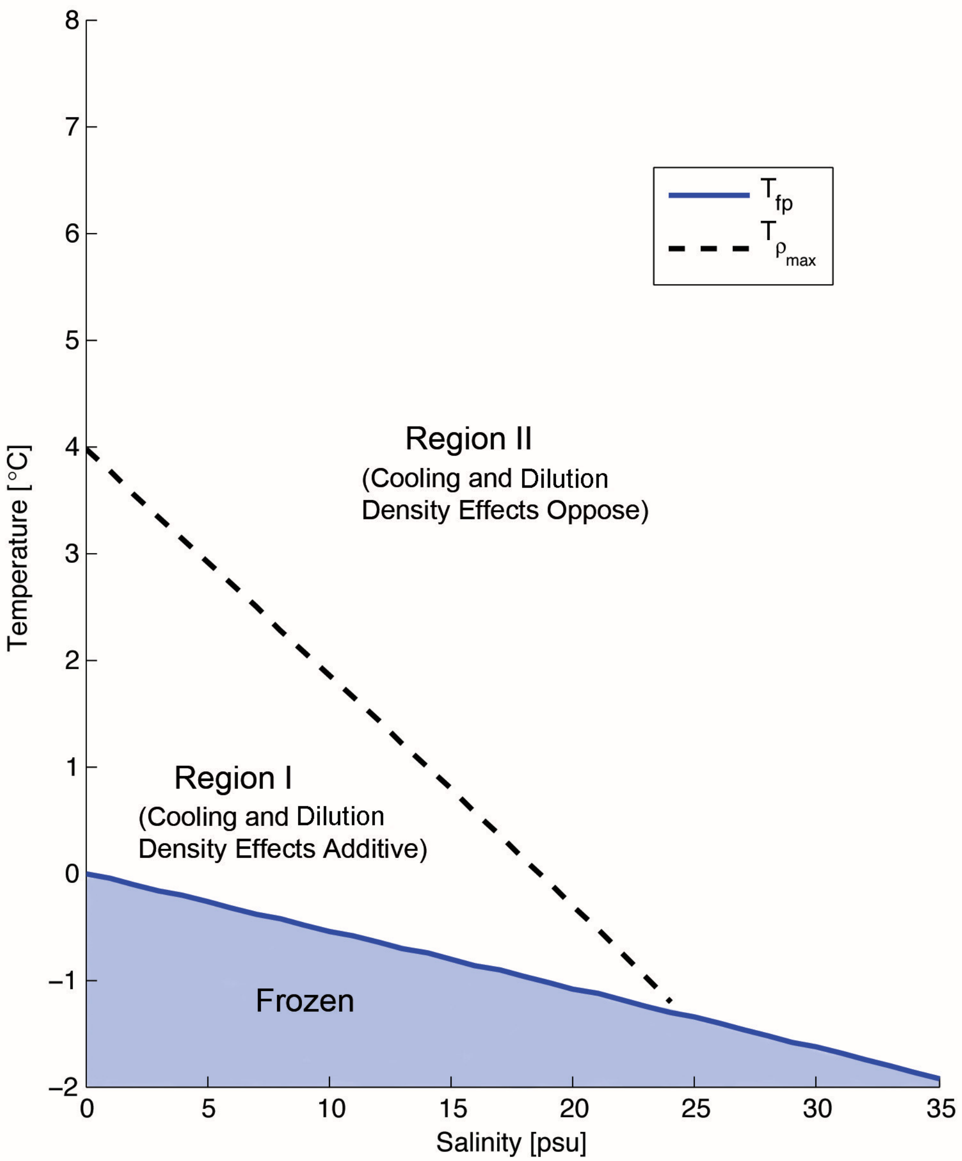

Figure 2.11: T-S diagram for salt-water solutions showing the location of the freezing point depression line T_{fp}, and maximum density line $T_{\rho max}$ (*Josberger and Martin*, 1981)

melt-driven convection in sea water. Focusing on the effect of thermal and saline diffusivities, bubble-free sheets of freshwater ice 0.2 m wide by 0.1 m thick by 0.5 to 1.0 m long were melted in NaCl solutions of oceanic salinities and temperatures. A thermistor array was frozen into the ice sheet to measure temperature, and the flow field was visualized by suspending mother-of-pearl flakes in the salt water. To investigate the effect of convective inversion, similar ice sheets were melted in NaCl solutions covering a wider range of far-field salinity and temperatures (*Josberger and Martin*, 1981). Three flow regimes were observed that depend on the far field temperature (T_∞) and salinity (S_∞).

Josberger defined a thermal driving temperature

$$T_d = T_\infty - T_{fp}(S_\infty) \tag{2.48}$$

where T_{fp} [°C] is the freezing point of the far-field fluid of salinity S_∞ [psu]. T_d [°C] is a convenient parameter for characterization of his experimental results, and is carried through the results presented in this work.

The first, and simplest, of the three flow regimes observed by *Josberger and Martin* (1981) occurred when T_∞ and S_∞ lay between the maximum density and freezing curve (region I) in Figure 2.11. Consistent with the discussion presented above, unidirectional upward flow was observed.

The second flow regime was observed for the typical oceanic melting case: i.e. $T_d <$ 20 °C and $30 \leq S_\infty \leq 35$ psu (region II). In this region *Josberger and Martin* (1981) observed a bidirectional laminar boundary layer at the bottom of the ice sheet that was separated from an upward flowing turbulent boundary layer higher up the ice by a horizontal jet approximately 100 mm thick with a velocity in the order of 1 mm/s. The horizontal jet supplied the inward flux of ambient water for the convective flow system. A bifurcation point was observed where the jet impinged upon the ice surface, above which water entered the upward salinity (meltwater) driven turbulent flow, and below which water entered the downward thermally driven flow. A sketch of flow observations for region II is provided as Figure 2.12.

The third flow regime was observed for values of $T_d >$ 20 °C and $30 \leq S_\infty \leq 35$ psu. Although the melting of icebergs in such warm waters must be considered to be rare, an interesting observation of the reversal of the second flow regime was made, such that a laminar bidirectional boundary layer was observed at the top of the ice sheet above a

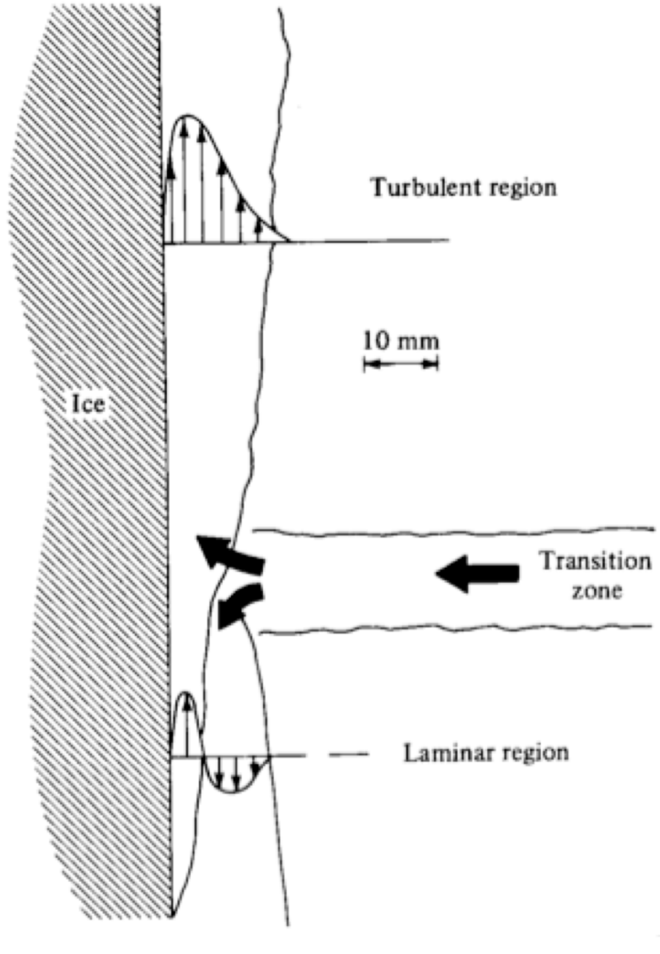

Figure 2.12: A sketch of the observed flow next to the ice for $T_d < 20$ °C and $30 \leq S_\infty \leq 35$ psu (region II) (*Josberger and Martin*, 1981)

downward flowing turbulent boundary layer. For this case T_d was sufficiently high for cooling to overwhelm dilution by fresh meltwater. A sketch of flow observations for region II is provided as Figure 2.13.

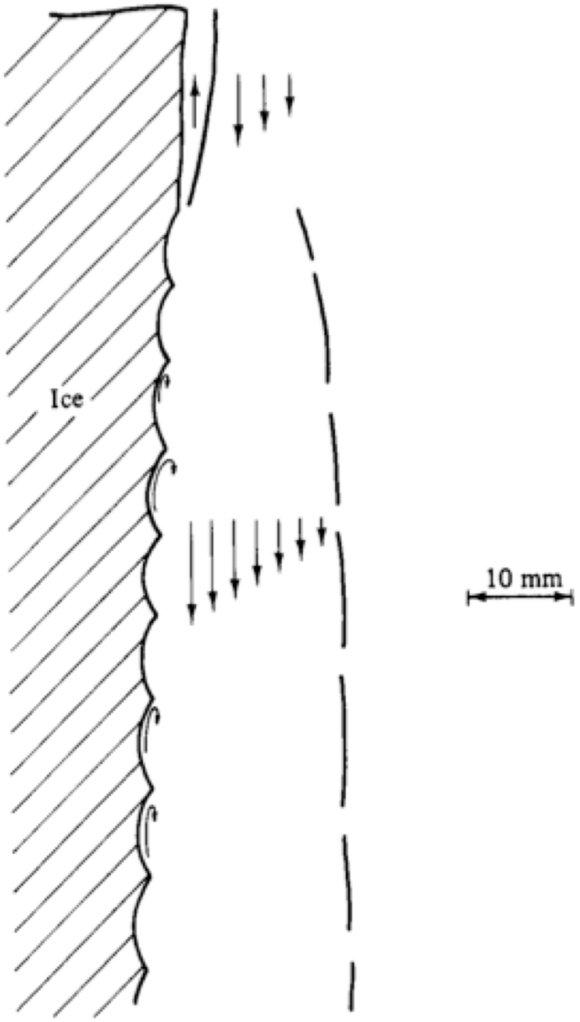

Figure 2.13: A sketch of the observed flow next to the ice for $T_d > 25$ °C (region III) (*Josberger and Martin*, 1981)

In the second flow regime, low salinity cool water was observed near the ice surface with a thickness of order 1 mm, increasing from the ice bottom. In this region the salinity difference dominated density, producing upward flow with a velocity on the order of 1 mm/s driven by positive dilution buoyancy. In the laminar region below the bifurcation point, moving away from the ice surface, salinity reached far-field values but a temperature gradient remained. The upward flow then transitioned to downward as negative buoyancy due to cooling gained dominance, consistent with the previous discussion of the large Lewis number. The outer flow was observed to have a thickness of order 10 mm increasing downward from the bifurcation point, except at the bottom of the ice sheet where the flow narrowed and accelerated under the ice. Within the upper third of the inner upward flow, small amplitude waves were observed with horizontal crests parallel to the ice surface at the outer edge of the saline layer. The waves propagated upward with order 1 mm/s phase speeds and wavelengths of about 5 mm. The wave amplitudes were observed to grow to approximately 3 mm at which point the waves broke to form horizontal vortices of 3 mm diameter.

In the turbulent region above the bifurcation point, the salinity deficit was mixed farther horizontally into the surrounding fluid to a distance comparable to δ_Q. The negative buoyancy due to cooling was overwhelmed by positive dilution buoyancy, such that the net result was an upward flowing turbulent boundary layer, with thicknesses of 10 mm to 30 mm, increasing with distance upward from the bifurcation point. The maximum flow velocity was of order 10 mm/s.

The transition from laminar to turbulent free convective flow can be characterized by the magnitude of the Grashof number. For the case of ice melting in seawater the Grashof number is best defined by

$$\mathrm{Gr} = \frac{g|\rho_w - \rho_\infty|L^3}{\rho_\infty \nu^2} \tag{2.49}$$

(*Josberger and Martin*, 1981), where ρ_w [kg m^{-3}] is the water density at the ice-water interface. Equation (2.49) can be compared to Equation (2.36). By calculating ρ directly for a given T and S, saline and thermal contributions to density are accounted for. *Josberger and Martin* (1981) found that transition to turbulence occurred at $\mathrm{Gr} \approx 2 \times 10^8$, which is an order of magnitude less than the critical values for natural convection flows driven by heat diffusion for $\mathrm{Pr} \approx 10$ (*Eckert and Jackson*, 1951) (*Turner*, 1973). The lower critical Gr may result from destabilization of laminar flow due to an increase in vertical shear resulting from the outer downward flow (*Josberger and Martin*, 1981). Using oceanic salinities and temperatures where melting occurs ($\rho_\infty \approx 1024$ kg m^{-3}, $\rho_w \approx 1000$ kg m^{-3}, and $\nu = 1.8 \times 10^{-6}$ m^2 s^{-1}) $\mathrm{Gr} > 2 \times 10^8$ for length scales $L > 0.15$ m.

Further investigation of the three flow regimes produced by the simultaneous cooling and dilution of seawater as ice melts is provided in a study of upwelling driven by melting of ice shelves and tidewater glaciers (*Greisman*, 1979). Notably, Greisman divides region

II of Figure 2.11 into subregions in which the net flow is either upward or downward. Griesman's work applies to the turbulent portion of the flow regimes discussed above, in which salt and heat are mixed within a single boundary layer. It is then assumed that the rates of heat and salt transport toward the melting ice surface across the turbulent boundary layer are equal. From conservation of mass and the latent heat of fusion, when 1 g of ice melts it releases 1 g of fresh water and 334 J of heat is removed from the surrounding water. If 1 g of ice melts in φ g of seawater, the change in salinity will be

$$\delta S = -\frac{S}{\varphi + 1} \tag{2.50}$$

where S is the initial salinity of the water. Similarly the change in temperature will be

$$\delta T = -\frac{\Delta T + F/c}{\varphi + 1} \approx -\frac{\Delta T + 80}{\varphi + 1} \tag{2.51}$$

where $F/c \approx 80$ °C for $F = 334$ J g^{-1}, $c = 4.18$ J g^{-1} °C^{-1} and $\Delta T = T_\infty - T_w$. From equation (2.51) Greisman observed that the amount of heat conducted away from the ice surface due to internal temperature gradients in the glacier is roughly two orders of magnitude smaller than the heat used in melting the ice, and therefore δT is nearly independent of heat flux through the glacier. The melting of a glacier wall in seawater is approximated to be a steady state process ($\partial S/\partial t = \partial T/\partial t = 0$). The mixing of ice meltwater and seawater are then represented in T-S space by lines with slopes [°C psu^{-1}] of

$$\left(\frac{\delta T}{\delta S}\right)_{melt} = \frac{\Delta T + 80}{S} \tag{2.52}$$

Greisman (1979) shows that the locus of points in the T-S space where the opposing effects of cooling and dilution balance divide region II. Along an isopycnal

$$d\rho = 0 = \left(\frac{\partial \rho}{\partial S}\right)_T dS + \left(\frac{\partial \rho}{\partial T}\right)_S dT \tag{2.53}$$

and the local slope of the isopycnal in T-S space is

$$\left(\frac{dT}{dS}\right)_\rho = \frac{-(\frac{\partial \rho}{\partial S})_T}{(\frac{\partial \rho}{\partial T})_S} \tag{2.54}$$

Therefore, the division of region II is defined by

$$\frac{\Delta T + 80}{S} = \left(\frac{dT}{dS}\right)_{\rho} \tag{2.55}$$

a negatively buoyant solution is formed when

$$\left(\frac{dT}{dS}\right)_{melt} = \frac{\Delta T + 80}{S} > \left(\frac{dT}{dS}\right)_{\rho} \tag{2.56}$$

and a positively buoyant solution is formed when

$$\left(\frac{dT}{dS}\right)_{melt} = \frac{\Delta T + 80}{S} < \left(\frac{dT}{dS}\right)_{\rho} \tag{2.57}$$

Equation (2.57) holds for most natural systems near ice shelves where seawater temperatures are relatively low resulting in upwelling at vertical ice faces (*Greisman*, 1979).

With respect to melt rate, Josberger observed high ablation on the lower part of the ice face, decreasing upward towards the bifurcation point at which point melt increased abruptly to a maximum creating a notch in the ice surface. Moving upward from the bifurcation point, Josberger's experimental results show the melt rate to decrease, while remaining higher than that observed in the lower laminar region. The dependence of the average melt rate ($\overline{M_0}$) on T_d was observed to change from non-liner to linear near 9 °C. For $T_d \leq 9$ °C,

$$\overline{M_0} = 0.76 T_d^{1.6} \times 10^{-3} \tag{2.58}$$

and for $9 \geq T_d \leq 20$ °C

$$\overline{M_0} = (3.55 T_d - 5.89) \times 10^{-3} \tag{2.59}$$

where $\overline{M_0} = M x^{1/4}$ [mm$^{5/4}$ s^{-1}], M is the measured melt rate [mm s^{-1}], and x is the distance of the measurement above the bifurcation point [mm].

Wall temperatures (T_w) were measured throughout Josberger's experiments. For experiments with Gr in the turbulent range, T_w remained constant to within 0.02 °C along the ice-water interface. For laminar flow, T_w was observed to increase with height. A dimensionless parameter $\overline{r_1}$ was defined as the average wall temperature divided by the

Experiment number	T_∞ (°C)	S_∞ (ppt)	T_{fp} (°C)	T_d (°C)	$\overline{T_w}$ (°C)	$\overline{r_1}$	r_2
1	-0.5	29.0	-1.58	1.08	-1.53	0.97	0.84
2	-0.72	33.7	-1.85	1.13	-1.81	0.98	0.83
3	0.0	29.0	-1.58	1.58	-1.49	0.94	0.77
4	1.55	29.0	-1.58	3.13	-1.11	0.70	0.56
5	2.20	30.0	-1.64	3.84	-0.97	0.59	0.48
6	2.70	29.0	-1.58	4.28	-0.80	0.51	0.43
7	2.66	34.4	-1.89	4.55	-1.03	0.55	0.41
8	6.85	34.0	-1.86	8.71	-0.32	0.17	0.14

Table 2.2: Conditions for freshwater ice melting in seawater in Josberger's experiments

freezing temperature of the far-field fluid,

$$\overline{r_1} = \overline{T_w}/T_{fp} \tag{2.60}$$

Josberger observed $\overline{r_1}$ to decrease with increasing thermal driving (T_d). The decrease was linear from near unity ($T_w \approx T_{fp}$) when the ice is near equilibrium with far-field conditions, then approached zero ($T_w \approx 0$) for $T_d > 9$ °C. Josberger presents the curve,

$$r_2 = 1.0 - \tanh(0.15T_d) \tag{2.61}$$

as a fit to his data. Some of Josberger's results are summarized in Table 2.2. [6]

The results summarized in Table 2.2 support the trend of $\overline{r_1}$ discussed above and show the occurrence of melting for far-field temperatures less than 0 °C. Although T_w approaches T_{fp} as T_d approaches 0, melting produces boundary layer fluid that will be somewhat fresher than the far-field seawater, resulting in a wall temperature that is slightly warmer

---

[6] It should be noted that the values of $\overline{r}$ presented by *Josberger and Martin* (1981) differ from those of $\overline{r_1}$ and r_2 in Table 2.2. The values of T_{fp} presented in Table 2.2 were calculated for one atmosphere of pressure using Unesco 1983 polynomials (*Fofonoff and Millard*, 1983) assuming $S(ppt) \approx S(psu)$. Using Equation (2.48) all values of T_d presented in 2.2 match those of *Josberger and Martin* (1981) with exception of a small discrepancy of 1.58 to 1.65 for experiment 3. This indicates the vales of T_{fp} presented in Table 2.2 are consistent with those of *Josberger and Martin* (1981), although not presented in their work. However, if we back-calculate T_{fp} using Equation (2.60) and the values of $\overline{r}$ presented by *Josberger and Martin* (1981) the following values result for experiments 1 through 8, respectively; -1.74, -2.01, -1.73, -1.73, -1.80, -1.74, -2.06, and -2.00. These back-calculated values for T_{fp} yield T_d values of 1.24, 1.29, 1.73, 3.38, 4.00, 4.44, 4.72, and 8.85, respectively, which differ from the results that are consistent between Table 2.2 and *Josberger and Martin* (1981). Similarly, for T_d back-calculated from Equation(2.61) we get 0.80, 0.67, 0.94, 2.51, 3.30, 4.00, 3.64, and 7.44, respectively. The source of the discrepancy remains unresolved.

than the freezing point of the far-field seawater. The temperature difference $\Delta T = T_\infty - T_w$ may then approach, but never equal, the temperature elevation of the far-field fluid above its freezing point $T_d = T_\infty - T_{fp}$ (*Greisman*, 1979). With respect to ice melt in salt water below 0 °C, *Loewe* (1961) presents a discussion of experiments conducted by submerging 10 to 15 kg fresh water ice blocks in polar regions near Greenland with seawater temperatures below 0 °C. His results show that appreciable melting occurs even when the far-field water temperature is less than one degree above its freezing point.

Wall temperature (T_w) calculated using Equations (2.48), (2.60), and (2.61) is plotted on Figure 2.14 over the range of $-1.5°\text{C} \leq T_\infty \leq 10°\text{C}$ for $S_\infty = 31$ psu. $T_d = T_\infty - T_{fp}$ and $\Delta T = T_\infty - T_w$ are plotted over the same range of T_∞ and $S_\infty = 31$ psu on Figure 2.15. Figures 2.14 and 2.15 show the trends presented by *Greisman* (1979) and *Josberger and Martin* (1981).

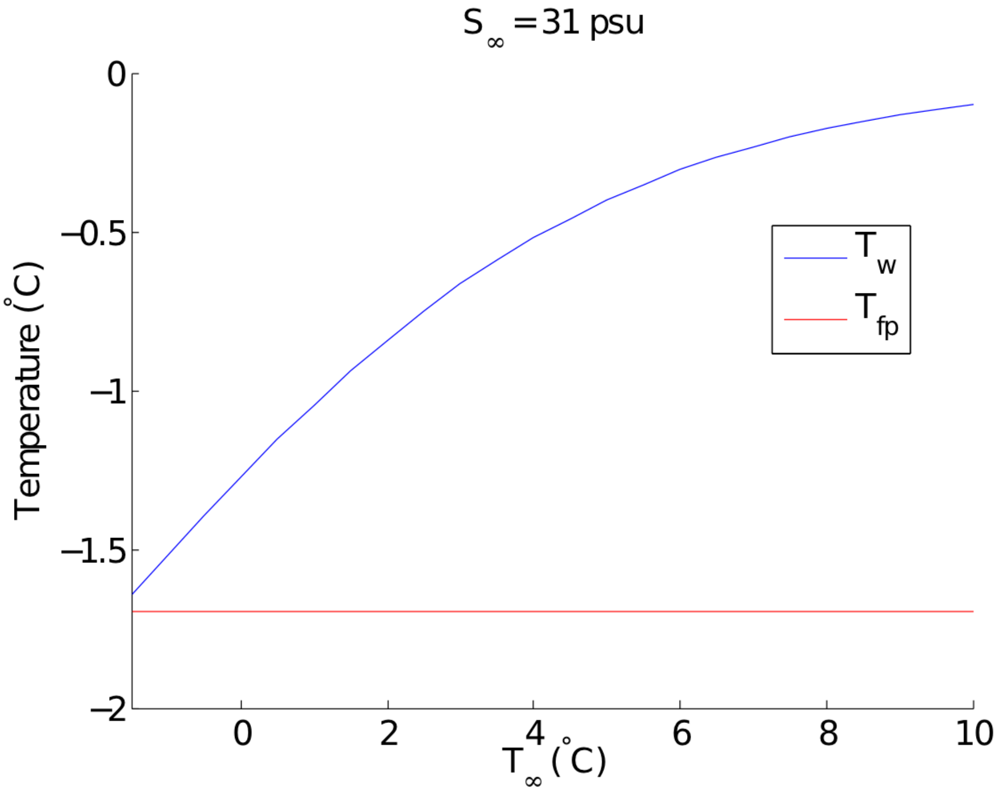

Figure 2.14: Effect of far-field temperature (T_∞) on ice wall temperature (T_w) for sea water salinity (S_∞) of 31 psu

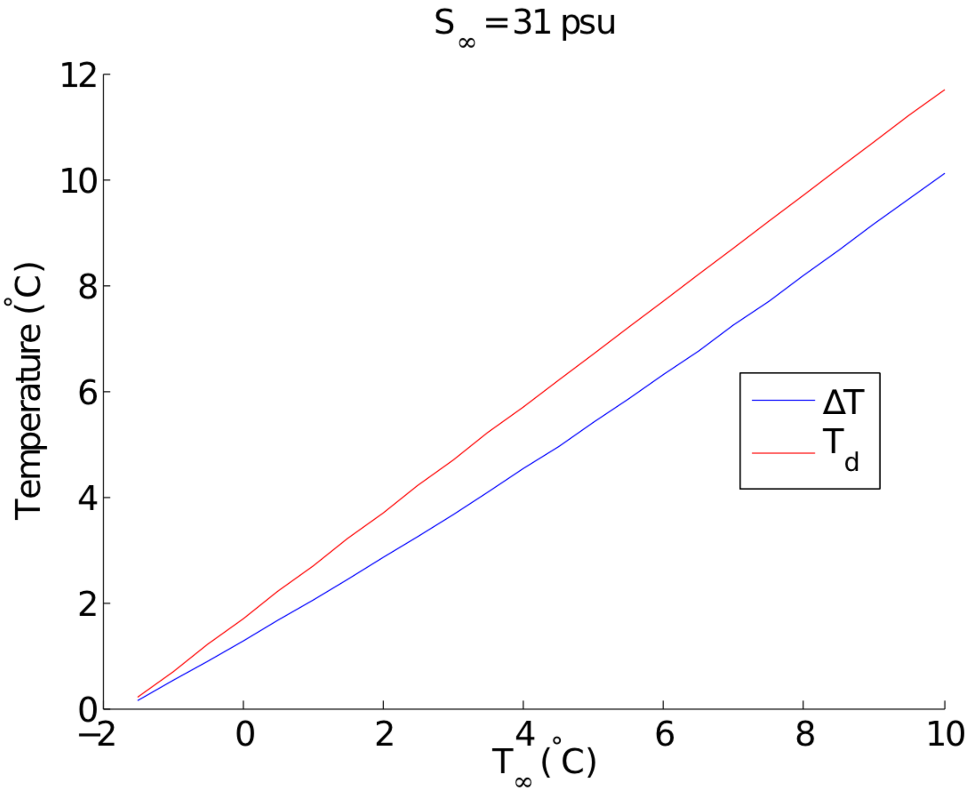

Figure 2.15: Effect of far-field temperature (T_∞) on $T_d = T_\infty - T_{fp}$ and $\Delta T = T_\infty - T_w$ for sea water salinity (S_∞) of 31 psu

CHAPTER 3

ICE MELT RATE THEORY

3.1 General Theory

Newton's law of cooling specifies that the rate of change of the temperature of an object is proportional to the difference between its own temperature and the ambient temperature. The formula for the rate of convective heat transfer to an ice block submerged in seawater is then:

$$q = h\Delta T \tag{3.1}$$

where q is heat flux [W/m^2], h is the convective heat transfer coefficient [W m^{-2} °C^{-1}], $\Delta T = T_\infty - T_w$, T_∞ is the far-field seawater temperature, and T_w is the ice wall temperature.

As discussed in Section 2.4.1, the Nusselt number $\mathrm{Nu} = hL/k$ is the ratio of convective to conductive heat transfer across a boundary, where k is thermal conductivity [W m^{-1} °C^{-1}] and L is characteristic length of the boundary surface (length scale) [m]. Rearranging the Nusselt number and substituting $h = \mathrm{Nu}\, k/L$ into (3.1) we get:

$$q = \mathrm{Nu}\frac{k\Delta T}{L} \tag{3.2}$$

or

$$Q = \mathrm{Nu}\frac{k\Delta T A}{L} \tag{3.3}$$

where A is the surface area [m^2] over which heat flux occurs, and Q is the rate of heat transfer [W].

As discussed in Section 2.2.3, the energy required for a change of state between solid and liquid, such as ice to water, is:

$$E = Q\Delta t = \Delta m F \tag{3.4}$$

where E is energy [J], Δt is the time step over which heat flux occurs [s], Δm is the mass of solid that changes state to fluid [kg], and F is the latent heat of fusion for the substance [J kg^{-1}]. As $\Delta t \rightarrow 0$ we have:

$$\frac{dm}{dt} = \frac{Q}{F} \tag{3.5}$$

where positive dm/dt [kg s^{-1}] represents the rate of mass lost from ice and gained by fluid. To include any additional heat required to raise the ice block temperature to its melting point Equation (3.5) becomes

$$\frac{dm}{dt} = \frac{Q}{F + c_i \Delta T} \tag{3.6}$$

where c_i is the heat capacity of ice [J kg^{-1} °C^{-1}], $\Delta T = T_\infty - T_i$, T_∞ is the far-field water temperature, and T_i is the ice block temperature.

The ratio of the heat required to raise the ice temperature to its melting point ($c_i \Delta T$) and the heat required to melt a unit mass of ice (F) is the Stefan number (St)

$$\mathrm{St} = \frac{c_i \Delta T}{F} \tag{3.7}$$

The Stefan number is plotted in Figure 3.1 for a range of ΔT using $T_\infty = 4$ °C. As shown, the assumption of $F >> c\Delta T$ (or $\mathrm{St} << 1$) is valid for freshwater ice. However, as discussed in Section 2.2.2 the effect of brine inclusions in saltwater ice complicates the relationship between F and c. The thermal properties of sea ice (F_{ci} and c_{ci}) are calculated as functions of ice salinity and temperature using parameterizations from experimental data that asymptote to negative and positive infinity as T_i approaches 0°C for F_{ci} and c_{ci}, respectively. The asymptotic behaviour is a limitation of the parameterizations and results in a predicted St with unstable behaviour for ice temperatures less than $T_i \approx -4$°C. This uncertainty is limited to the small saltwater ice blocks melted for this work, and for all ice types F is the total heat requirement to melt a unit mass of ice.

From Equation (3.5), any effect of sediment inclusion on melt rate must be related to a change in heat supply (Q) [J s^{-1}] or heat requirement (F) [J kg^{-1}] to melt a unit mass

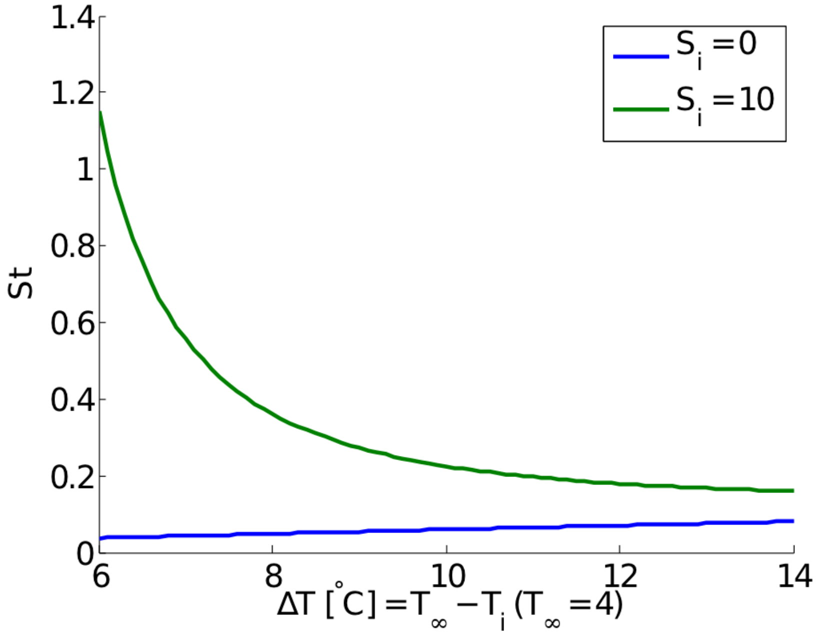

Figure 3.1: Stefan number (St) for freshwater ice ($S_i = 0$ ppt) and saltwater ice ($S_i = 10$ ppt) using a far-field water temperature of $T_\infty = 4$ °C and ice temperature ranging from $-10 \leq T_i \leq -2$ °C

of sediment-laden ice, where Q is affected by the strength of the convective current as described by Nu and F by the ice block sediment content, salinity, and temperature as described by Equation (2.33).

Combining (3.3) and (3.5), then rearranging to solve for Nu gives

$$\mathrm{Nu} = \frac{dm}{dt}\frac{FL}{k\Delta TA} \tag{3.8}$$

As discussed in Section 2.4.1, from experiments where natural convection in water is driven by a heated flat plate, or a melting sphere, it has been shown that the Nusselt number may be calculated as $\overline{\mathrm{Nu}} = B(\overline{\mathrm{Ra}})^n$ (Equation (2.40)), where the Rayleigh number (Ra) is the product of the dimensionless Grashof (Gr) and Prandtl (Pr) numbers, B is a dimensionless constant and $n = 1/4$ for laminar boundary layer flow or $n = 2/5$ for turbulent. Using Equations (2.49) and (2.37) for Gr and Pr, respectively, the Rayleigh number takes the form,

$$\mathrm{Ra} = \frac{g|\rho_w - \rho_\infty|L^3}{\rho_\infty \nu_w \kappa} \tag{3.9}$$

noting the substitution $\mu = \nu_w \rho_\infty$ [kg m^{-1} s^{-1}] has not been made as ν_w [m^2 s^{-1}] is representative of conditions at the ice-fluid interface rather than far-field values.

Now substituting (3.9) into (2.40) we have

$$\mathrm{Nu} = B\left[\frac{g|\rho_w - \rho_\infty|L^3}{\rho_\infty \nu \kappa}\right]^n \tag{3.10}$$

and Equation (3.3) becomes

$$Q = B\left[\frac{g|\rho_w - \rho_\infty|L^3}{\rho_\infty \nu \kappa}\right]^n \frac{k\Delta T A}{L} \tag{3.11}$$

For the case of a sphere $L = d$ [m], which also applies to a cylinder with an aspect ratio near $L = 2r$. For any other cylinder L is dependent on orientation, as it represents the length scale over which convection occurs, which must be the vertically oriented dimension for buoyancy induced flows. For all experiments conducted in this work, ice cylinders were oriented such that length was nearly perpendicular to the vertical (depth) axis. Thus, diameter (or $2r$) is the vertical length scale.

The surface area of a cylinder is $A = 2\pi r(L + r)$ [m^2]. For the general case of a cylinder with the aspect ratio $L = b_1 r$ (where b_1 is a real, non-zero, positive constant) we have $A = 2\pi r(b_1 r + r) = 2b_2\pi r^2$, where $b_2 = 1 + b_1$. For example, with $L = 2r$ we have $A = 6\pi r^2$. For a sphere $A = 4\pi r^2$.

Now taking all parameters in (3.11) to be constant, with the exception of r which decreases throughout the melt, we may write $Q \sim r^{3n+1}$.

3.1.1 *Laminar Case*

For the laminar case $n = 1/4$, so $Q \sim r^{7/4}$. For a cylinder, or sphere, mass (m) may be calculated as $m = b_1\rho\pi r^3$, where $b_1 = 4/3$ in the case of the sphere. We then have $m \sim r^3$ or $r \sim m^{1/3}$ and convective heat flow is $Q \sim m^{7/12}$.

From Equation (3.4) we have $Q/F = \Delta m/\Delta t$. Assuming a homogeneous material such that F is constant, $dm/dt \sim m^{7/12}$, or

$$\frac{dm}{dt} = \varphi_l m^{7/12} \tag{3.12}$$

where φ_l [kg$^{5/12}$ s^{-1}] is a constant and the subscript l denotes laminar. Integrating

$\int m^{-7/12}dm = \int \varphi_l dt$ and applying the initial condition of $m = m_0$ at $t = 0$

$$m^{5/12} = m_0^{5/12} + \alpha_l t \tag{3.13}$$

where $\alpha_l = \frac{5}{12}\varphi_l$ [kg$^{5/12}$ s^{-1}], which can be substituted into Equation (3.12) to give

$$\frac{dm}{dt} = \frac{12}{5}\alpha_l m^{7/12} \tag{3.14}$$

3.1.2 Turbulent Case

For the turbulent case $n = 2/5$, so $Q \sim r^{11/5}$. Similar to above, convective heat flow is then $Q \sim m^{11/15}$. Integrating $\int m^{-11/15}dm = \int \varphi_t dt$ gives

$$m^{4/15} = m_0^{4/15} + \alpha_t t \tag{3.15}$$

where $\alpha_t = \frac{4}{15}\varphi_t$ [kg$^{4/15}$ s^{-1}] and the subscript t denotes turbulent. It is then evident that

$$\frac{dm}{dt} = \frac{15}{4}\alpha_t m^{11/15} \tag{3.16}$$

3.1.3 General Case

Equations (3.13) and (3.15) may be written as

$$m^{\zeta} = m_0^{\zeta} + \alpha t \tag{3.17}$$

where $\zeta_l = 5/12$ for laminar and $\zeta_t = 4/15$ for turbulent conditions. Similarly, Equations (3.14) and (3.16) become

$$\frac{dm}{dt} = \frac{1}{\zeta}\alpha m^{1-\zeta} \tag{3.18}$$

where α has units of kg$^{\zeta}$ s^{-1} for dm/dt in kg s^{-1}.

The melt experiments described in the following chapters are used to evaluate these theoretical relationships and determine if Equation (3.18) can be substituted into Equation (3.8) to solve for Nu.

3.2 Simplified Spherical Theory

The law of heat conduction (Fourier's law) states that the rate of heat transfer (Q) through a material is proportional to the negative temperature gradient and to the area perpendicular to the gradient through which heat is flowing. For the case of a sphere, heat flux (q) [W m^{-2}] is then,

$$q = -k\frac{dT}{dr} \tag{3.19}$$

where k is thermal conductivity [W m^{-1} °C^{-1}], and r is radius [m]. Assuming heat flux to be constant over the surface area of a submerged sphere, heat transfer is then,

$$Q = -4\pi r^2 k\frac{dT}{dr}|_{r=r_o} \tag{3.20}$$

Substituting Equation (3.20) into Equation (3.5) melt rate for a submerged ice sphere is then,

$$\frac{dm}{dt} = \frac{-4\pi r^2 k}{F}\frac{dT}{dr} \tag{3.21}$$

The mass of a sphere is,

$$m = \frac{4\pi\rho r^3}{3} \tag{3.22}$$

thus,

$$r = (\frac{3m}{4\pi\rho})^{1/3} \tag{3.23}$$

Substituting Equation (3.22) into (3.21) the rate of change for radius due to melting of the sphere is,

$$\frac{dr}{dt} = -\frac{3k}{\rho F}\frac{dT}{dr} \tag{3.24}$$

Taking the temperature gradient to be constant as well as all other parameters on the right hand side, this gives radius decreasing linearly with time,

$$r = r_0 + \varphi t \tag{3.25}$$

and using equation (3.23)

$$m^{1/3} = m_0^{1/3} + \alpha t \tag{3.26}$$

where $\zeta = 1/3$ is in close agreement with $\zeta_l = 5/12$ and $\zeta_t = 4/15$ derived specifically for laminar and turbulent conditions.

CHAPTER 4

METHODS

All data used for the development of the melt rate model for sediment-laden ice were obtained through laboratory experiments conducted in the Aquatron laboratories at Dalhousie University. Two tanks were used: the 684,000 L "pool" tank and the 117,000 L "tower" tank. Melts were conducted with freshwater ice blocks of initial volume approximately equal to 18 L on April 14, 22, and July 28, 2009. In addition, sediment-laden freshwater, saltwater, and sediment-laden saltwater ice blocks of similar volume were also melted on July 28, 2009. Larger freshwater ice blocks of initial volume approximately equal to 160 L were melted on March 3 and 4, 2010, and on January 26 and 28, 2011. Sediment-laden freshwater ice blocks of similar volume were melted on February 21 and 22, and March 30, 2011. In addition to measuring the ice block melt rate on March 30, 2011 additional instrumentation was used to observe the behaviour of the sediment-laden melt plume.

4.1 Ice Formation

Ice blocks were formed in a walk-in freezer where temperature was maintained at -14 ± 1 °C, with occasional increases of approximately 3 to 4 °C when the door was opened. The smaller ice blocks ($V_0 \approx 18$ L) were formed in cylindrical 20 L plastic pails of dimension, diameter 0.26 to 0.29 m (tapered from base to rim) and length 0.36 m. The larger ice blocks ($V_0 \approx 160$ L) were formed in cylindrical 200 L plastic barrels, with the top removed, of dimension, diameter 0.55 to 0.60 m and length 0.70 m. Tap water was used to supply all freshwater ice blocks. Saltwater from the Aquatron supply (piped in from the Northwest Arm) was used for the saltwater ice blocks. Muddy sediment collected from the Shubenacadie and Avon River estuaries was used for the sediment-laden ice blocks. The sediment collection sites were near 45° 19’ 19” N ; 63° 29’ 57” W, and 45° 6’ 45” N ; 64° 11’ 46” W, respectively.

Ice formation was initially conducted by freezing the full fluid volume (approximately 16 L) in the pails. This procedure produced stress fractures throughout the ice, which resulted in preferential melting along fracture lines, calving, and the production of variable shapes through the melting process. A sample of ice photographs is provided in Appendix A. Although such shapes occur in nature, the surface area to volume ratio and length scales were difficult to quantify and considered undesirable for meeting the objectives of this study. The ice formation procedure was adapted to forming the ice by a series of layers, each a fraction of the total desired initial volume. Prior to adding each layer, water was allowed to cool to approximately 4 °C in a walk-in refrigerator. For the case of the small ice blocks, layers of approximately 2 to 3 L were used. For the larger ice blocks layers of 8 to 15 L were used. This procedure was most successful when each layer had frozen solid prior to adding the successive layer, however in some cases fracturing and diameter deformation occurred. It should be noted that although care was taken to transfer water with minimal disturbance, this procedure did not preclude the formation of air bubbles in the ice.

4.1.1 Sediment Addition

Fine-grained sediment from the Shubenacadie River basin was added to the small ice blocks melted on July 28, 2009 and from the Avon River basin to the large ice blocks melted on February 21 and 22, and March 30, 2011. The objective was to produce homogeneous ice blocks of near neutral buoyancy (favouring slightly negative $\rho_{si} = 1.04$ kg/L) in seawater. Homogeneous composition is difficult to obtain, however this goal was approached though addition of thin well-mixed layers of approximately constant sediment concentration. The layers were thin such that the ratio of surface area (A) over which heat flux occurred (when freezing) to fluid depth (d_f) was large. This relationship ensured that the fluid layer solidified prior to complete settling of the sediment. For the case of the large ice blocks melted in 2011, layers of approximately 8.5 L were used. Calculating the surface area to depth ratio we use an average barrel diameter of 0.575 m to obtain $A/d_f = 0.26/0.033 = 7.9$ m^2/m.

To produce sediment-laden ice of near neutral buoyancy ($\rho_\infty \approx \rho_{si}$) the following equations were used in addition to simple density (ρ), mass (m), and volume (V) relationships

$$V_s = V_{si}\left(\frac{\rho_{si} - \rho_i}{\rho_s - \rho_i}\right) \tag{4.1}$$

$$\rho_{sf} = \frac{m_T}{\rho_i/\rho_{fw}V_i + V_s} \tag{4.2}$$

$$C_s = \frac{\rho_s}{\rho_{si}}\left(\frac{\rho_{si} - \rho_i}{\rho_s - \rho_i}\right) \tag{4.3}$$

where freshwater ice density $\rho_i \approx 0.9$ kg/L, sediment density $\rho_s \approx 2.6$ kg/L, freshwater density $\rho_{fw} \approx 1$ kg/L, and Equation (4.3) gives sediment concentration (C_s) with units of mass sediment / total mass.

For example, to produce $V_{si} = 1$ L of sediment-laden ice of density $\rho_{si} = 1.04$ kg/L the total mass is $m_T = 1.04$ kg, of which (using Equation (4.1)) $V_s = 0.0824$ L and $m_s = 0.2141$ kg must be sediment, with the remaining $V_i = 0.9176$ L and $m_i = 0.8259$ kg as ice. Using Equation (4.2) the required density of the initial sediment freshwater mixture is $\rho_{sf} = 1.145$ kg/L, which expands when frozen to produce neutrally buoyant ice. Using Equation (4.3) the required sediment concentration for $\rho_{si} = 1.04$ kg/L is $C_s = 205.9$ ppt, which holds for solid and liquid state. If concentration were reported in units of mass / volume it would be necessary to account for the liquid to solid expansion of water as in Equation (4.2).

4.1.2 Ice Density

Ice block density was measured by volume displacement for all ice blocks prior to melting on July 28, 2009. An Archimedes displacement tank was constructed for this purpose. The results are presented in Table 4.1, where m_i is the mass of the ice block, m_f is the mass of the displaced fluid, ρ_f is the density of the displaced fluid (fresh and saltwater were used), V_f is the volume of the displaced fluid, which is equal to the ice block volume (V_i), and ρ_b is the ice block density. Ice blocks are identified by ice type, experiment number, block number. For example, $FW_{sed}3_2$ represents the second sediment-laden freshwater ice block melted during experiment number 3, which was conducted on July 28, 2009.

A target density of $\rho_{si} = 1.04$ kg/L was used for the large sediment-laden ice blocks melted on February 21 and 22, 2010. As outlined in the example calculation presented in

Ice block	m_i (kg)	m_f (kg)	ρ_f (kg/L)	$V_f = V_i$ (L)	ρ_b (kg/L)
$FW_{sed}3_1$	19.432	18.713	1.002	18.676	1.040
$FW_{sed}3_2$	19.587	19.236	1.024	18.785	1.043
$FW_{sed}3_3$	19.575	19.189	1.024	18.739	1.045
$\overline{FW_{sed}3}$	-	-	-	-	1.043
$FW3_1$	17.632	19.563	1.002	19.524	0.903
$FW3_2$	-	-	-	-	-
$FW3_3$	17.639	20.233	1.026	19.720	0.894
$\overline{FW3}$	-	-	-	-	0.899
$SW_{sed}3_1$	19.933	18.835	1.003	18.779	1.061
$SW_{sed}3_2$	19.983	19.388	1.026	18.897	1.057
$SW_{sed}3_3$	19.928	19.164	1.024	18.714	1.065
$\overline{SW_{sed}3}$	-	-	-	-	1.061
$SW3_1$	17.970	19.228	1.002	19.190	0.936
$SW3_2$	18.075	19.627	1.024	19.167	0.943
$SW3_3$	-	-	-	-	-
$\overline{SW}$	-	-	-	-	0.940

Table 4.1: Small block ice density (ρ_b) measurements by volume displacement

Section 4.1.1, the corresponding target mixture density was $\rho_{sf} = 1.145$ kg/L. Sediment was thoroughly mixed with water in batches of $V = 17$ L corresponding to a target mass of $m_T = 19.465$ kg. Similar to equations 4.1 and 4.2, actual sediment-laden ice density was then calculated from the total volume (V_{sf}) and total mass added to each block using

$$V_s = V_{sf} \frac{\rho_{sf} - \rho_f}{\rho_s - \rho_f} \tag{4.4}$$

$$\overline{\rho_{si}} = \frac{m_T}{\rho_f / \rho_i V_f + V_s} \tag{4.5}$$

Listed in Table 4.2 are the actual total fluid volume, total mass, fluid density, and calculated ice volume, density, and sediment concentration for each large sediment-laden ice block.

4.1.3 Ice Salinity

As discussed in Section 2.1, the formation of an ice cover on sea water is a refining process, by which most of the salt is rejected; however, the growth rate is usually too rapid for complete rejection (*Pounder*, 1965). Part of the salt is retained as liquid brine inclusions within the solid ice, while a larger fraction is rejected (*Thomas and Dieckmann*, 2003).

Ice block	V_{sf} (L)	m_T (kg)	ρ_{sf} (kg/L)	V_{si} (L)	ρ_{si} (kg/L)	C_{sed} (kg/kg)
$FW_{sed}7_1$	153	175.25	1.145	168.5	1.040	0.206
$FW_{sed}7_2$	153	175.24	1.145	168.5	1.040	0.206
$FW_{sed}8_1$	153	175.22	1.145	168.5	1.040	0.206

Table 4.2: Large block ice density by calculation

The salinity of the small salt water ice blocks was estimated by observation of the ice growth rate v_g for a 6 cm layer of sea water with salinity $S = 31.16$ psu, which was contained in a 20 L plastic pail. Consistent with formation of the ice blocks used in the melt experiments the sea water was stored in a 4 °C refrigerator overnight prior to placing in the walk-in freezer of temperature -14 ± 1 °C. A 1.8 cm ice cover formed after 340 min, corresponding to $v_g = 8.8 \times 10^{-5}$ cm/s. Using Equation (2.8), $S_i = 0.26 S_{cw}/(0.26 + 0.74 \exp(-7243 v_g))$, valid for $v_g > 3.6 \times 10^{-5}$ cm/s the estimated ice salinity is $S_i = 12.5$ ppt.

4.2 Setup

Small ice blocks ($V_0 \approx 18$ L) were melted in the pool tank of the Aquatron Laboratory on April 14 and 22, 2009. The pool tank is 15.24 m in diameter with a depth ranging from 3.54 m along the side walls to 3.91 m in the centre with an approximate volume of 684,000 L. All subsequent melts were conducted in the tower tank of the Aquatron Laboratory. The tower tank is 10.64 m deep and 3.66 m in diameter with an approximate volume of 117,000 L. Both tanks are constructed of reinforced concrete and are sealed with a fiberglass and epoxy liner. Up to four small ice blocks were melted simultaneously. The larger ice blocks ($V_0 \approx 160$ L) were melted individually.

In the pool tank ice blocks were suspended in netting from a bridge that spans the diameter of the tank. The blocks were positively buoyant, and forcefully submerged to approximately 1 m below the water surface by attaching a 4.55 kg lead weight to the bottom of line anchored to the bridge, which ran through the netting.

In the tower tank, ice blocks were suspended in netting from planks arranged to span the diameter of the tank for experiments conducted on July 28, 2009 and February 2 and 3, 2010. All positively buoyant ice blocks were forcefully submerged similar to the description provided in the previous paragraph; however, for the case of the large ice blocks additional ballast was required. The setup involving an above surface anchor point was modified for the melt experiments conducted in January and February 2011 to allow for simultaneous acoustic measurements. A sonar was positioned at the centre of the tower tank, directed downward through the water column at the melting ice. A single line extending down from surface would have interfered with the acoustic signal. The positively buoyant blocks were anchored from the bottom of the tank with a line extending up to the ice netting. The sediment-laden ice blocks melted on February 21 and 22, 2011 were suspended from above (to account for slightly negative buoyancy) by attaching three fishing lines to the netting. The lines extended outward to above-surface anchor points. The ice blocks were submerged to a depth of approximately 5 m to account for the 3 m blanking distance of the sonar. The sediment-laden ice block melted on March 30, 2011 was anchored from above by a single line connected to a dynamometer.

4.3 Conditions (S,T,P)

The pool and tower tanks were supplied with continuous flow of seawater from the Northwest Arm. Flow through the tanks was maintained such that influence of forced convection would be minimal and slight variations in far-field tank temperature during a melt would result from a change in the intake temperature from the Northwest Arm, rather than continuous positive heat flux from the observation room and cooling from the ice.

A minimum of two internally recording RBR pressure-temperature (PT) sensors were deployed during each melt experiment. Salinity was measured for all melts with exception to April 14 and 22, 2009 and February 2, 2010 with an internally recording RBR conductivity, temperature, and depth (CTD) sensor. A refractometer was used for these melts, but the recorded value of 33 psu was inconsistent with CTD measurements. An approximate salinity of 31 psu has been applied in place of the refractometer measurements. In addition to collecting data during the melt experiments, sensors were also deployed on February 2 and April 15, 2010, and January 25, 2011 for tests of the optic and sonar systems.

Sensors were placed at the ice depth, and approximately equidistant on the horizontal plane for the purpose of monitoring far-field conditions. Measurements of the ice wall temperature and salinity were attempted immediately prior to volume measurements during the January 28 melt experiment. These measurements were conducted by removing

Experiment date	T_∞ (°C)	S_∞ (psu)	ρ_∞ (kg/m^3)	T_{fp} (°C)	T_d (deg)
2009-April-14	3.34	31	1024.7	-1.69	5.03
2009-April-22	3.99	31	1024.6	-1.69	5.68
2009-July-28	13.30	31.47	1023.6	-1.72	15.02
2010-Feb-02	3.03	31	1024.7	-1.69	4.72
2010-March-03	2.41	30.53	1024.4	-1.67	4.08
2010-March-04	2.43	30.46	1024.3	-1.66	4.09
2010-April-15	2.98	31.51	1025.1	-	-
2011-Jan-25	4.37	30.56	1024.2	-	-
2011-Jan-26	4.24	30.72	1024.4	-1.68	5.92
2011-Jan-28	4.07	30.73	1024.4	-1.68	5.75
2011-Feb-21	2.87	30.77	1024.5	-1.68	4.55
2011-Feb-22	2.85	30.76	1024.5	-1.68	4.53
2011-Mar-30	2.72	31.16	1024.8	-1.70	4.42

Table 4.3: Summary of averaged far-field conditions

one PT sensor and the CTD from the tank to mark a break in the far-field data. The CTD was then lowered from the surface to the top of the ice block. The PT sensor was lowered and brought along-side of the ice. Decreased salinity and temperature values were observed, indicating that the salinity and temperature probes were within the boundary layer. However the instruments were not appropriate for collecting data close to the ice wall. The minimum distance from the ice wall to the CTD and PT sensor probes was approximately 5 cm. *Josberger and Martin* (1981) used a thermistor chain to observe an upward flowing turbulent boundary layer with thickness of about 10 mm to 30 mm adjacent to a melting vertical ice wall in saltwater. The CTD and PT sensors were removed from the tank to clearly mark the end of the boundary layer measurements prior to returning to far-field position. In addition to the far-field measurements and attempts at ice wall values, a PT sensor was positioned beneath the sediment-laden ice block melted on March 30, 2011. A summary of the far-field conditions is provided in Table 4.3. Thermal driving (T_d) was calculated for the melt experiments using Equation 2.48. Plots and statistics are provided in Appendix B.

Temperature and salinity profiles were collected in the tower tank on July 28, 2009; April 15, 2010; January 25, February 21, and March 30, 2011. In all cases the tower tank was found to be gravitationally stable. Near surface and near bottom density measurements and an average Brunt-Vaisala frequency are presented in Table 4.4.

Experiment date	$\rho(d \approx 0)$ (kg/m^3)	$\rho(d \approx h)$ (kg/m^3)	N (s^{-1})
2009-July-28	1023.6	1023.7	0.0119
2010-April-15	1025.2	1025.3	0.0071
2011-Jan-25	1023.7	1024.3	0.0250
2011-Feb-21	1024.5	1024.6	0.0081
2011-Mar-30	1024.8	1024.9	0.0094

Table 4.4: Tower tank gravitational stability

$$N^2 = -\frac{g}{\rho_0}\frac{\partial \rho}{\partial z} \tag{4.6}$$

for each depth cast. The profiles are included in Appendix B.

4.4 Measuring the Rate of Change

Melt rate is expressed as the rate of change of mass with respect to time (dm/dt). dm/dt may be obtained by measuring mass directly, measuring volume and multiplying by a representative density, or by measuring the tension on an anchor line running to an ice block suspended in the water column. For the case of the small blocks it was possible to remove each ice block from the tank by hand to obtain direct mass measurements using a balance scale. The weight of the large blocks (approximately 1600 N in air) necessitated an alternate in-situ approach. Volume was measured through use of a calibrated camera system for all large block melts with the exception of the sediment-laden block melted on March 30, 2011. The measurement of line tension for ice block mass was tested during the March 30, 2011 melt. Details for each method are presented in the subsequent subsections.

4.4.1 Directly Measured Mass

The mass of the small ice blocks was measured directly by removing the blocks from the seawater and placing them on a scale accurate to ± 0.05 g. Measuring mass directly is advantageous as it accounts for ice blocks with complex geometry and heterogeneous density. The uncertainties are difficult to quantify, but were addressed as follows.

Uncertainty rises from the effect on melt rate produced by removing the ice block from the water to measure its mass. One approach is to stop the running melt time upon removal of the ice block from the sea water, then restart following submergence. This approach may be the most accurate, however it does not account for melting which takes place (although at a reduced rate) while the block is exposed to warm air, and also introduces potential for error if start and stop times are not recorded accurately, as may be the case if one person is responsible for conducting measurements on several blocks melting simultaneously. Care was taken to minimize the ice block out-of-water time. The time taken to conduct each mass measurement was approximately 1 to 2 min. Melt time ranged from approximately 100 to 350 min for the small block experiments, and 2 to 4 mid-melt (excluding initial and final) mass measurement were conducted. The resulting cumulative error in the time axis is less than 5%, which may be considered a minor uncertainty.

Additional uncertainty arises from the amount of melt water present on the ice block, netting, lines, and ballast (lead weight) during each mass measurement. The majority of the melt water was allowed to run off prior to placement on the scale, and a wet tare weight was collected for the netting, line, and ballast following the completion of each melt. Assuming a uniform layer of melt water on the ice block surface and a constant length-to-diameter ratio, the contribution of ice block melt water to uncertainty throughout the experiment can be assessed. An ice block of initial diameter 0.28 m and length 0.28 m (similar to our pail) has a volume of 17.2 L and a surface area of 0.3695 m^2. For a ballpark estimation of melt water error, assuming a uniform melt water thickness of 1 mm this yields 0.3695 L of melt water and a melt water to ice volume ratio of 0.0215 or 2.15%. Now for a smaller block with diameter and length equal to 0.10 m, the volume and surface area are equal to 0.7854 L and 0.0471 m^2, respectively. Again, assuming a uniform melt water thickness of 1 mm this yields 0.0471 L of melt water and a melt water volume (V_{mw}) to ice volume (V_i) ratio of 0.0600 or 6.00%. It is evident that the influence of melt water on the ice block surface is minor, however it increases throughout the melt and may be calculated as

$$\frac{V_{mw}}{V_i} = 2d(\frac{1}{L} + \frac{1}{r}) \tag{4.7}$$

where d is the depth (or thickness) of the melt water on the ice surface, L is the length of the ice block, and r is the radius. Due to difficulty in quantifying the uncertainties related to time out of water and melt water volume, and the objective of producing a first-order accurate melt rate model a conservative relative uncertainty of $\pm 10\%$ is applied. Some of the errors will appear as block-to-block variations in the measured melt rate.

4.4.2 Optical Measurement of Volume

The weight of the large blocks (approximately 1600 N in air) necessitated an in-situ measurement of melt rate. For homogenous ice blocks of positive or negative buoyancy the rate of change of the buoyancy force could be used to calculate dm/dt. The buoyancy force could be measured from the tension on the anchor line. However, for sediment-laden ice blocks of near neutral buoyancy, the change in tension would be small compared to the volume of ice melted, leading to large uncertainty. Volume was measured through use of a calibrated camera system. A target of known diameter was positioned close to the ice and used to determine a scale (pixels/m) for each photograph, which was then applied to measurements of ice diameter and length. Further details on camera calibration, image rectification, verification and testing of the system, and application to ice measurements follow.

4.4.2.1 Camera Calibration

A DeepSea Power & Light Multi-SeaCam low-light black and white camera with a fisheye lens (SN 1146T) was used to photograph the melting ice. The camera was calibrated for image rectification using the Camera Calibration Toolbox for Matlab® (*Bouguet*, 2010). The purpose of camera calibration is to determine focal length, principal point, skew coefficient (the angle between x and y pixel axes), and coefficients for radial and tangential distortions, which then may be used to rectify the image.

The toolbox uses several images (approximately 15 to 25) of a planar checkerboard in water. Each image of the checkerboard is taken from a different orientation to the camera. It is important to collect images from variable distance, angles in the x, y, and z, planes, and covering nearly the full field of view. For each image the user specifies the four extreme corners of the rectangular checkerboard pattern then inputs the size of each square in the x and y directions. From this the toolbox generates a first guess at the grid corners. When predicted corners are close to the actual image corners, the user proceeds to the next image. In some cases where significant image distortion is present it is necessary to provide an initial guess at the first-order lens distortion coefficient. A series of iterations through guesses and subsequent calculation of image corners proceeds until the toolbox calculates image corners near actual, or the image is considered unfit for use and is rejected.

Following corner extraction from all images, a Matlab data file is automatically generated and calibration is performed in two steps; initialization followed by nonlinear optimization.

Parameter	x-axis (pixels)	y-axis (pixels)
Focal Length	756.22 ± 4.07	689.13 ± 3.79
Principal point	338.26 ± 3.19	236.95 ± 2.40
Radial distortion	-0.39 ± 0.008	0.14 ± 0.03
Tangential distortion	0.003 ± 0.0007	-0.002 ± 0.0006
Pixel error	0.09	0.10

Table 4.5: Camera calibration parameters

The initialization step calculates a closed-form solution for the calibration parameters, not including lens distortion. The non-linear optimization step minimizes the total reprojection error (least squares error) over all calibration parameters. Optimization is performed by iterative gradient descent. Further details and associated references can be found in *Bouguet* (2010). Calibration parameters for the camera (SN 1146T) are presented in Table 4.5. The skew and angle of pixel axis were found to be 0.00129 ± 0.00041 radians and 89.93 ± 0.02 degrees, respectively. The compete distortion model is presented in Figure 4.1.

Notably from Table 4.5 the parameters fc_1 and fc_2 are the focal length for the *x*-axis and *y*-axis, respectively, expressed in units of horizontal and vertical pixels, where pixel coordinates are defined such that $[0, 0]$ is the center of the upper left pixel of the image. The ratio of fc_2/fc_1 is the aspect ratio, which in this case is equal to 0.91 indicating that pixels in the CCD array are rectangular.

4.4.2.2 Verification and Testing

The performance of the camera system for measuring the volume of submerged ice blocks was tested on three occasions. First, on February 2, 2010 a small ice block was melted in the tower tank with the rigging designed for larger blocks. Photographs were taken of each end (showing diameter) and one side (showing length and diameter) of the cylinder. The use of a small block allowed removal from the tank following image collection for direct mass measurement (m_{scale}). Direct comparison was then possible between the two methods for measuring dm/dt. Volume was calculated three times from each set of photographs to assess sensitivity to user determination of ice edges. Mass was calculated from the average of three volume measurements (m_{ave}) by applying the average freshwater ice density ($\rho_i = 0.9$ kg/L) from Table 4.1. The results are summarized in Table 4.6.

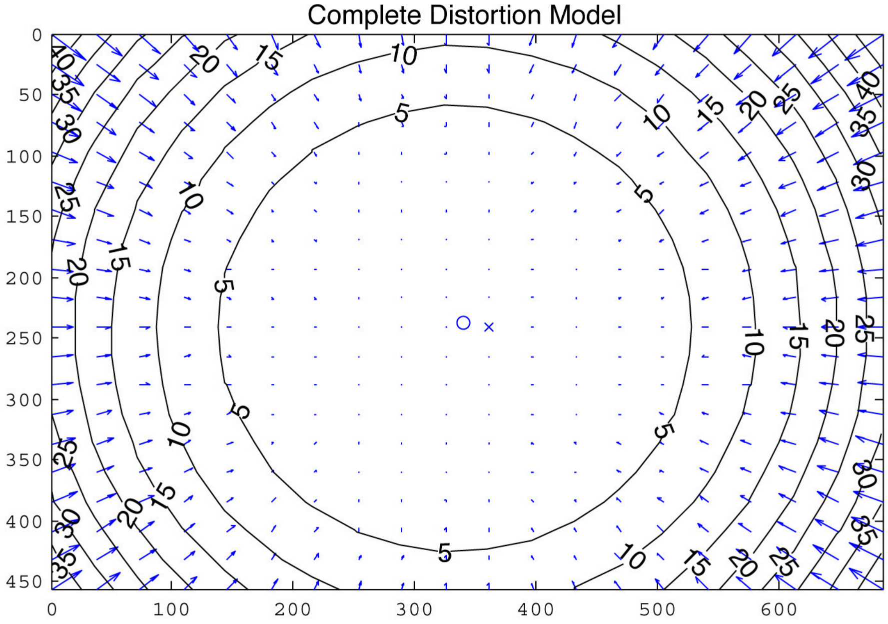

Figure 4.1: Complete distortion model. Contours and arrows representative of spatial correction in pixels due to fisheye lens.

Time (min)	V_1 (L)	V_2 (L)	V_3 (L)	m_{ave} (kg)	m_{scale} (kg)	m_{ave}/m_{scale}
0	18.30	17.57	17.60	16.04	15.59	1.03
78	14.25	13.90	14.36	12.75	11.71	1.09
132	10.18	10.06	10.09	9.10	9.43	0.96
178	9.08	8.20	8.74	7.81	7.65	1.02
245	5.94	5.97	5.93	5.35	5.44	0.98

Table 4.6: Small ice block camera test

This initial test demonstrated that the camera system is suitable for measuring the mass of a melting ice cylinder. However, following the first of the large melts (conducted on March 3, 2010) it became apparent that further refinement of the procedure was necessary. Calculated initial volumes for the ice blocks were significantly larger than the quantity of water (accounting for expansion upon freezing) added to the barrels. A test was conducted on April 15, 2010 in which a full barrel of known dimensions ($V \approx 225$ l) was forcefully submerged in the large block net rigging. Initial estimates of barrel volume were greater than 300 L. The first source of error identified was the sensitivity of length measurements to the position of the scale buoy with respect to the plane of measurement. As shown in Figures 4.2 and 4.3, the buoy was positioned at a static location approximately 1 m below the barrel.

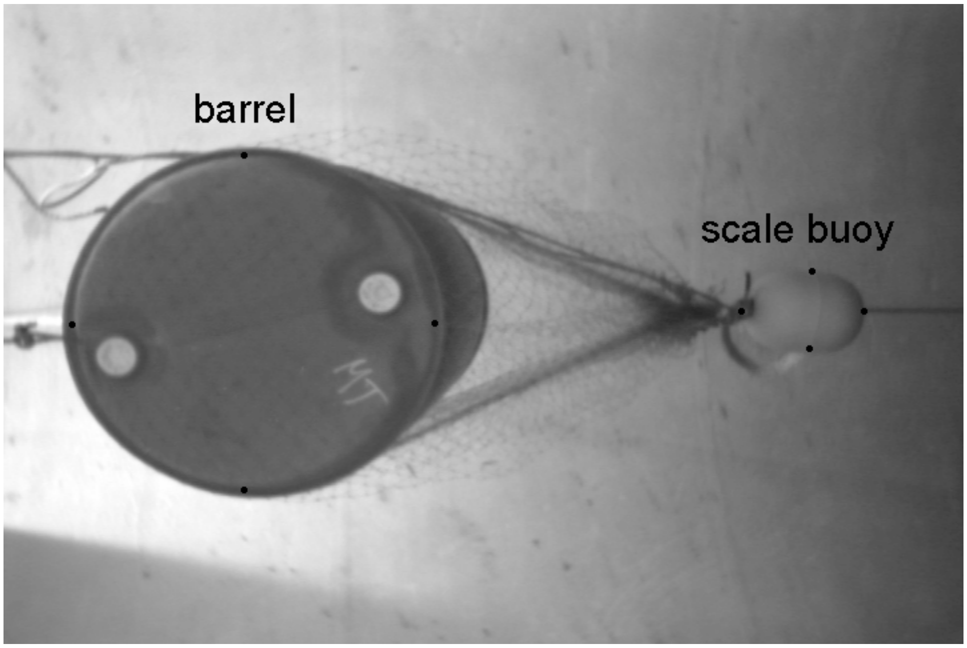

Figure 4.2: Barrel camera test photograph - end view

If positioned beneath the centre of the cylinder, the scale buoy was half the cylinder length (≈ 0.45 m) farther from the camera than the plane of the cylinder end. With the camera positioned at the edge of the tower tank with a radius of 1.83 m and the cylinder positioned at its centre, this led to significant magnification of cylinder diameter measurements. Similarly, when in side view the buoy was positioned one cylinder radius (≈ 0.29 m) from the nearest point on the cylinder. However, for this case all diameter

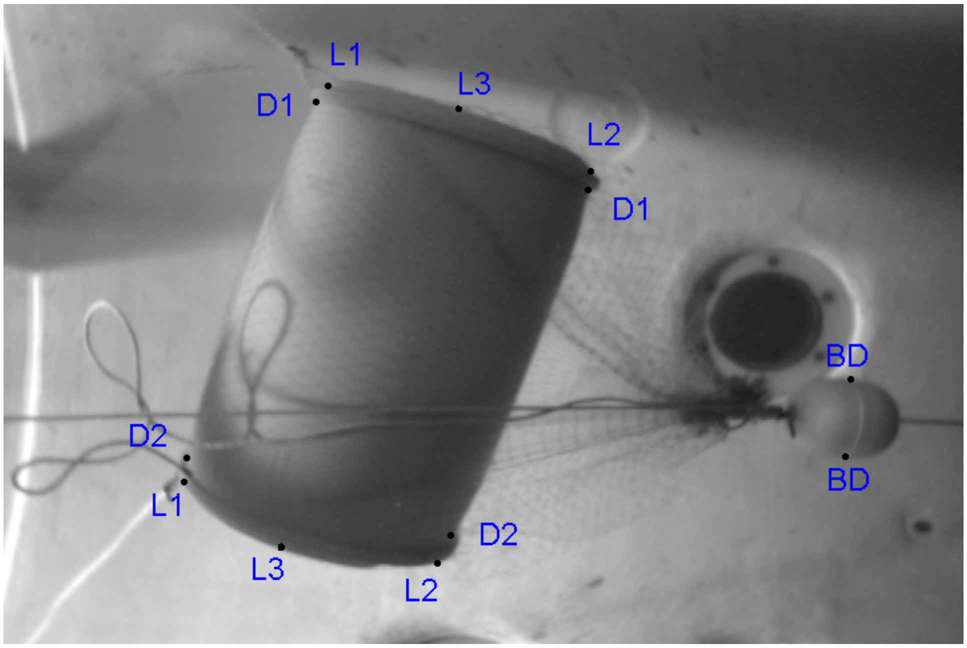

Figure 4.3: Barrel camera test photograph - side view

measurements and the length parings L1 and L2 shown in Figure 4.3 are unaffected as the measurement planes for the barrel and the scale buoy coincide. Length measurements taken moving towards L3 (the minimum camera to barrel distance) are magnified with increasing significance. Of course, when applied to a melting ice block this magnification of error decreases through the melting process. With a known buoy diameter of 0.175 m, a barrel volume of $V \approx 260$ l is calculated from diameter and length pairings D1, D2, L1, and L2; approximately 15% larger than the known barrel volume.

Further testing of the camera system was conducted on June 6, 2010 by collecting several photographs of a dot board with known constant dot spacing of 0.05 m. A sample photograph is provided in Figure 4.4.

The dot board was used to assess the x and y spacing in pixels measured from the photographs. For the dot board orientation shown in Figure 4.4, assuming the board width to be aligned with the x-axis and length with the y-axis $dy/dx = 0.913$ was calculated by obtaining averages of $dy = 21$ pix ($S_y = 420$ pix/m) and $dx = 23$ pix ($S_x = 460$ pix/m) from the full board length and width, respectively. The calculation of dy/dx was repeated with the dot board positioned near surface, at depth, and with 90 degree rotation of orientation with similar results, all remarkably close to $fc_2/fc_1 = 0.911$ from the camera

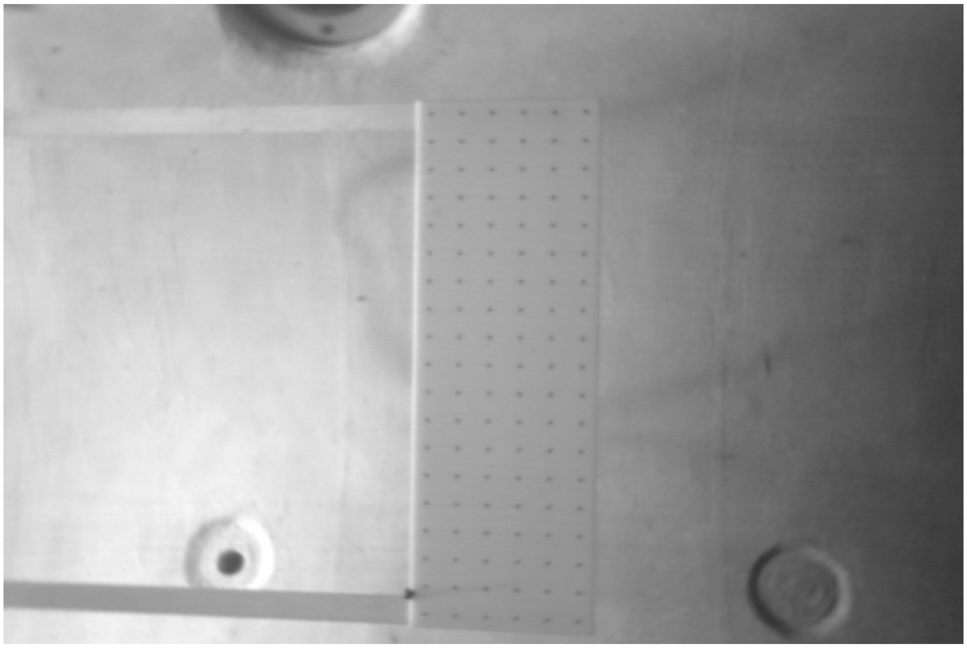

Figure 4.4: Sample dot board camera test photograph

calibration. It was then evident that either a correction factor (d_x) must be applied to account for rectangular pixels, or separate scales used for measurements in the *x* and *y* directions. Choosing the simpler and more robust method of applying a correction factor, distances between points $A(X_A, Y_A)$ and $B(X_B, Y_B)$ were then calculated in square pixels, as follows

$$\Delta x = |X_A - X_B| \times d_x \tag{4.8}$$

$$\Delta y = |Y_A - Y_B| \tag{4.9}$$

$$D = (\Delta x^2 + \Delta y^2)^{1/2} \tag{4.10}$$

where $d_x = 0.91$. Use of d_x is consistent with *Crawford and Hay* (1998), which provides additional information on extracting world coordinates from pixel coordinates.

For the case of a known distance, it follows to divide through to obtain a scale independent of angle on the *x*,*y* plane in units of pix/m. This scale may be applied to measure any object in the photograph with distance from the camera approximately equal to the distance to the scale object of known size.

For the dot board, measuring $3 \times dx$ and $3 \times dy$ then dividing each by the known spacing for this distance of 0.15 m, scales in the *x* and *y* direction of $S_x = 416.48$ pix/m and

Image	Trial	S_x (pix/m)	S_y (pix/m)	S_y/S_x	$Width$ (m)	$\Delta W/W$ (%)	$Length$ (m)	$\Delta L/L$ (%)
1	1	416.48	429.55	1.03	0.252	0.8	0.899	0.1
	2	427.38	432.12	1.01	0.250	0.0	0.887	1.4
	3	416.48	426.28	1.00	0.244	2.4	0.891	1.0
2	1	450.31	432.79	0.96	0.253	1.2	0.876	2.7
	2	450.45	432.79	0.96	0.256	2.4	0.878	2.4
	3	437.44	427.24	0.98	0.259	3.6	0.905	0.5
3	1	454.96	440.00	0.97	0.249	0.4	0.887	1.4
	2	453.87	432.21	0.95	0.249	0.4	0.889	1.2
	3	442.05	450.42	1.02	0.253	1.2	0.889	1.2
4	1	392.58	410.42	1.05	0.240	4.0	0.900	0.0
	2	386.15	404.73	1.05	0.244	2.4	0.914	1.6
	3	392.58	398.63	1.02	0.242	3.2	0.914	1.6
5	1	424.58	438.43	1.03	0.255	2.0	0.874	2.9
	2	437.48	438.48	1.00	0.252	0.8	0.859	4.6
	3	418.14	438.48	1.05	0.257	2.8	0.881	2.1
6	1	444.20	432.93	0.97	0.249	0.4	0.888	1.3
	2	431.35	438.62	1.02	0.249	0.4	0.894	0.7
	3	438.04	438.62	1.00	0.246	1.6	0.890	1.1
7	1	437.44	438.48	1.00	0.248	0.8	0.901	0.1
	2	443.88	432.79	0.98	0.247	1.2	0.898	0.2
	3	450.31	438.48	0.97	0.244	2.4	0.884	1.8
Ave				1.00		1.6		1.4

Table 4.7: Dot board camera test

$S_y = 429.55$ pix/m are obtained, and an associated scale ratio of $S_y/S_x = 1.03$. Two subsequent measurements produced scale ratios of 1.01 and 1.00 indicating no significant bias. Attributing the discrepancy to manual error in selecting the dot centres an average scale of 423.02 pix/m is used to measure overall dot board width 0.25 m and length 0.90 m, which match the known dimensions. Three trials were conducted for each of the images. The results are summarized in Table 4.7.

As shown in Table 4.7, the camera system accurately measured the length and width of the dot board with an average relative uncertainty of $\pm 1.5\%$ and average scale ratio of 1.00. Through propagation of uncertainty this relative uncertainty for length results in $\pm 4 - 5\%$ for volume. Applying $C_f = 0.91$ to the measurements of the barrel shown in Figure 4.3, where only length pairings D1, D2, L1, and L2 were used to avoid magnification error, volumes of 219.7, 210.5, and 218.8 l rate obtained in three trials. Comparing the average to the actual volume of approximately 225 l gives a relative error of 4%.

It is evident through this assessment that the most significant error associated with the camera system is distance distortion resulting from variable distance from the camera to the known object (scale buoy) with respect to the target object. Distance distortion is defined as the ratio of observed and physical length scales $D = L_{obs}/L_{phy}$, and is present in the form of magnification ($D > 1$), and de-magnification ($D < 1$).

This error is difficult to quantify, but it may be observed not only in the barrel test but with the dot board photographs, most notably where the length was positioned parallel to tank depth. The dot board was slightly buoyant, resulting in a tilt along the board length, sloping from the bottom nearest to the camera to the top farther away. Additionally, for Dot Board Image 5 the bottom of the board was positioned centered with the camera, such that the 0.9 m length of a flat object results in further de-magnification of the board width near surface. To minimize this effect for the assessment presented in Table 4.7, scale values and corresponding measurements were taken near the centre of the dot board. To illustrate the effect, width measurements taken from Dot Board Image 5 vary by $7 - 10\%$ from actual when the scale is taken from near bottom and measurement near surface leading to de-magnification.

Distance distortion was reduced for the melts conducted on January 26 and 28 and February 21 and 22, 2011 by adapting the prior procedure such that the scale buoy was rigged separately from the ice block and positioned close to the target for collection of each image. Prior to the melts the new rigging was tested by forcefully submerging a glass sphere on January 25, 2011. However, a reflection of the buoy is present in each image of the sphere, indicating that the buoy must have been positioned slightly closer to the camera than the sphere. From this set of images, four were used to measure the volume of the sphere. From each image, sphere diameter was measured twice relative to the scale buoy of diameter ($D_{buoy} = 0.64/\pi$ m) and an average applied. The known diameter and corresponding volume of the glass sphere are $D_{sphere} = 0.432$ m and $V_{sphere} = 42.2$ l, respectively. The results of the sphere measurements are summarized in Table 4.8. A sample photograph of the sphere, with *x* and *y* axes in pixels and measurement lines included is provided as Figure 4.5.

From the measurements presented in Table 4.8 it appears that scale buoy drifted closer to the camera throughout image collection, resulting in progressive de-magnification of

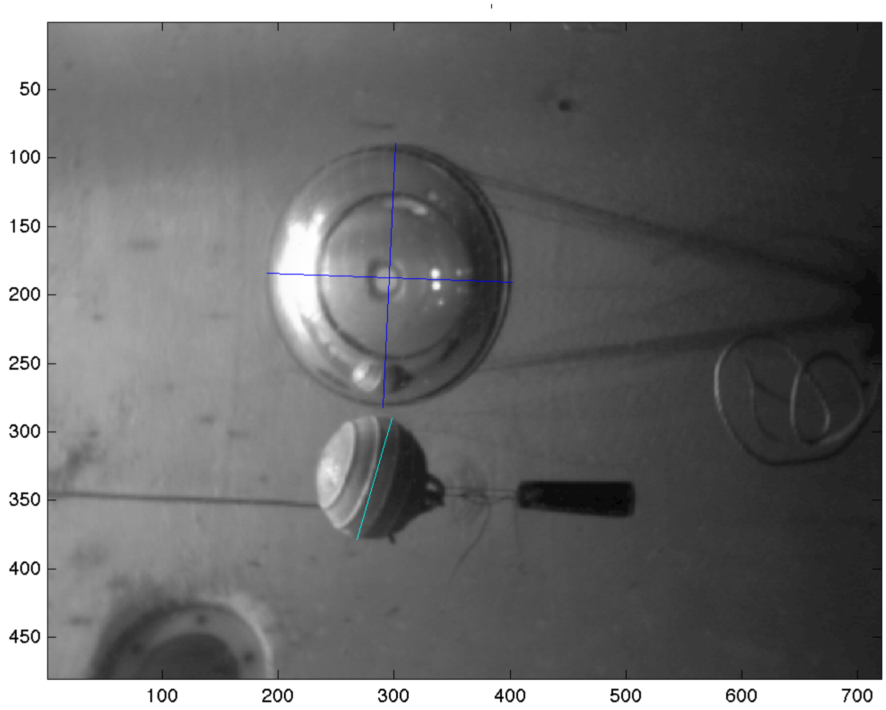

Figure 4.5: Sample glass sphere image

Image	D_1 (m)	D_2 (m)	$\overline{D}$ (m)	$\Delta D/D$ (%)	V (m^3)	$\Delta V/V$ (%)
1	0.425	0.423	0.424	1.9	39.8	5.7
2	0.409	0.437	0.423	2.1	39.7	5.9
3	0.404	0.434	0.419	3.0	38.6	8.5
4	0.398	0.429	0.413	4.4	36.9	12.6

Table 4.8: Glass sphere camera test

apparent size of the target sphere. Propagation of uncertainty from length to volume as $3 \times \Delta D/D \approx \Delta V/V$, where D is diameter and V is volume is also illustrated in Table 4.8.

Based on the results from the dot board, barrel, and glass sphere tests, the relative error for the camera system when applied to measuring objects of simple geometry is estimated to be 5% for length, corresponding to 15% for volume.

4.4.2.3 Application to Ice Measurements

Further uncertainty is introduced when applying the camera system to melting ice due to irregular melting, producing slightly more complex geometries than that observed for the dot board, barrel, and glass sphere tests. Processes during ice block formation and melting affect the underlying assumption that the ice melts as a cylinder.

Although care was taken in the formation of ice blocks through the layer procedure outlined in Section 4.1, air bubbles, fractures, and sediment concentration gradients were present. Air bubble concentrations were not homogenous through the ice, leading to faster melting where bubble concentrations were highest. The open top end of the ice cylinder was most affected by fractures, leading to irregularity in cylinder length as the melt progressed. Small layers of approximately 8.5 L were used in the formation of the sediment-laden ice blocks to minimize particle settling. However, for each layer settling created a sediment concentration gradient increasing downward towards the frozen surface of the previous layer. The effect of sediment concentration on melt rate (discussed later) resulted in the formation of bands in the surface of the cylinder as it melted. Additionally, expansion pressure on the barrel wall during ice formation resulted in diameter deformation in some blocks, most notably the freshwater ice block melted on January 26, 2010. The initial diameter of the January 26, 2010 ice block ranged from 0.53 to 0.66 m. Calculating volume using the upper and lower diameter limits and an initial length of 0.80 m corresponding volume estimates are 0.1765 m^3 and 0.2737 m^3, respectively.

The ice blocks maintained a cylindrical shape to a first-order approximation throughout most melts. However, in addition to the formation processes outlined above, variation in melt rates were observed that must be attributed to corresponding variations in flow around the block. Consistent with the observations of *Josberger and Martin* (1981), turbulent flow produced cusps on the ice surface. Increased flow along the cylinder sides and a decrease at the separation point also resulted in diameter deformation during the later stages of the melt.

Sample photographs are included in Appendix A to illustrate each of the effects outlined above. Irregular shapes were best accounted for when photographs of the ice ends were available such that the benefit of their use for capturing variations in diameter outweighed potential distance distortion error. This was not the case for the large block melts conducted in 2010 with the static buoy setup. However, photographs taken in the later stages of the ice melts conducted in 2011 were useful for calculating volume as the area of an ellipse times the length of the block.

Additionally, the presence of fine grained sediment released from the ice blocks melted on February 21 and 22, 2011 reduced visibility in the tower tank creating difficulties for positioning the scale buoy relative to the ice. Scaleable end view images were not captured for all time steps, and in some cases the side view was subject to significant distance distortion. For these images the stripes produced by sediment gradients resulting from the addition of consistent layers were used for scale. Measurements taken from both blocks were used to calculate an average layer thickness of 3.5 cm. For comparison, using the diameter range for the barrels of 0.55 m bottom to 0.60 m at the top, and the layer volume of 8.5 l a thickness range of 3.0-3.6 cm is calculated. The applicability of using the stripes for scale was confirmed in instances where accurate side view measurements from the scale buoy were available. For example, the sediment-laden ice photograph taken at 16:25 on February 21, 2011 resulted in values of $V = 0.0899$ m^3 and $V = 0.0859$ m^3 using the stripes and buoy for scale, respectively.

As a result of irregular melting an additional 5% relative uncertainty is added to the camera system volume measurements. The total 20% relative uncertainty is considered acceptable for the development of a first order accurate melt rate model. However, it is worth noting that an improved setup for future work may be the projection of two laser light sheets of known separation onto the target for measurement.

4.4.3 Line tension

Due to the uncertainty and subjectiveness of the camera system a test was conducted using a dynamometer to measure the weight of the large sediment-laden ice block melted on March 30, 2011. The ice block was created with sediment concentration sufficient to result in slightly negative buoyancy. The ice block was then anchored to a dynamometer installed above the centre of the Tower Tank. Weight in air was measured at the beginning and near the end of the melt. Weight in water was measured throughout the melt and used to calculate mass (m) [kg] following

$$m = \rho_{si} \frac{F_T}{g \Delta \rho} \tag{4.11}$$

where F_T is the tension force measured by the dynamometer [N], g is gravitational acceleration [m s^{-2}], and $\Delta\rho = \rho_{si} - \rho_\infty$ [kg m^{-3}]. The accuracy of Equation (4.11) is most sensitive to the $\rho_{si}/\Delta\rho$ term. As previously noted, for sediment-laden ice blocks of near neutral buoyancy, the change in tension is small compared to the volume of ice melted. As $\Delta\rho$ decreases, uncertainty related to this method increases due to sensitivity in the accuracy of ρ_{si} and ρ_∞.

The desired ice block density (1 040 kg m^{-3}) as calculated using Equation (4.5) (and presented in Table 4.2) was evaluated using a comparison of the weight in air to weight in water measurements collected at the beginning and end of the melt. From these measurements ice block density is

$$\rho_{si} = \frac{\rho_\infty}{1 - F_T/(mg)} \tag{4.12}$$

where F_T is the dynamometer tension force for the ice block in water and m is the ice block mass calculated from the tension force in air. The density of the sediment-laden ice block increased from 1049.1 kg m^{-3} to 1063.6 kg m^{-3} over a 503 min melt duration. For data analysis linear interpolation was used to calculate

$$\rho_{si}(t) = 1049.1 + 0.029t \tag{4.13}$$

where t is melt time in min. Density increasing through the melt indicates either a density increase towards the ice core, or potential growth of a sediment layer on the ice surface due to cohesion. For future melts, calculation of ρ_{si} using Equation (4.12) at points through the melt duration is recommended. However, care should be taken to ensure minimal disturbance of the ice block, presenting a trade off between minimizing disturbance and measurement of ρ_{si}.

CHAPTER 5

RESULTS

5.1 Observations

Melt rate observations are initially presented as plots with mass on the y-axis and time on the x-axis. Separate plots are presented for the small ($V_0 \approx 18$ L) and large ($V_0 \approx 180$ L) blocks. The mass of the large blocks was calculated from the camera system volume measurements as $m = \overline{\rho_{si}} V$, where $\overline{\rho_{si}}$ is determined as outlined in Section 4.1.2.

Melt rate dependency on thermal driving is presented in Figure 5.1 for small freshwater ice blocks. A full summary of far-field conditions is presented in Table 4.3. Prior to adopting the layer methodology for ice formation, an increased melt rate was observed for the $T_d = 5.03$ °C experiment associated with complex ice geometry resulting in an increasing surface area to volume ratio through the melt. Melt rate dependency on sediment content is presented in Figures 5.2 and 5.3 for small freshwater and saltwater ice blocks, respectively. Melt rate dependency on ice salinity is presented in Figures 5.4 and 5.5 small sediment-free and sediment-laden ice blocks, respectively. Consistent with the estimate provided in Section 4.4.1, a relative uncertainty of $\pm 10\%$ is shown for all small block mass measurements. **For the case of the small ice blocks, Figures 5.1 through 5.5 show melt rate increasing with thermal driving (T_d) and salinity (S) and decreasing with increasing sediment content (C_i).**

Experiments were conducted with large ice blocks to evaluate the effect of an order of magnitude increase in the length scale. Melt rate dependency on thermal driving and sediment concentration is presented in Figure 5.6 for large freshwater ice blocks. Consistent with the estimate provided in Section 4.4.2, a relative uncertainty of $\pm 20\%$ is shown for all large block mass measurements. Large saltwater ice blocks have not been melted for this thesis. Due to the significant effort required in formation of large

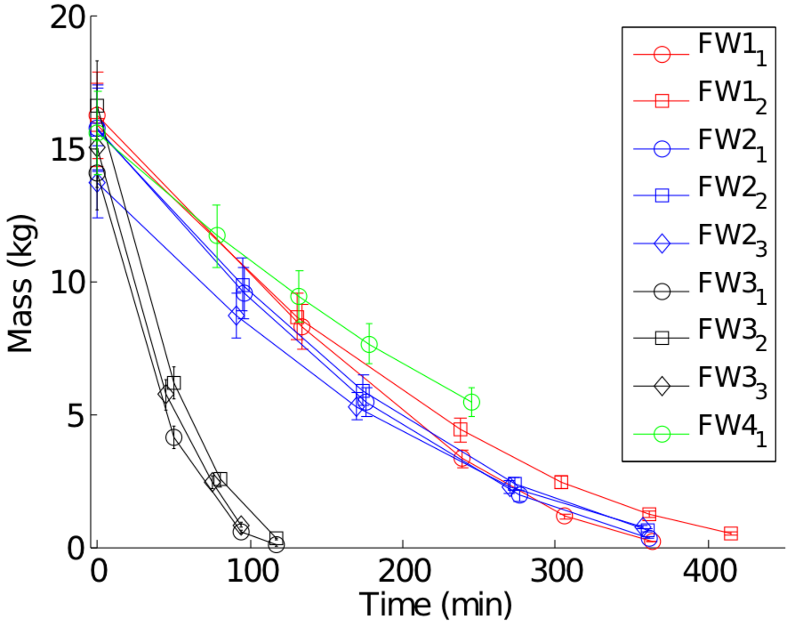

Figure 5.1: Small block sediment-free freshwater (FW) ice, showing melt rate dependence on thermal driving (T_d) for length scales up to 0.3 m ($L \leq 0.3$ m), $T_d(FW1) = 5.03$ °C, $T_d(FW2) = 5.68$ °C, $T_d(FW3) = 15.02$ °C, $T_d(FW4) = 4.72$ °C

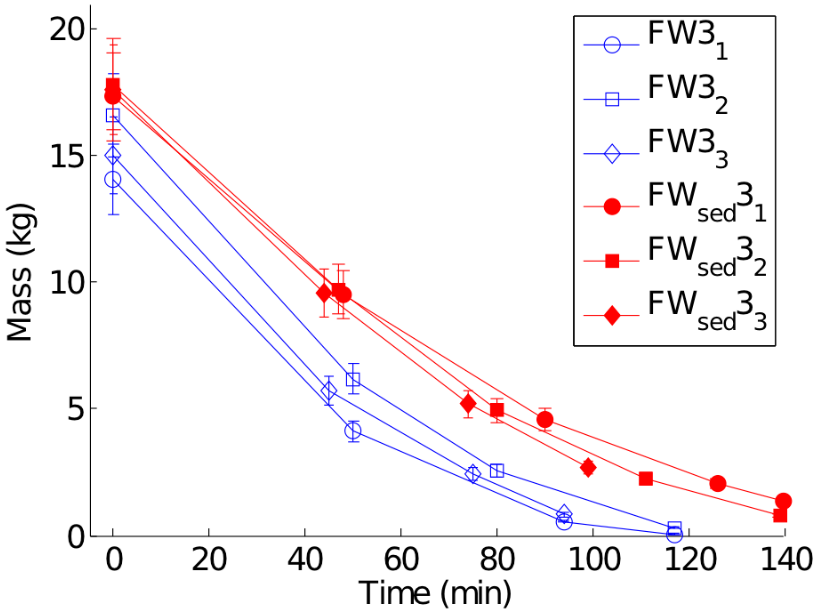

Figure 5.2: Small block sediment-free freshwater (FW) and sediment-laden freshwater ($\mathrm{FW_{sed}}$) ice, showing melt rate dependence on sediment content for length scales up to 0.3 m ($L \leq 0.3$ m), ($T_d = 15.02$ °C)

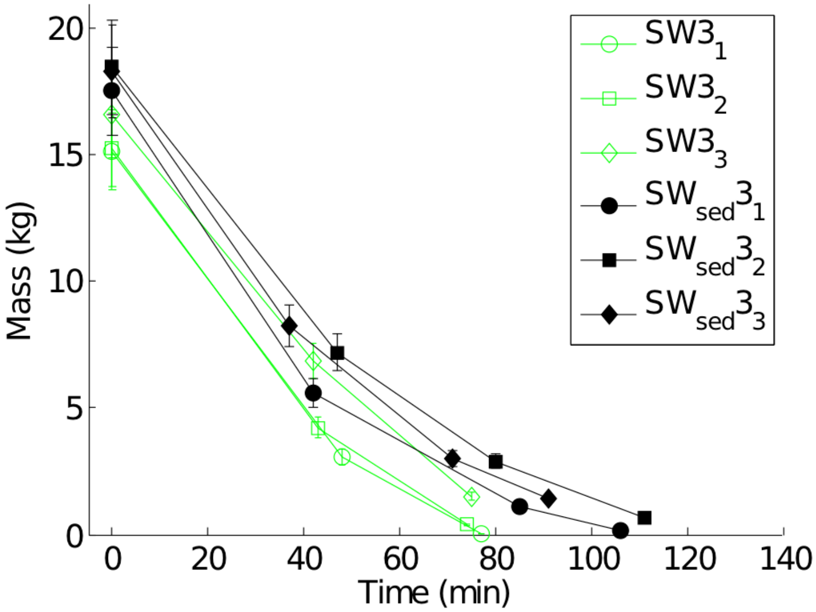

Figure 5.3: Small block sediment-free saltwater (SW) and sediment-laden saltwater ($\mathrm{SW_{sed}}$) ice, showing melt rate dependence on sediment content for length scales up to 0.3 m ($L \leq 0.3$ m), ($T_d = 15.02$ °C)

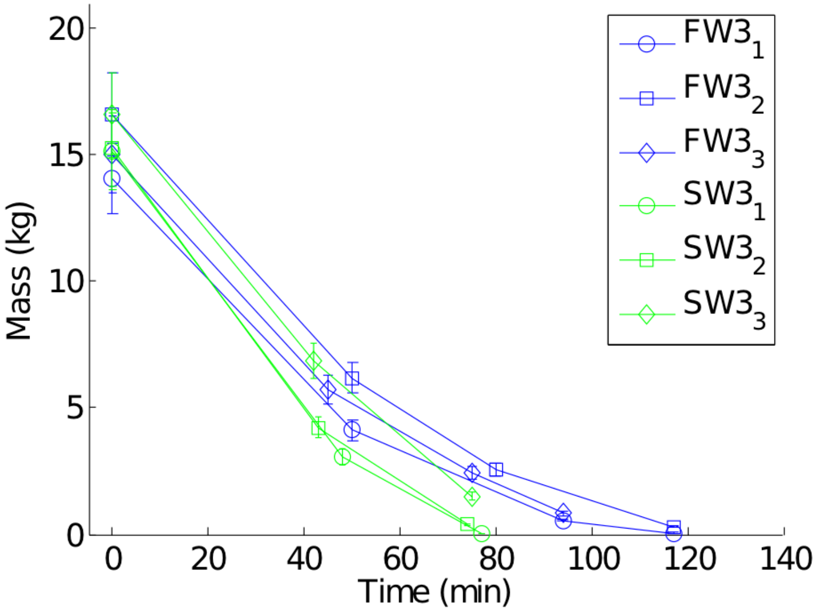

Figure 5.4: Small block sediment-free freshwater (FW) and sediment-fee saltwater (SW) ice, showing melt rate dependence on salinity for length scales up to 0.3 m ($L \leq 0.3$ m), ($T_d = 15.02$ °C)

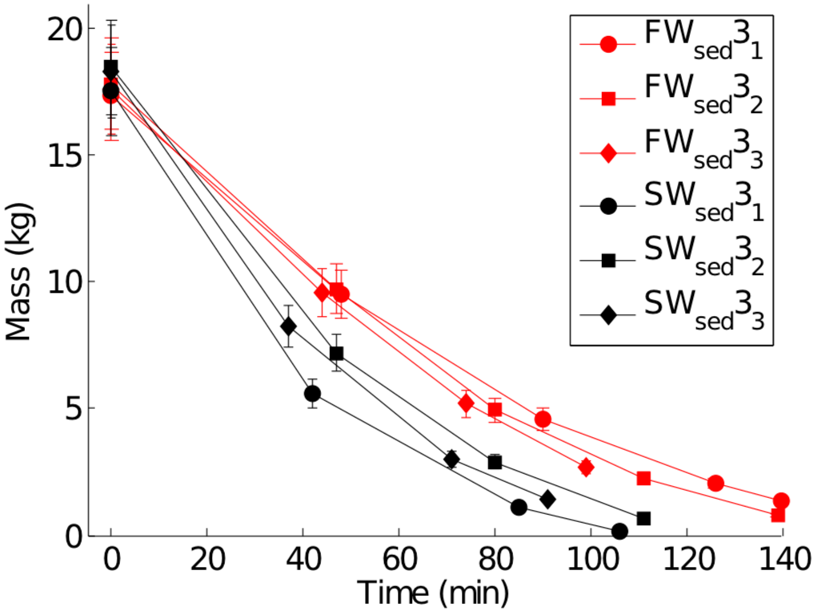

Figure 5.5: Small block sediment-laden freshwater (FW_{sed}) and sediment-laden saltwater (SW_{sed}) ice, showing melt rate dependence on salinity for length scales up to 0.3 m ($L \leq 0.3$ m), ($T_d = 15.02$ °C)

ice blocks, the work has focused on the effect of sediment concentration on melt rate. **As shown in Figure 5.6, melt rate is seen to increase with T_d as observed for the small ice blocks. However, the variations in tank temperature between experiments obscure the effect of sediment concentration from this dimensional plot. The dimensionless Nusselt and Rayleigh numbers allow further comparison in subsequent sections.**

5.2 Interpretation

5.2.1 Statistics

Statistical analysis for the fit of Equations (3.13) and (3.15) to the observed melt data for each block are presented in Tables 5.1 and 5.2. All values with the exception of γ^2 were calculated using the Matlab Statistics Toolbox *regstats* linear regression diagnostics. *Regstats* performed a multilinear regression of the measurements in *y* [m^ζ (kg^ζ)] on the predictors in *x* [time (min)]. The regression coefficients representing the initial mass (m_0^ζ) and α provide the characteristics of the line. The mean squared error (MSE) and γ^2 quantify the goodness of fit between the calculated ($\hat{m^\zeta}$) and measured (m^ζ) values. Using

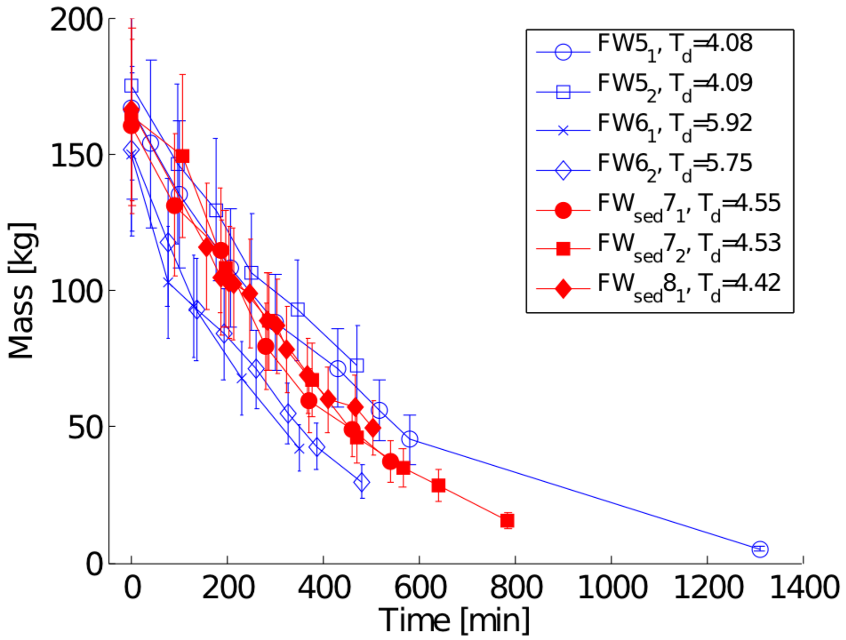

Figure 5.6: Large block sediment-free freshwater (FW) and sediment-laden freshwater (FW$_{\text{sed}}$) ice, showing melt rate dependence on thermal driving (T_d [°C]) and sediment content for length scales greater than 0.3 m ($L > 0.3$ m)

general algebraic terms where y is the measured value and $\hat{y}$ predicted, n is the number of observations, and p is the number of unknown coefficients, MSE and γ^2 are

$$MSE = \frac{1}{n-p-1}\sum_{i=1}^{n}(\hat{y}_i - y_i)^2 \tag{5.1}$$

$$\gamma^2 = \frac{\sigma^2(y-\hat{y})}{\sigma^2(y)} \tag{5.2}$$

Variance (σ^2) is calculated as

$$\sigma^2 = \frac{1}{n-1}\sum_{i=1}^{n}(y_i - \overline{y})^2 \tag{5.3}$$

where $n-1$ is used to provide an unbiased estimate of the variance. Note that a) low values are desired for MSE and γ^2, and b) γ^2 is $1 - R^2$ where R^2 is the coefficient of determination.

Table 5.1 has been partitioned into low ($T_d < 6$ °C) and high ($T_d > 15$ °C) thermal driving, with subsections for ice type. The divisions were made for the purpose of assessing the potential transitions between laminar and turbulent conditions. Table 5.2 has been divided between sediment laden and freshwater ice blocks. For convenience, the lower of the MSE and γ^2 values for each of the ice blocks are in **bold**.

The MSE and γ^2 tests show excellent correlation between predicted and observed results. With only a few minor exceptions, the small block melts best fit laminar conditions ($\zeta = 5/12$) and the large block melts best fit turbulent ($\zeta = 4/15$), although transition from turbulent to laminar likely occurred at some point during the large block melt. The small block melt data are plotted for $m^{5/12}$ in Figures 5.7 through 5.11 with fits to Equation (3.13) included. The large block ice melt data are plotted in Figure 5.12 for $m^{4/15}$ with fits to Equation (3.15) included.

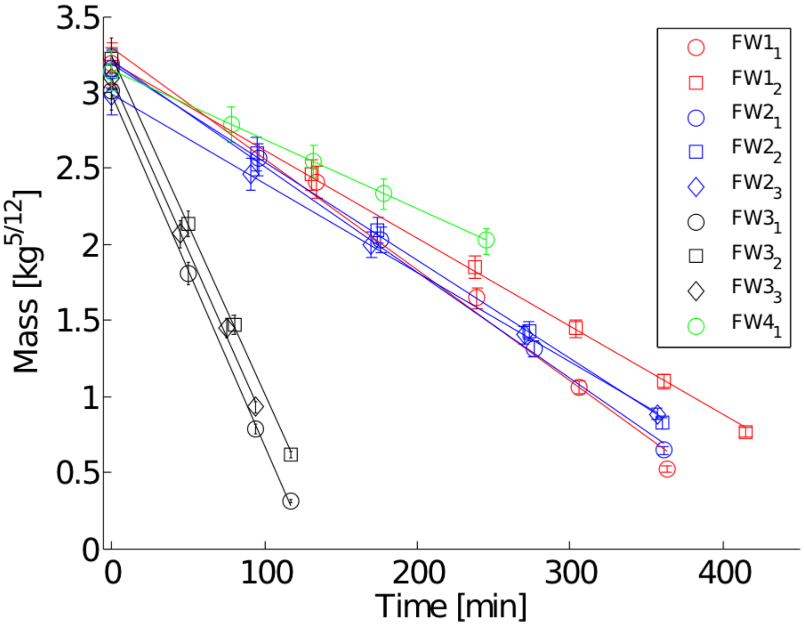

Figure 5.7: Small block sediment-free freshwater (FW) ice, showing melt rate dependence on thermal driving (T_d) for length scales up to 0.3 m ($L \leq 0.3$ m), $\zeta = 5/12$. $T_d(FW1) = 5.03$ °C, $T_d(FW2) = 5.68$ °C, $T_d(FW3) = 15.02$ °C, $T_d(FW4) = 4.72$ °C

The results in Tables 5.1 and 5.2 show the melt rate relationship to thermal driving, ice salinity, and sediment concentration, quantified by changes in α, where melt rate is inversely related to α. As observed in Figure 5.7 melt rate increases with thermal driving. The melt rate increase associated with ice salinity is shown in Figures 5.10 and 5.11. For the small ice blocks $\overline{\alpha}$ decreases from -0.0062 kg$^{5/12}$/min to -0.0227 kg$^{5/12}$/min as we move from $T_d < 6$ °C to $T_d \approx 15$ °C, and is further decreased to -0.0320 kg$^{5/12}$/min

Melt date	T_d °C	Block	ζ	m_0^{ζ} (kg$^{\zeta}$)	α (kg$^{\zeta}$/min)	MSE	γ^2
2009-April-14	5.03	$FW1_1$	5/12	3.2940	-0.0073	0.0152	**0.0101**
			4/15	2.1962	-0.0039	**0.0151**	0.3480
		$FW1_2$	5/12	3.1962	-0.0058	**0.0010**	**0.0010**
			4/15	2.1408	-0.0030	0.0028	0.0104
2009-April-22	5.68	$FW2_1$	5/12	3.2051	-0.0070	**0.0029**	**0.0022**
			4/15	2.1509	-0.0037	0.0058	0.0156
		$FW2_2$	5/12	3.1883	-0.0065	**0.0014**	**0.0013**
			4/15	2.1344	-0.0033	0.0031	0.0104
		$FW2_3$	5/12	2.9909	-0.0059	**0.0001**	**0.0002**
			4/15	2.0435	-0.0030	0.0014	0.0055
2010-Feb-02	4.72	$FW4_1$	5/12	3.1428	-0.0045	**1.26e-05**	**5.21e-05**
			4/15	2.0862	-0.0021	4.97e-05	0.0010
Ave, FW	< 6 °C		5/12	3.1695	-0.0062	**0.0034**	**0.0025**
			4/15	2.1253	-0.0032	0.0047	0.0651
2009-July-28	15.02	$FW3_1$	5/12	2.9893	-0.0232	**0.0013**	**0.0006**
			4/15	2.0620	-0.0132	0.0041	0.0058
		$FW3_2$	5/12	3.2374	-0.0223	**0.0004**	**0.0002**
			4/15	2.1615	-0.0117	0.0055	0.0109
		$FW3_3$	5/12	3.0993	-0.0227	**0.0023**	**0.0018**
			4/15	2.0832	-0.0115	0.0030	0.0091
Ave, FW	≈ 15 °C		5/12	3.1087	-0.0227	**0.0013**	**8.667e-04**
			4/15	2.1022	-0.0121	0.0042	0.0086
		$FW_{sed}3_1$	5/12	3.2859	-0.0154	**0.0001**	**0.0001**
			4/15	2.1627	-0.0075	0.0006	0.0024
		$FW_{sed}3_2$	5/12	3.3532	-0.0175	**0.0013**	**0.0010**
			4/15	2.2022	-0.0088	0.0025	0.0082
		$FW_{sed}3_3$	5/12	3.3283	-0.0182	0.0012	**0.0013**
			4/15	2.1711	-0.0085	**0.0011**	0.0057
Ave, FW_{sed}	≈ 15 °C		5/12	3.3225	-0.0170	**8.667e-04**	**8.000e-04**
			4/15	2.1787	-0.0083	0.0014	0.0054
		$SW3_1$	5/12	3.1672	-0.0361	**0.0406**	**0.0102**
			4/15	2.1370	-0.0204	0.0554	0.0423
		$SW3_2$	5/12	3.1504	-0.0328	**0.0104**	**0.0035**
			4/15	2.1109	-0.0172	0.0148	0.0177
		$SW3_3$	5/12	3.2659	-0.0270	0.0150	**0.0072**
			4/15	2.1486	-0.0132	**0.0091**	0.0181
Ave, SW	≈ 15 °C		5/12	3.1945	-0.0320	**0.0220**	**0.0070**
			4/15	2.1322	-0.0169	0.0264	0.0260
		$SW_{sed}3_1$	5/12	3.2548	-0.0266	0.0058	**0.0025**
			4/15	2.1702	-0.0143	**0.0054**	0.0078
		$SW_{sed}3_2$	5/12	3.3600	-0.0226	**0.0003**	**0.0002**
			4/15	2.2007	-0.0113	0.0018	0.0042
		$SW_{sed}3_3$	5/12	3.3370	-0.0243	0.0017	0.0012
			4/15	2.1798	-0.0118	**0.0001**	**0.0004**
Ave, SW_{sed}	≈ 15 °C		5/12	3.3173	-0.0245	0.0026	**0.0013**
			4/15	2.1836	-0.0125	**0.0024**	0.0041

Table 5.1: Small ice block melt statistics

Melt date	T_d °C	Block	ζ	m_0^{ζ} (kg$^{\zeta}$)	α (kg$^{\zeta}$/min)	MSE	γ^2
2010-Mar-03	4.08	$FW5_1$	5/12	8.1261	-0.0049	0.0707	0.0154
			4/15	3.8741	-0.0018	**0.0015**	**0.0025**
2010-Mar-04	4.09	$FW5_2$	5/12	8.5452	-0.0056	0.0073	0.0063
			4/15	3.9540	-0.0018	**0.0006**	**0.0044**
2011-Jan-26	5.92	$FW6_1$	5/12	7.8371	-0.0090	0.0415	0.0203
			4/15	3.7447	-0.0030	**0.0033**	**0.0149**
2011-Jan-28	5.75	$FW6_2$	5/12	7.9229	-0.0081	0.0171	0.0085
			4/15	3.7804	-0.0027	**0.0013**	**0.0059**
2011-Feb-21	4.55	$FW_{sed}7_1$	5/12	8.3091	-0.0072	0.0203	0.0085
			4/15	3.8947	-0.0024	**0.0021**	**0.0081**
2011-Feb-22	4.53	$FW_{sed}7_2$	5/12	8.4594	-0.0070	0.0315	0.0083
			4/15	3.9635	-0.0024	**0.0025**	**0.0055**
2011-Mar-30	4.42	$FW_{sed}8_1$	5/12	8.2901	-0.0065	0.0103	0.0119
			4/15	3.8894	-0.0021	**0.0009**	**0.0100**

Table 5.2: Large ice block melt statistics

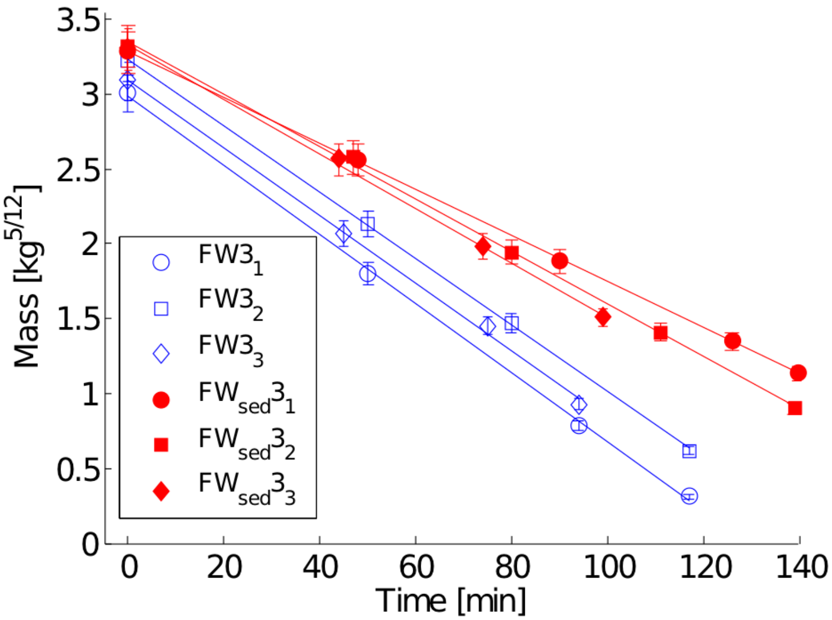

Figure 5.8: Small block sediment-free freshwater (FW) and sediment-laden freshwater (FW_{sed}) ice, showing melt rate dependence on sediment content for length scales up to 0.3 m ($L \leq 0.3$ m), ($T_d = 15.02$ °C), $\zeta = 5/12$

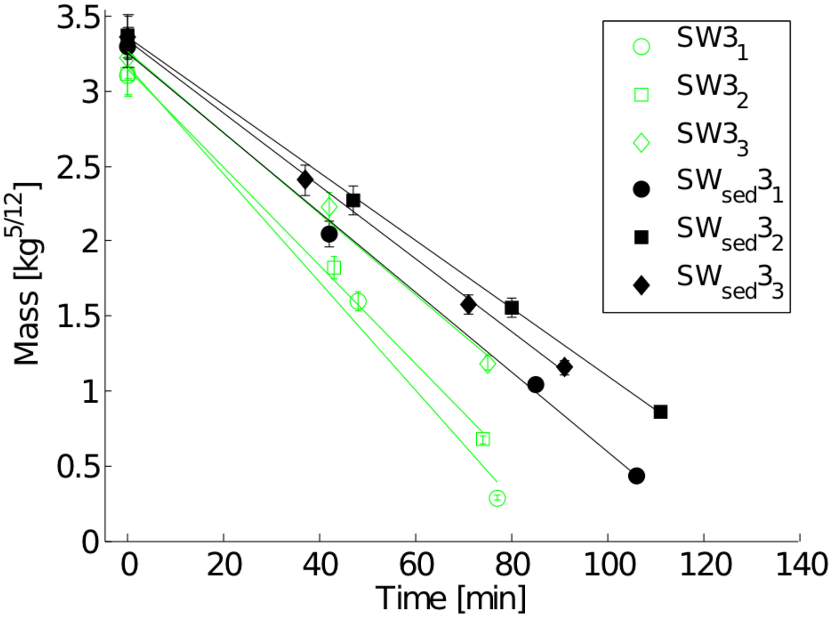

Figure 5.9: Small block sediment-free saltwater (SW) and sediment-laden saltwater ($\mathrm{SW}_{\mathrm{sed}}$) ice, showing melt rate dependence on sediment content for length scales up to 0.3 m ($L \leq 0.3$ m), ($T_d = 15.02\,^{\circ}$C), $\zeta = 5/12$

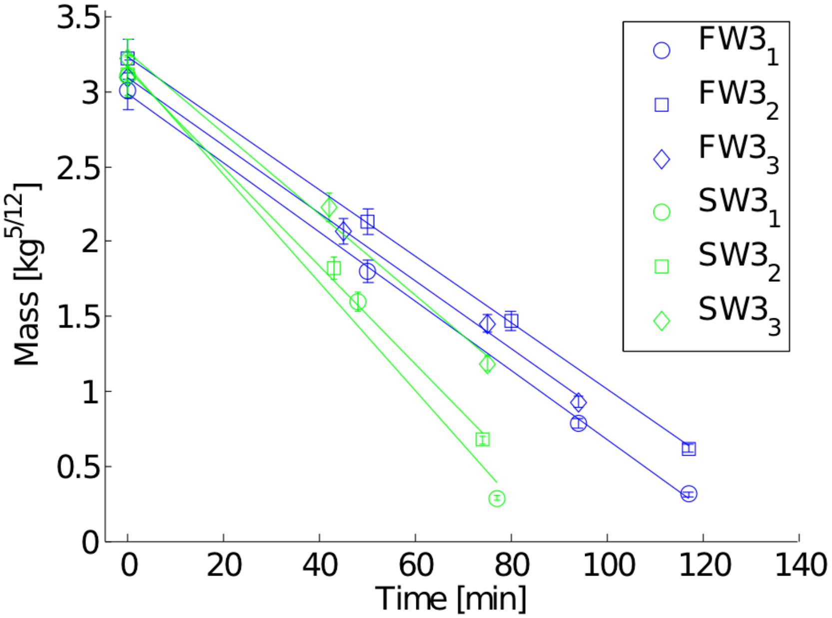

Figure 5.10: Small block sediment-free freshwater (FW) and sediment-fee saltwater (SW) ice, showing melt rate dependence on salinity for length scales up to 0.3 m ($L \leq 0.3$ m), ($T_d = 15.02\,^{\circ}$C), $\zeta = 5/12$

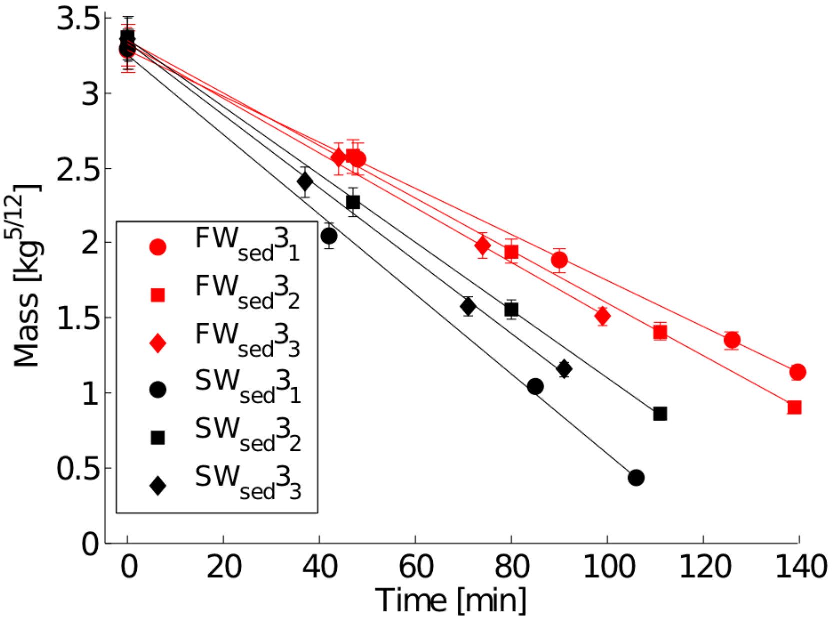

Figure 5.11: Small block sediment-laden freshwater ($\mathrm{FW_{sed}}$) and sediment-laden saltwater ($\mathrm{SW_{sed}}$) ice, showing melt rate dependence on salinity for length scales up to 0.3 m ($L \leq 0.3$ m), ($T_d = 15.02$ °C), $\zeta = 5/12$

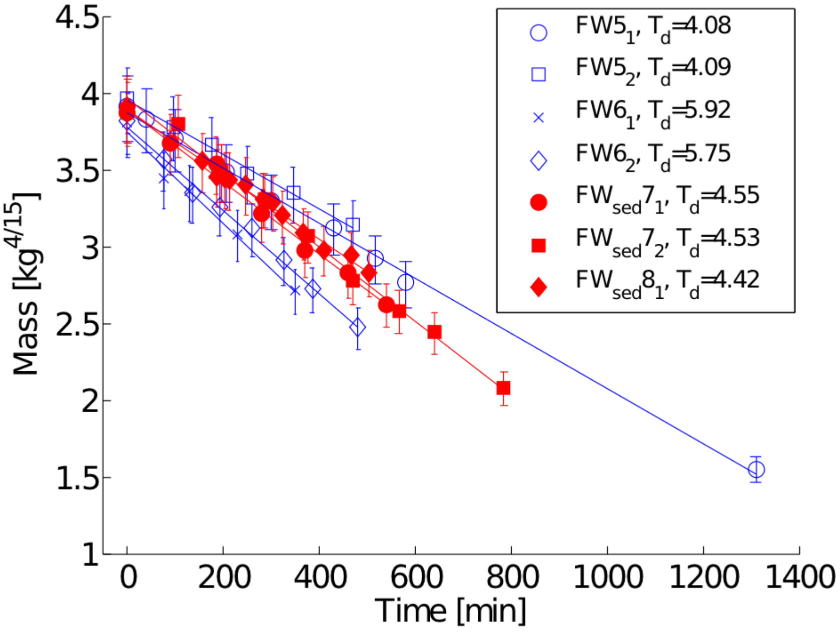

Figure 5.12: Large block sediment-free freshwater (FW) and sediment-laden freshwater ($\mathrm{FW_{sed}}$) ice, showing melt rate dependence on thermal driving (T_d [°C]) and sediment content for length scales greater than 0.3 m ($L > 0.3$ m), $\zeta = 4/15$

for the saltwater blocks melted at $T_d \approx 15$ °C. The dependence of melt rate on sediment concentration is shown in Figures 5.8 and 5.9 for the small freshwater and saltwater blocks, respectively. In both cases, the small sediment-laden ice blocks melted more slowly. $\overline{\alpha}$ increases to -0.0170 kg$^{5/12}$/min and -0.0245 kg$^{5/12}$/min for the small sediment-laden fresh and salt water ice blocks melted with $T_d \approx 15$ °C.

With respect to the large ice blocks, although Figure 5.12 and the statistics included in Table 5.2 show Equation (3.15) to be a good fit to the melt data, the effects of sediment concentration are not (yet) definitively separated from temperature dependence.

5.2.2 *Nusselt number (Nu) from ice melt data*

Although α from Equation (3.17) quantifies melt rate, it is difficult to separate the effects of temperature, salinity, and sediment concentration. The Nusselt number allows comparison of the magnitude of the convective current for each melt, without thermal dimensions. Given that the ice melt data support the relationships given by Equations (3.17) and (3.18), Equation (3.18) can be substituted into Equation (3.8) to obtain

$$\mathrm{Nu} = \frac{1}{\zeta}\alpha m^{1-\zeta}\frac{FL}{k\Delta TA} \tag{5.4}$$

with the following units α [kg$^{\zeta}$ s^{-1}], m [kg], F [J kg^{-1}], L [m], k [W m^{-1} °C^{-1}], T [°C], and A [m^2].

Equation (5.4) can be used to calculate a Nusselt number for any ice block mass measured during the melt experiments, requiring a shape assumption to allow calculation of surface area from mass. For the large blocks, length and diameter measurements obtained from the camera system were used when available. As with the Grashof number, due to the horizontal orientation of the ice cylinders throughout the melts, diameter was used for the vertical length scale over which convection took place. It should be noted that at the later stages of the large block melts elliptical shapes were observed due to preferential melting along the ice block sides. An average diameter was used which leads to a slight underestimate of the Nusselt number.

For the small ice blocks, measurements of length and radius were not consistently collected. It is then necessary to assume an aspect ratio. Consistent with observations we use $L \approx 2r$. The length scale is then $L = 2r$ and surface area is $A = 6\pi r^2$, so $L/A = 1/(3\pi r)$. The mass of a cylinder is $m = \rho\pi r^2 L$, thus for $L = 2r$ we have

$r = [m/(2\pi\rho)]^{1/3}$.

Similarly, measurements of ice block length and diameter were not consistently collected throughout the sediment-laden ice block melt conducted on March 30, 2011 when using the dynamometer for mass measurement. An average length to diameter ratio of $L/D = 1.25$ was observed for the sediment-laden ice blocks melted on February 21 and 22, 2011, which was applied for the March 30, 2011 melt. Length scale is then $L = 2r = 0.8l$ and surface area is $A = 7\pi r^2$, giving $L/A = 2/(7\pi r)$ and $r = [m/(2.5\pi\rho)]^{1/3}$.

The thermal conductivity (k) [W m^{-1} °C^{-1}] of sea water was calculated using,

$$k = 0.5715(1 + 0.003T - 1.025 \times 10^{-5}T^2 + 6.53 \times 10^{-3}P - 0.00029S) \qquad (5.5)$$

from *Sharqawya et al.* (2010) where T is sea water temperature [°C], S is sea water salinity [psu], and P is pressure [MPa] and one standard atmosphere was used ($P = 0.1013$ MPa).

The latent heat of fusion (F) [J g^{-1}] was calculated using Equations (2.32) and (2.33), which combined give

$$F(C_i, T_i, S_i) = (1 - C_i)(333.40 - 2.113T_i - 0.114S_i + 18.04(\frac{S_i}{T_i})) \qquad (5.6)$$

where an ice temperature of $T_i = -2$ °C was assumed to avoid the tendency of Equation (2.32) to approach $-\infty$ as $T_i \to 0$ for $S_i > 0$ as shown in Figure 2.7. The latent heat of fusion calculated using Equation (5.6) requires conversion to J kg^{-1} for use in all melt rate equations, including (5.4).

Wall temperatures were not measured during the melts. The relationship between T_d, T_{fp}, and $\overline{T_w}$ observed by *Josberger and Martin* (1981) was used. Rearranging Equations (2.60) and (2.61) to solve for average wall temperature we have

$$\overline{T_w} = T_{fp}(1.0 - \tanh(0.15T_d)) \qquad (5.7)$$

which was used for calculating $\Delta T = T_w - T_\infty$ [°C].

Nu is plotted against length scale $L = D$ [m] for the small and large blocks in Figures 5.13 and 5.14, respectively. Nu is plotted against length scale for all melt data in Figure 5.15. Statistics for the best fit lines $\mathrm{Nu} = \mathrm{Nu}_0 + \omega L$ are presented in Table 5.3, where Nu_0 is the $L = 0$ intercept.

Ice type	Nu_0	ω (Nu/m)	MSE	γ^2
$L < 0.3$m				
FW	25.6	383.6	171.6	0.182
SW	21.7	418.8	198.0	0.114
FW_{sed}	15.4	288.4	31.6	0.087
SW_{sed}	14.9	274.7	22.4	0.044
$L > 0.3$m				
FW	-26.3	543.0	86.5	0.036
FW_{sed}	-63.4	613.2	59.6	0.025
$Both$	-46.3	580.1	87.5	0.036

Table 5.3: Nusselt number statistics

As shown in Figures 5.13 through 5.15 and Table 5.3 a significant reduction in convective heat transfer (Nu) is observed for the small ice blocks containing sediment. For the large ice blocks, convective heat transfer increases to approach and potentially exceed that of sediment free ice near $L = 0.5$ m. With respect to salinity, an expected slight reduction in Nu is observed for sediment-laden ice, but not for sediment free ice, potentially due to the scatter in the small freshwater ice block data set. Use of the Nusselt number appears to be useful for removing the dimensional effects of temperature, but does not collapse the data. Scatter remains which is likely related to the $L = 2r$ shape assumption for calculation of surface area and length scale from mass.

As previously noted, many of the early melts conducted prior to adopting the layer methodology resulted in complex geometry with ratios of surface area to volume much larger than that for a cylinder. This effect is most noticeable in Figure 5.13 in which high values of Nu for the first melt experiment can be seen. Use of $\Delta T = T_\infty - 0$ [°C] reduces the spread in these data, however it is unknown if this is coincidence or if $T_w \approx 0$°C is a better representation than Josberger's relation as given by Equation (5.7). Also, the negative $L = 0$ intercept (Nu_0) for the large block melts (Figure 5.15) emphasizes the need to consider laminar and turbulent flow regimes. Further discussion and interpretation of results is presented in Chapter 6.

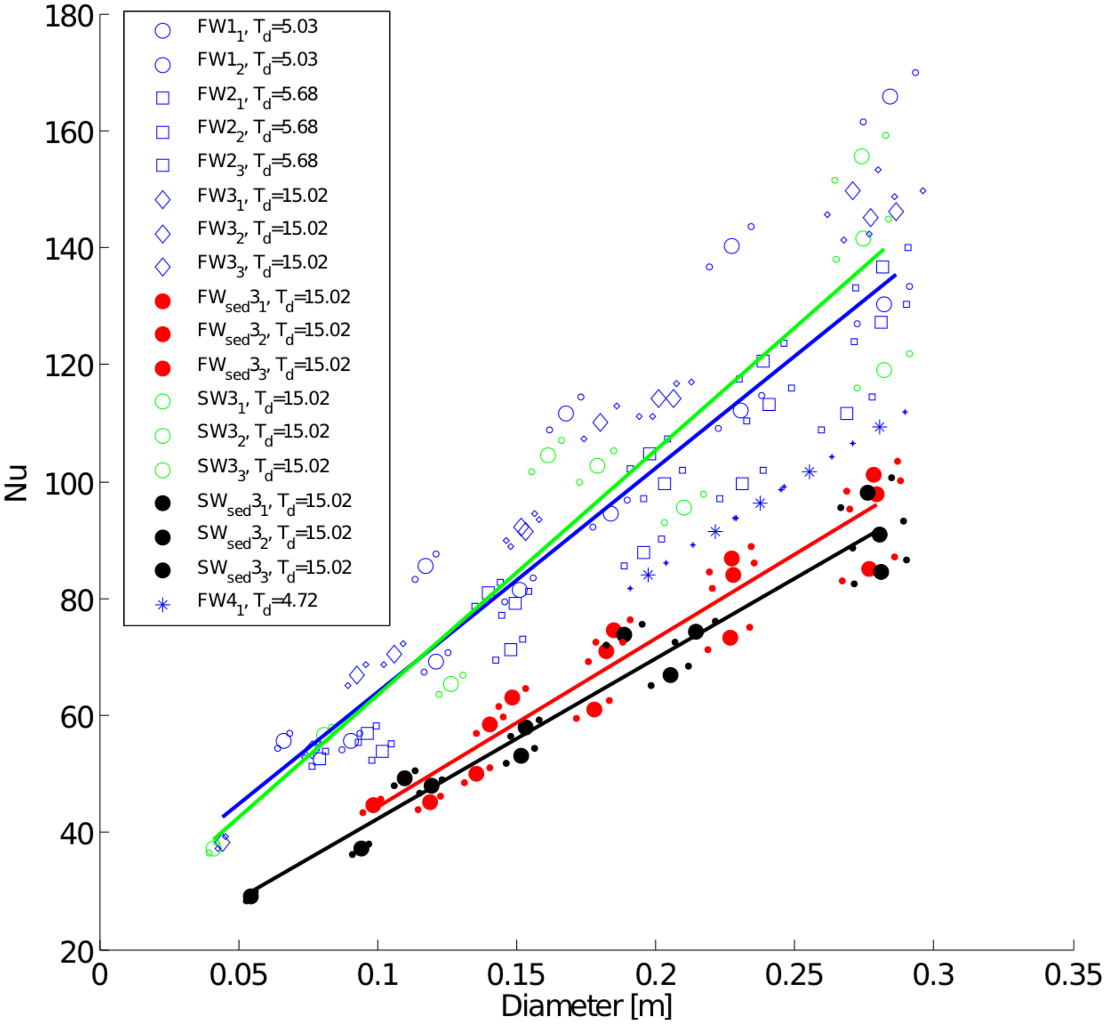

Figure 5.13: Nusselt number vs length scale ($0 < L < 0.3$) for sediment-free freshwater (FW), sediment-free saltwater (SW), sediment-laden freshwater ($\mathrm{FW}_{\mathrm{sed}}$), and sediment-laden saltwater ($\mathrm{SW}_{\mathrm{sed}}$) small ice block melts. Small marks show upper and lower limits of error based on relative uncertainty applied to calculation of Nu and D.

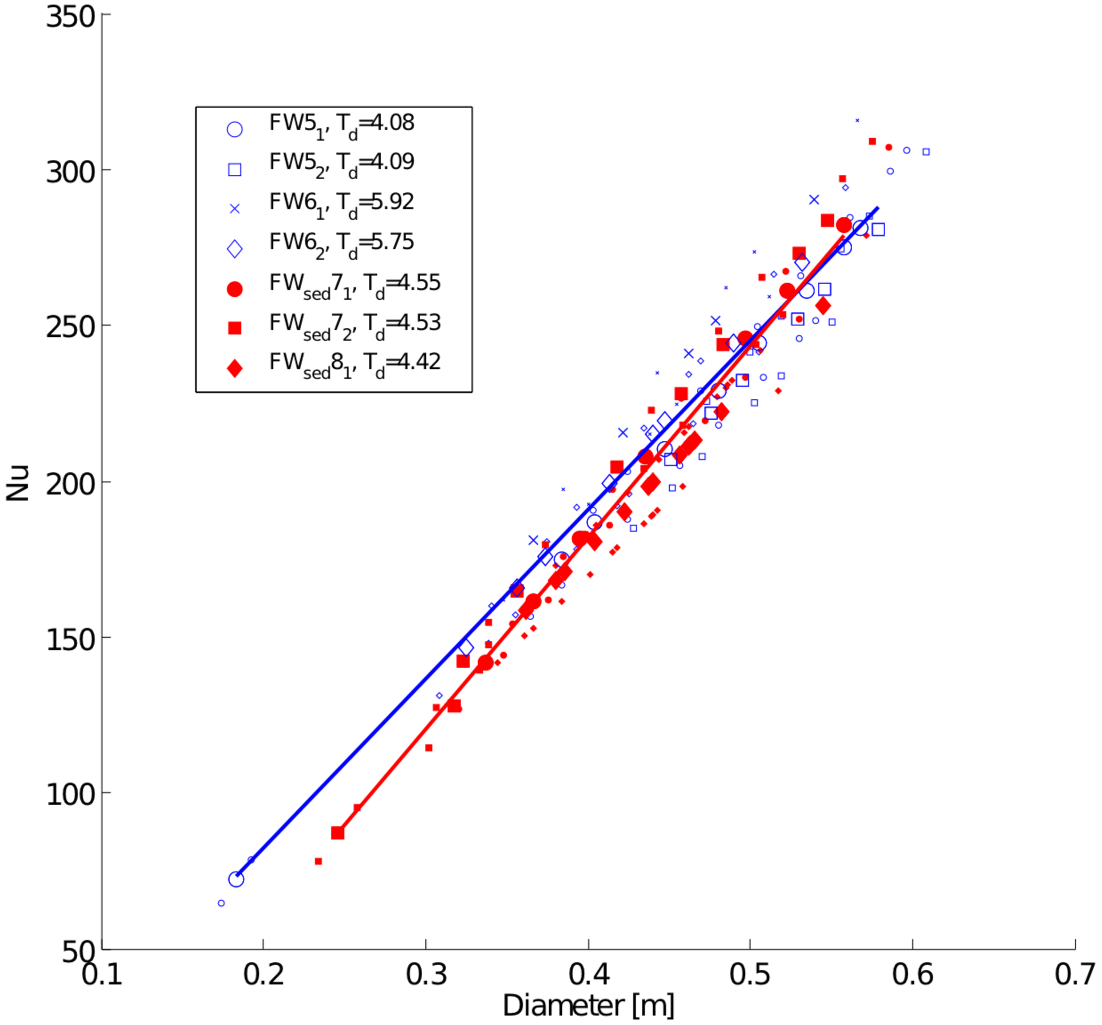

Figure 5.14: Nusselt number vs length scale ($0.2 < L < 0.6$) for sediment-free freshwater (FW) and sediment-laden freshwater ($\mathrm{FW}_{\mathrm{sed}}$) large ice block melts. Small marks show upper and lower limits of error based on relative uncertainty applied to calculation of Nu and D.

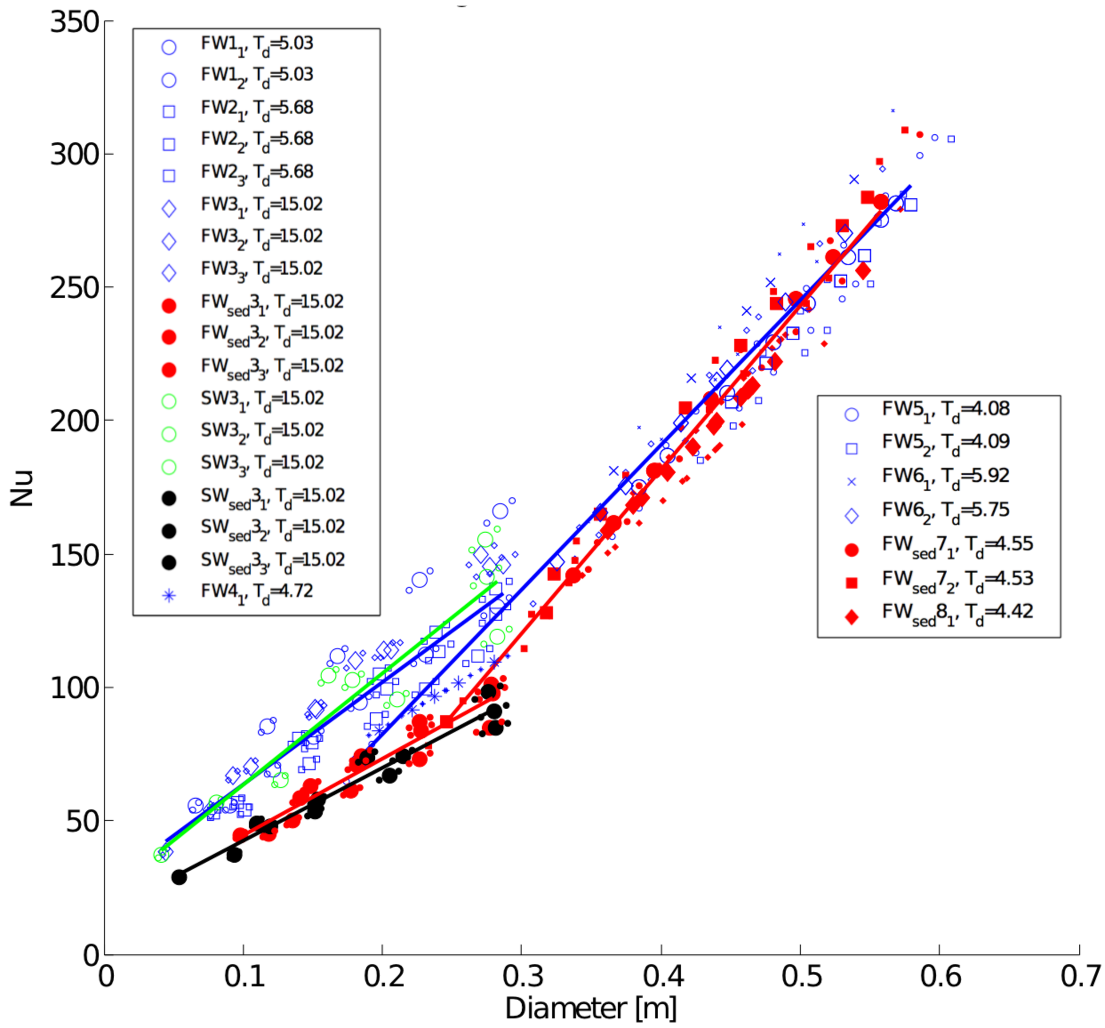

Figure 5.15: Nusselt number vs length scale ($0 < L < 0.6$) for sediment-free freshwater (FW), sediment-free saltwater (SW), sediment-laden freshwater ($\mathrm{FW}_{\mathrm{sed}}$), and sediment-laden saltwater ($\mathrm{SW}_{\mathrm{sed}}$) small ice block melts and FW and $\mathrm{FW}_{\mathrm{sed}}$ large ice block melts. Small marks show upper and lower limits of error based on relative uncertainty applied to calculation of Nu and D.

CHAPTER 6

DISCUSSION

The Nusselt number has been used to explain the data from the melt experiments leading to some interesting observations. Most notably, we see a significant reduction in convective heat transfer (Nu) associated with sediment inclusion at small length scales. However, convective heat transfer increases to approach and potentially exceed that of sediment free ice near $L = 0.5$ m. Also, the negative $L = 0$ intercept (Nu_0) for the large block melts supports the necessity for considering laminar and turbulent flow regimes. The following discussion evaluates the use of additional dimensionless numbers for use as predictors of heat flow (Nu) observed in the melt experiments following $\overline{\mathrm{Nu}} = B(\overline{\mathrm{Ra}})^n$ (Equation (2.40)).

As previously discussed in Section 2.4 the onset and magnitude of natural convection is governed by the Rayleigh number (Ra), which is the product of the Prandtl (Pr) and Grashof (Gr) numbers, the Prandtl number being the ratio of momentum diffusivity to thermal diffusivity, and the Grashof number the ratio of buoyancy to viscous forces. The Prandtl, Grashof, and Rayleigh numbers are discussed in the following sections, with associated interpretation applicable to results of the melt experiments. The Grashof number analysis reveals complications related to the effects of fine grained sediment on the buoyancy and viscosity of the melt water and cohesion of sediment to the ice block surface. Results are then extended to obtain an equation for melt rate (dm/dt) of sediment-laden freshwater and saltwater ice.

6.1 Prandtl Number (Pr)

The Prandtl number is (restated from Equation (2.37))

$$\mathrm{Pr} = \frac{\nu}{\kappa} = \frac{c\,\mu}{k} \tag{6.1}$$

and provides a measure of the ratio of the momentum boundary layer and thermal boundary layer thicknesses (*Schlichting*, 1960). Pr and its parameters are presented in Figures 6.1 and 6.2 as functions of temperature and salinity. Equations for molecular shear (dynamic) viscosity (μ) [kg m^{-1} s^{-1}], specific heat capacity (c) [J kg^{-1} °C^{-1}], and thermal conductivity (k) [W m^{-1} °C^{-1}] were obtained from *Sharqawya et al.* (2010). We see Pr to be weakly affected by salinity within the oceanic range. Pr decreases with increasing temperature, associated with the corresponding decrease in kinematic viscosity (ν) [m^2 s^{-1}] and increase in thermal diffusivity (κ) [m^2 s^{-1}]. Within the temperature range that we may consider applicable for oceanic melting of sea ice $0 < T < 10$ °C and using $S = 30$ ppt the Prandtl number is $13.39 \geq \mathrm{Pr} \geq 9.54$, indicating that the thermal boundary layer is expected to be much thinner than the viscous boundary layer under laminar conditions.

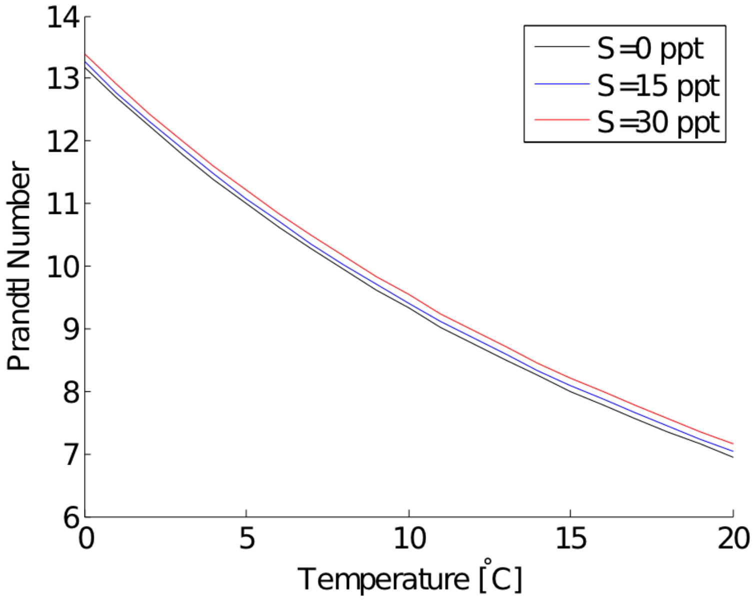

Figure 6.1: Prandtl number as a function of temperature and salinity

The Prandtl number calculated evaluating ν and κ using S_w and T_w and without accounting for viscosity increase due to the presence of sediment ranged from $13.21 \leq \mathrm{Pr} \leq 13.58$,

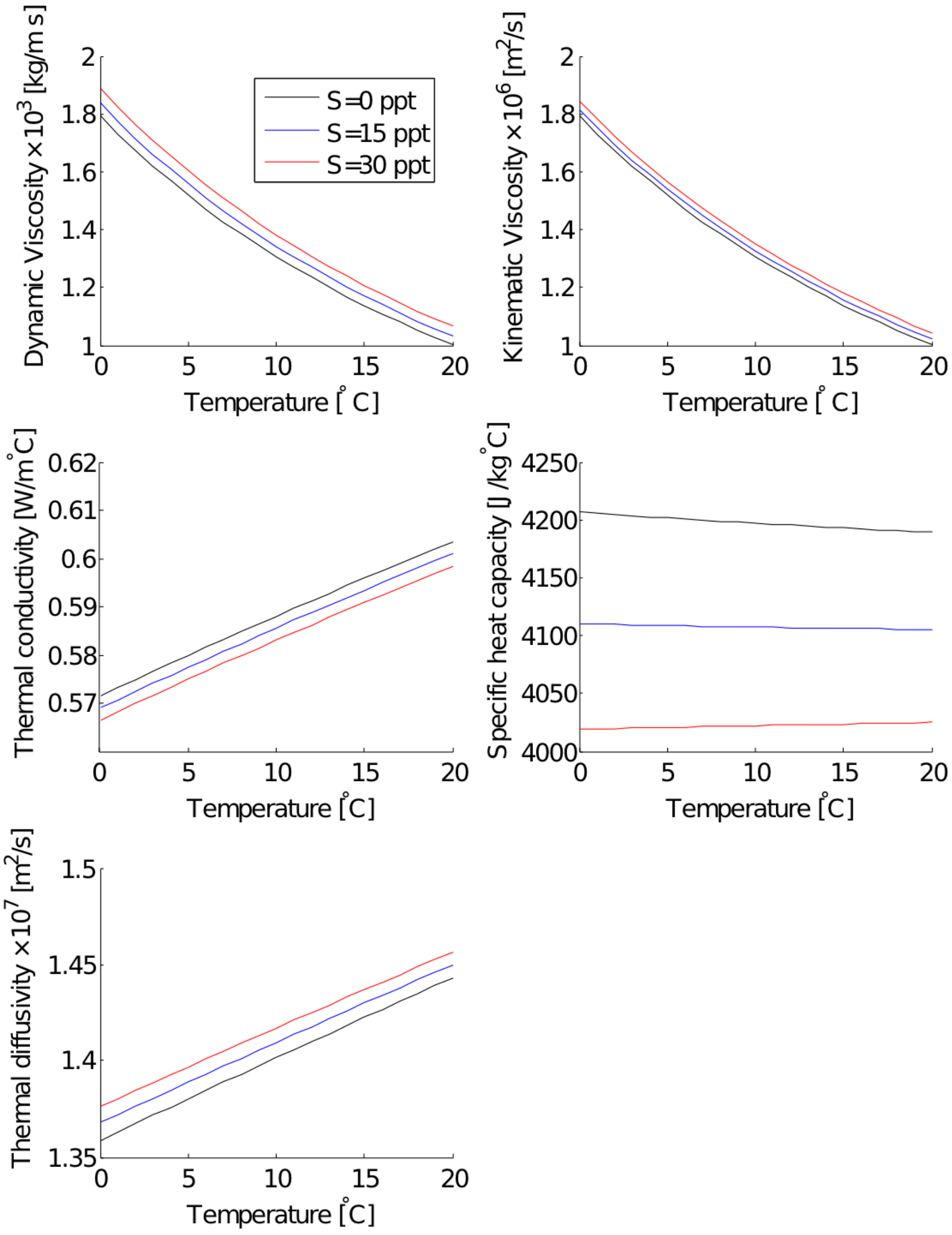

Figure 6.2: Prandtl number parameters as functions of temperature and salinity

Ice type	$\mathrm{Pr}_{\min}$	$\mathrm{Pr}_{\max}$	$\overline{\mathrm{Pr}}$
FW	13.21	13.58	13.43
FW_{sed}	13.21	13.55	13.37
SW	13.27	13.27	13.27
SW_{sed}	13.27	13.27	13.27

Table 6.1: Summary of Prandtl numbers by ice type

with an average of $\overline{\mathrm{Pr}} = 13.38$ for the melt experiments. A summary of maximum, minimum, and mean Pr by ice type is presented in Table 6.1.

6.2 Grashof Number (Gr)

The Grashof number is (restated from Equation (2.49))

$$\mathrm{Gr} = \frac{g|\rho_w - \rho_\infty|L^3}{\rho_\infty \nu_w^2} \tag{6.2}$$

and provides a measure of the ratio of buoyancy to viscous forces. ν_w is the kinematic viscosity [m^2 s^{-1}] of the meltwater at the wall, and ρ_w [kg m^{-3}] is calculated using the general equation for the density of sediment-laden fluid,

$$\rho_{sf} = \frac{\rho_f \rho_s}{\rho_s - C_f(\rho_s - \rho_f)} \tag{6.3}$$

where ρ_s, $\rho_f(S_w, T_w)$, and $\rho_{sf}(S_w, T_w, C_f)$ are the densities of sediment, sediment-free fluid, and sediment-laden fluid, respectively, and $C_f = C_i$ is sediment concentration in units of sediment mass per total mass. Note that viscosity is evaluated for S_w [psu] and T_w [°C] as motion must originate at the ice-water interface.

The Grashof number is plotted against length scale for all melt data in Figure 6.3. The effect of sediment is pronounced; the values for sediment-laden ice being grouped separately from the sediment-free ice.

6.2.1 Buoyancy

The partition of the sediment-laden and sediment-free data by the Grashof number suggests a strong effect of sediment concentration on the buoyancy of the meltwater plume. Average

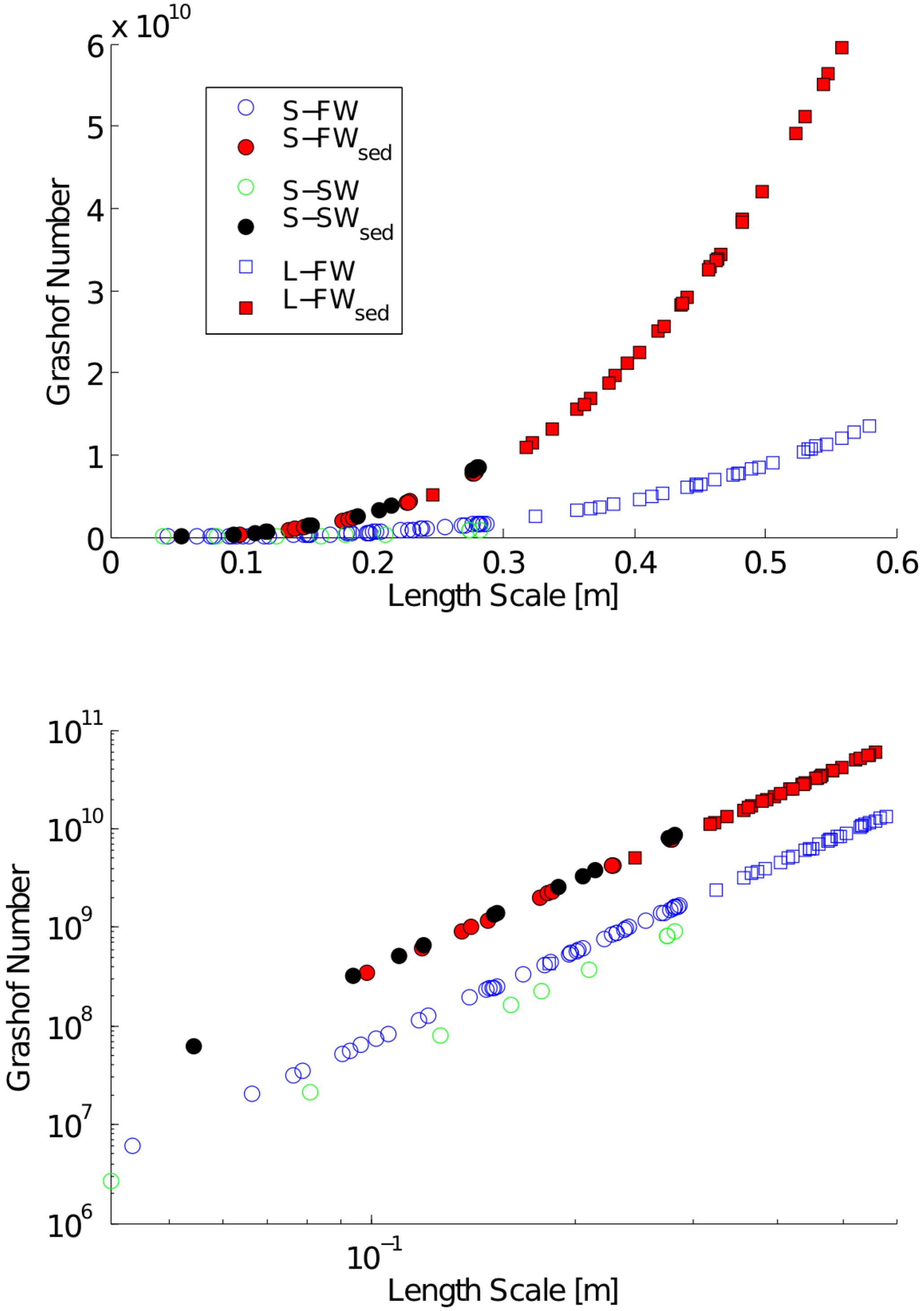

Figure 6.3: Grashof number vs length scale. Plotted for the following ice types, small sediment-free freshwater (S-FW), small sediment-free saltwater (S-SW), small sediment-laden freshwater (S-FW$_{\text{sed}}$), small sediment-laden saltwater (S-SW$_{\text{sed}}$), large sediment-free freshwater (L-FW), and large sediment-laden freshwater (L-FW$_{\text{sed}}$).

Ice type	ρ_∞ (kg/m^3)	ρ_w (kg/m^3)	$\Delta\rho$ (kg/m^3)
SW	1023.6	1010.0	13.6
FW	1024.3	999.8	24.5
FW_{sed}	1024.1	1145.0	-120.9
SW_{sed}	1023.6	1155.5	-131.9

Table 6.2: Average wall and far field density

wall and far-field densities for each ice type are presented in Table 6.2 together with $\Delta\rho = \rho_\infty - \rho_w$, such that positive $\Delta\rho$ indicates positive buoyancy and upward flow. Table 6.2 has been organized by the magnitude of $\Delta\rho$, which corresponds to the results presented in Figure 6.3 where, for a given length scale, Gr increases progressively from salt water ice, to fresh water ice, then to sediment-laden fresh water ice, and finally to sediment-laden salt water ice.

Observations indicating a downward flowing density (a.k.a turbidity) current were made during the large sediment-laden ice block melts. These observations support the direction of flow indicated by the Grashof numbers in Table 6.2. Measuring the flow field around the melting ice block falls outside the scope of work for this thesis. However, an experiment was conducted in conjunction with the March 30, 2011 large sediment-laden ice block melt. Three acoustic Doppler velocimeters (ADV) and a laser projecting a sheet of light perpendicular to the field of view for two camera systems were positioned approximately 1 m below the ice block.

Initial results indicate a downward flow velocity of $w \approx -2$ cm/s from the centre ADV supporting the presence of a density current. Recalling the results of *Josberger and Martin* (1981) for fresh water ice melting in saltwater, a maximum flow velocity of 1 cm/s was observed in the upward flowing turbulent boundary layer.

Given that maginitude of flow velocities observed for sediment-laden and sediment-free ice are similar, the Grashof numbers presented in Table 6.2 may overestimate the buoyancy induced flow from sediment-laden ice. The potential effects of sediment cohesion and increased fluid viscosity due to the presence of sediment are discussed in the following sub-sections.

6.2.2 Viscosity

Viscosity is the fluid's ability to resist shear, and also its ability to transmit it. The effective viscosity for a suspension of particles is greater than the viscosity of the ambient fluid (*Batchelor*, 1967). For a dilute suspension of uniformly distributed spherical particles the viscosity is represented by Einstein's formula,

$$\mu_r = 1 + 2.5\overline{\phi_s} \tag{6.4}$$

where μ_r is the relative viscosity (μ_{sf}/μ_f) [dimensionless], $\overline{\phi_s}$ is the concentration of particles by volume, and $\overline{\phi_s}$ is less than about 0.2 (*Batchelor*, 1967). *Happel and Brenner* (1973) discuss larger concentrations where the effect of neighbouring particles on the disturbance flow must be considered. Several equations are presented including,

$$\ln \mu_r = \frac{2.5\phi_s}{1 - \varphi\phi_s} \tag{6.5}$$

$$\mu_r = 1 + 2.5\phi_s + (3.125 + 2.5\varphi)\phi_s^2 + \ldots \tag{6.6}$$

where φ is an experimentally derived factor to account for hydrodynamic interaction. Experimental results show the value of φ to lie roughly between the limits of 1 and 2. For the case of spherical particles of equal size *Happel and Brenner* (1973) present,

$$\mu_r = 1 + \frac{3}{(1/\phi_s) - (1/0.52)} \tag{6.7}$$

which agrees reasonably well with observed values of several experiments. Near the upper limit of $\phi_s = 0.52$ (which corresponds with the maximum attainable solids fraction, which is the volume fraction of solids for cubical packing of spheres of equal size) the formula asymptotically approaches an infinite viscosity due to interparticle frictional effects (*Happel and Brenner*, 1973).

As discussed in Section 4.1.1, the required sediment concentration for $\rho_{sf} = 1145$ kg m^{-3} and $\rho_{si} = 1040$ kg m^{-3} is $C_s = 206$ ppt. The corresponding volumetric ratio is $\phi_s \approx 0.1$. Using Equation (6.4) the relative viscosity is $\mu_r = 1.25$ [dimensionless]. Assuming the density of sea water $\rho_w = 1.025$ kg/L, and using $\nu = \mu/\rho$, this gives $\nu_{sf} \approx 1.4\nu_f$. The effect of increased viscosity due to sediment is shown in Figure 6.4 where the viscosity of sediment-laden fluid has been estimated as $\nu_{sf} = \Gamma\nu_f$, for $\Gamma = 1$, 1.33, 1.66, and 2. A doubling of kinematic viscosity is required to bring together the magnitude of the buoyancy driven flows from sediment-laden ice and sediment-free ice. Note that increasing ν to account for sediment has a linear effect on Pr, such that for $\Gamma = 2$, $\overline{Pr} = 26.75$ and 26.53 for sediment-laden fresh and saltwater ice, respectively. Measurement of ν_{sf} for fluids of varying sediment concentration is recommended.

6.2.3 Cohesion

Saturated fine grained sediments from the banks of the Avon and Shubenacadie rivers are known to be highly cohesive (Figure 6.5). Sediment flocs of varying size were observed to break free intermittently from the melting ice blocks in addition to the steadier sediment flux. An example of sediment breaking free from a large block melt is presented in Figure 6.6, causing a turbidity current of higher density than average.

It is now convenient to mention a few early attempts at making sediment-laden ice. Prior to collecting sediment from the field and adopting the layer methodology, sand was added to roughly 16 L of water and then frozen. Of course, the sand settled to the bottom of the pail prior to freezing. Data from these melts has not been included in this work due to the heterogenous, stratified nature of these blocks. However, an important observation was made in connection to the use of non-cohesive material. As shown in Figure 6.7, increased melt rate was observed in the sediment-laden portion of sandy ice blocks; supporting the hypothesis of melt rate increasing with sediment concentration as presented in Section 2.2.3. In contrast, as shown in Figure 6.8 the opposite effect was observed for the small fine grained sediment-laden ice blocks. Figure 6.8 also includes photographs of large sediment-laden ice blocks where more uniform melting was observed over gradients of sediment concentration. The areas of higher sediment concentration were slightly recessed from the surface of the ice block, indicating preferential melting. Sediment laden ice structure is also visible on the photos of the larger blocks and is covered by a layer of sediment and water on the smaller ice blocks, indicating cohesion at small length scales.

The balance between cohesion and the forces of gravity (W) [N] and friction (or shear) (τ) [N] which act to strip sediment from the ice block must be considered to evaluate the effect of cohesion at different length scales. The apparent weight of sediment in sea water is $W_s = m_s g' = m_s g(\rho_s - \rho_f)/\rho_s \approx 5.95 m_s$. Provided cohesion is present, m_s for sediment adhered to the ice block increases with time through the melt, until it is released at some critical value $F_c = W_s + \tau$. The frictional force is proportional to the roughness

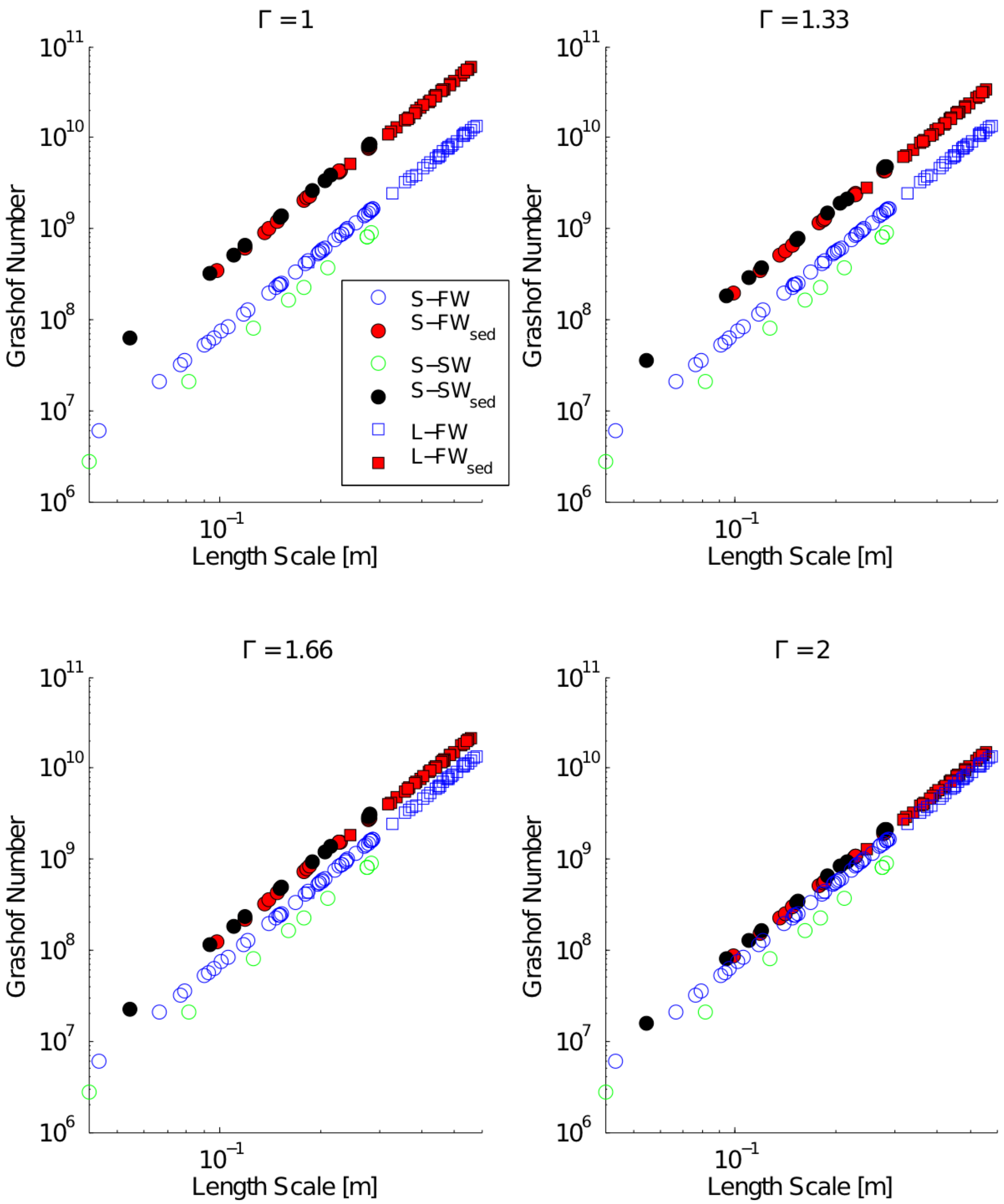

Figure 6.4: Grashof number vs length scale, showing the effect of increasing viscosity due to sediment. Plotted for the following ice types, small sediment-free freshwater (S-FW), small sediment-free saltwater (S-SW), small sediment-laden freshwater (S-FW$_{sed}$), small sediment-laden saltwater (S-SW$_{sed}$), large sediment-free freshwater (L-FW), and large sediment-laden freshwater (L-FW$_{sed}$).

Figure 6.5: Evidence of Shubenacadie River sediment cohesion. Showing sediment transport to Shad Bay, NS.

Figure 6.6: Large block sediment-laden ice photo, showing presence of a turbidity current.

Figure 6.7: Sandy sediment-laden ice melt photos, showing increased melt rate where sand is present.

Figure 6.8: Fine grained sediment-laden ice melt photos, showing reduced melt rate where sediment is present for small ice blocks (top) and more uniform melting for large ice blocks (bottom).

of the sediment, flow velocity, and the sediment to fluid contact area. As with m_s, the contact area increases with time until the sediment is stripped at F_c. The implication is, for a given flow velocity (u) tangential to the ice surface there is a maximum amount of sediment able to accumulate on the ice surface prior to being stripped at F_c. In addition, there is also a critical flow velocity u_c at which frictional force alone shall be sufficient to overcome cohesion. This assessment is supported by the decrease in conductive heat flow (Nu) shown in Figure 5.15 for length scales less than approximately 0.5 m. Significant effects of cohesion include a turbidity current of lower density due to a decrease in steady sediment flux from the melting ice, and the presence of an insulating sediment-water layer on the ice wall.

A turbidity current of reduced density and the presence of an insulating layer could explain the observed reduction in Nu for small sediment-laden ice blocks compared to small sediment-free ice blocks. Additionally, $\Delta\mathrm{Nu} = \mathrm{Nu}_\mathrm{i} - \mathrm{Nu}_\mathrm{si}$, where subscript i denotes fresh water ice and subscript si sediment-laden fresh water ice, evaluated over the range of lengths scales presented in Figure 5.15 gives information with respect to the balance between W_s and τ at F_c. At small length scales associated with weaker buoyancy induced flow (lower Gr) W_s must dominate, therefore resulting in greater accumulation of sediment and larger $\Delta\mathrm{Nu}$. As $\Delta\mathrm{Nu}$ decreases, length scale (and flow velocity) increases and the balance shifts to increasing τ. The intersection of Nu_i and Nu_si ($\Delta\mathrm{Nu} = 0$) occurs at approximately $L = 0.5$ m corresponding with u_c. However, I am hesitant to connect this length scale with a critical Gr due to uncertainties in the viscosity and concentration of the turbidity current.

6.2.4 Transition to turbulence

As discussed in Section 2.4.3 researchers have identified the transition from laminar to turbulent flow over a range of Grashof numbers. *Eckert and Jackson* (1951) suggest the transition occurs within the range of $10^8 < \mathrm{Ra} < 10^{10}$ for a fluid of $\mathrm{Pr} \approx 1$, giving $10^8 < \mathrm{Gr} < 10^{10}$. *Eckert* (1959) states the critical Grashoff number for turbulent flow to be around $\mathrm{Gr}_\mathrm{c} = 10^9$. *Turner* (1973) reports an extension of this from the work of *Tritton* (1963) for flow adjacent to a heated sloping plate, where Gr_c ranges from 5.5×10^{10} to 1.3×10^9 for slope angles from $\theta = 40^\circ$ to 90° (vertical). *Josberger and Martin* (1981) found the transition at $\mathrm{Gr} \approx 2 \times 10^8$, which they attributed to destabilization of the upward laminar flow due to increased shear from the outer downward flow.

Ice type	L_c for $\mathrm{Gr_c} = 10^8$ (m)	L_c for $\mathrm{Gr_c} = 10^9$ (m)
SW_{sed}	0.06	0.14
FW_{sed}	0.07	0.14
FW	0.11	0.24
SW	0.14	0.29

Table 6.3: Critical length scales for transition to turbulent flow over the region $10^8 \leq \mathrm{Gr_c} \leq 10^9$. Cohesion and sediment effect on meltwater viscosity not accounted for.

Table 6.3 contains a summary of the range of length scales (L_c) that correspond to $10^8 \leq \mathrm{Gr_c} \leq 10^9$ for each ice type using the mean far-field density for our melts $\overline{\rho_\infty} = 1024.4$ kg/m^3, mean wall temperature $\overline{T_w} = -0.6$ ° C, $S_w = S_i = 12.5$ ppt for salt water ice and $S_w = 0$ for fresh, ρ_w calculated using Equation (6.3) with $C_f = C_i = 206$ ppt, and kinematic viscosity evaluated at T_w and S_w. These estimates do not take into account the effects of sediment cohesion or increased viscosity due to sediment in suspension.

The values of $L_c = 0.24$ and 0.29 m for sediment-free freshwater (FW) and sediment-free saltwater (SW) ice corresponding to $\mathrm{Gr_c} = 10^9$ are both in good agreement with the location of the break in slope in Figure 5.15 indicated by fits to Equations (3.13) and (3.15) for laminar and turbulent flow conditions, respectively. However, the values of L_c for sediment-laden ice seem somewhat low. As a thought exercise, tuning a) the concentration of the turbidity current released from the ice block using $C_f = \lambda C_i$ with $\lambda = 0.5$ to account for significant cohesion at small length scales prior to the transition to turbulent flow, and b) a conservative increase in kinematic viscosity due to sediment contribution using $\nu_{sf} = \Gamma \nu_f$ with $\Gamma = 1.2$; the critical length scales for sediment-laden freshwater (FW$_{\mathrm{sed}}$) and sediment-laden saltwater (SW$_{\mathrm{sed}}$) ice are increased to $L_c = 0.24$ and 0.21 m respectively[1]. Although the values of λ and Γ were chosen somewhat arbitrarily, this shows that a reduction in C_f and thus ρ_w is required to account for cohesion at small length scales, the effect being a decrease in the buoyancy differential driving the flow. Also, an increase in ν_{sf} corresponding with C_f is required to provide additional resistance to flow and the formation of turbulent eddies. Using the tuning equations from above, λ shall approach its maximum value of 1 as length scale increases and $u \rightarrow u_c$, and Γ must

---

[1] Note the following values applied for this exercise, $C_f = 103$ ppt; $\nu_{sf} = 2.19 \times 10^{-6}$ and 2.22×10^{-6} m^2/s at the ice-fluid interface for fresh and salt water ice, respectively; and $\rho_w = 1067.5$ and 1077.8 kg/m^3 again for fresh and salt water ice, respectively.

increase from 1 at $\lambda = 0$ (sediment free ice, or 100% cohesion) at an unknown rate to be representative of $\nu_{sf}(C_f)$, which should be determined by experimentation. A refinement of both parameters is required for accurate calculation of the Grashof number.

6.3 Rayleigh Number (Ra)

The onset and magnitude of natural convection can be determined by the Rayleigh number, which is essentially an extension of the Grashof number, where by multiplying by the Prandtl number, Ra accounts for two diffusive processes (thermal and momentum) which retard the buoyancy induced motion and tend to stabilize it (*Turner*, 1973). The Rayleigh number for thermohaline convection resulting from a melting ice block in sea water is (restated from Equation (3.9))

$$\mathrm{Ra} = \frac{g|\rho_w - \rho_\infty|L^3}{\rho_\infty \nu_w \kappa} \tag{6.8}$$

again noting the substitution $\mu = \nu_w \rho_\infty$ has not been made as ν_w is representative of conditions at the ice-fluid interface rather than far-field values. As with the Grashof number, the effect of evaluating the temperature and salinity of fluid parameters which oppose flow at the wall, far-field, and a mid point was assessed.

The Rayleigh number plotted against length scale is presented in Figure 6.9 for all melt data. With an average Prandtl number of $\overline{\mathrm{Pr}} = 13.38$ for our melt experiments Ra is an order of magnitude higher than Gr.

With Ra being the product of Gr and Pr previous discussions regarding the effects of cohesion on the density of the turbidity current, and sediment on the viscosity of melt fluid apply. The effect of $\lambda = 0.5$ and $\Gamma = 1.2$ on our data set is presented in Figure 6.10. As previously discussed both parameters are a function of length sale. Applying constants is not ideal; however, the cumulative effect, resulting in $\mathrm{Ra_{si}} \approx \mathrm{Ra_i}$ better matches the observation of $\mathrm{Nu_{si}} \approx \mathrm{Nu_i}$.

6.4 Nusselt Number (Nu)

The Nusselt number (Nu) is defined as the ratio of the actual heat transport to the purely diffusive flux which would occur through a linear temperature gradient between two

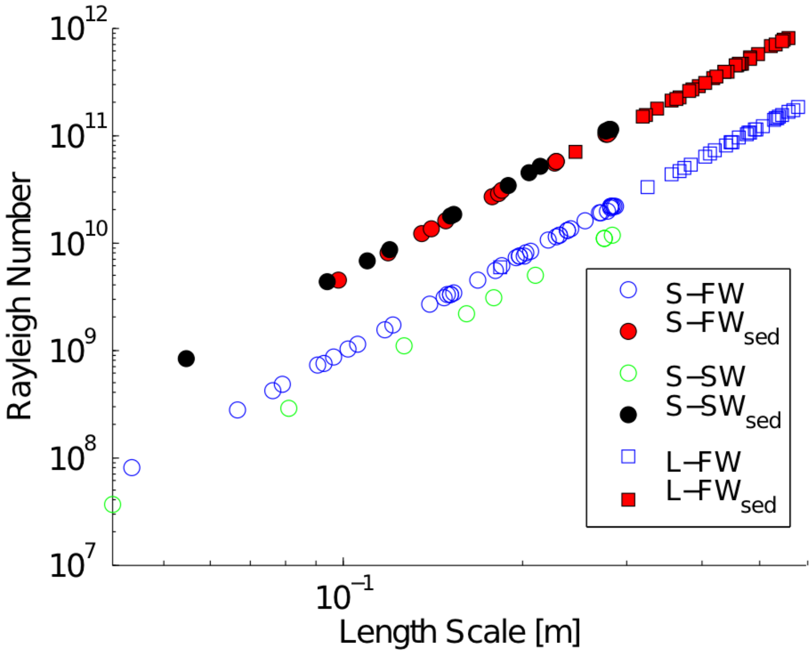

Figure 6.9: Rayleigh number vs length scale. Plotted for the following ice types, small sediment-free freshwater (S-FW), small sediment-free saltwater (S-SW), small sediment-laden freshwater (S-FW$_{sed}$), small sediment-laden saltwater (S-SW$_{sed}$), large sediment-free freshwater (L-FW), and large sediment-laden freshwater (L-FW$_{sed}$).

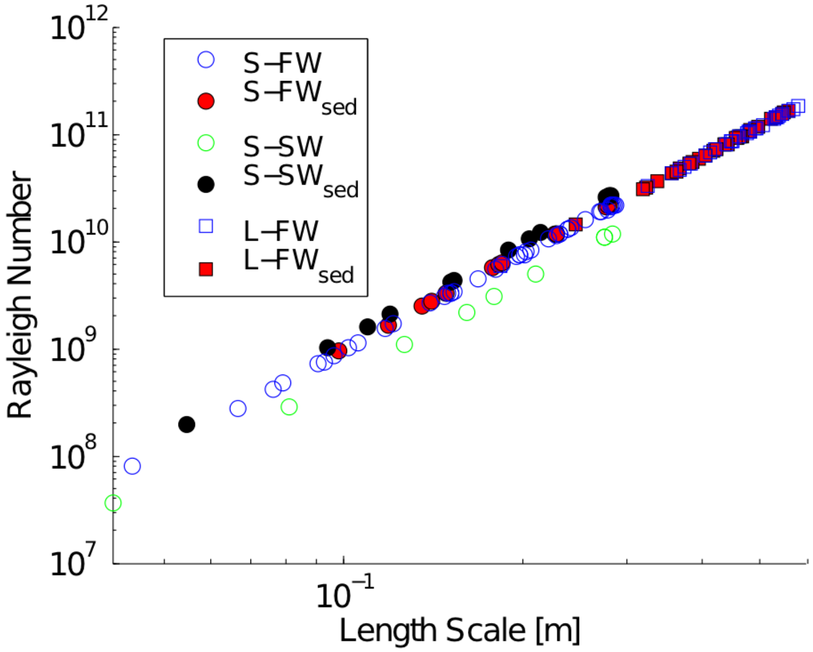

Figure 6.10: Rayleigh number vs length scale - with adjustments for cohesion, and viscosity of sediment-laden fluid ($\lambda = 0.5$ and $\Gamma = 1.2$)

Ice type	Laminar $n = 1/4$, $L < 0.3$ m	Turbulent $n = 2/5$, $L > 0.3$ m
FW	0.355	9.17 $\times 10^{-3}$
FW_{sed}	0.166	4.69 $\times 10^{-3}$
SW	0.427	-
SW_{sed}	0.158	-

Table 6.4: Summary of B, from $\overline{\mathrm{Nu}} = B(\overline{\mathrm{Ra}})^n$

boundaries (***Turner***, 1973), and is (restated from equation (2.39)),

$$\mathrm{Nu} = \frac{hL}{k} \tag{6.9}$$

where $h = q/\Delta T$ is the convective heat transfer coefficient [W m^{-2} °C^{-1}], and q is the heat flux [W m^{-2}].

Following Equation (2.40), $\overline{\mathrm{Nu}} = B(\overline{\mathrm{Ra}})^n$, where B is a dimensionless constant, $n = 1/4$ for laminar flow and $2/5$ for turbulent (supported by theory presented in Sections 2.4.1 and 3.1) Ra is then plotted against Nu calculated from the melt rate data (Equation (5.4)). The plot is presented in Figure 6.11 without adjustment for sediment cohesion or the effect of sediment on the viscosity of melt fluid at the ice-fluid interface.

The constant B was calculated for each ice block as $B = \overline{\mathrm{Nu}}/\overline{\mathrm{Ra}}^n$, using the Nu values presented in Figure 5.15 and Ra calculated for each data point using Equation (6.8). Average values of B for each ice type are presented in Table 6.4.

The second subplot in Figure 6.11 shows the predictive capacity of Equation (2.40) with the average B values. We see that despite uncertainties in Ra the coefficient B provides tuning of the model to the experimental results. The scatter observed shows the variability in B among ice blocks of same type.

Focusing on the use of Ra to predict heat flow to submerged freshwater ice, a data to theory comparison is shown in Figure 6.12. The theoretical values are for the simple case of a horizontal heated cylinder submerged in freshwater (***Incropera et al.***, 2006). Theory 1 is the general Equation (2.42). Theory 2 is $\mathrm{Nu} = B(\mathrm{Ra})^n$, where $B_l = 0.480$ and $n_l = 1/4$ for laminar and $B_t = 0.125$ and $n_t = 1/3$ for turbulent with $Ra_c = 10^7$. The data fit uses $B_l = 0.335$ and $n_l = 1/4$ for laminar and $B_t = 0.009$ and $n_t = 2/5$ for turbulent (as presented in Table 6.4) with $Ra_c \approx 10^{10}$. The data shows, a) reduced,

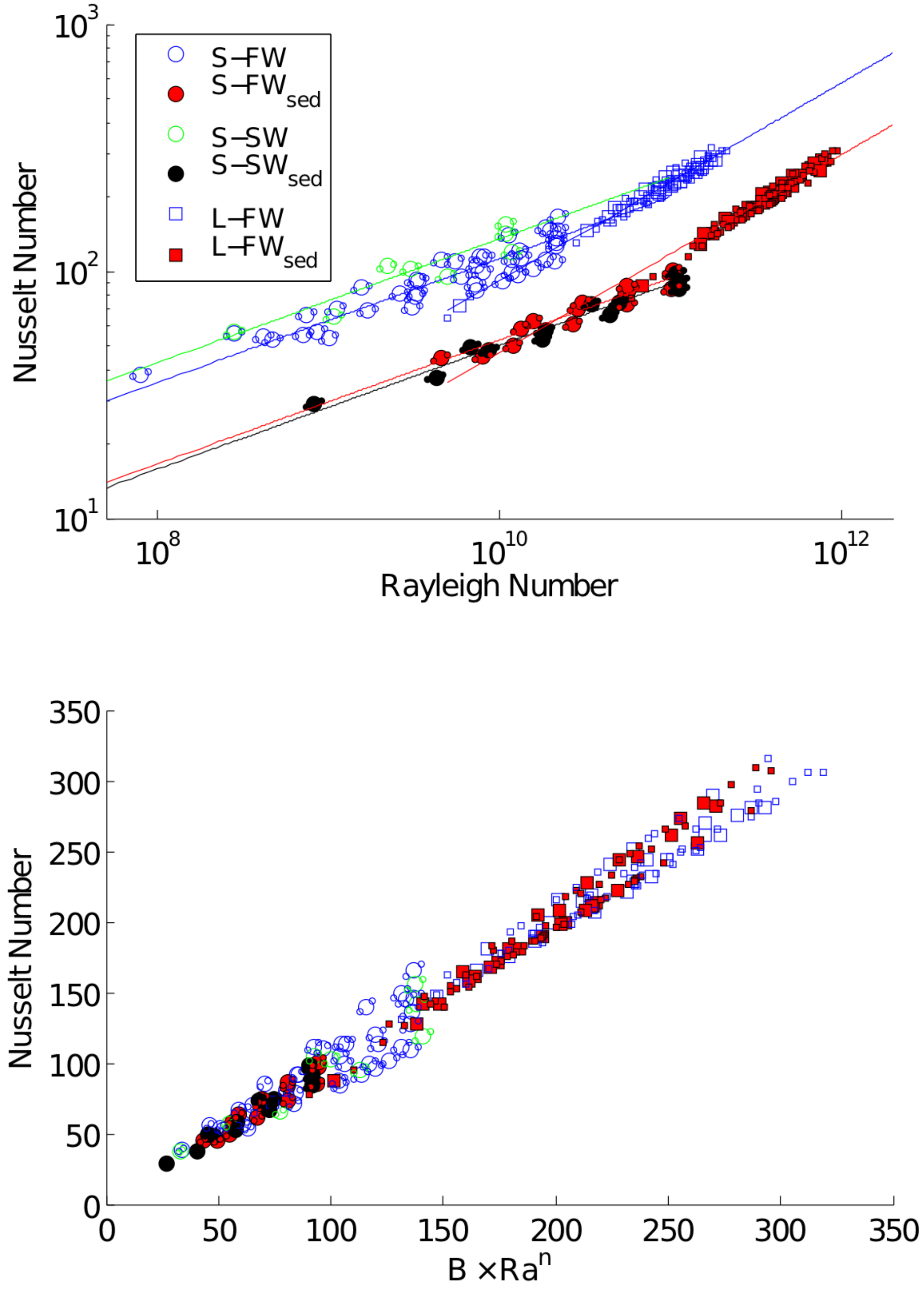

Figure 6.11: Nusselt number vs Rayleigh number. Plotted for the following ice types, small sediment-free freshwater (S-FW), small sediment-free saltwater (S-SW), small sediment-laden freshwater (S-FW$_{sed}$), small sediment-laden saltwater (S-SW$_{sed}$), large sediment-free freshwater (L-FW), and large sediment-laden freshwater (L-FW$_{sed}$).

but reasonable heat flow compared to theory for a much simpler convective flow, and b) an increase in $\mathrm{Ra}_{\mathrm{crit}}$ for the transition from laminar to turbulent flow. The reduced heat flow is likely related to opposing salinity and temperature buoyancy effects. This dual flow system may not be properly captured by Gr $(\mathrm{Ra} = \mathrm{GrPr})$, which predicts convection based on the difference between the wall and far-field density, which is appropriate for a single boundary layer.

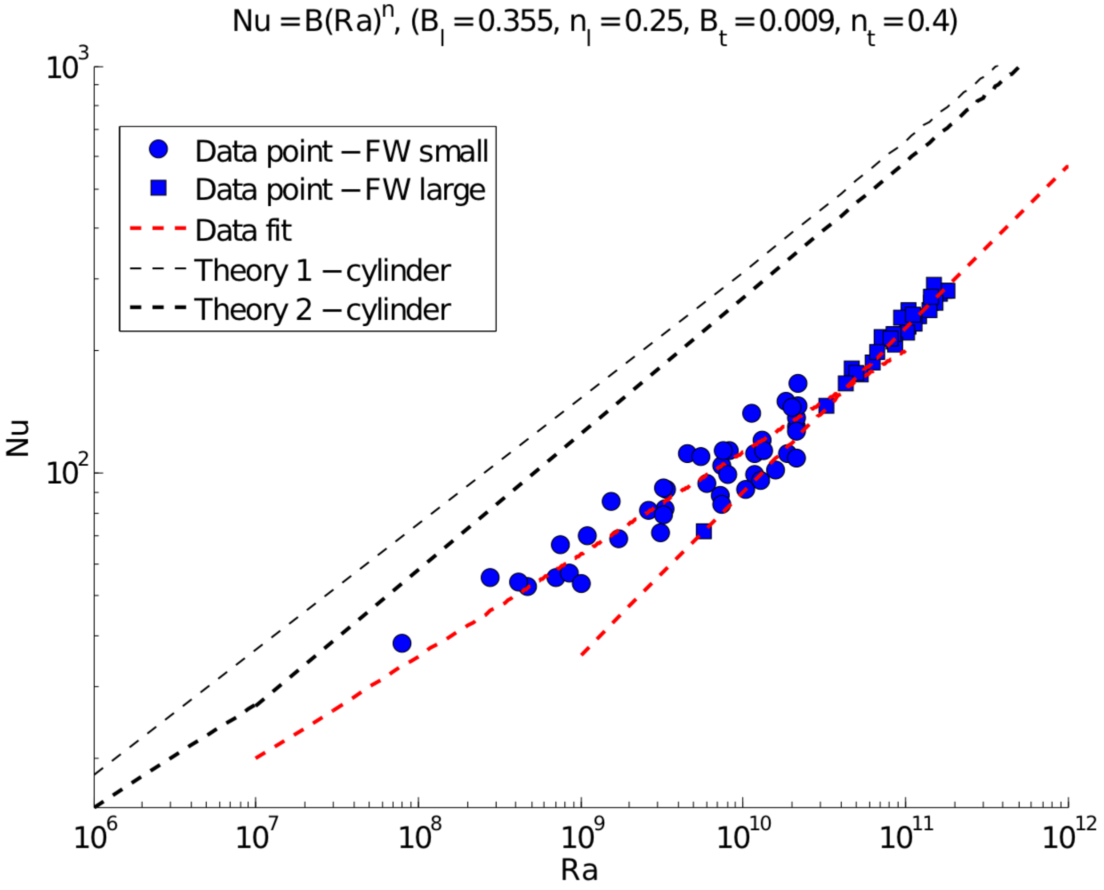

Figure 6.12: Data and theory comparison for Nu as a function of Ra. Plotted for small sediment-free freshwater ice and large sediment-laden freshwater ice. The theoretical values are for the simple case of a horizontal heated cylinder submerged in freshwater. Theory 1 is the general Equation (2.42). Theory 2 is $\mathrm{Nu} = B(\mathrm{Ra})^n$, where $B_l = 0.480$ and $n_l = 1/4$ for laminar and $B_t = 0.125$ and $n_t = 1/3$ for turbulent with $Ra_c = 10^7$. The data fit uses $B_l = 0.335$ and $n_l = 1/4$ for laminar and $B_t = 0.009$ and $n_t = 2/5$ for turbulent with $Ra_c \approx 10^{10}$

6.5 Melt rate predictions

This section outlines the equations and parameters used to predict the melt rate of submerged ice. The melt rate is validated and used to predict lifetimes of large submerged ice blocks. Equations and symbol definitions are repeated from previous sections for the benefit of the reader.

As outlined below, a numerical approach is used here to allow predictions over a range of heat transfer conditions. However, in principle melt-rate predictions could also be made using $m^{\zeta} = m_0^{\zeta} + \alpha t$ (Equation (3.17)) with the appropriate value of ζ for the laminar or turbulent case, and a suitable choice for α. The value of α depends on the parameters governing the heat transfer, including the far-field temperature, as is clear from the values listed in Tables 5.1 and 5.2.

For the numerically-computed predictions, the melt rate (dm/dt) [kg s^{-1}] of submerged ice due to free (or natural) convection is governed by Equation (3.8)

$$\frac{dm}{dt} = \mathrm{Nu}\frac{k\Delta TA}{FL} = \frac{Q}{F} \tag{6.10}$$

where Q is the rate of heat transfer to the ice block [W], F is the latent heat of fusion [J kg^{-1}], Nu is the Nusselt number [dimensionless] ($Nu = hL/k$), k is the thermal conductivity [W m^{-1} °C^{-1}] of sea water at the wall temperature (T_w) [°C] and salinity (S_w) [psu], $\Delta T = T_w - T_\infty$ [°C] using $T_w = T_{fp}(1 - \tanh(0.15T_d))$ from *Josberger and Martin* (1981), A is surface area [m^2], and L is the characteristic length of the boundary surface (length scale) [m]. Nu, F, ΔT, k, A, and L require knowledge of the far-field sea water temperature (T_∞) and salinity (S_∞), characteristic ice salinity (S_i) and sediment concentration (C_i), a shape assumption, and the length scale over which free convection occurs.

The thermal conductivity (k) [W m^{-1} °C^{-1}] of sea water was calculated using Equation (5.5),

$$k = 0.5715(1 + 0.003T - 1.025 \times 10^{-5}T^2 + 6.53 \times 10^{-3}P - 0.00029S) \tag{6.11}$$

from *Sharqawya et al.* (2010) where T is sea water temperature [°C], S is sea water salinity [psu], and P is pressure [MPa] and one standard atmosphere was used ($P = 0.1013$ MPa).

The latent heat of fusion is calculated as a function of ice block temperature T_i [°C], salinity S_i [ppt], and sediment concentration (C_i) [m_s/m_T] using Equation (5.6),

$$F_{sci}(C_i, T_i, S_i) = (1 - C_i)(333.40 - 2.113T_i - 0.114S_i + 18.04(\frac{S_i}{T_i})) \tag{6.12}$$

where an ice temperature of $T_i = -2$ °C was assumed to avoid the tendency of Equation (2.32) to approach $-\infty$ as $T_i \to 0$ for $S_i > 0$ and requiring conversion from J g^{-1} to J kg^{-1} for use in all melt rate equations, including (6.10).

Equation (6.10) shows that the effect of sediment inclusion on melt rate must be related to a change in heat supply (Q) or heat requirement (F) to melt a unit mass of sediment-laden ice. Equation (6.12) shows that under constant rate of heating we expect the relationship $dm/dt \propto C_i$ due to a decreased heat requirement to melt a unit mass of sediment-laden ice.

Two methods for calculating Nu, and thus $Q = \mathrm{Nu}k\Delta TAL^{-1}$, have been presented; first, directly from melt data as $\mathrm{Nu} = \mathrm{Nu}_0 + \omega L$, and secondly as $\mathrm{Nu} = B(\mathrm{Ra})^n$. Both methods are supported by strong correlation between data and theory. However, the first is presently preferred due to uncertainties in the Rayleigh number related to cohesion of sediment, the density of the turbidity current, and the effect of sediment concentration on fluid viscosity. The coefficient B effectively tunes the Ra assessment to the data set without full understanding of a complex hydrodynamic system. Further investigation of the Rayleigh number is merited, with $\mathrm{Nu} = B(\mathrm{Ra})^n$ being a more flexible approach, with the ability to predict Nu and account for the effect of far field concentration on ρ_∞ and variations in S_∞.

Applying a cylindrical shape assumption with $L = b_1 r$, surface area becomes $A = b_2\pi r^2$, where $b_2 = 1 + b_1$. Assuming $L = 2r$ gives $A = 6\pi r^2$ and allows $L = 2r$ independent of cylinder orientation. Equation (6.10) then reduces to,

$$\frac{dm}{dt} = \mathrm{Nu}\frac{3\pi rk\Delta T}{F} \quad (cylinder\ with\ L = 2r) \tag{6.13}$$

or alternatively, for a sphere

$$\frac{dm}{dt} = \mathrm{Nu}\frac{2\pi rk\Delta T}{F} \quad (sphere) \tag{6.14}$$

with some uncertainty of the applicability of our constants from cylindrical melt data.

Equation (6.13) is plotted on Figure 6.13 for $T_\infty = 5$ °C. Nu was calculated as $\mathrm{Nu} = \mathrm{Nu}_0 + \omega L$ using the values presented in Table 5.3. The dashed lines were plotted using $\mathrm{Nu} = -46.3 + 580.1L$ (valid for $L > 0.3$ m) for all ice types. Following the inversion connected to the reduction in sediment cohesion at length scales greater than 0.3 m, the dashed lines provide a good approximation to the ice-type specific values of Nu_0 and ω from Table 5.3, indicating that the majority of the ice salinity and sediment concentration effect on melt rate is accounted for by the decrease in heat requirement (F). This indicates the model may perform well for a range of S_i and C_i.

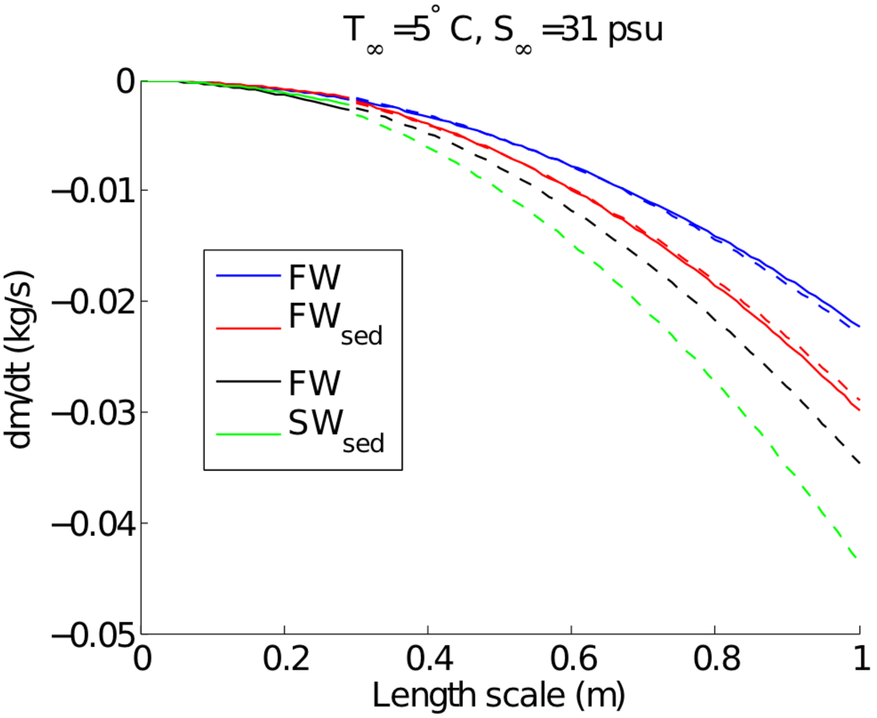

Figure 6.13: Melt rate dm/dt for $T_\infty = 5$ °C and $S_\infty = 31$ psu, plotted for the following ice types, sediment-free freshwater (FW), sediment-free saltwater (SW), sediment-laden freshwater ($\mathrm{FW_{sed}}$), and sediment-laden saltwater ($\mathrm{SW_{sed}}$). Solid lines plotted using ice type specific values for Nu_0 and ω from Table 5.3. Dashed lines plotted using $\mathrm{Nu} = -46.3 + 580.1L$ for all ice types for $L > 0.3$ m.

Equation (6.13) was used to simulate the large block melts conducted for this work using the general form of Nu for $L > 0.3$ m, and $m_j = m_{j-1} + \Delta t \, dm/dt_{j-1}$. $\Delta t = 5$ s was used to produce smooth lines in Figure 6.14, however the model performed well for $\Delta t = 15$ min over the 5 to 20 hr melt duration. As shown in Figure 6.14 the model is well within the objective of first order accuracy at this length scale.

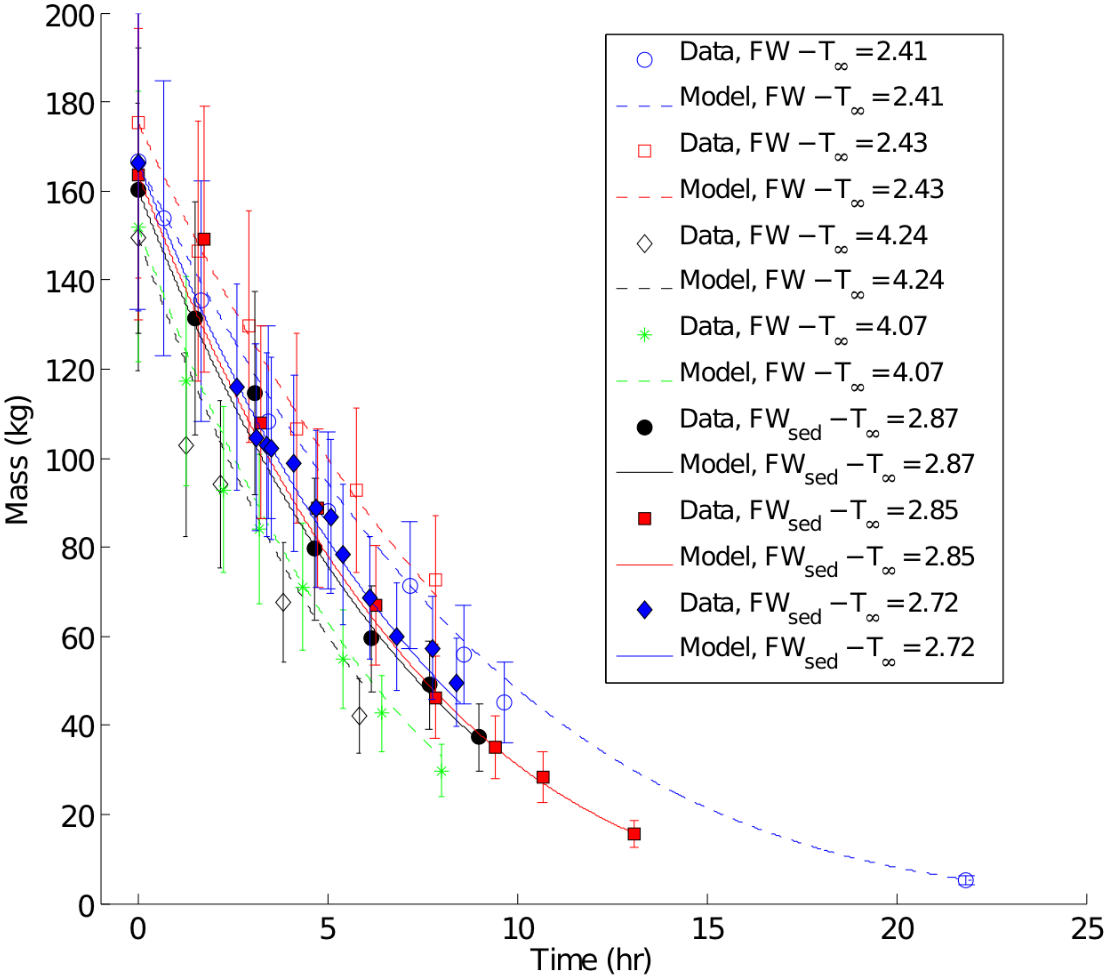

Figure 6.14: Melt rate model and data comparison for sediment-laden and sediment-free freshwater ice. Data points marked by symbols and model predictions by lines. Solid lines and filled marks used for sediment-laden ice, dashed lines and unfilled marks for sediment-free ice.

The effect of the reduction in heat flow due to sediment-inclusion near $L = 0.3$ m is shown in Figure 6.15, resulting in crossing points in the melt of sediment-laden and sediment-fee ice. The location and presence of crossing points is dependent on initial mass, and exist up to approximately $m_0 = 200$ kg.

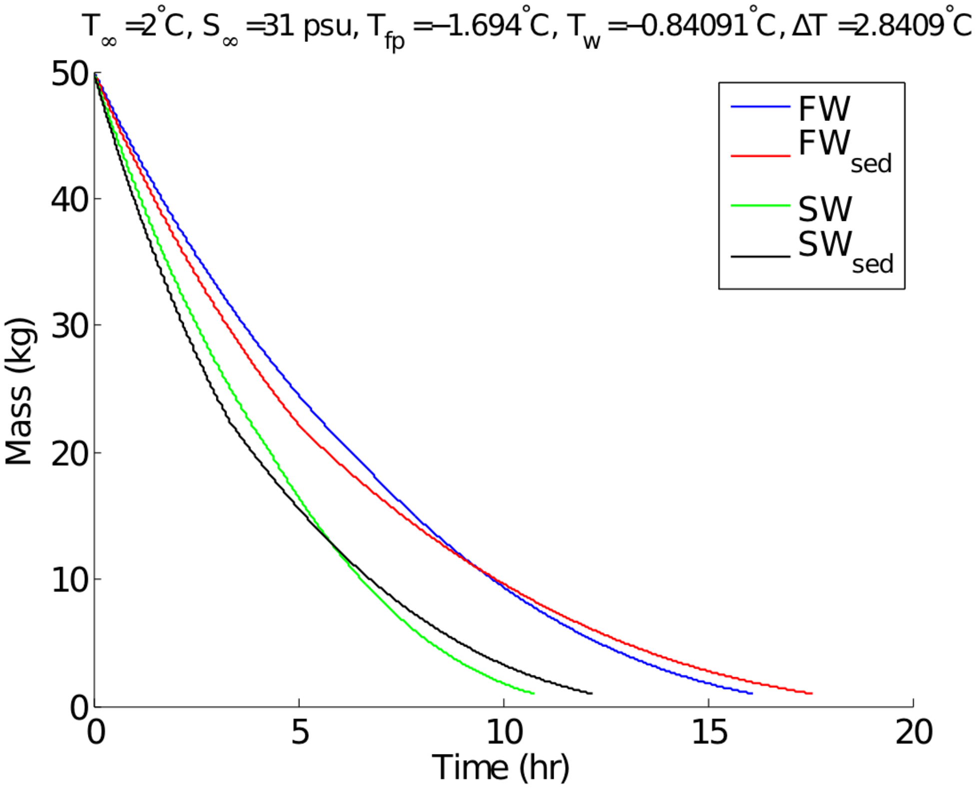

Figure 6.15: Melt prediction for an ice block with an initial mass (m_0) of 50 kg, showing the effect of sediment inclusion at small length scales. Plotted for $T_\infty = 2$°C, $S_\infty = 31$ psu, and the following ice types, sediment-free freshwater (FW), sediment-free saltwater (SW), sediment-laden freshwater ($\mathrm{FW}_{\mathrm{sed}}$), and sediment-laden saltwater ($\mathrm{SW}_{\mathrm{sed}}$)

T_∞ (°C)	FW (hrs)	FW_{sed} (hrs)	SW (hrs)	SW_{sed} (hrs)
-1	494	452	335	306
0	201	184	137	124
1	125	114	85	77
2	90	82	61	56
4	56	52	38	35

Table 6.5: Predicted lifetimes for freshwater sediment-free (FW), freshwater sediment-laden ($\mathrm{FW}_{\mathrm{sed}}$), saltwater sediment-free (SW), and saltwater sediment-laden ($\mathrm{SW}_{\mathrm{sed}}$) ice blocks with initial mass (m_0) of 5000 kg and final mass of 1 kg

Drinkwater et al. (1992), *Envirosphere* (2012), and *Sanderson et al.* (2012) suggest a temperature range of approximately $-2°\mathrm{C} \leq T_\infty \leq 2°\mathrm{C}$ for seawater in the Minas Basin and estuaries of the Inner Bay of Fundy in February and March. The effect of far-field temperature on melt rate is shown for melt predictions of ice blocks with cylindrical shape and an initial mass (m_0) of 5 000 kg in Figures 6.16 through 6.19 for far-field temperatures of $T_\infty = -1$, 0, 1, 2, and 4 °C. Predicted lifetimes to reduce the 5 000 kg ice blocks to a final mass of 1 kg are summarized in Table 6.5.

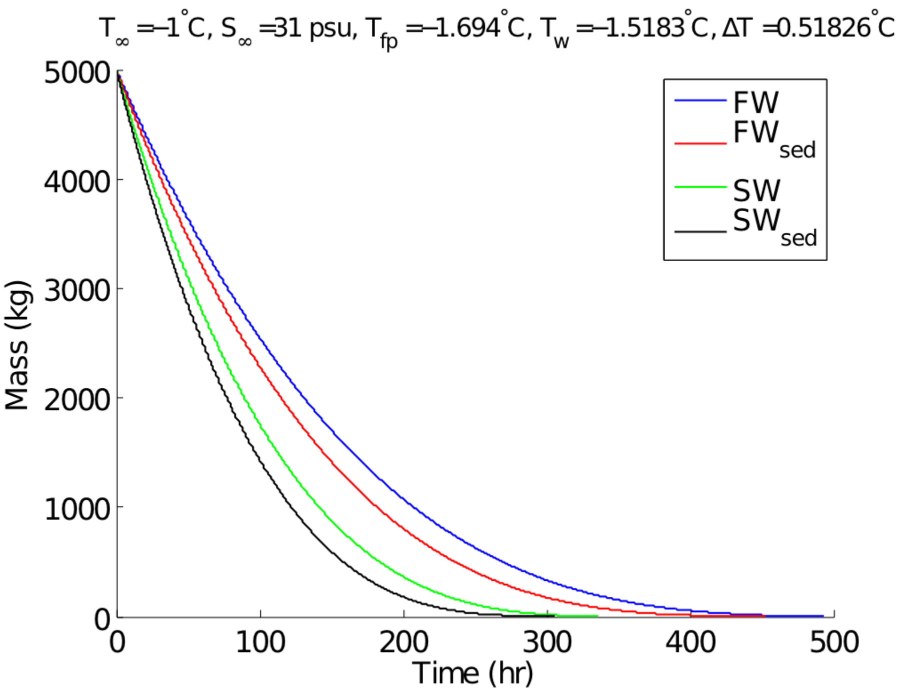

Figure 6.16: Melt predictions for ice blocks with initial mass (m_0) of 5000 kg for $T_\infty = -1°\text{C}$

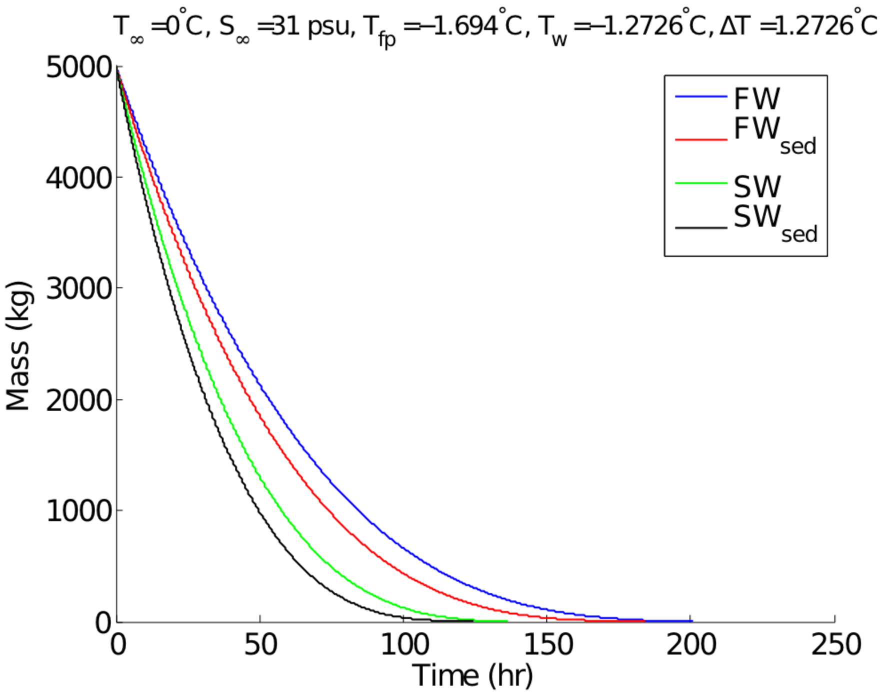

Figure 6.17: Melt predictions for ice blocks with initial mass (m_0) of 5000 kg for $T_\infty = 0°\text{C}$

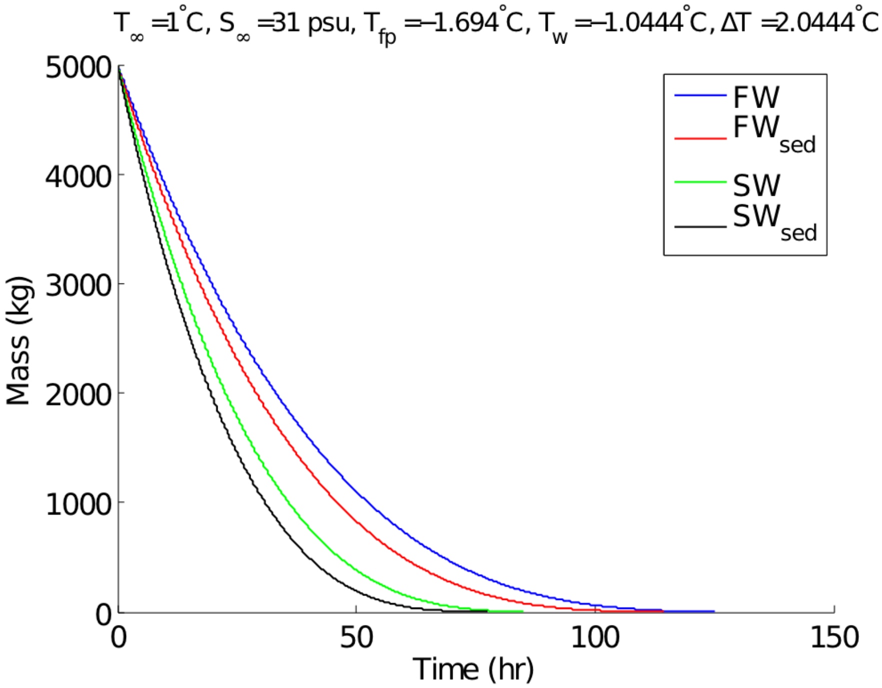

Figure 6.18: Melt predictions for ice blocks with initial mass (m_0) of 5000 kg for $T_\infty = 1°\text{C}$

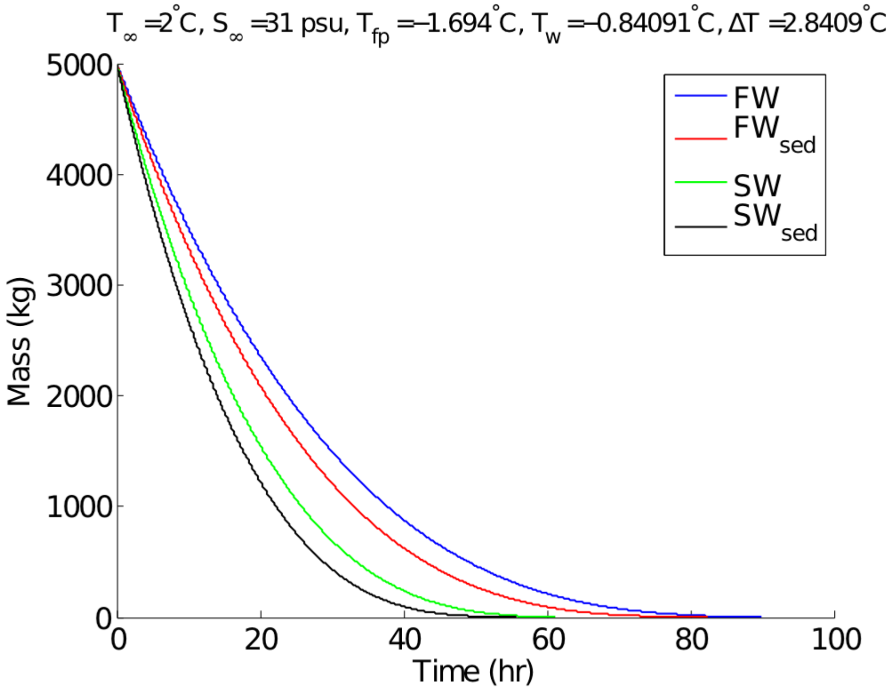

Figure 6.19: Melt predictions for ice blocks with initial mass (m_0) of 5000 kg for $T_\infty = 2°\text{C}$

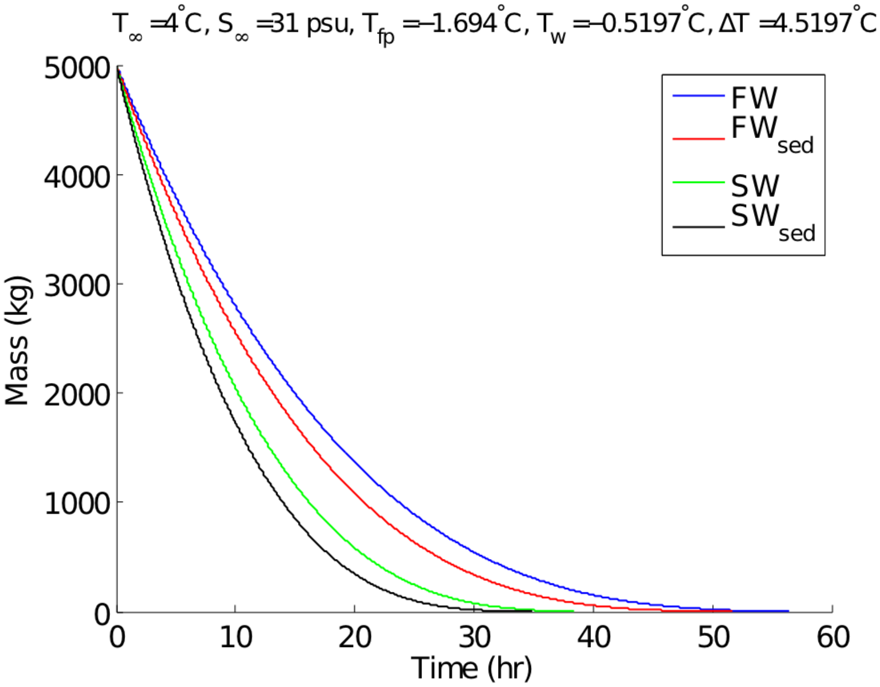

Figure 6.20: Melt predictions for ice blocks with initial mass (m_0) of 5000 kg for $T_\infty = 4°\text{C}$

The predicted half-lives (times for 50% melt) for ice blocks with cylindrical shape and an initial mass over the range of $500 \le m_0 \le 10000$ kg are shown in Figure 6.21 for $T_\infty = 1°\text{C}$. The predicted times to melt to a final mass of 1 kg are shown in Figure 6.22 for the same T_∞ and range of m_0 used for Figure 6.21. The solid lines were plotted using the ice type specific values for Nu_0 and ω from Table 5.3 for all length scales. The dashed lines were plotted using $\text{Nu} = -46.3 + 580.1L$ for all ice types for $L > 0.3$ m and ice type specific values for $L \le 0.3$ m. The tight grouping of predicted lifetimes shown by the solid and dashed lines suggests that for length scales (and flow conditions) sufficient to avoid complications due to cohesion of sediment to the ice surface, the most significant effect of sediment inclusion on melt rate is a reduction in the heat requirement to melt a unit mass of sediment-laden ice.

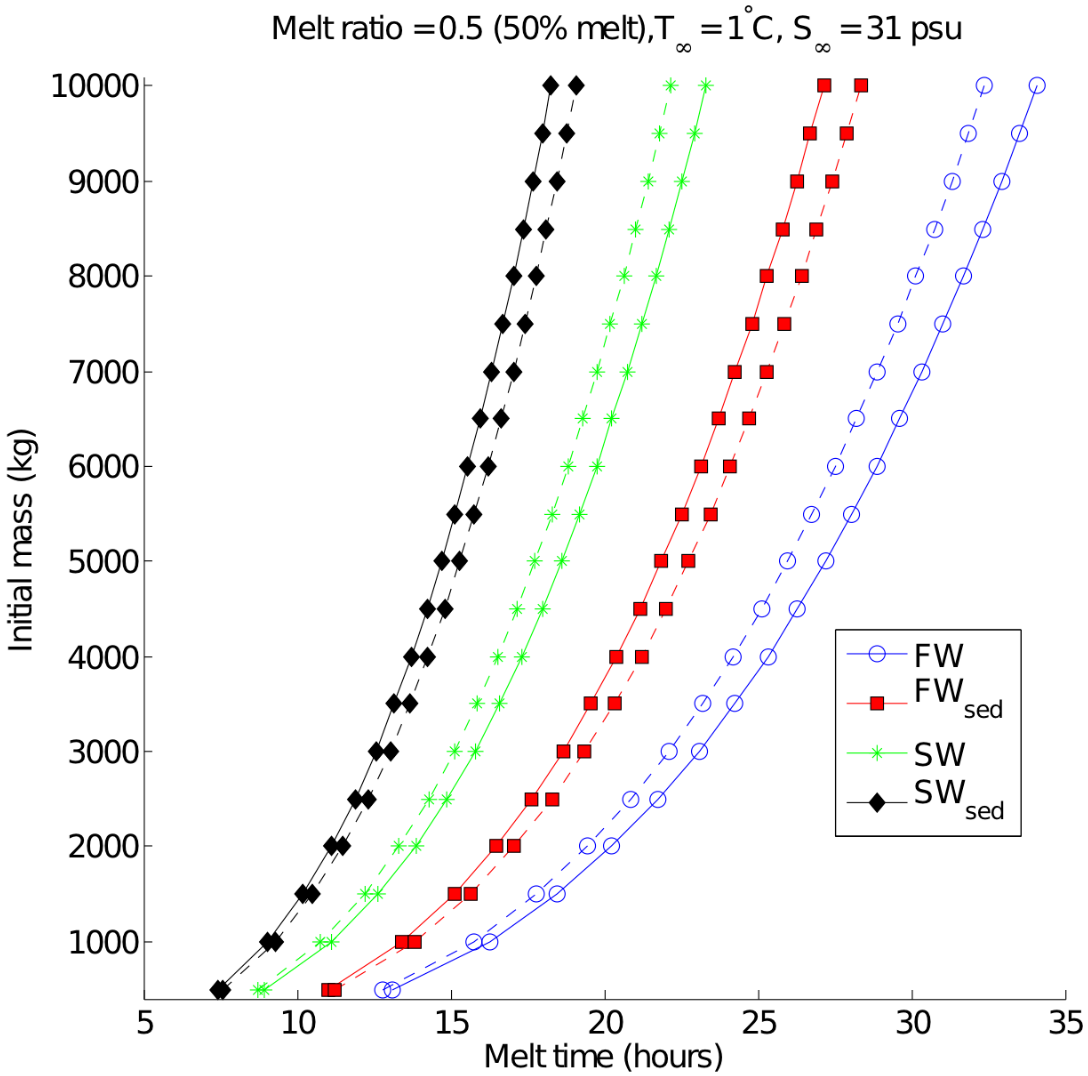

Figure 6.21: Half-life melt predictions for freshwater sediment-free (FW), freshwater sediment-laden ($\mathrm{FW_{sed}}$), saltwater sediment-free (SW), and saltwater sediment-laden ($\mathrm{SW_{sed}}$) ice blocks with initial mass (m_0) of $500 \leq m_0 \leq 10000$ kg for $T_\infty = 1$°C. Solid lines plotted using ice type specific values for Nu_0 and ω from Table 5.3. Dashed lines plotted using $\mathrm{Nu} = -46.3 + 580.1L$ for all ice types for $L > 0.3$ m.

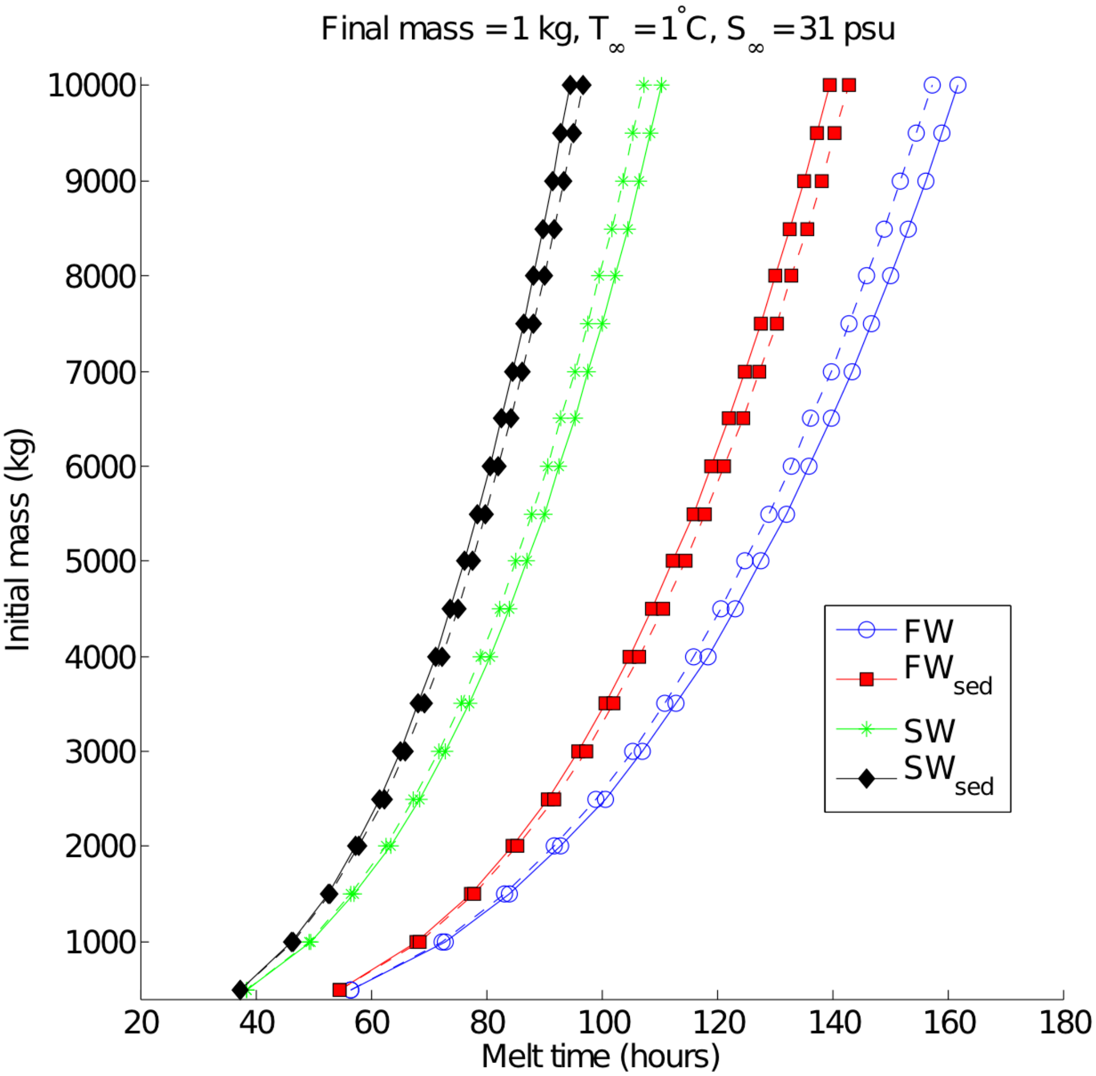

Figure 6.22: Melt predictions for freshwater sediment-free (FW), freshwater sediment-laden ($\mathrm{FW_{sed}}$), saltwater sediment-free (SW), and saltwater sediment-laden ($\mathrm{SW_{sed}}$) ice blocks with initial mass (m_0) of $500 \leq m_0 \leq 10000$ kg to be reduced to 1 kg for $T_\infty = 1$°C. Solid lines plotted using ice type specific values for Nu_0 and ω from Table 5.3. Dashed lines plotted using $\mathrm{Nu} = -46.3 + 580.1L$ for all ice types for $L > 0.3$ m.

CHAPTER 7

CONCLUSIONS

A first-order accurate melt rate model for sediment-laden ice in seawater has been developed. Submerged sediment-laden ice is not subjected to wind forcing or wave erosion. Ice blocks of approximate neutral buoyancy are assumed to travel with the mean fluid flow and buoyancy-induced free convection shall be the dominant deterioration mechanism. Previous studies of ice deterioration have been built upon, with a focus on determining the effect of fine-grained sediment inclusions on free convective melting of ice in seawater.

From the melt rate equation $dm/dt = Q/F$ (Equation (1.1)), the effect of sediment inclusion on melt rate must be related to a change in heat supply (Q) or heat requirement (F) to melt a unit mass of sediment-laden ice, where Q is affected by the strength of the convective current and F by the ice block sediment content, salinity, and temperature.

Melt experiments were conducted with submerged freshwater, sediment-laden freshwater, saltwater, and sediment-laden saltwater ice blocks over different length scales and far-field temperatures to evaluate the effects of sediment on melt rate. The experiments produced interesting results. For small length scales ($<\approx$ 0.3 m) the presence of sediment decreased melt rate, and at larger length scales melt rate increased with sediment concentration.

7.1 Heat Requirement (F)

The thermodynamic properties of sea ice are considerably more complex than those of fresh water ice, and even more so when accounting for the presence of sediment. *Pounder* (1965) suggests that,“in fact a definite latent heat of fusion for sea ice must be abandoned since the phase change from solid to liquid is a continuous process.”

Combined with the effects of salinity, the heat capacity of sediment-laden sea ice becomes the total amount of heat required to raise the temperature of ice, brine, and sediment by one unit of temperature, plus the heat associated with the phase change as the brine becomes less saline by melting pure ice at the brine-ice interfaces.

No phase change occurs for sediment over the range of temperatures where ice melts in natural conditions. Solid sediment is incorporated in the ice crystal lattice during formation, then released from the ice block upon melting provided gravitational and frictional forces exceed sediment cohesion. There is then no change in enthalpy related to the presence of sediment upon ice melting, and the latent heat of fusion is considered as the energy required to reduce sediment-laden ice (with brine, sediment, and air inclusions) by one unit mass.

Using basic dimensional analysis and algebraic relationships, the latent heat of fusion for sediment-laden ice is shown to be $F_{si} = (1 - C_i)F_i$ (Equation (2.29)). Combined with the results of previous works this expands to $F_{sci}(C_i, T_i, S_i) = (1 - C_i)(333.40 - 2.113T_i - 0.114S_i + 18.04(S_i/T_i))$ (Equation (5.6)) as a function of ice sediment concentration, temperature, and salinity.

Accounting for the effect of sediment concentration on the latent heat of fusion, melt rate is then (restated from Equation (2.31)),

$$\frac{dm}{dt} = \frac{Q}{(1 - C_i)F_i} \tag{7.1}$$

which shows that under constant rate of heating and $C_i << 1$ we expect the relationship $dm/dt \propto C_i$ due to a decreased heat requirement to melt a unit mass of sediment-laden ice.

7.2 Heat Supply (Q)

The rate of heat transfer by free convection is $Q = \mathrm{Nu} k \Delta T A L^{-1}$ (Equation (3.3)), and two methods for calculating Nu have been presented. First, directly from melt data using Equation (5.4), and secondly as $\mathrm{Nu} = B(\mathrm{Ra})^n$ noting that B must be determined based on experimental results. Both methods are supported by strong correlation between data and theory. However, the first is presently preferred due to uncertainties in the Rayleigh number related to cohesion of sediment, the density of the turbidity current, and the effect of sediment concentration on fluid viscosity. The coefficient B effectively tunes the Ra assessment to the data set without full understanding of a complex hydrodynamic system. Further investigation of the Rayleigh number is merited, with $\mathrm{Nu} = B(\mathrm{Ra})^n$ being a more flexible approach, providing the ability to predict Nu and account for the effect of far-field sediment concentration on ρ_∞ and variations in S_∞.

For the Nusselt number calculated from ice melt data, Nu was plotted against length scale and the best fit lines $\mathrm{Nu} = \mathrm{Nu}_0 + \omega L$ (where Nu_0 is the $L = 0$ intercept) were calculated. Nu shows a significant reduction in convective heat transfer associated with sediment inclusion at small length scales. However, convective heat transfer increases to approach and potentially exceed that of sediment free ice near $L = 0.5$ m. The decrease in melt rate at small length scales is likely due to cohesion, creating a sediment coating between the convective heat flow and the ice surface with insulating properties, and reducing the sediment concentration of the turbidity current entering the fluid flow. Both effects decrease the rate of heat supply to the ice surface.

Focusing on $L > 0.3$ m, for sediment-free ice $\mathrm{Nu}_0^{\mathrm{i}} = -26.3$ and $\omega_i = 543.0$ (with a best-fit of $\gamma^2 = 0.036$), sediment-laden ice $\mathrm{Nu}_0^{\mathrm{si}} = -63.4$ and $\omega_{si} = 613.2$ ($\gamma^2 = 0.025$), and for both data sets $\mathrm{Nu}_0 = -46.3$ and $\omega = 580.1$ ($\gamma^2 = 0.036$). Accurate representation of both data sets by a single equation for $\mathrm{Nu}(L)$ indicates approximately equal heat flow to the large sediment-free and sediment-laden ice blocks at the sediment concentration required for neutral buoyancy of sediment-laden ice in seawater. Note that the presence of a negative $L = 0$ intercept for the large block data necessitates treatment of large and small length scales to account for: a) laminar and turbulent flow conditions, and b) other complicating factors discussed above. A positive intercept and reduced values of ω were observed for the small-block melts.

7.3 Melt Rate (dm/dt)

For length scales $0.3 < L < 1$ m, the melt rate equation (restated from Equation (3.8))

$$\frac{dm}{dt} = \mathrm{Nu}\frac{k\Delta T A}{FL} = \frac{Q}{F} \tag{7.2}$$

has been shown to provide an excellent fit to experiment data for sediment-laden and sediment-free ice.

The use of $\mathrm{Nu} = -46.3 + 580.1L$ for sediment-laden and sediment-free ice blocks suggests that for the case of neutrally buoyant sediment-laden ice with length scales sufficient to avoid complications due to cohesion of sediment to the ice surface, the most significant effect of sediment inclusion on melt rate is a reduction in the heat requirement to melt a unit mass of sediment-laden ice.

The model has been used to predict lifetimes of large submerged ice blocks using far-field temperatures representative of seawater in the Minas Basin in February and March. Predicted lifetimes for freshwater sediment-laden ice with initial mass of 5 000 kg decrease from approximately 450 to 55 hours as far-field temperatures increase from -1°C to 4°C. Similarly, predicted lifetimes for saltwater sediment-laden ice decrease from 300 to 35 hours over the same temperature range.

This initial model neglects wallowing and overturning which will likely occur under natural conditions as a result of shear forces generated from small scale eddies and ambient turbulence in the tidal flow. Consequently, the predicted lifetimes represent the probable upper limits to actual lifetimes under field conditions. These lifetimes, when incorporated into existing numerical models of the tidal flow, will yield a probable range of trajectories. Combined with initial conditions and ice strength characteristics this would form the basis for assessing the risk of damage to tidal turbines deployed near regions where sediment-laden ice forms.

7.4 Future Work

This initial model predicts the probable upper limits to actual lifetimes of submerged sediment-laden ice in high energy tidal environments such as the Bay of Fundy and Cook Inlet. The major deterioration mechanism has been considered to be melting due to natural convection. Under natural conditions additional losses will result from turbulence, wallowing, overturning (resulting in mixed or forced convection) and calving.

Moving beyond this initial model, field studies may determine if additional deterioration mechanisms are significant in comparison to the magnitude of the free convective current. Further work may consider the Reynolds number (Re) for calculating $\mathrm{Nu} = B\mathrm{Re}^m\mathrm{Pr}^n$ as mixed, or forced convection. With F_{sci} accounting for the effect of sediment concentration on heat requirement, future work could focus on determining a relative fluid to ice velocity.

Additional recommendations include:

- For the case of the large ice blocks the observation that $\mathrm{Nu_i} \approx \mathrm{Nu_{si}}$ for C_i to produce neutral buoyancy is interesting. This indicates a balancing of convective currents associated with predominantly upward freshwater driven flow from sediment-free ice and the downward turbidity current from sediment-laden ice. Building upon the flow field analysis of *Josberger and Martin* (1981) by conducting additional melt experiments over a range of C_i, T_∞, and S_∞ would be complicated but scientifically interesting. Potential exists for $\mathrm{Nu_{si}} < \mathrm{Nu_i}$ at low C_i, $\mathrm{Nu_{si}} > \mathrm{Nu_i}$ at high C_i, and also $\mathrm{Nu} \approx 2$ at some value of C_i. Recalling that $\mathrm{Nu} = 2$ is the value for pure conduction in a stationary infinite fluid, this minimum value may occur due to flow stagnation where the sediment-laden melt plume would be of near neutral buoyancy with the surrounding seawater resulting in minimum heat transfer. However, sediment-laden ice with C_i less than or greater than the concentration required to produce neutrally buoyant ice (C_i used for this thesis) would require forceful submergence or suspension, respectively. It follows that such concentrations may not be of significant interest for risk analysis of potential collisions between sediment-laden ice and tidal turbines. Floating ice would be subjected to additional deterioration mechanisms as listed by *Job* (1978) and high density ice would interact with the sea bed.

- The data suggest $\mathrm{Nu_i} \approx \mathrm{Nu_{si}}$ over the length scales tested. However, the plot of Nu in Figure 5.15 shows $L \approx 0.5$ m as a potential crossing point of $\mathrm{Nu_{si}}$ and $\mathrm{Nu_i}$. A continued positive increase of $\Delta\mathrm{Nu} = \mathrm{Nu_{si}} - \mathrm{Nu_i}$ may be present, indicating increased heat flow to large sediment laden ice blocks. This warrants investigation by melting larger ice blocks.

- Viscosity as a function of sediment concentration should be measured. With $\nu(C, S, T)$ this leaves the concentration of the turbidity current released from the ice block ($C_f = \lambda C_i$) as the unknown in Gr, which may be a concern only at small length scales and low energy tidal flows. Calculation of Gr allows prediction of the Nusselt number as $\mathrm{Nu} = B(\mathrm{Ra})^n$.

- Ice mass should be measured from tension in the anchor line with a dynamometer. By comparing weight in air to weight in fluid at beginning, end, and mid-points throughout the melt we gain information on the ice density structure. This would be interesting for ice blocks brought back from the field.

- Melts of laboratory prepared ice blocks should be conducted with a thermistor chain frozen through a section of the ice block to accurately record T_w and the temperature gradient through the ice block. This measurement may verify use of $\overline{T_w} = T_{fp}(1.0 - \tanh(0.15T_d))$ (Equation (5.7)) for predicting T_w.
- The effect of air inclusions on melt rate should be investigated.
- Similar to work conducted for other off-shore industries, charts should be generated showing probabilities of encountering submerged sediment-laden ice in regions surrounding the upper estuary source areas. Field studies should be conducted to determine size distributions at sediment-laden ice source locations, density distributions, and mechanisms for sediment-laden ice formation and release. In order to make decisions regarding the risk of damage to submerged structures an engineering study is required to quantify sediment-laden ice strength characteristics. In combination with mass and velocity distributions we may then calculate a range of probable point load forces. From this, engineers may design devices capable of withstanding impacts with ice blocks less than a given design criteria, and/or implement mitigative measures to prevent impacts, if necessary.
- Acoustic detection should be evaluated as a potential means for identifying sediment-laden ice blocks during site characterization activities at potential tidal turbine berth sites and/or following installation of tidal turbines.

BIBLIOGRAPHY

Batchelor, G., *An Introduction to Fluid Dynamics*, Cambridge University Press, 1967.

Blanchfield, J., C. Garrett, A. Rowe, and P. Wild, Tidal stream power resource assessment for Masset Sound, Haida Gwaii, *Proc. IMECHE*, *222*, 485–492, 2008.

Bouguet, J. Y., Camera calibration toolbox for matlab, *Tech. rep.*, Caltech, 2010.

Burgh, J. V. D., Thermal convection at a melting benzene surface, *Appl. Sci. Res.*, *A9*, 293–296, 1960.

Caldwell, D. R., The effect of pressure on thermal and fickian diffusion of sodium chloride, *Deep Sea Research*, *21*, 369–375, 1974.

CIS, Manice manual of standard procedures for observing and reporting ice conditions, *Tech. rep.*, Environment Canada, 2005.

Cox, G. F. N., and W. F. Weeks, Numerical simulations of the profile properties of undeformed first-year ice during the growth season, *J Geophys Res*, *47*, 12,449–12,460, 1981.

Crawford, A., and A. Hay, A simple system for laser-illuminated video imaging of sediment suspension and bed topography, *IEEE Journal of Oceanic Engineering*, *23*, 12–19, 1998.

Crocker, G., J. English, R. McKenna, and R. Gagnon, Evaluation of bergy bit populations on the grand banks, *Cold Regions Sci. and Tech.*, *38*, 239–250, 2004.

Drinkwater, K. F., P. C. Smith, and R. Pettipas, Spatial and temporal scales of temperature variability in the bay of fundy, *Tech. rep.*, Bedford Institute of Oceanography, Department of Fisheries and Oceans, 1992.

Dumore, J. M., H. J. Merk, and J. A. Prins, Heat transfer from water to ice by thermal convection, *Nature*, *172*, 460–461, 1953.

Eckert, E. R. G., *Heat and Mass Transfer*, McGraw Hill Book Company, Inc, 1959.

Eckert, E. R. G., and T. W. Jackson, Analysis of turbulent free-convection boundary layer on flat plate, *Tech. Rep. Report 1015*, National Advisory Committee for Aeronautics, 1951.

Eicken, H., E. Reimnitz, V. Alexandrov, T. Martin, H. Kassens, and T. Viehoff, Sea-ice processes in the laptev sea and their importance for sediment export, *Cont. Shelf Res.*, *17*, 205–233, 1997.

El-Tahan, M., S. Venkatesh, and H. El-Tahan, Validation and quantitative assessment of the deteriation mechanisims of arctic icebergs, *J. Offshore Mech. and Arctic Eng.*, *109*, 102–108, 1987.

Envirosphere, Environmental Assessment Appendix 6 - Physical Oceanography - Oceanographic Survey, Oceanographic Measurements - Salinity, Temperature and Turbidity, Minas Passage Study Site, August 2008 - March 2009, *Tech. rep.*, AECOM, 2012.

Fofonoff, P., and R. C. Millard, Algorithms for computation of fundamental properties of seawater, *Tech. Rep. 44*, Unesco, 1983.

Gade, H. G., Melting of ice in sea water: A primitive model with application to antarctic ice shelf and icebergs, *J. Phys. Ocea.*, *9*, 189–198, 1979.

Garrett, C., Tidal resonance in the Bay of Fundy and Gulf of Maine, *Nature*, *238*, 444–443, 1972.

Garrett, C., and D. Greenberg, Predicting changes in tidal regime: The open boundary problem, *J. Phys. Ocea.*, *7*, 171181, 1977.

Greisman, P., On upwelling driven by the melt of ice shelves and tidewater glaciers, *Deep Sea Research*, *26A*, 1051–1065, 1979.

Happel, J., and H. Brenner, *Low Reynolds number hydrodynamics*, Noordhoff International Publishing, 1973.

Incropera, F., D. DeWitt, T. Bergman, and A. Lavine, *Introduction to Heat Transfer*, Wiley, 2006.

Job, J. G., Numerical modelling of iceberg towing for water supplies – a case study, *J. Glaciology*, *20*, 533–542, 1978.

Josberger, E. G., A labratory and field study of iceberg deteriation, in *Proceedings of the First International Conference on Iceberg Utilization*, pp. 245–264, 1977.

Josberger, E. G., and S. Martin, A labratory and theoretical study of the boundary layer adjacent to a melting ice wall in salt water, *J. Fluid Mech.*, *111*, 439–473, 1981.

Karsten, R. H., J. M. McMillan, M. J. Lickley, and R. D. Haynes, Assessment of tidal current energy in the minas passage, bay of fundy, *Proc. IMECHE*, *222*, 493–507, 2008.

Kranse, A. A., and J. Schenk, Thermal free convection from a solid sphere, *Appl. Sci. Res.*, *A15*, 397–403, 1965.

Kubat, I., M. Sayed, S. B. Savage, T. Carrieres, and G. Crocker, An operational iceberg deteriation model, in *Proceedings of the Seventh International Offshore and Polar Eng. Conf.*, pp. 652–657, 2007.

Lock, G. S. H., *The Growth and Decay of Ice*, Cambridge University Press, 1990.

Loewe, F., On melting of fresh-water ice in sea-water, *J. Glaciology*, pp. 1051–1052, 1961.

Merk, H. J., The influence of melting and anomalous expansion on the thermal convection in laminar boundary layers, *Appl. Sci. Res.*, *A4*, 435–452, 1954.

Merk, H. J., and J. A. Prins, Thermal convection in laminar boundary layers i, *Appl. Sci. Res.*, *A4*, 11–24, 1954a.

Merk, H. J., and J. A. Prins, Thermal convection in laminar boundary layers ii, *Appl. Sci. Res.*, *A4*, 195–206, 1954b.

Merk, H. J., and J. A. Prins, Thermal convection in laminar boundary layers iii, *Appl. Sci. Res.*, *A4*, 207–221, 1954c.

Nakawo, M., and N. K. Sinha, Growth rate and salinity profile of first-year sea ice in the high arctic, *J Glaciology*, *27(96)*, 315–330, 1981.

Neshyba, S., Upwelling by icebergs, *Nature*, *267*, 507–508, 1977.

Neumann, G., and W. J. Pierson, *Principals of Physical Oceanography*, Prentice Hall, 1966.

NOAA, NOAA tides and currents, FAQ, *http://tidesandcurrents.noaa.gov/faq2.html*, 2011.

OEER, Fundy tidal energy strategic environmental assessment, *Tech. rep.*, Nova Scotia Department of Energy, 2008.

Ono, N., Specific heat and heat of fusion of sea ice, *Physics of Snow and Ice : proceedings Hokkaido University collection of scholarly and academic papers*, pp. 599–610, 1967.

OReilly, C., R. Solvason, and C. Solomon, Where are the worlds largest tides?, *BIO Annual Report 2004 in Review*, pp. 44–46, 2005.

Pounder, E. R., *The Physics of Ice*, Pergamon Press, 1965.

Reimnitz, E., P. Barnes, and W. Weber, Particulate matter in the pack ice of the beaufort gyre, *J Glaciology*, *39*, 186–198, 1993.

Sanders, R., and E. Baddour, Documenting ice in the bay of fundy canada, *Tech. rep.*, Natural Research Council Canada, 2006.

Sanders, R., and E. Baddour, Tidal power and ocean ice in the bay tidal power and ocean ice in the bay of fundy, canada, 1968-2007, in *Proceedings of the 2007 International Conference On Offshore Mechanics and Arctic Engineering*, 2007.

Sanders, R., C. Byers, and E. Baddour, Tidal power and migratory sub-surface ice in the bay of fundy, canada, *Tech. rep.*, Fundy Tidal Energy Tech. Advisory Group and OEER, 2008.

Sanderson, B., A. Redden, and J. Broome, Sedimentladen ice measurements and observations, and implications for potential interactions of ice and large woody debris with tidal turbines in minas passage, *Tech. rep.*, Acadia Centre for Estuarine Research, 2012.

Savage, S. B., G. B. Crocker, M. Sayed, and T. Carrieres, Size distributions of smal ice pieces calved from icebergs, *Cold Regions Sci. and Tech.*, *31*, 163–172, 2000.

Savage, S. B., G. B. Crocker, M. Sayed, and T. Carrieres, Bergy bit and growler melt deteriation, *J. Geo. Phys. Res.*, *106*, 11,493–11,504, 2001.

Schenk, J., and F. A. M. Schenkels, Thermal free convection from an ice sphere in water, *Appl. Sci. Res.*, *19*, 465–476, 1968.

Schlichting, H., *Boundary Layer Theory*, 4 ed., McGraw-Hill, 1960.

Sharqawya, M. H., J. H. L. Va, and S. M. Zubairb, Thermophysical properties of seawater: a review of existing correlations and data, *Desalination and Water Treatment*, pp. 354–380, 2010.

Smedsrud, L. H., Frazil-ice entrainment of sediment: large-tank laboratory experiments, *J Glaciology*, *47*, 461–471, 2001.

Smith, O., Observers guide to sea ice, *Tech. rep.*, NOAA, 2007.

Smith, O., personal correspondence, *email*, 2009.

Smith, O., D. Krause, and N. Mulherin, Distribution of salt and sediment in cook inlet sea ice cores 2/15/99, *Proceedings of Cook Inlet Oceanography Workshop*, p. 95, 1999.

Smith, O., A. Khokhlov, S. Buchanan, and W. Lee, Beach stability measurements and analysis at nikiski, alaska, *Tech. rep.*, University of Alaska Anchorage, School of Engineering, 2003.

Thomas, D. N., and G. S. Dieckmann, *Sea Ice: An Introduction to its Physics, Chemistry, Biology, and Geology*, Blackwell Publishing, 2003.

Tritton, D. J., Transition to turbulence in the free convection boundary layers on an inclined heated plate, *J of Fluid Mech*, *16*, 417–435, 1963.

Trowse, G. C., and R. H. Karsten, Bay of fundy tidal energy development - opportunities and challenges, in *Proceeding of the 3rd International Conference on Ocean Energy*, 2010.

Turner, J. S., *Buoyancy Effects in Fluids*, Cambridge University Press, 1973.

Vanier, C. R., and C. Tien, Letter to the editor (thermal free convection from an ice sphere in water), *Appl. Sci. Res.*, *21*, 387–388, 1969.

Vanier, C. R., and C. Tien, Free convection melting of ice spheres, *AIChE*, *16*, 76–82, 1970.

Weeks, W. F., *On Sea Ice*, University of Alaska Press, 2010.

White, F. M., M. L. Spaulding, and L. Gominho, Theoretical estimates of the various mechanisms involved in iceberg deterioration in the open ocean environment, *Tech. rep.*, Department of Transportation, United States Coast Guard, 1980.

Whitman, W. G., Elimination of salt from seawater ice, *Amer J Sci*, *211*, 126–132, 1926.

APPENDIX A

PHOTOGRAPHS

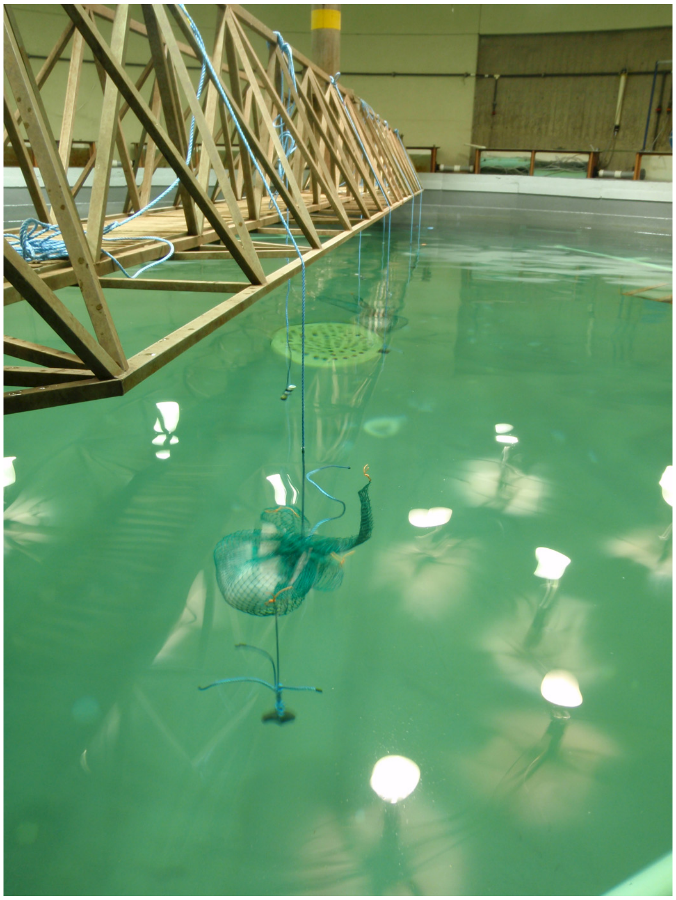

Figure A.1: April 14, 2009 - Aquatron Pool Tank 1

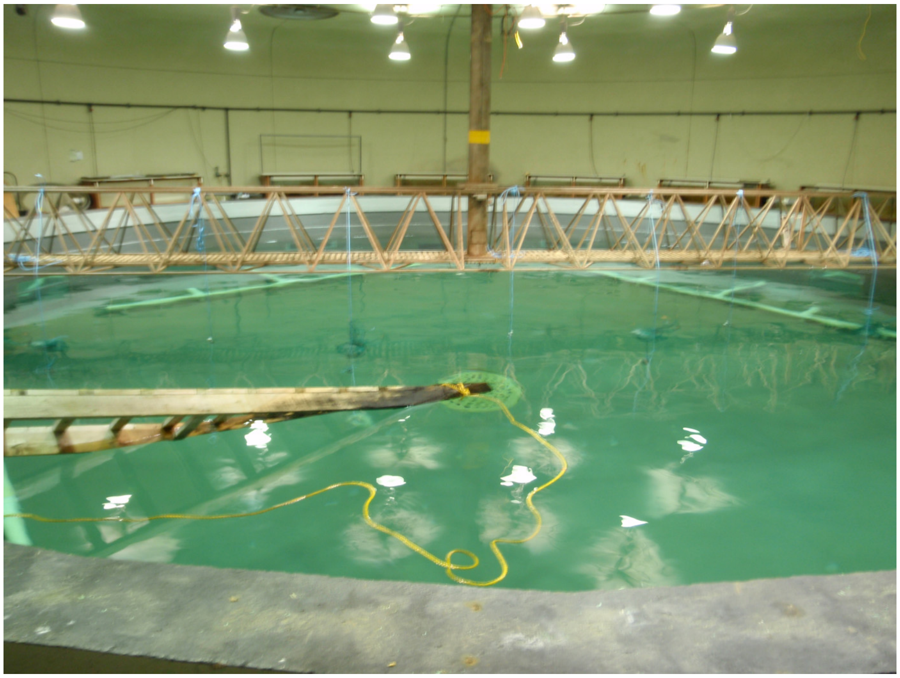

Figure A.2: April 14, 2009 - Aquatron Pool Tank 2

Figure A.3: January 28, 2011 - Aquatron Tower Tank 1

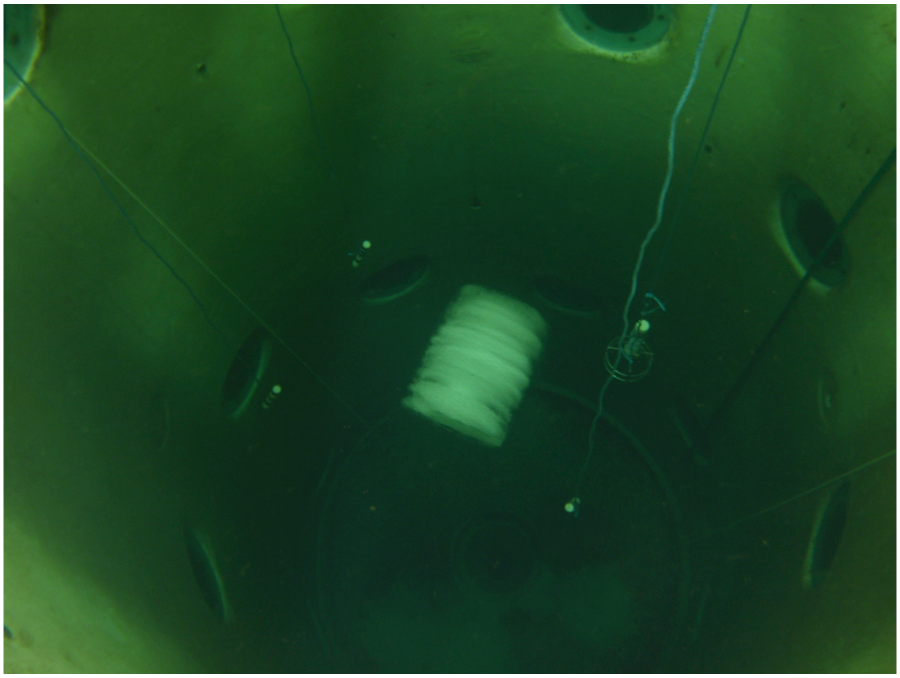

Figure A.4: January 28, 2011 - Aquatron Tower Tank 2

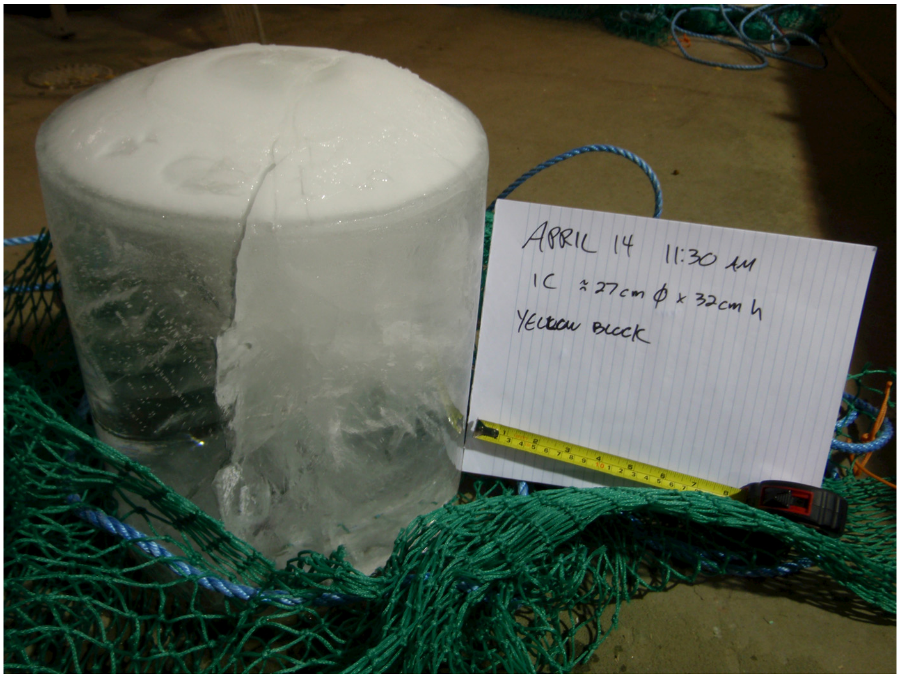

Figure A.5: April 14, 2009 - freshwater ice - initial condition, fractured block

Figure A.6: April 14, 2009 - freshwater ice - melt photo, complex geometry

Figure A.7: July 28, 2009 - freshwater ice - initial conditions

Figure A.8: July 28, 2009 - saltwater ice - initial conditions

Figure A.9: July 28, 2009 - sediment laden freshwater ice - initial conditions

Figure A.10: July 28, 2009 - sediment laden saltwater ice - initial conditions

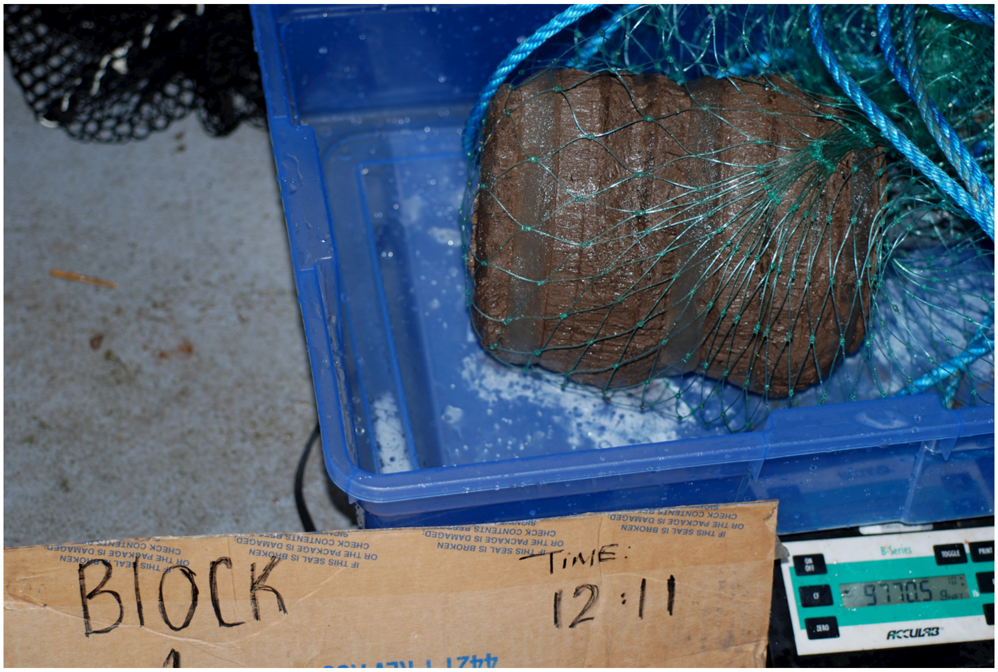

Figure A.11: July 28, 2009 - sediment laden freshwater ice - melt photo (12:11)

Figure A.12: January 28, 2011 - freshwater ice - top fracturing

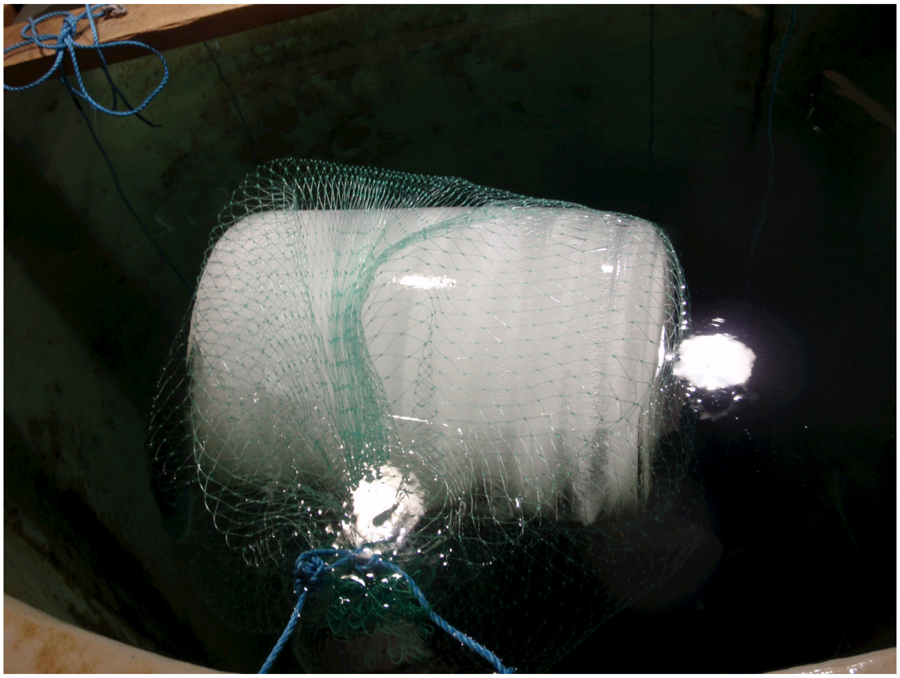

Figure A.13: January 28, 2011 - freshwater ice - initial conditions

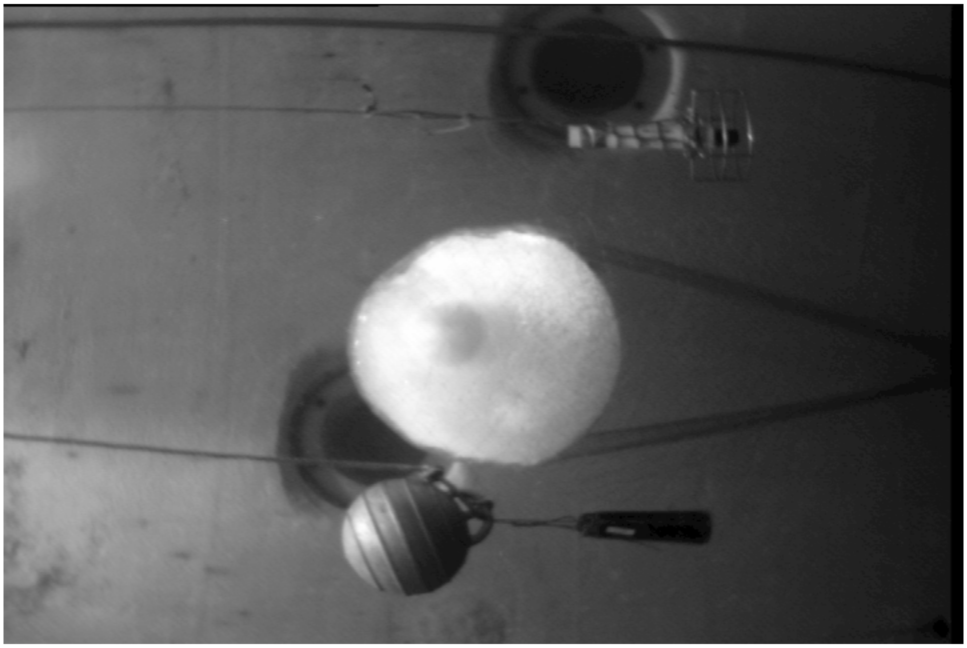

Figure A.14: January 28, 2011 - freshwater ice - melt photo 1, bottom end view(16:20)

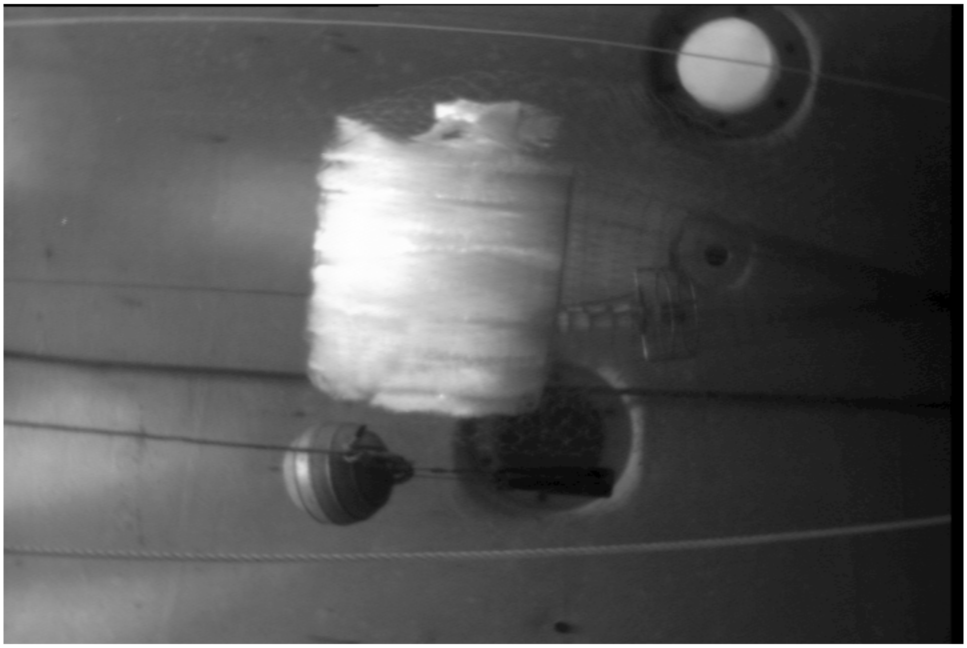

Figure A.15: January 28, 2011 - freshwater ice - melt photo 2, side view (16:20)

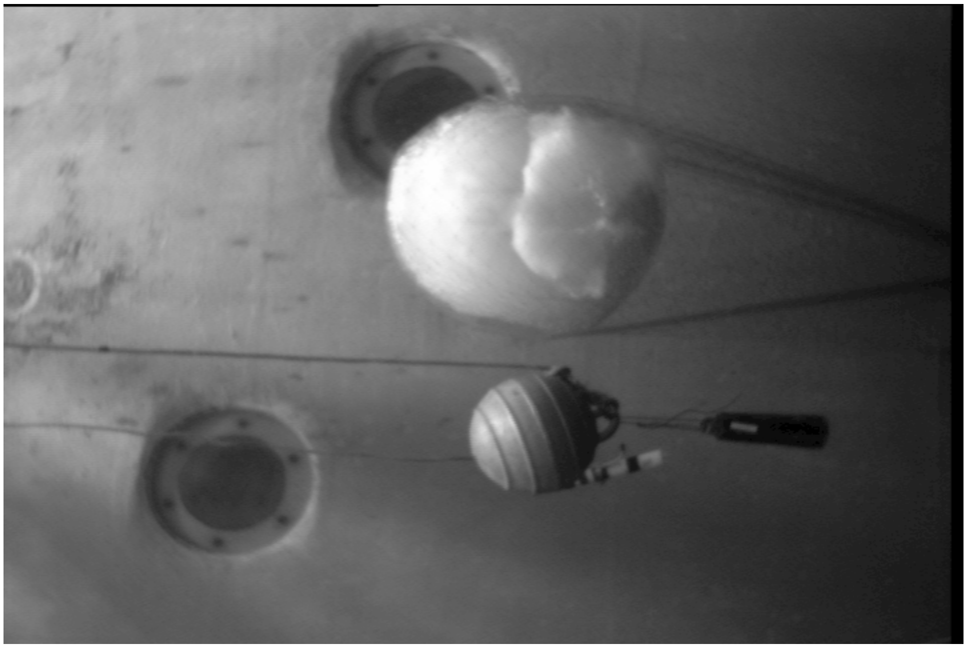

Figure A.16: January 28, 2011 - freshwater ice - melt photo 3, top end view (16:20)

APPENDIX B

PT AND CTD SENSOR DATA

Experiment date	Sensor	t (sec)	$\bar{D}$ (m)	D_{max} (m)	D_{min} (m)	$Var(D)$ (m)	$Linear\ Poly$ (m/hr), (m)
2009-April-14	PT_B	5	1.2527	1.2772	1.2100	3.742e-04	0.0084, 1.2062
	PT_G	5	1.1713	1.2030	1.1307	4.372e-04	0.0095, 1.1227
	PT_Y	5	1.1684	1.2135	1.1217	4.636e-04	0.0099, 1.1184
2009-April-22	PT_B	5	1.5529	1.5693	1.5396	3.490e-05	-0.0009, 1.5570
	PT_G	5	1.4147	1.4337	1.3945	4.059e-05	-0.0015, 1.4208
	PT_Y	5	1.4587	1.4866	1.4387	3.748e-05	-0.0014, 1.4650
2009-July-28	CTD	5	1.2655	1.2884	1.2514	9.113e-05	-0.0033, 1.2819
	PT_G	5	1.1664	1.2165	1.1258	9.452e-04	-0.0100, 1.2067
	PT_Y	5	1.3627	1.3815	1.3485	9.333e-05	-0.0029, 1.3773
2010-Feb-02	PT_G	10	1.5260	1.6175	1.4295	3.180e-03	-0.0387, 1.7527
	PT_Y	10	1.7963	1.9047	1.6732	6.270e-03	-0.0523, 2.0985
2010-March-03	CTD	60	1.7490	1.8075	1.7081	7.224e-04	-0.0049, 1.8093
	PT_B	300	0.5992	0.6259	0.5446	6.430e-04	-0.0041, 0.6414
	PT_G	300	1.7121	1.7906	1.6803	9.291e-04	-0.0056, 1.8247
	PT_Y	300	1.8861	1.9443	1.8469	7.626e-04	-0.0052, 1.9805
2010-March-04	CTD	60	1.7125	1.7405	1.6984	1.205e-04	0.0036, 1.5926
	PT_B	300	0.5362	0.5605	0.5240	1.191e-04	0.0055, 0.3514
	PT_G	300	1.6941	1.7064	1.6788	1.200e-04	0.0043, 1.5441
	PT_Y	300	1.8750	1.8921	1.8627	9.826e-05	0.0036, 1.7527
2010-April-15	CTD	1	0.7569	0.7849	0.7509	9.876e-05	-0.0838, 0.7837
2011-Jan-25	CTD	10	4.8875	6.7906	4.8457	0.0680	-0.3385, 7.0339
	PT_B	10	5.2083	5.7125	5.0136	0.0954	-0.4642, 7.9499
	PT_G	10	4.9825	5.5991	4.8899	0.0549	-0.2914, 6.7339
	PT_Y	10	5.1314	5.7319	5.0557	0.0433	-0.3402, 7.1603
2011-Jan-26	CTD	5	5.1493	5.1740	5.1378	4.662e-05	-0.0033, 5.1620
	PT_B	5	5.0980	5.1112	5.0868	2.526e-05	-0.0019, 5.1050
	PT_G	5	4.8013	4.8254	4.7924	2.752e-05	-0.0022, 4.8106
	PT_Y	5	4.8303	4.8525	4.8193	5.089e-05	-0.0032, 4.8427
2011-Jan-28	CTD	5	5.0780	5.1042	5.0621	1.626e-05	-5.502e-04, 5.0494
	PT_B	5	5.0032	5.0473	4.9695	3.968e-04	-0.0050, 5.2630
	PT_G	5	4.7269	4.7468	4.7156	3.051e-05	0.0012, 4.6674
	PT_Y	5	4.6978	4.7692	4.5330	6.755e-03	-0.0199, 5.7186
2011-Feb-21	CTD	5	5.3395	5.7807	5.3218	0.0022	-0.0088, 5.3965
	PT_B	5	5.2205	5.2487	5.2004	9.834e-05	-0.0038, 5.2446
	PT_G	5	5.4297	5.4679	5.4146	1.096e-04	-0.0047, 5.4592
	PT_Y	5	5.2748	5.3019	5.2586	8.283e-05	-0.0038, 5.2990
2011-Feb-22	CTD	5	5.3828	5.4188	5.3394	3.255e-04	0.0060, 5.1975
	PT_B	5	5.2629	5.2953	5.2199	2.517e-04	0.0053, 5.0983
	PT_G	5	5.4661	5.5090	5.4276	3.965e-04	0.0058, 5.2864
	PT_Y	5	5.3084	5.3504	5.2746	2.237e-04	0.0034, 5.2016
2011-Mar-30	CTD	1	3.8477	3.8795	3.8394	3.143e-05	-0.0019, 3.8601
	PT_B	5	3.6822	3.7014	3.6754	1.835e-05	-0.0012, 3.6905
	PT_Y	5	4.8851	5.2107	3.7456	0.2592	0.0310, 4.5685

Table B.1: PT and CTD sampling period and depth

Experiment date	Sensor	$\bar{T}$ ($\circ C$)	T_{max} ($\circ C$)	T_{min} ($\circ C$)	$Var(T)$ ($\circ C$)	$Linear\ Poly$ ($^\circ C/hr$), ($^\circ C$)
2009-April-14	PT_B	3.3431	3.4112	3.2958	8.807e-04	-0.0115, 3.4067
	PT_G	3.3617	3.4178	3.2893	9.153e-04	-0.0116, 3.4215
	PT_Y	3.3368	3.4321	3.2805	6.021e-04	-0.0062, 3.3681
2009-April-22	PT_B	4.0021	4.0613	3.9321	1.036e-03	0.0121, 3.9479
	PT_G	3.9879	4.0711	3.9391	5.764e-04	0.0069, 3.9593
	PT_Y	3.9719	4.0319	3.9198	7.473e-04	0.0100, 3.9268
2009-July-28	CTD	13.3062	13.3481	13.2400	6.393e-04	-0.0068, 13.3486
	PT_G	13.3050	13.3546	13.2423	4.113e-04	-0.0063, 13.3302
	PT_Y	13.2989	13.3436	13.2524	5.127e-04	-0.0069, 13.3331
2010-Feb-02	PT_G	3.0357	3.0491	3.0125	7.256e-05	0.0056, 3.0031
	PT_Y	3.0333	3.0473	3.0147	8.538e-05	0.0058, 2.9995
2010-March-03	CTD	2.4104	2.4339	2.3629	1.313e-04	0.0012, 2.3879
	PT_B	2.3985	2.4209	2.3837	1.390e-04	6.293e-04, 2.3896
	PT_G	2.4133	2.4411	2.3805	1.661e-04	0.0014, 2.3850
	PT_Y	2.4092	2.4395	2.3807	1.242e-04	0.0016, 2.3809
2010-March-04	CTD	2.4315	2.4399	2.4167	2.667e-05	-0.0019, 2.4932
	PT_B	2.4286	2.4357	2.4171	2.608e-05	-0.0024, 2.5107
	PT_G	2.4285	2.4346	2.4219	9.906e-06	-6.683e-04, 2.4517
	PT_Y	2.4298	2.4389	2.4220	3.151e-05	-0.0020, 2.4960
2010-April-15	CTD	2.9842	3.5407	2.8212	0.0354	-1.0442, 3.3182
2011-Jan-25	CTD	4.3737	4.5532	4.3672	2.446e-04	-0.0250, 4.4326
	PT_B	4.3717	4.3935	4.3636	4.366e-05	-0.013, 4.5320
	PT_G	4.3749	4.3880	4.3685	1.769e-05	-0.0077, 4.4209
	PT_Y	4.3730	4.3839	4.3635	1.765e-05	-0.0093, 4.4284
2011-Jan-26	CTD	4.2455	4.3169	4.2105	4.366e-04	-0.0122, 4.2924
	PT_B	4.2447	4.2874	4.2093	4.702e-04	-0.0119, 4.2885
	PT_G	4.2423	4.2913	4.2181	3.150e-04	-0.0112, 4.2906
	PT_Y	4.2410	4.2888	4.2118	4.081e-04	-0.0116, 4.2860
2011-Jan-28	CTD	4.0660	4.1331	4.0230	9.110e-04	-0.0136, 4.7707
	PT_B	4.0671	4.1322	4.0261	1.046e-03	-0.0133, 4.7593
	PT_G	4.0729	4.1345	4.0148	1.152e-03	-0.0138, 4.7852
	PT_Y	4.0693	4.1351	4.0232	1.130e-03	-0.0136, 4.7768
2011-Feb-21	CTD	2.8657	2.8774	2.8579	1.178e-05	-0.0015, 2.8751
	PT_B	2.8640	2.8754	2.8548	1.543e-05	-0.0016, 2.8740
	PT_G	2.8669	2.8810	2.8593	1.615e-05	-0.0017, 2.8773
	PT_Y	2.8650	2.8801	2.8544	1.426e-05	-0.0016, 2.8753
2011-Feb-22	CTD	2.8558	2.8934	2.8347	1.811e-04	-0.0045, 2.9944
	PT_B	2.8525	2.8925	2.8301	1.781e-04	-0.0044, 2.9906
	PT_G	2.8564	2.8920	2.8354	2.002e-04	-0.0045, 2.9939
	PT_Y	2.8541	2.9009	2.8334	1.800e-04	-0.0043, 2.9887
2011-Mar-30	CTD	2.7263	2.7479	2.7088	1.076e-04	-0.0043, 2.7551
	PT_B	2.7206	2.7417	2.6998	1.165e-04	-0.0043, 2.7494

Table B.2: Far-field temperature measurements

Experiment date	Sensor	$\bar{S}$ (psu)	S_{max} (psu)	S_{min} (psu)	$Var(S)$ (psu)	$Linear\ Poly$ (psu/hr), (psu)
2009-April-14	$Refract$	3	-	-	-	-
2009-April-22	$Refract$	3	-	-	-	-
2009-July-28	CTD	31.4680	31.5108	31.4254	1.759e-04	-0.0042, 31.4886
2010-Feb-02	$Refract$	3	-	-	-	-
2010-March-03	CTD	30.5251	30.5785	30.4821	2.726e-04	-0.0027, 30.5739
2010-March-03	CTD	30.4638	30.4920	30.4274	3.284e-04	-0.0072, 30.7041
2010-April-15	CTD	31.5129	31.7279	31.0438	0.0301	0.6234, 31.3135
2011-Jan-25	CTD	30.5637	30.5828	30.3773	3.077e-04	0.0329, 30.3549
2011-Jan-26	CTD	30.7201	30.7462	30.6800	1.051e-04	0.0052, 30.7003
2011-Jan-28	CTD	30.7344	30.7533	30.7140	3.159e-05	6.545e-04, 30.7004
2011-Feb-21	CTD	30.7683	30.7880	30.7456	3.086e-05	-7.890e-04, 30.7734
2011-Feb-22	CTD	30.7577	30.7983	30.7256	1.846e-04	-0.0042, 30.8876
2011-Mar-30	CTD	31.1638	31.1875	31.1309	7.201e-05	0.0021, 31.1454

Table B.3: Far-field salinity measurements

The following plots present far-field data collected with the RBR PT and/or CTD sensors. Subscripts B, G, and Y correspond to blue, green, and yellow electrical tape colour coding of the PT sensors which was consistent through the experiments. The left panel of the plots presents all data collected by the sensors. The right panel presents pruned data based on depth greater than $1\ m$ and separate stability criteria for temperature, conductivity, and depth measurements. For cases where the sensors were deployed for multiple days, the duration of each melt experiment is marked on the left panel by red lines and a subsequent figure presents separate plots for each melt. Dashed lines correspond with the linear polynomials presented in the proceeding tables.

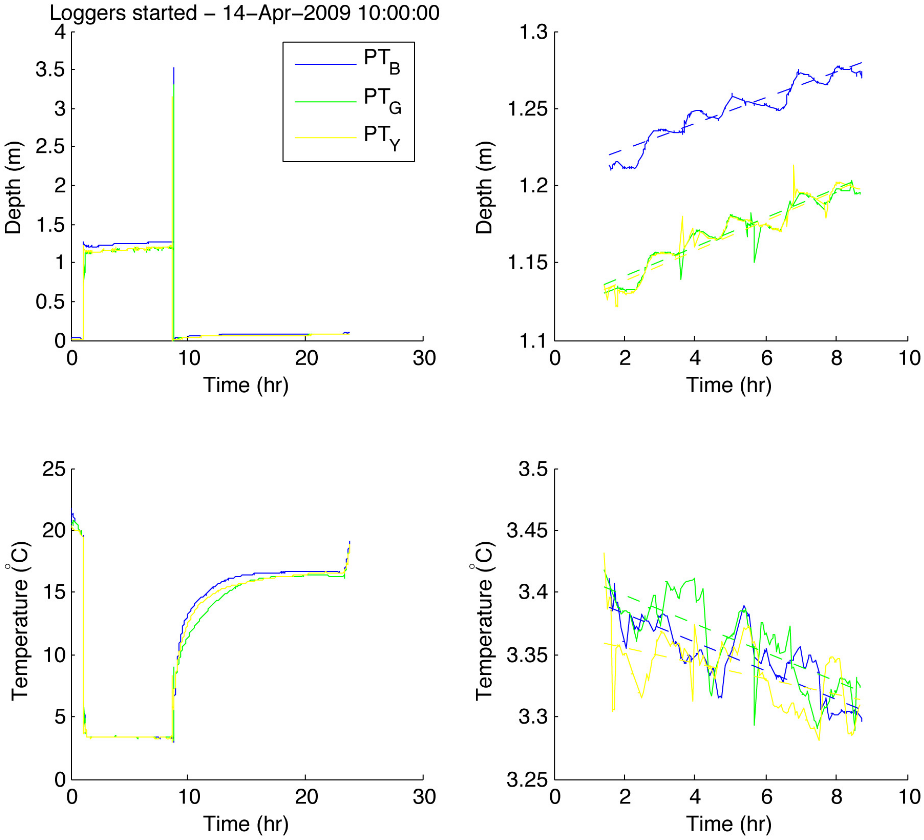

Figure B.1: Far-field PT sensor data - April 14, 2009

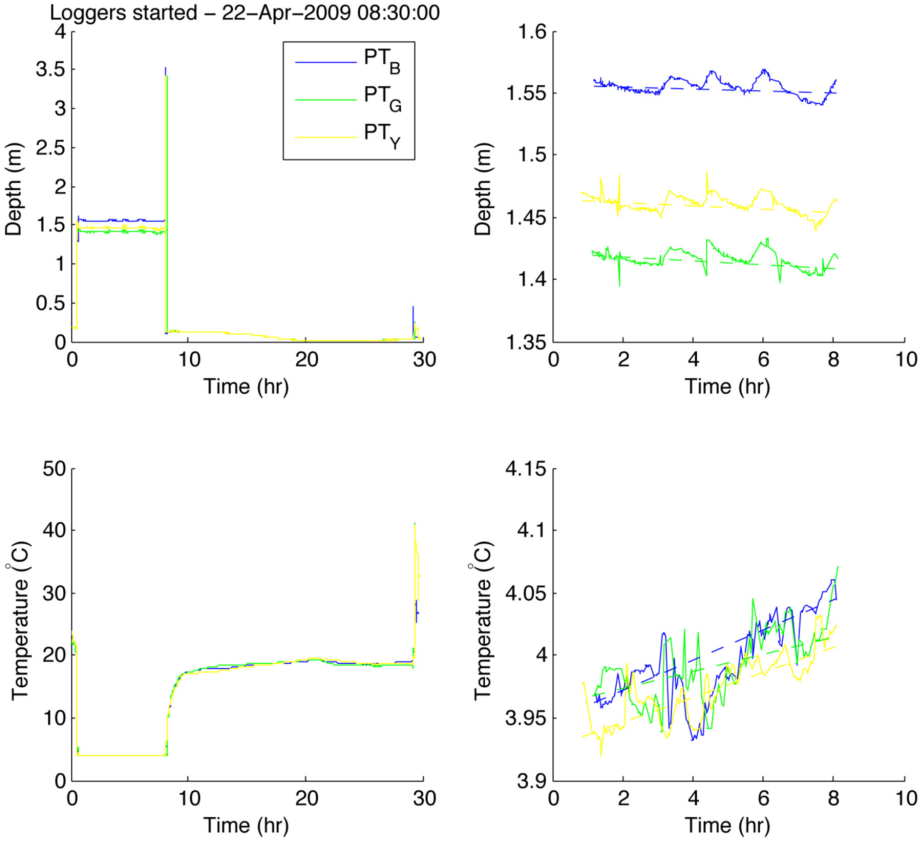

Figure B.2: Far-field PT sensor data - April 22, 2009

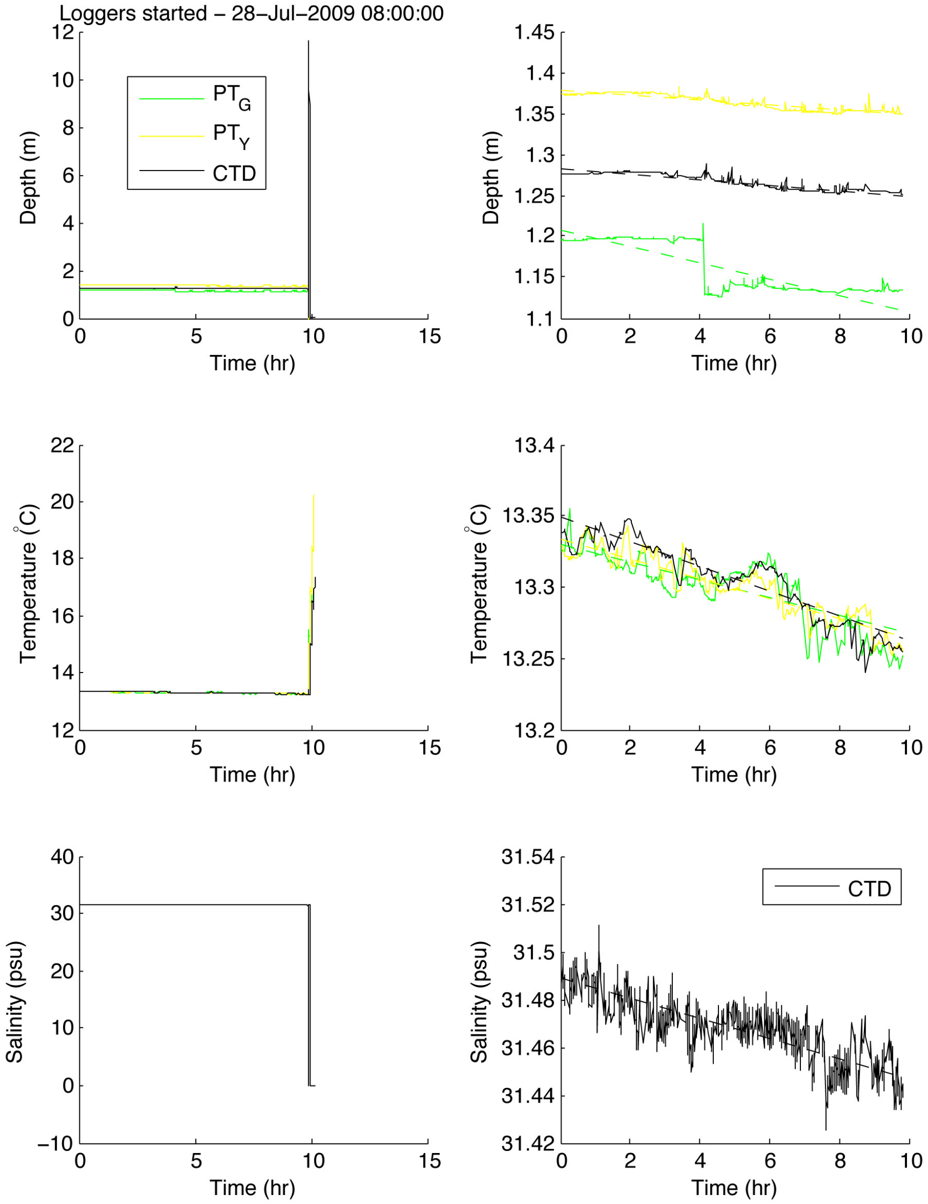

Figure B.3: Far-field PT and CTD sensor data - July 28, 2009

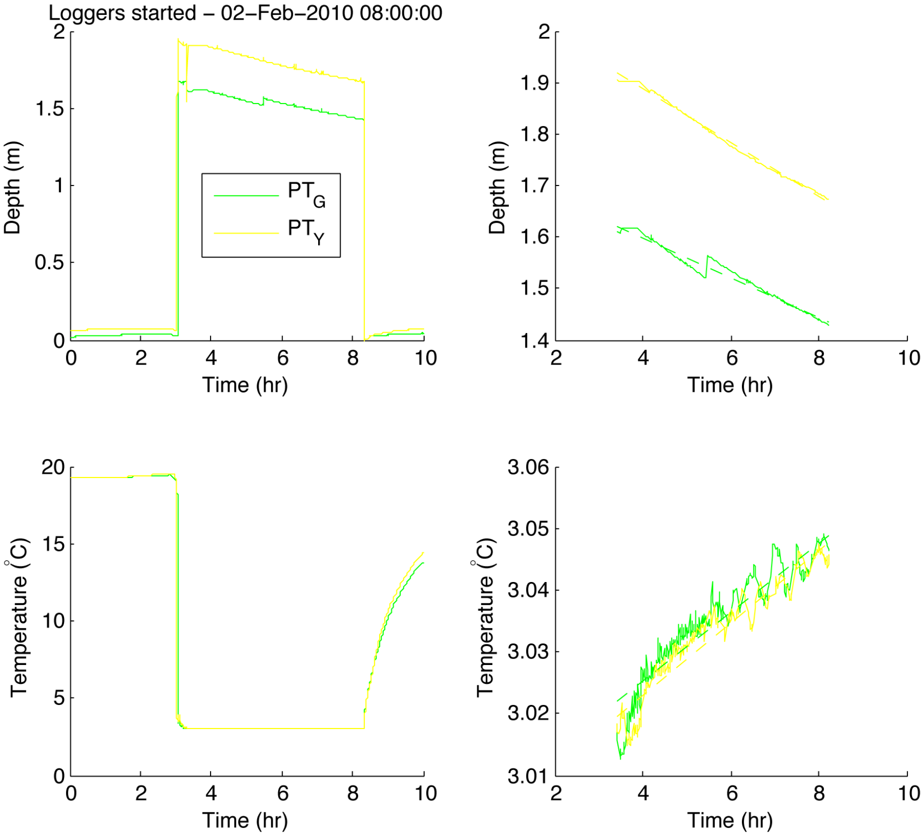

Figure B.4: Far-field PT sensor data - Feb 2, 2010

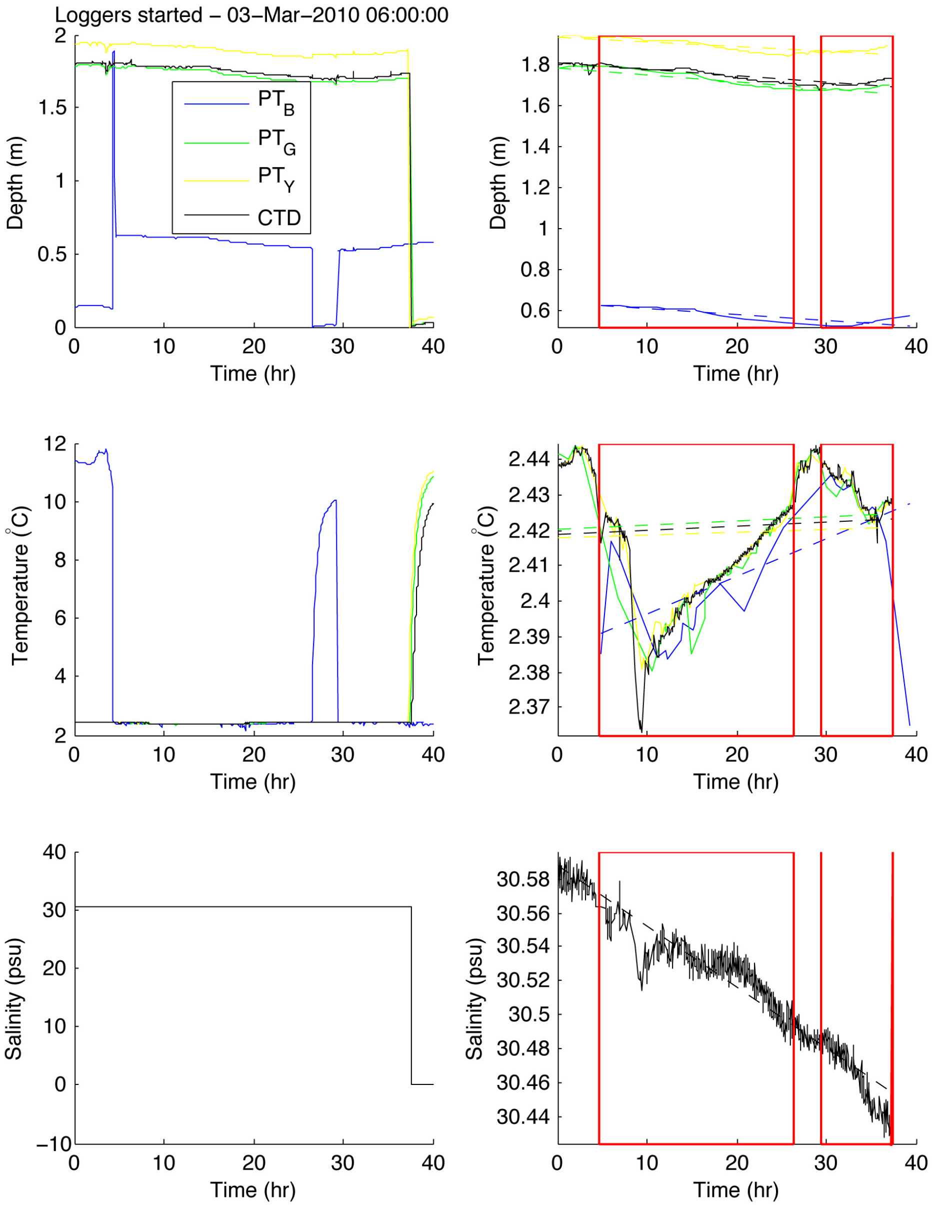

Figure B.5: Far-field PT and CTD sensor data 1 - March 3 and 4, 2010

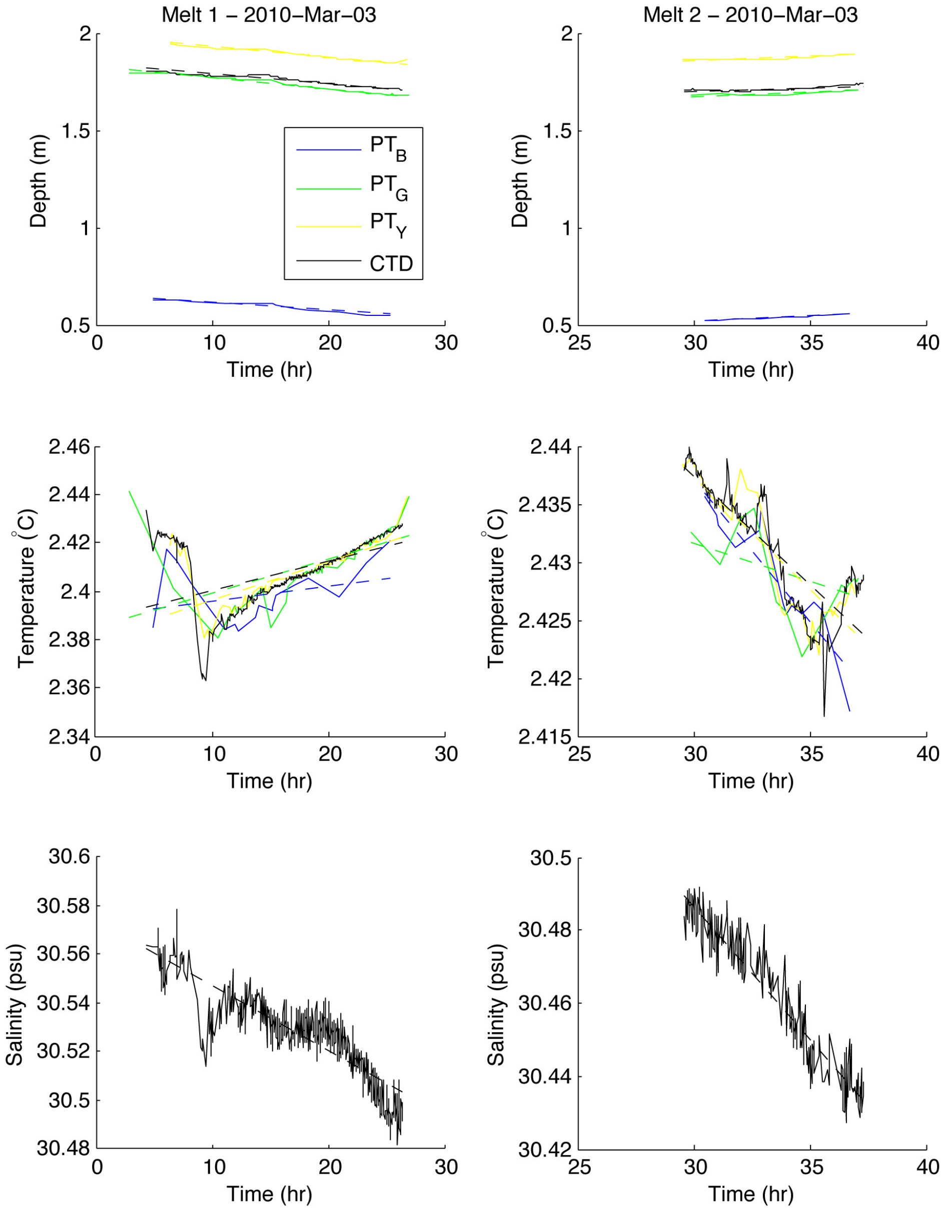

Figure B.6: Far-field PT and CTD sensor data 2 - March 3 and 4, 2010

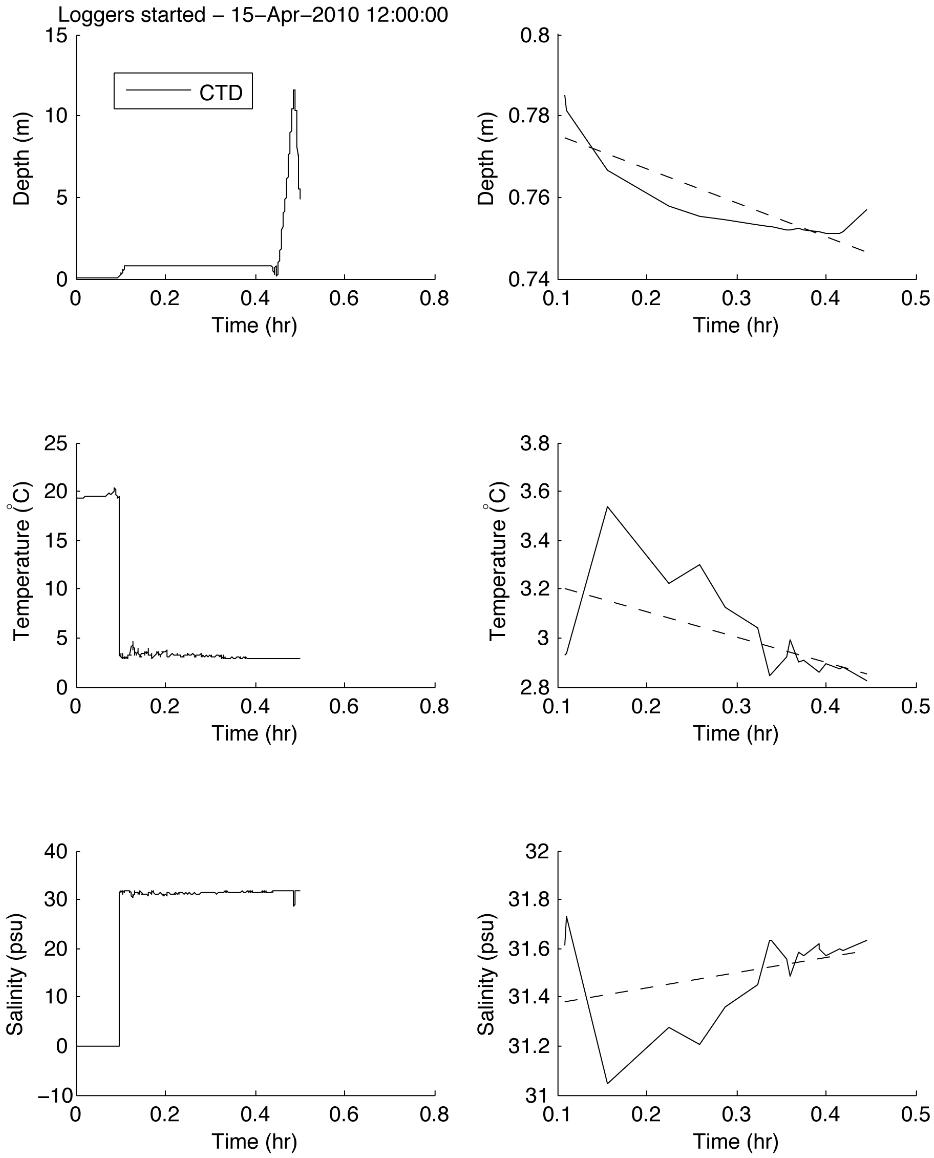

Figure B.7: Far-field CTD sensor data - April 15, 2010

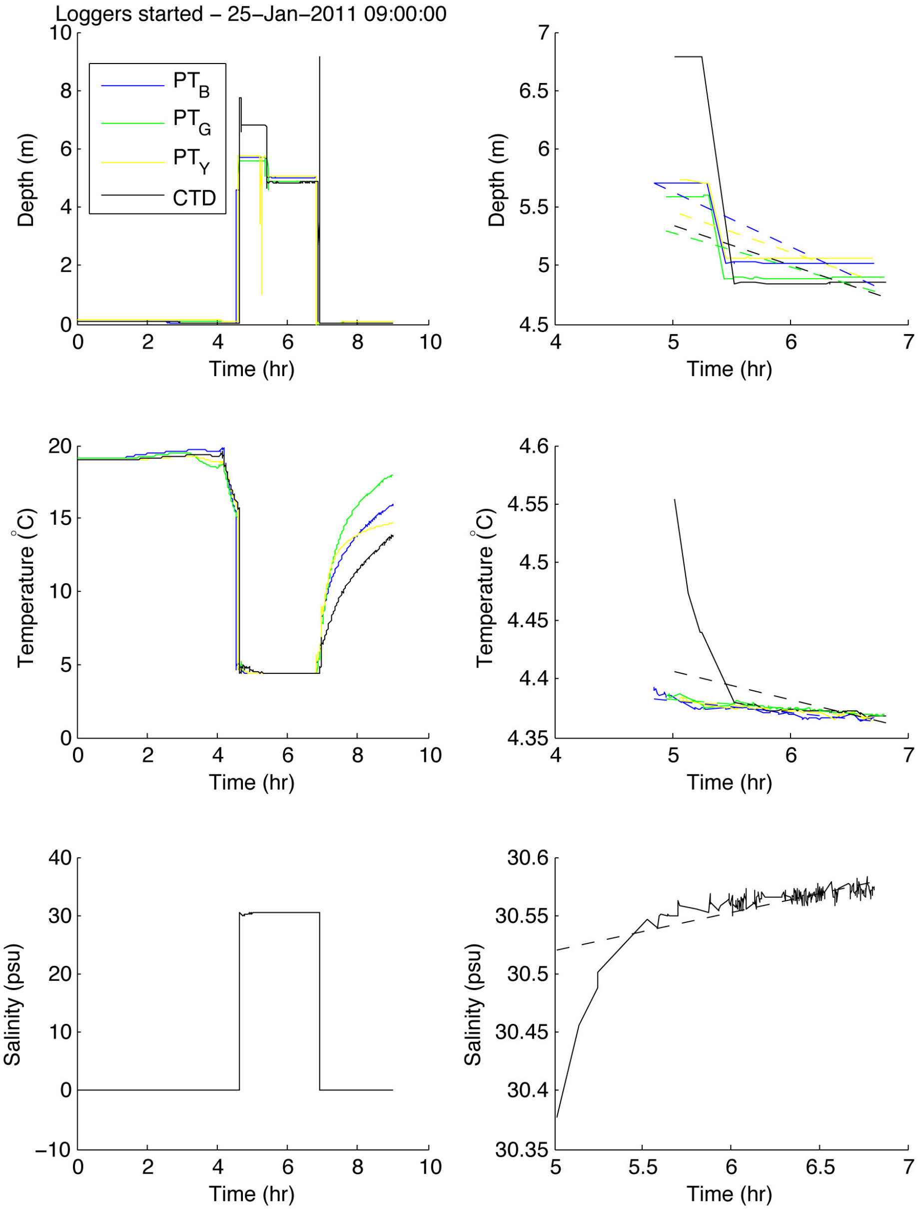

Figure B.8: Far-field PT and CTD sensor data - Jan 25, 2011

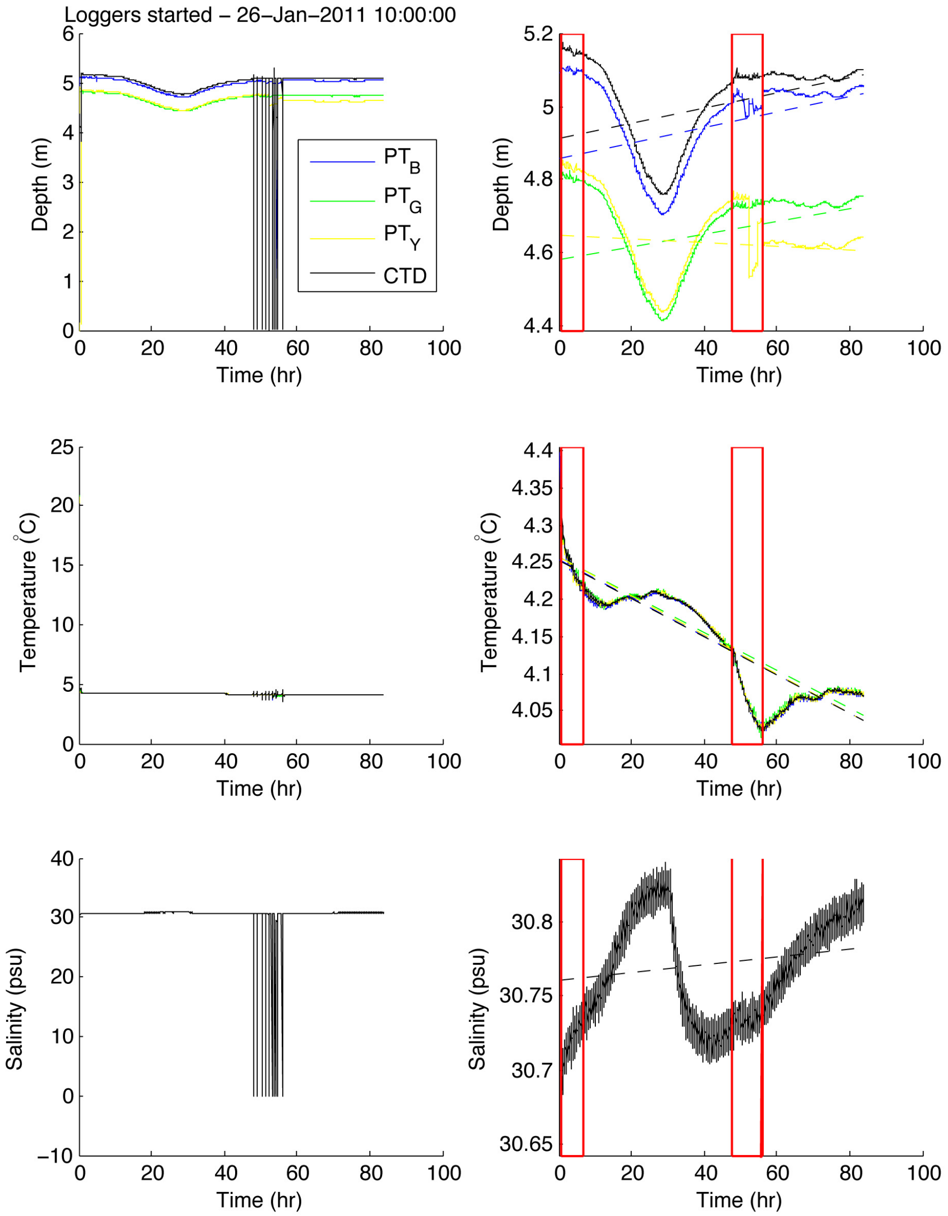

Figure B.9: Far-field PT and CTD sensor data 1 - Jan 26 and 27, 2011

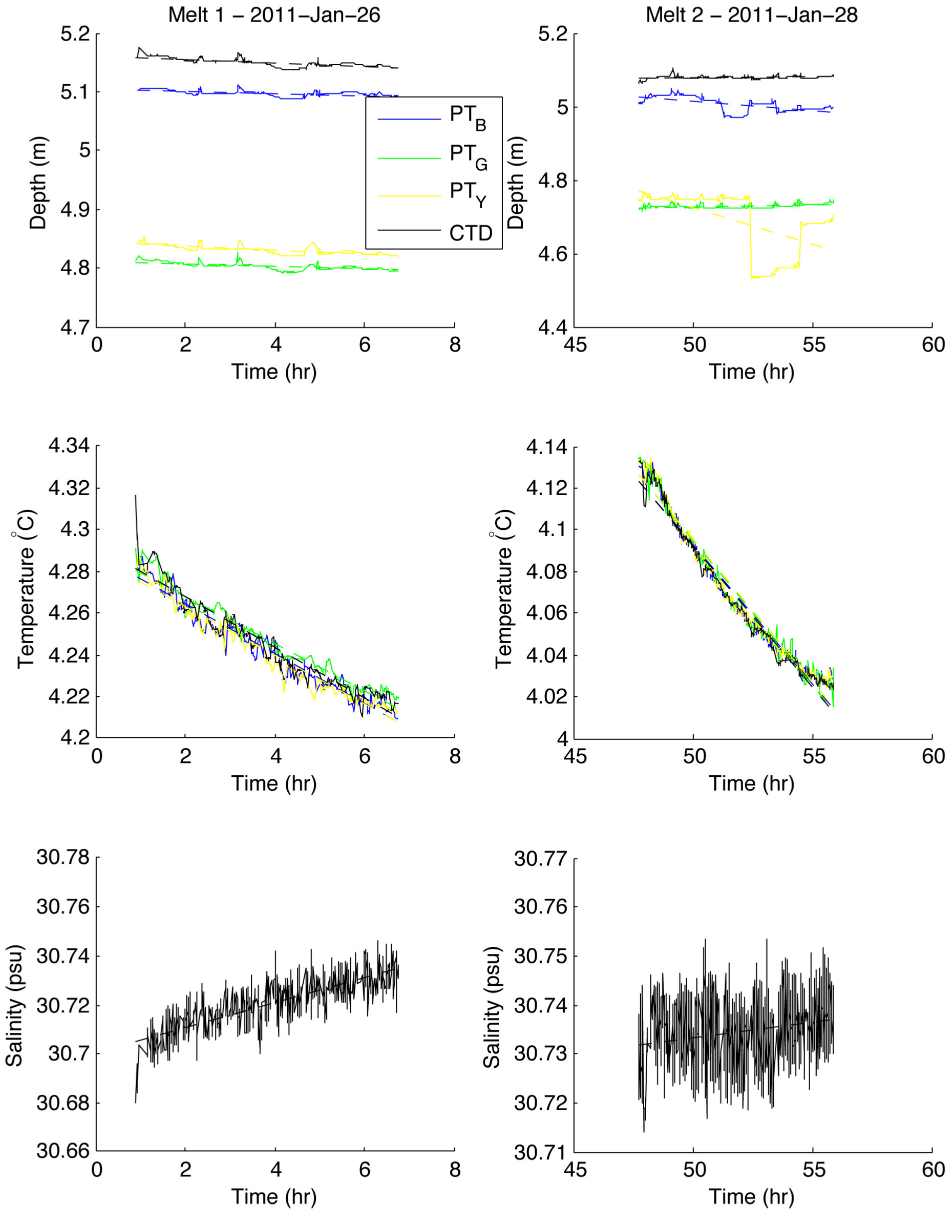

Figure B.10: Far-field PT and CTD sensor data 2 - Jan 26 and 27, 2011

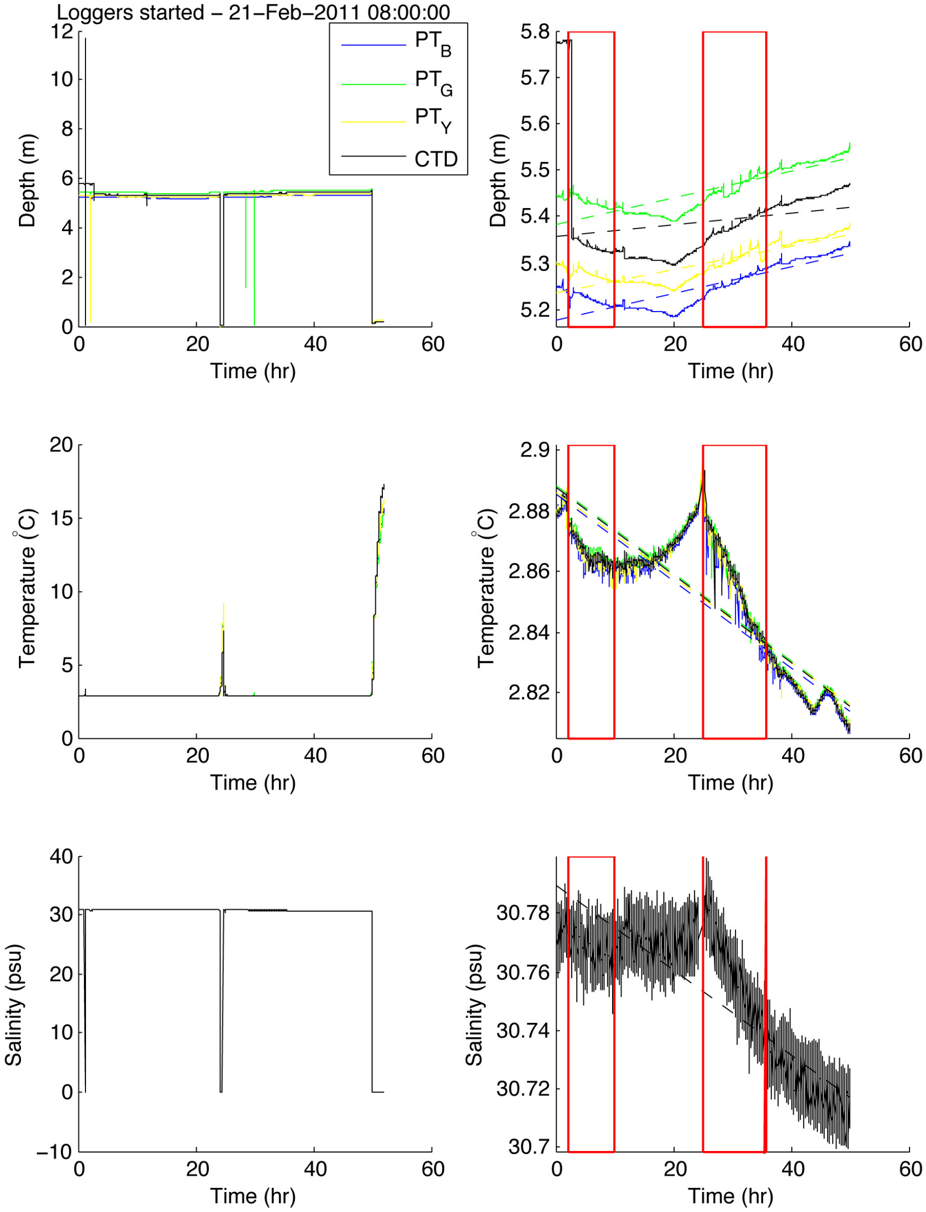

Figure B.11: Far-field PT and CTD sensor data 1 - Feb 21 and 22, 2011

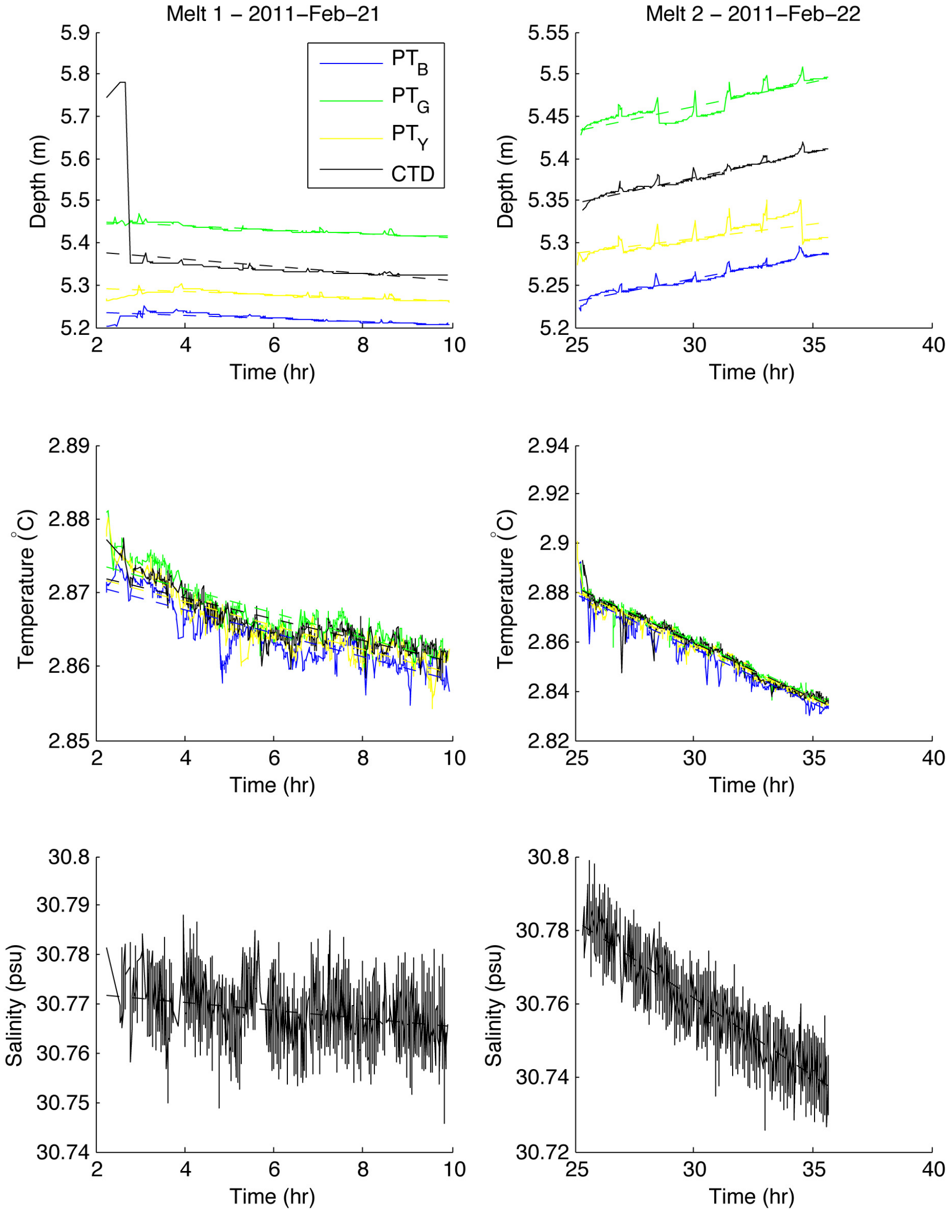

Figure B.12: Far-field PT and CTD sensor data 2 - Feb 21 and 22, 2011

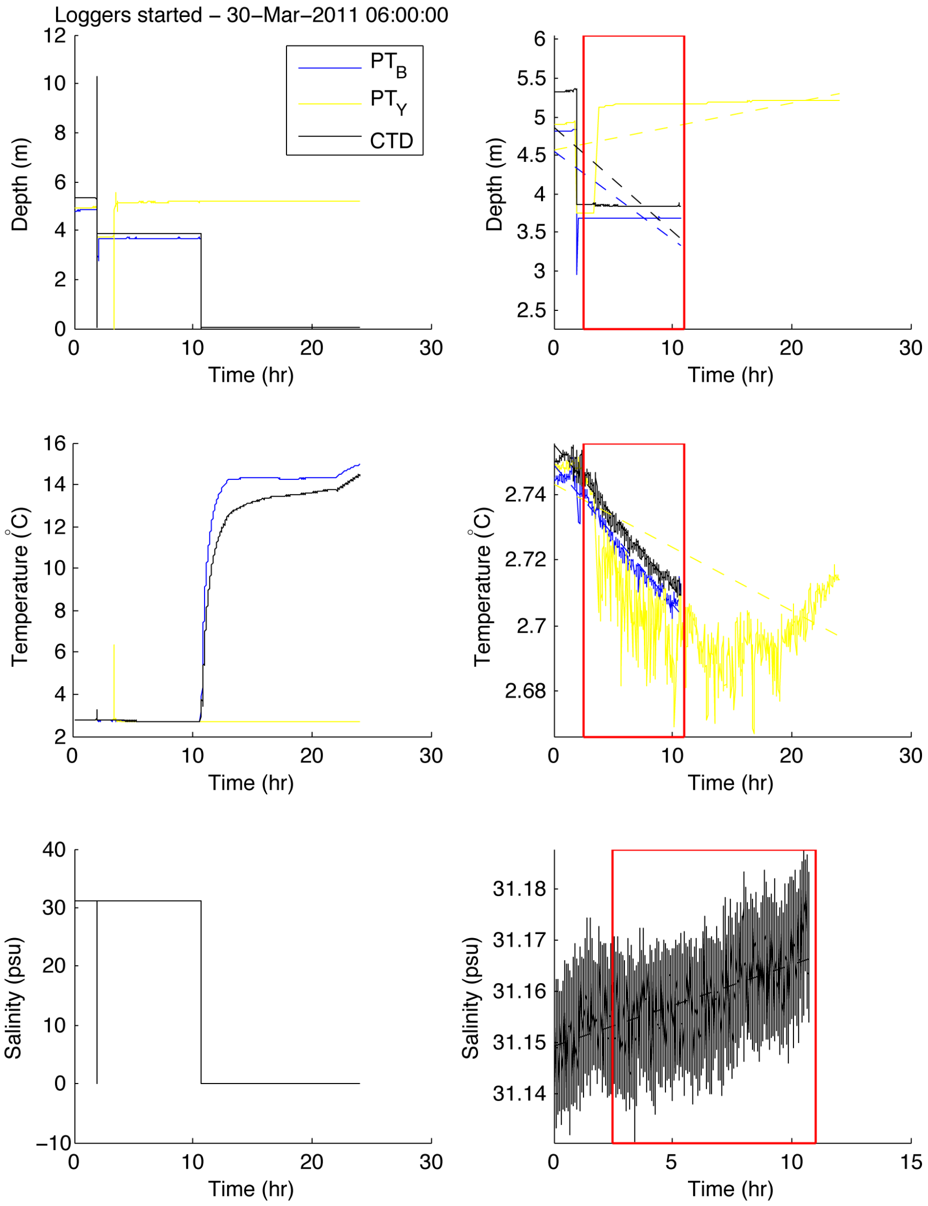

Figure B.13: PT and CTD sensor data - Mar 30, 2011

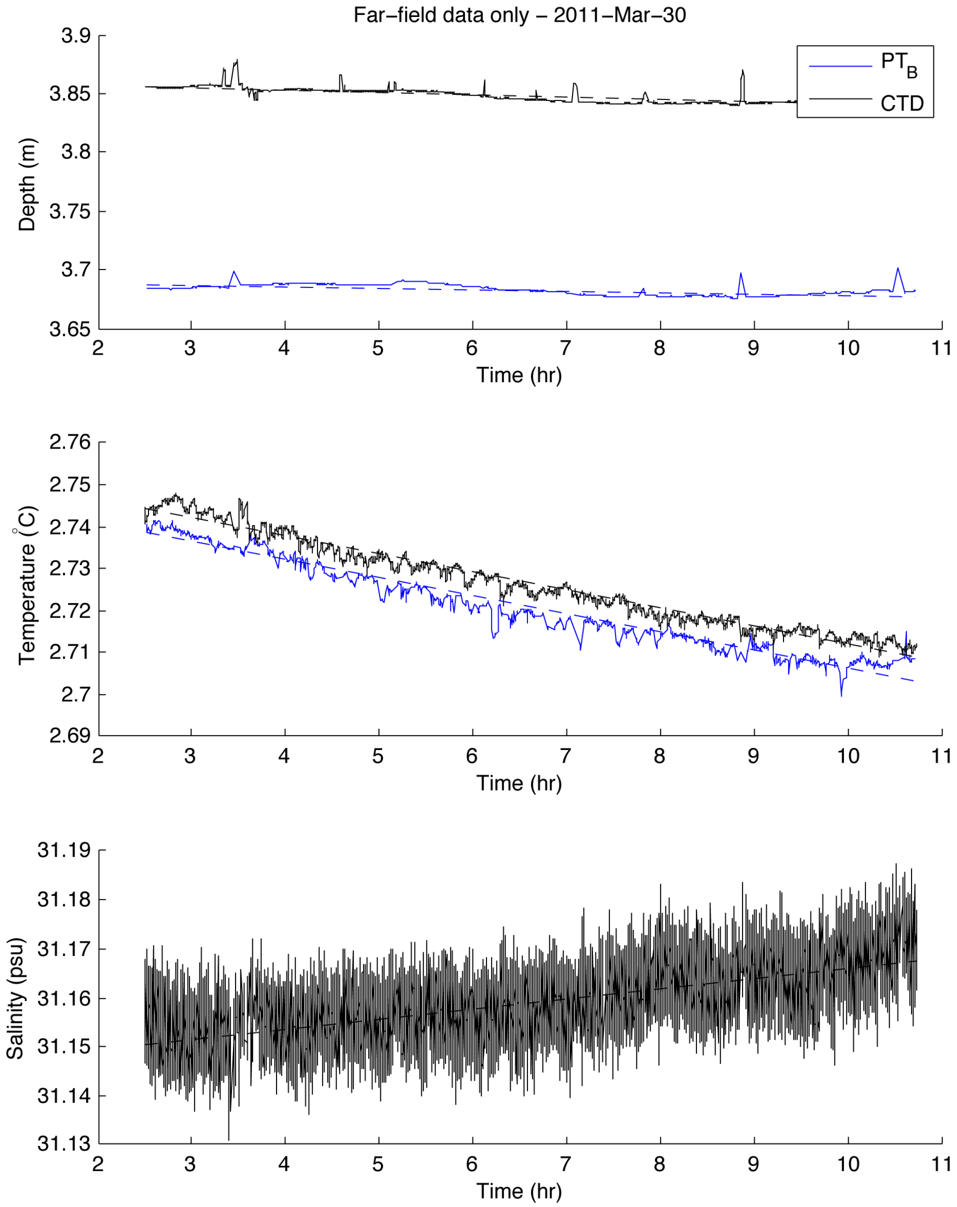

Figure B.14: Far-field PT and CTD sensor data - Mar 30, 2011

The following plots present depth profiles collected from the tower tank by down casts with the RBR CTD. Data points are marked and solid lines plotted using Matlab polynomial fit $p(x) = p_1x^n + p_2x^{n-1} + \cdots + p_nx + p_{n+1}$ with $n = 4$. Brunt-Vaisala frequency (N^2) was calculated using equation 4.6 and a centered scheme for $\partial\rho/\partial z$.

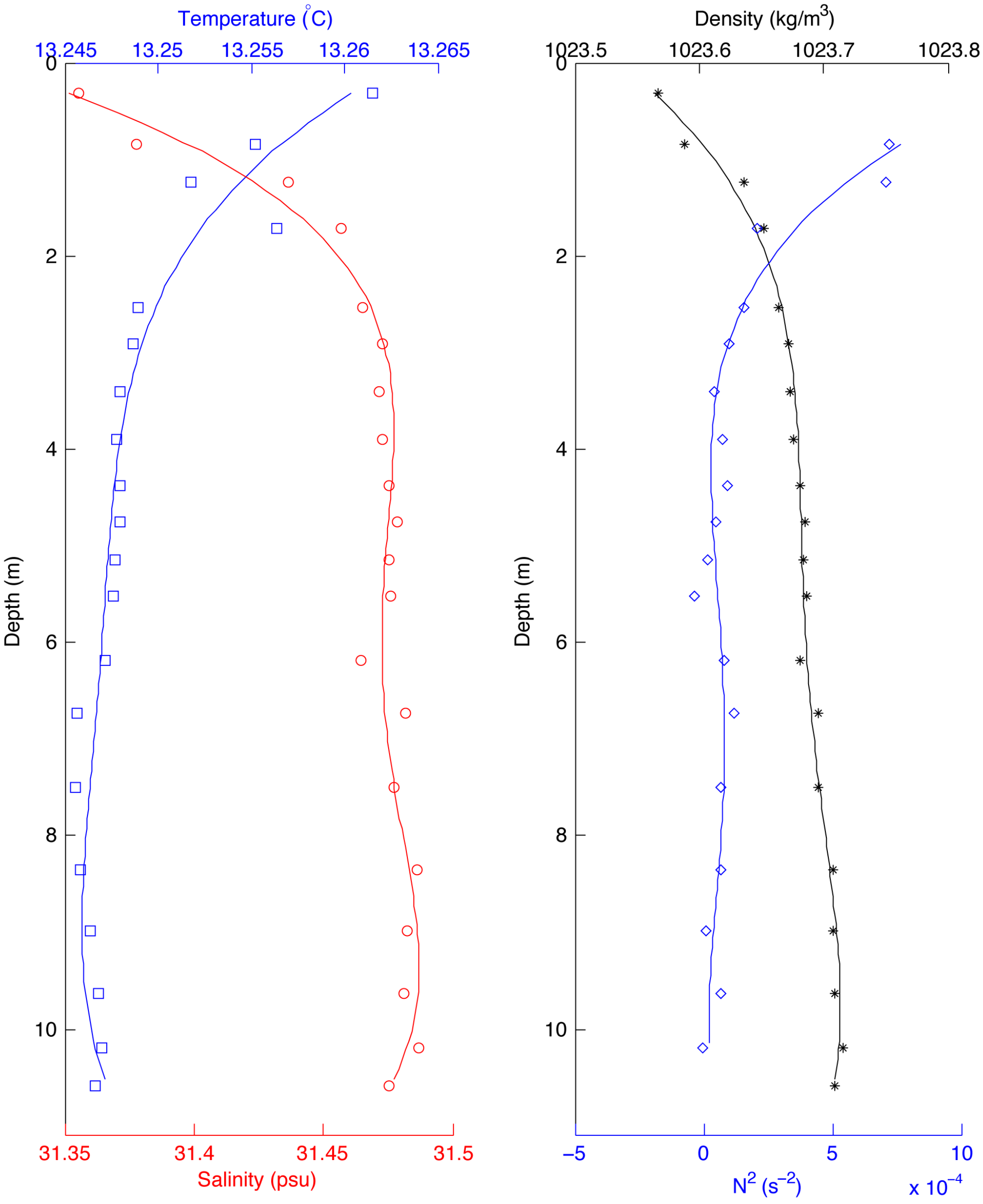

Figure B.15: Tower tank depth profile - July 28, 2009

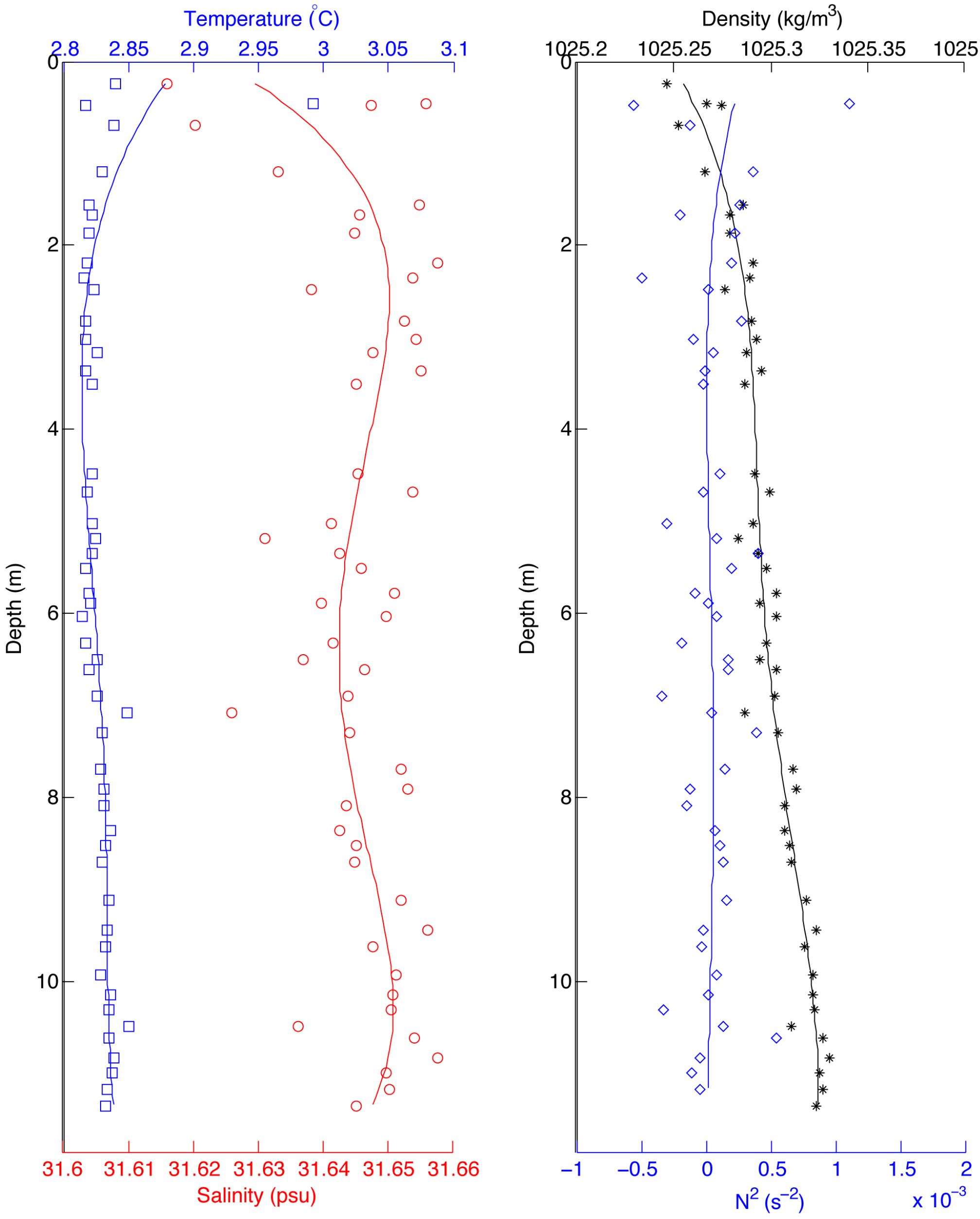

Figure B.16: Tower tank depth profile - April 15, 2010

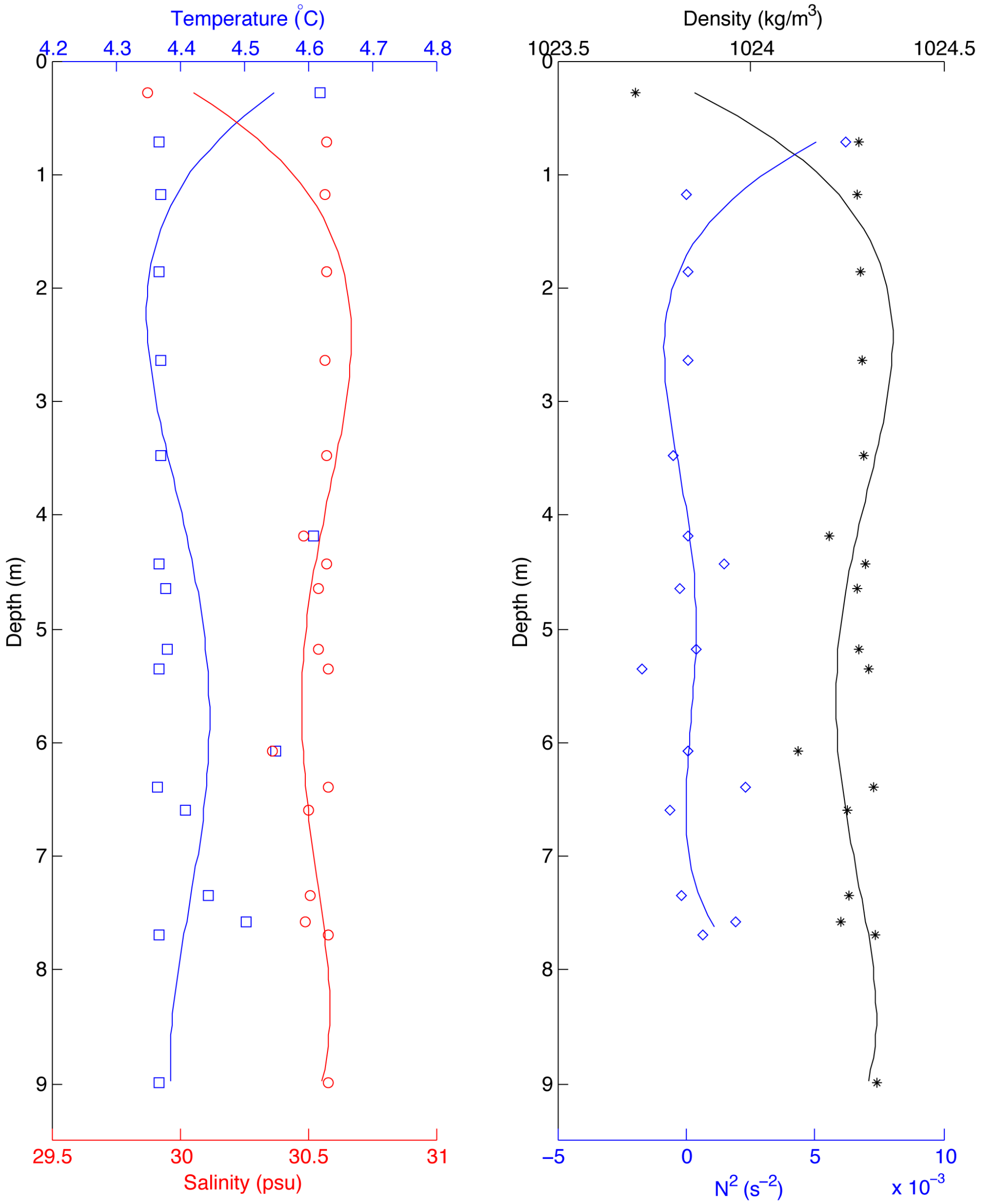

Figure B.17: Tower tank depth profile - Jan 25, 2011

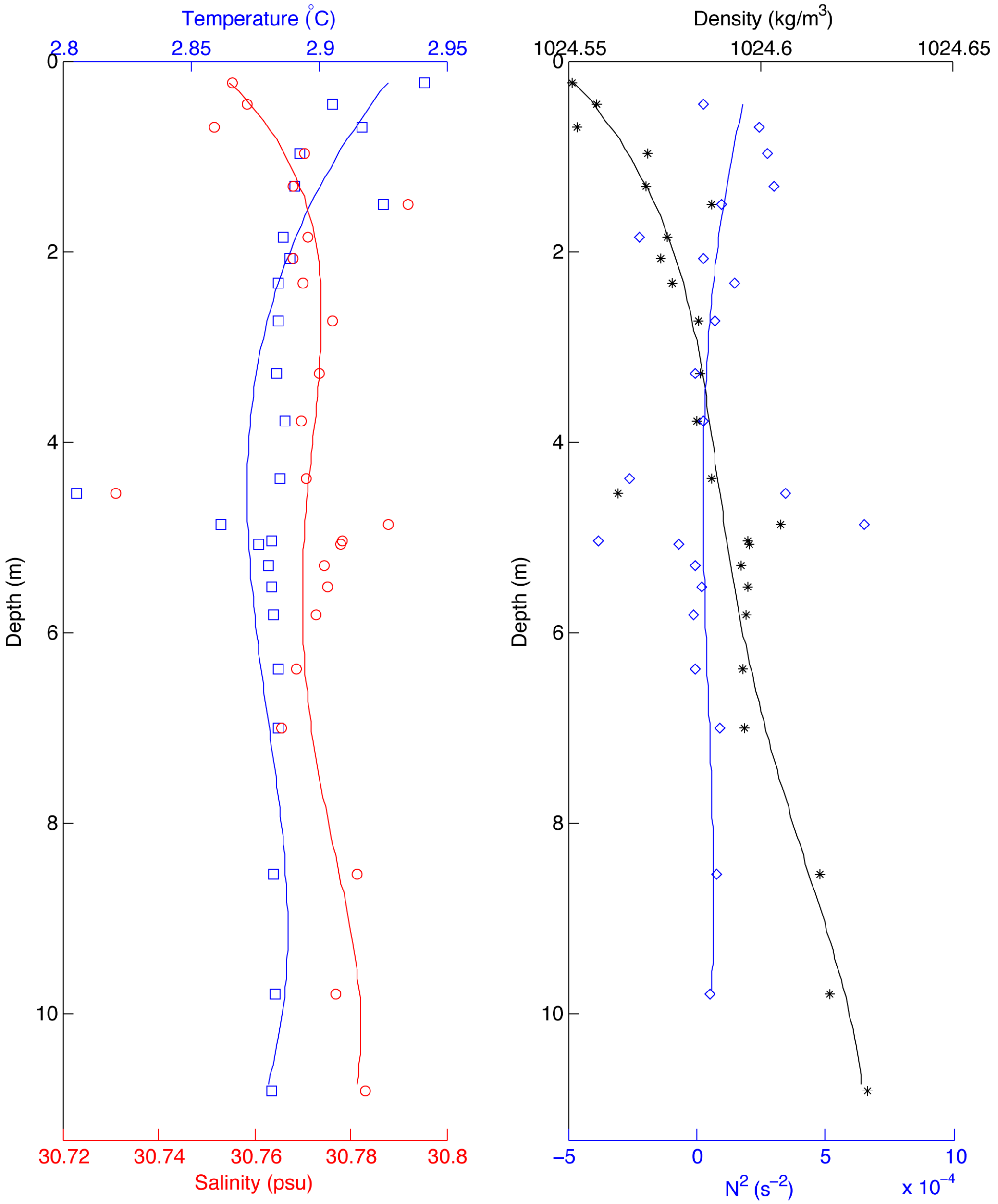

Figure B.18: Tower tank depth profile - Feb 21, 2011

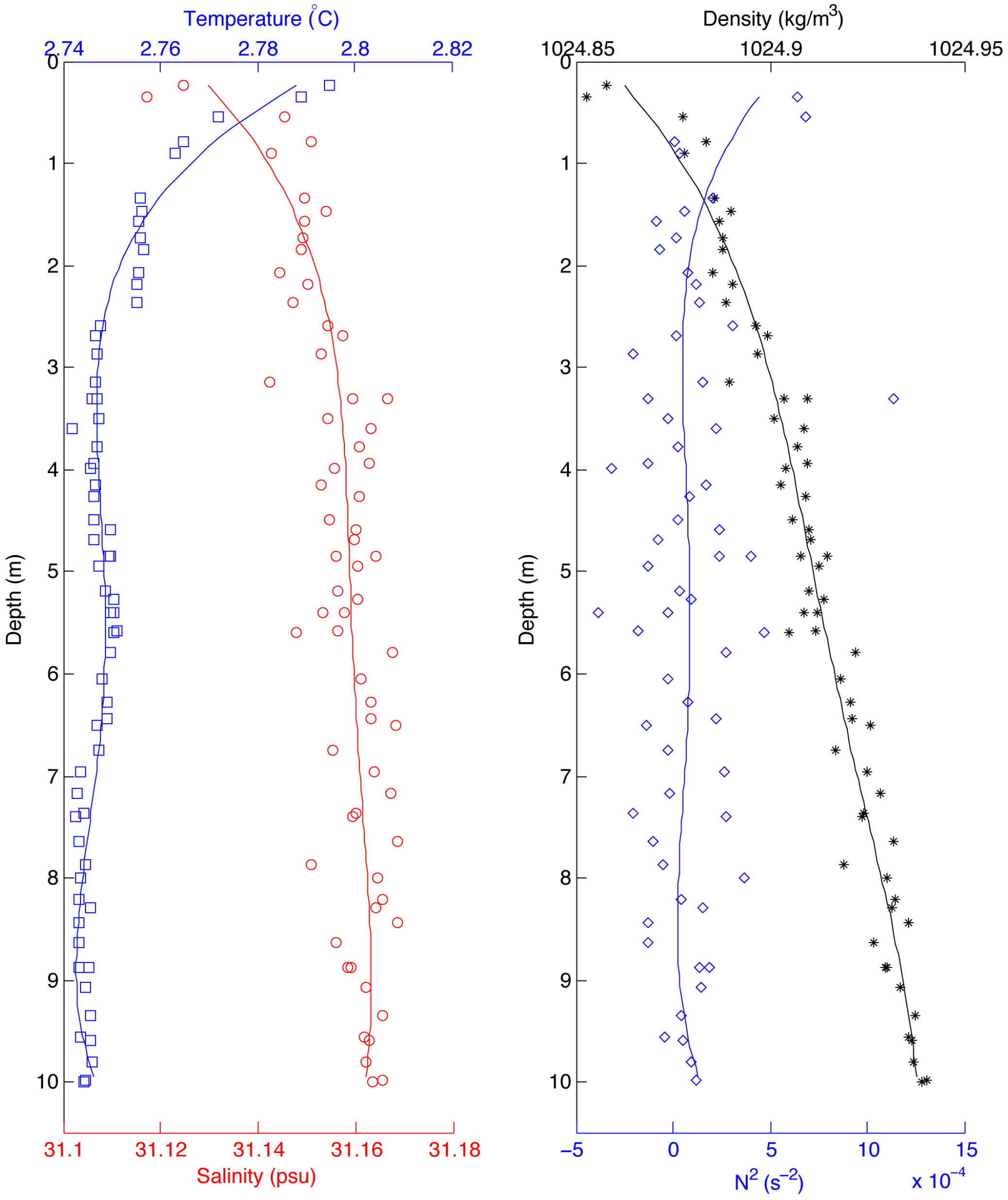

Figure B.19: Tower tank depth profile - Mar 30, 2011